APPLICATION OF THREE PHASE EBULLIETED BED REACTORS TO PETROLEUM UPGRADING

by

Deepak Anant Deshpande

A dissertation submitted to the faculty of
The University of Utah
in partial fulfillment of the requirements for the degree of

Doctor of Philosophy

Department of Fuels Engineering

The University of Utah

August 1992

THE UNIVERSITY OF UTAH GRADUATE SCHOOL

SUPERVISORY COMMITTEE APPROVAL

of a dissertation submitted by

Deepak Anant Deshpande

This dissertation has been read by each member of the following supervisory committee and by majority vote has been found to be satisfactory.

	Chair: Francis V. Hanson
	Milind D. Deo
	Alex G. Oblad
	Donald A. Dahlstrom
	A. Lamont Tyler

THE UNIVERSITY OF UTAH GRADUATE SCHOOL

FINAL READING APPROVAL

To the Graduate Council of The University of Utah:

I have read the dissertation of Deepak Anant Deshpande in its final form and have found that (1) its format, citations, and bibliographic style are consistent and acceptable; (2) its illustrative materials including figures, tables, and charts are in place; and (3) the final manuscript is satisfactory to the Supervisory Committee and is ready for submission to the Graduate School.

Date

Francis V. Hanson
Chair, Supervisory Committee

Approved for the Major Department

Larry L. Anderson
Chair/Dean

Approved for the Graduate Council

B. Gale Dick
Dean of The Graduate School

ABSTRACT

Three phase ebullieted bed reactors are appropriate for processing petroleum residues, bitumen and bitumen derived liquids. The length of a three phase ebullieted bed reactor, which is long at the commercial scale, can be reduced, for process research and development studies in the laboratory, by decreasing the superficial liquid velocity and solid particle size. It is necessary to maintain same phase holdups of the commercial reactor, to simulate the process kinetics in a laboratory reactor.

Similarity criteria that ensured identical phase holdups in commercial and laboratory units were identified, through extensive similitude studies. These criteria required the equality of six dimensionless numbers. It was impractical to establish all the parameters in the set of dimensionless numbers at the desired values for reacting systems. Therefore, a procedure was developed to achieve similarity by varying a minimum number of parameters, such as liquid and gas superficial velocities and particle size. This resulted in two conditions, which when satisfied yielded essentially equal holdups in the two reactors. These criteria and procedure were validated using the generalized wake model and experimental data for three phase systems.

The similitude studies identified the importance of the bubble rise velocity for scale down. Two different approaches were developed to predict the bubble rise velocity in three phase ebullieted beds. In the first approach, a mathematical model was developed to predict the volume of a single bubble generated at an orifice in a gas-liquid system at a constant gas flow rate. The model was based on a rigorous bubble closure mechanism and incorporated the interaction between the primary bubble and subsequent bubbles formed at the orifice at high gas flow rates. The

model also calculated the distance traveled by the bubble from the orifice before it detached. The model is applicable for both viscous and nonviscous liquids and for systems over wide ranges of hydrodynamic properties. The model was validated by comparison with the available experimental data and it was found that this model represented an improvement over previous models. This model was used to approximate the value of the bubble size in a high pressure three phase ebullieted bed with small solid particles.

In the second approach the concept of effective bubble rise velocity was introduced. The generalized wake model equations were manipulated to give correlations for the effective bubble rise velocity at atmospheric pressure. The parameters for the correlations were liquid and gas superficial velocities, liquid viscosity, surface tension and solid particle size. These correlations were categorized as per the type of three phase system, solid particle size and liquid and gas superficial velocities. Flow transition liquid velocities for various three phase systems were identified. Forms of the correlations were explained by addressing various hydrodynamic phenomena for three phase ebullieted beds such as flow regimes and their transitions, flow transition liquid velocity, solid wettability, bubble behavior, apparent bed viscosity and the effect of solid particles. The performance of the correlations was tested with experimental phase holdup data.

The influence of pressure on bubble behavior and bubble rise velocity in a three phase ebullieted bed was considered. This led to the introduction of a pressure factor in the bubble rise velocity correlations. The modified correlations were used to predict the bubble rise velocity in three phase ebullieted bed operating at high temperature and high pressure. The predictions of the modified bubble rise velocity correlations were evaluated, using the concept of drift flux, against experimental plots available from the literature. The trends of drift flux vs. gas holdup in the plots were found satisfactory.

Values of the gas and liquid densities, liquid viscosities and surface tensions at high temperature and high pressure were required for reactor scale down. A plot for temperature versus weight fraction distilled up to 813 K was obtained by simulated distillation for the native bitumen. A method was then developed to extrapolate the low temperature (813 K -) SIMDIS curve to high temperature (813 K +) region by matching the measured value of specific gravity of the native bitumen with the specific gravity calculated from the extrapolated curve. The extrapolated SIMDIS curve was used to develop a predictive correlative procedure for estimating the viscosity and surface tension of bitumen fractions and bitumen at high temperature and high pressure. The predictive method identified a new mixing rule for fractions of heavy feeds, where the viscosities of the individual fractions vary over a few orders of magnitude.

An overall procedure for scaling down a commercial three phase ebullieted bed reactor to a laboratory scale was then developed. The procedure ensured reduction in reactor length and maintained identical phase holdups and bubble rise velocity in both the reactors. The space velocity in the laboratory reactor was adjusted to achieve similar intraparticle mass transfer as the commercial reactor. Using the methods mentioned above for calculating the bubble rise velocity and physical properties of the feed and the overall scale down procedure, a detailed design of a laboratory scale three phase ebullieted bed reactor was carried out. This reactor can be used to carry out process development studies for hydrotreating/hydrocracking of bitumens and bitumen derived liquids in the laboratory, under conditions similar to the commercial reactor.

To my family

CONTENTS

LIST OF TABLES

LIST OF FIGURES

ACKNOWLEDGEMENTS

I would like to thank Professors Francis V. Hanson, Milind D. Deo and Alex G. Oblad for their motivation and support during this investigation. I would also like to thank the other members of my supervisory committee Professors A. Lamont Tyler and Donald A. Dahlstrom for their interest in this work.

I wish to express my sincere appreciation to the Laramie Projects Office of the Morgantown Energy Technology Center, U. S. Department of Energy for the financial support provided to the University of Utah Tar Sand Research Program.

Finally, I would like to thank my wife Anjali, my son Alok, and my daughter Dhruti for their encouragement throughout this work.

CHAPTER 1

INTRODUCTION

1.1 Nature of Bitumen

The large volume of imported oil moving into the United States at lower costs, coupled with political uncertainties in the Middle East and ever increasing exploration, drilling, completion and production costs have made the amount of oil in the bituminous sandstone deposits an important alternative source of fuel.

The recovery of hydrocarbon values from the extensive tar sand deposits of North America has been approached by one of two methods: in-situ thermal production of bitumen or of a bitumen derived liquid and surface mining of the deposit followed by processing of the mined ore. The produced hydrocarbon liquids must be upgraded to produce a suitable feedstock for subsequent processing in a conventional petroleum refinery. The in-situ thermal methods include steam injection (1), steam drive (2) and combustion (3). Recovery of bitumen from surface mined deposits is done by one of the following methods; water assisted separation (4), solvent extraction (5), solvent assisted aqueous separation (6), or thermal processing of tar sands (7).

The Uinta Basin samples have characteristically higher hydrogen contents and contain about twice as much nitrogen, but only about one tenth as much sulphur as compared to Athabasca samples. Vanadium and nickel metal contents are important because of the poisoning effect of these metal on catalytic refining processes. Uinta basin bitumens have a lower vanadium content, which is characteristic of

lower sulphur petroleum, but slightly higher nickel content when compared to bitumens of higher sulphur but lower nitrogen contents. These differences are related to the origin of bitumen. Dorius (8) and Oblad et al. (9) have presented the specific analyses of bitumens from Utah tar sands. The average bitumen properties from Whiterocks tar sand deposit are presented by Tsai et al. (10).

Viscosity and penetration data show that Uinta Basin samples are notably more viscous. The temperature-viscosity relationships for specific native bitumens are presented by Dorius (8) and Hupka and Miller (11). Higher viscosity affects recovery and upgrading processes and makes handling of the primary bitumen difficult. The viscosity data are consistent with the high average molecular weights and low percentage of naturally occurring distillables.

Uinta Basin bitumens have both a lower specific gravity and a higher molecular weight than the bitumens of marine origin, which suggests that these bitumens are significantly less aromatic and more naphthenic than bitumen of marine origin (9). The results are consistent with the higher hydrogen contents and heating values of Uinta Basin samples.

The amounts and types of heteroatomic functionality (molecules containing N, S, and O) have profound effects on the upgrading and processing of bitumen. The principal effects of high concentrations of heteroatoms are to increase viscosity, to increase the strength of chemical association of bitumen with minerals, to reduce yields and increase difficulty to catalytic processing of bitumen or bitumen products. Oblad et al. (9) have summarized the heteroatom compound types in the native PR Spring bitumen and indicated that the hydrocarbon skeletal structure of bitumen tends to be quite naphthenic due to the youthful era of tar sand deposition. Uinta Basin samples consist predominantly of bicyclic and tricyclic saturates. Carbon 13 - NMR analysis of total bitumen reveals that less than 20 % of carbon is aromatic. The saturate portion of the bitumen is highly complex, reflecting the

naphthenic/alkyl substituted nature of the bitumen. The lower molecular weight fractions of the bitumen from Whiterocks tar sands contain predominantly naphthenic hydrocarbons and lesser concentrations of aromatic hydrocarbons (10).

1.2 Processes for Upgrading Bitumen

Native bitumen cannot be used directly as a fuel due to its heavy nature and high heteroatom contents. It has to be therefore upgraded to reduce viscosity and heteroatom contents. The upgrading of bitumen and bitumen derived liquids can be accomplished by a variety of thermal and catalytic process. Visbreaking, while providing high yields, does not go very far in converting bitumen to distillates. Furthermore thermal cracking by delayed coking would probably be required to handle a visbreaker product. Coking of Uinta Basin bitumen results in good yields of liquids, owing to the favorable H/C ratio. Coker distillates tend to contain large amounts of heavy and vacuum gas oils that need to be catalytically cracked for gasoline and diesel production (9). Direct catalytic cracking has been shown to produce higher yields of high quality products when compared to coking. The naphthenic nature of the bitumen renders it responsive to catalytic cracking. The catalyst adds selectively to the cracking process and makes better use of the available hydrogen than does thermal cracking by coking.

Yields, product distribution and the liquid product quality of the hydrocarbons produced by pyrolysis of bitumen impregnated sandstone in a fluidized bed reactor have been investigated for a number of Utah tar sand deposits (8.12,13,14). The quality of the hydrocarbon liquids produced was superior to that of the native bitumen for all the deposits investigated except for the PR Spring South material. In general, the viscosities of the product liquids were lower than those of the corresponding native bitumens by several orders of magnitude. The volatilities

of the liquid increased relative to the native bitumen. The Conradson carbon residue, the asphaltene content, the molecular weights and the heteroatom and metal contents of the bitumen derived liquids were considerably lower than the native bitumen.

Pipelineable syncrude produced from the tar sands bitumen will be required to meet certain specifications especially for sulfur contents and viscosity before it can be accepted in existing pipelines. Catalytic hydroprocessing will be required to meet the heteroatom specification and as a result of this treatment sulfur content requirement will most likely be met. Bitumen has been processed in both coking/hydrotreating(C/HT) and hydropyrolysis/ hydrotreating (HP/HT) sequences. With (HP/HT), the yields of both gaseous and liquid hydrocarbon show major increase compared to C/HT yields. Results of hydrotreating of virgin bitumen and upgraded bitumen have also been reported (15,16). This work showed that nitrogen, sulphur, and metal can be removed under normal process condition (< K, 13.79 MPa and a liquid hourly space velocity of 1 hr^{-1} provided the molecular weight of the feed stock is modest. Resistance to hydrodenitrogenation increases as the molecular weight increases, suggesting that poor hydrodenitrogenation is due mainly to poor accessibility to the catalyst surface and not necessarily due to the functional types presents (9). This implies that the objective in upgrading bitumen should be to reduce either the molecular weight or the mass transfer resistance to the catalyst surface during the hydrotreating process. A three phase ebullieted bed would be appropriate for catalytic hydroprocessing of bitumen and bitumen derived liquids to satisfy the latter objective.

1.3 Need for Scale-down

Three phase ebullieted bed reactors have been widely used for physical, chemical, petrochemical and electrochemical processing (17). In petroleum and synthetic fuel industry, three phase ebullieted bed reactors have been used for hydrotreating and upgrading of heavy petroleum and synthetic crude (18).

Typical phases and operating conditions in a three phase ebullieted bed reactor processing bitumen derived liquids are:

1. Liquid phase: bitumen derived liquids
2. Solid phase: pelleted catalyst
3. Gas phase: hydrogen and light hydrocarbon gases.
4. Temperature range: 698 - 758 K.
5. Pressure: 13.5 - 20.0 MPa.
6. Liquid hourly space velocity: 0.5 - 1.5 volume of feed/volume of catalyst-hour
7. Hydrogen to bitumen ratio 0.55 to 0.65 by volume.

Due to the relative high mass of the catalyst pellet, the liquid velocity required for ebullietion is high. High liquid velocity coupled with low liquid hourly space velocity makes three phase ebullieted bed reactors long. The Exxon Donor Solvent Coal Liquefaction pilot plant process studies were conducted in the following systems (18).

1. Recycle coal liquefaction unit with 10, 1.2 m. long reactors connected in series.
2. Coal liquefaction unit with three, 7.3 m. long reactors connected in series.
3. EDS coal liquefaction pilot plant with four, 18 m. long reactors connected in series.

The length of the fluid dynamic unit used by Amoco Oil Company to study the three phase ebullieted bed hydrodynamics for H -Coal was 24 m. long (19).

A three phase ebullieted bed reactor for processing bitumen, operating under the process condition mentioned above, with 1.6 mm diameter x 4.8 mm long catalyst pellets would have a length around 22 m. Such long reactors are expensive to build and cannot be used in the laboratory for carrying out bench scale studies. It is therefore imperative to reduce the length of the reactor so that the hydrodynamics and the kinetics of the process can be conviniently studied in the laboratory. Scaling down the three phase ebullieted bed reactor is the final objective of this study. The methodology used to arrive at this objective is presented in the subsequent chapters, the contents of which are noted very briefly below.

1.4 Overall Approach

A literature survey of hydrotreating and hydrocracking, three phase ebullieted beds, models of the hydrodynamic of three phase ebullieted beds and bubble behavior in multiphase systems is presented in Chapter 2. This information is used to select the upgrading process for bitumen derived liquids and an appropriate reactor for the upgrading process. A suitable mathematical models to represent the hydrodynamics of three phase ebullieted beds is chosen. This model is frequently used to arrive at and validate the various criteria, procedures and correlation formulate throughout these studies. The survey on three phase ebullieted beds and the bubble behavior in multiphase systems is used to formulate the bubble models and justify the form of correlations for the bubble rise velocity.

After identifying the need for scaling down the three phase ebullieted bed reactor for laboratory studies, the development of the scale down criteria and practical scale down procedure is undertaken in Chapter 3. The philosophy for scale down,

to ensure reduction in reactor length with same phase holdups and liquid hourly space velocity as the large scale reactor. The hydrodynamic parameters which govern the phase holdups in three phase ebullieted beds were then identified. A rigorous dimensional analysis was used to derive the similarity criteria for reactor scale down. The limitations on the applicability of the similarity criteria to reacting systems led to the development of a practical scale down procedure. The algorithms for the generalized wake model and stagewise partition models, which are used for validating the similarity criteria are discussed. The computer codes for the generalized wake model are presented in Appendix A.

The importance of bubble rise velocity (u_{br}) and the need to predict its value was identified in the similitude studies. Two different approaches for predicting u_{br} were developed. The first approach attempted to predict bubble size by considering the single bubble behavior in a multiphase system and is detailed in Chapter 4. The second approach, which applied the concept of effective bubble rise velocity was used to generate correlations for u_{br}. This approach is presented in Chapter 5.

The development of a bubble model for predicting bubble volume at constant gas flow rate in a gas-liquid system is discussed in Chapter 4. The procedure for applying this model for various ranges of gas flow rates is then presented and the output of the model is compared with the experimental data. The effect of pressure on bubble formation was also incorporated in the model. Next, the procedure for using the bubble model to approximate the bubble size in three phase ebullieted bed reactors operating at high pressure is presented. The computer codes covering the proposed bubble model are presented in Appendix B.

The correlations for u_{br} are developed in Chapter 5. Prevailing methodologies for predicting u_{br} and the concept of effective bubble rise velocity are discussed. The correlations for u_{br} were then derived by manipulating the equations of the generalized wake model and using experimental hydrodynamic data for three phase

ebullieted beds. After a detailed description of the various hydrodynamic phenomena in three phase ebullieted beds, the forms of correlations were shown to be consistent with these phenomena. The concept of drift flux and its applications for predicting high pressure behavior of three phase ebullieted bed are discussed. The correlations for u_{br} were modified to incorporate the pressure effect. The computer code used to determine the optimum bubble rise velocity from the hydrodynamic data for three phase ebullieted beds is presented in Appendix C.

The significance of the physical properties during scale down of three phase ebullieted bed is examined in Chapter 6. A methodology was developed to extrapolate low temperature SIMDIS data to a higher temperature range. A predictive correlative scheme was then developed for estimating the viscosity and surface tension of bitumens and bitumen fractions at high temperature and high pressure. A new mixing rule, for mixing bitumen fractions, to give the viscosity of the mixture was incorporated in the scheme. The performance of the scheme was compared with the experimental data for viscosity of bitumen and bitumen fraction at low temperatures. Finally the predicted values and trends of physical properties of bitumen and bitumen fractions are presented. The computer code covering the predictive correlative procedure is presented in Appendix D.

The conceptualization of a laboratory system and the design of a high temperature , high pressure three phase ebullieted bed reactor, to study process hydrodynamics and kinetics of hydrotreating/ hydrocracking of bitumen derived liquids is described in Chapter 7. Using the methods for predicting d_b, u_{br} and physical properties and the practical scale down procedure, a detailed hydrodynamic design of the reactor was carried out followed by mechanical design and specifications. The computer code for scaling down the commercial reactor to laboratory scale is presented in Appendix E. The conclusions and recommendations for future work are presented in Chapter 8.

CHAPTER 2

LITERATURE SURVEY

Information, available in the literature, on following topics is covered in this chapter.

1. Hydrotreating

2. Hydrocracking

3. Feedstock characterization

4. Hydrodynamics of three phase ebullieted bed.

5. Mechanics of bubbles and bubble wakes in three phase ebullieted bed.

The information on hydrotreating, hydrocracking and three phase ebullieted beds is used to identify a suitable process for hydrotreating and hydrocracking bitumen and bitumen derived liquids. The survey on mathematical models for hydrodynamics of three phase ebullieted beds is used to select appropriate models, which are then frequently used to arrive at and validate the various criteria, procedures and correlations formulated throughout these studies. The survey on hydrodynamics of three phase ebullieted bed has been used to study and explain the behavior of various correlation derived in these studies.

2.1 Hydrotreating

2.1.1 Applicability of Hydrotreating

The main objective in hydrotreating is product upgrading of heavy feedstocks through the removal of heteroatoms and metals. Hydrotreating processes include several types of reactions which compete for the available hydrogen. These reactions include hydrodesulfurization (HDS), hydrodenitrogenation (HDN), hydrodemetalization (HDM), hydrodeoxygenation (HDO), and some hydrocracking, coking and thermal cracking.

2.1.2 Hydrodesulfurization

Hydrodesulfurization (HDS) reactions can be represented by the following general formula

Organic Sulfur Compound + H_2 $\longrightarrow$ H_2S + Desulfurized Product

HDS may occur through a combination of hydrogenation and hydrogenolysis reactions or directly through hydrogenolysis reactions. HDS occurs catalytically with both the sulfur compound and hydrogen adsorbed onto the catalyst surface. Sulfur adsorption appears to control the reaction sequence. Adsorption through the sulfur atom leads directly to sulfur removal. However, adsorption of the sulfur compound with an orientation parallel to the catalyst surface allows initial hydrogenation steps to occur (). Several general reviews exist on hydrodesulfurization (21-28). HDS reactions are exothermic with heat of reactions from 445 to 890 kcal per m^3 of hydrogen consumed at STP (22). Those reactions that involve the most hydrogenation show the highest heat of reaction.

Desulfurization rates vary according to the type of organic sulfur compound being reacted. Aromatic fraction sulfur compounds show the highest reactivity and those in the asphaltenes the lowest. However, as the extent of desulfurization increases, the sulfur compounds remaining are increasingly less reactive (29). The

lower reactivity of the asphaltene fraction towards desulfurization leads to a lower degree of hydrogen selectivity for desulfurization over hydrogenation than is experienced in removing the nonasphaltenic sulfur. Laboratory studies of HDS reactions focussing on model compounds have established a relative order of reactivity for various sulfur compounds (21).

2.1.3 Hydrodenitrogenation

Hydrodenitrogenation HDN reactions have been suggested to occur through the adsorption of the nitrogen compounds on one site and noncompetitive adsorption of hydrogen on another site. The difficult step in HDN reactions is the heterocyclic C-N bond scission giving ring opened products (30). Hydrogenation steps are required for activation of the C-N bond.

Hydrogen consumption in HDN reactions reflects both the hydrogen required to remove nitrogen directly and that used in activation and saturation of C-N bond. Laine (11) suggested that the H_2 promotes denitrogenation through nucleophillic attack on the metal complexed (adsorbed) ring structure.

The relative reactivities of nitrogen compounds depend on both their relative susceptibility to nitrogen elimination and their relative affinity for adsorption on the catalyst active sites. Koros et al. (31) found that quinoline type compounds showed a higher rate of reaction than indole type compounds despite their lower reactivity in an isolated environment. Basic nitrogen compounds strongly adsorb on acidic sites on the catalyst surface, whereas nonbasic compounds adsorb mildly.

2.1.4 Hydrodeoxygenation

For coal liquids and other synthetic crude oils, oxygen removal contributes significantly to hydrogen consumption in a hydrotreator. As in the case of HDN reactions, a combination of hydrogenation and hydrogenolysis steps is required.

Rollman (32) and Badilla-Ohlbaum et al. (33) observed significantly higher hydrogen consumption for oxygen removal compared to that of sulfur removal for corresponding heterocyclic compounds. This behavior suggests a greater need for hydrogenation steps in Hydrodeoxygenation (HDO) (34). Similarities in the electron withdrawing effects and unpaired electrons of sulfur and oxygen atoms suggest similar behavior on the catalyst surface; however, the significant difference in atom size may lead to a greater degree of steric hindrance by the hydrocarbon portion of the molecule in oxygen compounds (34). In model compounds such as dibenzofuran, the initial hydrogenation pathway is favored under high hydrogen partial pressures, but as the availability of surface hydrogen decreases the extent of initial hydrogenation decreases and the ring scission or oxygen removal pathways becomes more prominent.

2.1.5 Hydrometallization

The removal of vanadium and nickel from complex organometallic compounds can occur through the coordination of the metal with sulfur (35) or through a combination of hydrogenation and ring scission steps (36,37). The reaction sequence proposed by Ware and Wei (36,37) shows two initial, reversible hydrogenation steps followed by ring scission and metal deposition. Metal deposition occurs either directly or following an additional hydrogenation step. The reactions occur on or near the catalyst surface.

The metal deposited on the catalyst surface promotes further demetalization activity. For demetalization, the activity of the carrier increased as vanadium was deposited and ultimately attained the activity of the metal/carrier catalyst (38). Galiasso et al. (39) reported that the HDM reactions follow first order kinetics with respect to metals content for both the resin and asphaltene fractions and different orders with respect to hydrogen partial pressure.

2.1.6 Catalysts

Typically, hydrotreating catalysts for petroleum resids consist of Mo on γAl_2O_3 with Co or Ni promoters. Tungsten also shows good catalytic behavior but its use is limited commercially due to its high cost. The specific surface area of hydrotreating catalysts ranges from 100 to over 300 m^2/g and pore sizes regularly show a distribution between 40 and 200 Å. Several commercial catalysts along with the preferred metals and other important properties have been listed by Fan (20).

Catalyst sites active in hydrotreating result both from any acidic nature of the support material (alumina) and Co-Mo interactions. The acidic sites show activity for cracking reactions and are subjected to strong adsorption by basic compounds (nitrogen compounds). A lack of understanding exists about the interactions between Mo and Co or Ni and the resulting active sites they form. Discussions about these interactions and the resulting active sites can be found in 21, 22, 24, 28, 40 and 41. It is generally believed that the sulfur compounds adsorb at atomic vacancies on the catalyst surface. Interactions with nearby hydrogen adsorption sites through proton and electron transfers make up the HDS reactions.

2.1.7 Catalyst Infrastructure

The mean pore size distribution, the surface area, and the pore volume are all important to the effectiveness of the catalyst towards desulfurization and demetalization. Increasing the surface area, pore size, and pore volume increases the desulfurization rate (42,43). The pore size affects the desulfurization and demetalization rates through diffusional and surface area effects. Pore sizes less than about 40 Å are ineffective for desulfurization due to molecular size considerations. The low effectiveness towards demetalization below 100 Å results from the exclusion of asphaltenes from the catalyst pores. For the same pore size limit, the decrease in

the extent of desulfurization may be due to a decrease in overall surface area with increasing pore size.

The effect of particle size on desulfurization suggests that mass transfer limitations exist. Ohtsuka (43), using a fixed capacity layer of catalyst, found that the extent of sulfur removal increased as catalyst size decreased. In addition, for a constant bed volume, Kato et al. (44) found that, for catalyst sizes smaller than 1 mm, a first order rate constant varied proportionally with the reciprocal of the catalyst size, but above 1 mm the rate constant was nearly independent of catalyst size. A limit exists on the size of an individual catalyst above which mass transfer limits the observed reaction rate and below which intraparticle diffusion becomes important; the exact value of the limit depends on the internal pore structure.

2.1.8 Catalyst Deactivation

Deactivation of HDS catalysts occurs through surface area loss and active site poisoning. Products from both coking and HDM reactions form deposits on the catalyst surface. Consequently these deposits prevent access for the reactant molecules to the internal active sites, by blocking the pores. Typically, the deposits of HDM reactions block the internal pore structure and those of coking reactions block the pore mouths. Only a small portion of that lost surface area may be regenerated by burning off the coke. Most of the permanent loss is due to irreversible metal deposition.

Metals deposit profiles depend on the diffusional limitations of the organometalic compounds from which they originate. For the demetalization of resins, the resulting metal deposit profile proves to be homogeneous whereas for asphaltenes the profile shows large deposits in the external surface regions (39). Vanadium deposits mainly near the external surface whereas Ni deposits more uniformly. In a high hydrogen partial pressure environment, which is essentially a coke suppressing

environments, smaller catalyst show longer lives than larger catalyst because of a more uniform distribution of metal deposits (45).

The pore size distribution significantly affects the deposit distribution of vanadium. A bimodal pore size distribution allows greater access to the internal pore structure and consequently a more complete penetration by the metal complexes. However, changes in pore structure towards a bimodal distribution also result in reduced overall surface area.

Hydrogen partial pressure affects catalyst deactivation through the relative rates of metal, or coke deposition. High hydrogen pressures reduce coke formation and increase HDM reaction rates. Under conditions where the deactivation rate is controlled by coke formation, high hydrogen partial pressure will reduce the deactivation rate. However, when HDM reactions control the deactivation rate, an increase in hydrogen partial pressure will increase the demetalization rate (26).

Catalyst demetalization activity varies as a unique function of the weight fraction, based on fresh catalyst, of metals deposited on the catalyst (46). Catalyst deactivation behavior shows an initial rapid decline in activity followed by a relatively long period of nearly linear decay. The sharp decrease in the activity during the very early stage of the catalyst life is attributed to coke deposition (46). Metals deposition is a slow process relative to coke deposition and contributes to deactivation during the bulk of the catalyst life. Thus, catalyst deactivation kinetics can be expressed solely in terms of the extent of metal deposition on catalyst. Dautzenberg et al. (47,48) proposed a two parameter pore mouth plugging model to describe catalyst deactivation behavior due to metal deposition. The model assumes zero order kinetics with respect to metal content.

$$\frac{A_m}{A_{mo}} = 1 - t^* \tag{2.1}$$

$$\frac{C_m}{C_{m,max}} = 2t^* - t^{*2} \tag{2.2}$$

In these equations, t^* is a dimensionless time (0 for fresh catalyst and 1 for spent catalyst); A_m and A_{m0} are the activity and initial activity, respectively; and C_m and $C_{m,max}$ are the metal content and metal uptake capacity, respectively. The two parameters for this model A_{m0} and $C_{m,max}$ can be expressed in terms of catalyst dimensions and physiochemical constants of the reaction system (48).

2.1.9 Catalyst Selectivity

An important issue in the design of catalysts for hydrotreating stems from the conflict between HDS activity and metal tolerance. HDS reactions occur within the catalyst infrastructure and rates show an increase with an increase in total surface area. Metal deposition poses the most serious problem in terms of deactivation. For a long catalyst life, large pores, and consequently smaller surface area are required for adequate use of the entire catalyst for metal deposition. Thus the two optimum cases, a high surface area for desulfurization and large pores for demetalization, are not compatible. The catalyst may be tailored for either HDS or HDM reactions but not for both as mentioned. A high extent of metal removal can be obtained at a sacrifice in extent of HDS.

In recent years, the trend has been to carry out the hydrotreating process in stages. The initial stage is designed for demetalization with a catalyst optimized accordingly. The succeeding stages are designed for desulfurization. Toulhoat et al. (49) suggested several guidelines for the development of HDM catalysts. First, whereas metals are complexed in large molecules a proper pore size distribution is necessary to allow the metals to reach all the active sites. Second, the catalyst should use efficiently the available porosity for metal accumulation by having the

HDM reaction as rate limiting. Third, coke deposits have to be minimized during the early operational age of the catalyst.

2.2 Hydrocracking

2.2.1 Applicability of Hydrocracking

Hydrocracking is a highly flexible process for producing varying ratios of gasoline and middle distillate. Even greater flexibility is possible during design stages, when the process can be tailored to convert heavy residue into lighter oils or to change straight run naphthas to LPG.

Distillate feedstocks suitable for such processing range from heavy naphthas, kerosene and refractory catalytically cracked cycle stocks to high boiling virgin and coker gas oils. At high severities, hydrocracking can completely convert these materials to gasoline and lower boiling paraffins. Lesser severities allow substantial conversion of the higher boiling point material into middle distillate fraction of high quality for diesel and jet fuels (50).

Hydrocracking has been successfully used for upgrading bitumen from Athabasca tar sands. The properties of this bitumen and the product obtained by hydrocracking this bitumen in the H-Oil process are presented by Rapp and Driesen (51). Inspection of the properties of bitumen indicates that the bitumen is sour and heavy. Upgrading and refining will require cracking, sulfur reduction and hydrogen addition, which is possible by hydrocracking. Inspection of properties of products shows that hydrocracking is greatly effective. The products are not in the finished condition, but ready for sale as synthetic crude. The distillate fractions need further processing to saturate the olefines and to reduce sulfur and nitrogen contents. However, by performing the primary conversion at relatively mild hydrogenation conditions , it can be seen that the unconverted bottoms have a low API gravity.

Thus, the quantity of hydrogen in these bottoms has been minimized. This is the proper approach because the bottom would often be burned as fuel and would not need to be of high quality.

Because the properties of the Utah tar sand bitumen are similar to Athabasca tar sand bitumen (52) (except for the lower sulfur and higher nitrogen contents) we can expect that the hydrocracking process will be similarly effective for upgrading Utah tar sand bitumen.

2.2.2 Commercial Processes

2.2.2.1 Isocracking Process

Licensor: California Research Corporation (53).

Application: The process may be operated once through for the production of gasoline and a bottom product that can be fractionated to give a jet fuel component, or marketed as a high quality middle distillate stock. For gasoline production alone, the process operates at about 60 % conversion per pass, with recycle of higher boiling point components for ultimate conversion. Decreasing gasoline end point below 400 F° increases the yield of C_4 and C_5-180 F° at the expense of 180 F° +, with the total butane plus yield increasing only slightly.

Description: The process operates in the temperature range of 478-644 K (400-700° F) and pressure between 3.445-10.335 MPa (500-1500 psi). Most feedstocks require extensive hydrofining in a feed pretreatment section to remove undesirable nitrogen compounds. This helps maintain catalyst activity at a high level and thereby allows low temperature in the fixed bed reactor with minimum light gas formation. Composition of catalyst has not been revealed, but its cost is said to be much less than that of conventional noble metal reforming of isomerization catalysts.

2.2.2.2 Lomax Process

Licensor: Universal Oil Product Company (54,55).

Description: The Lomax process is adaptable to processing virgin stocks boiling from kerosene through heavy vacuum gas oil, and including thermal and conventional catalytic cracked cycle stocks as well. The process can produce either high quality gasoline or middle distillates as primary products. For maximizing middle distillates, the process flow is single stage, with 40-80 % conversion per pass and recycle of material boiling above the desired end point. For maximizing gasoline, a second process stage is used. In this arrangement, the first stage fixed bed reactor is operated once through for middle distillate production. The 400 ° F +, first stage product, low in undesirable components such as nitrogen compounds and metals, is then processed through the second stage fixed bed reactor, with recycle of material boiling above the gasoline end point.

2.2.2.3 BASF-IFP Process

Licensor: Institute Francais du Petrole and Badische Anilin and Soda-Fabrik AG (56).

Application: This process is adapted especially to handle heavy sour feedstocks (such as heavy vacuum straight run or cracked distillates and deasphalted vacuum residuum) and to produce gasoline, jet fuel and/or diesel oil.

Desription: From heavy vacuum gas oil and/or deasphalted vacuum residuum maximum middle distillates or jet fuel are produced in a single stage fixed bed down flow reactor operating once through or with liquid recycle, depending mainly on the characteristics of the feed stock and quality of products required.

Starting from the above mentioned heavy stock a maximum amount of gasoline is produced in a two stage process. In the first stage the heavy stock is thoroughly desulfurized, denitrogenated and cracked. In the second stage, cracking is achieved

in order to complete the production of a very high quality gasoline. Unconverted feed may be recycled to the reactor system as desired.

2.2.2.4 H-Oil Process

Licensor: Hydrocarbon Research Inc. and Cites Services Research and Development Co (57).

Applications:

1. To convert heavy residue and asphalt into lighter fractions including naphthas, distillates, petrochemical feed stock and cat cracker charge.

2. To convert heavy gas oils into lighter fractions, also applicable to processing of dirty stocks including those containing solids.

3. To upgrade bitumen to give synthetic crude oil.

Description: Hydrogen and heavy oils are reacted in a three phase ebullieted bed reactor. The system achieves extremely efficient catalys-oil-hydrogen contact, while providing an isothermal environment for the extremely exothermic reactions taking place. Catalyst is added to and withdrawn from the operating unit, permitting a constant level of product quality and operating conditions.

The catalyst addition and withdrawal feature enables the refiner to process extremely heavy stocks, including those with high metal content, since it is not necessary to interrupt operations for catalyst replacement or regeneration.

2.2.2.5 Unicracking - JHC Process

Licensor: Union Oil Co. of California and Esso Research & Engineering Co.(58).

Application: Production of high quality gasoline, jet fuel and midbarrel products by catalytic hydrocracking.

Charge: Catalytic cycle oil, coker, virgin and thermal gas-oil, catalytic, thermal and virgin heavy naphthas.

Product: Gas oil can be converted totally to gasoline stocks or to blends of gasoline and high quality midbarrel stocks. Liquid product yield is generally from 110 to 125 volume % of feed. Methane and ethane yields are very low. The C_4, C_5 and C_6 fractions contain a higher than equilibrium percentage of high octane isoparaffins. The C_7-400 F° end point product gasoline in many case may be blended directly to gasoline and is an excellent reformer feedstock requiring no pretreatment.

Description: The Unicracking - JHC process is a fixed bed down flow catalytic hydrocracking process using a high activity regenerable catalyst having excellent activity maintainance capacity in the presence of nitrogen and sulfur compounds. Either two stage or single stage cracking can be utilized. Because of the unique catalyst, total conversion of most feedstocks can be effected with recycle to a single stage. Normal process conditions are in the range of 400-800° F, at a pressure of 3.445-10.335 MPa. (500-1500 psi.).

2.2.2.6 BOC Isomax Process

Licensor: Cheveron Research Co. (59).

Application: The Isomax process has the flexibility to produce gasoline, jet fuel and middle distillate products and to vary the yields of these products by on line process control.

Description: Isomax first stage reactor section consists of a down flow fixed bed reactor and produces gasoline and middle distillate products as well as demetalized, low nitrogen content feed for fluid catalytic cracking and further hydrocracking. Normally a larger portion of the product above desired middle distillate is a superior feed stock for FCC. A second stage reactor can be added to the process which serves to produce gasoline and jet fuels.

2.2.3 Solid Catalyst Requirement and Behavior

2.2.3.1 Requirements of Solid Catalyst

The composition of solid catalysts, which are most generally used for hydrocracking, is consistent with the viewpoint that the reaction mechanism combines the features of catalytic cracking with hydrogenation. Effective hydrocracking catalyst usually contain a good cracking component, such as silica-alumina, silica-zirconia, silica-magnesia, zeolites (faujasites and mordenites) and a hydrogenation component, such as platinum, tungsten oxide or nickel. The cracking component may be altered by promotion with another metal or by some pretreatment, such as sulfiding.

Hydrocracking catalyst is made by depositing the hydrogenation component upon solid, microporous cracking constituents. The hydrogenation catalyst tends to cover some of the acid sites and exclude them from the reaction. To obtain an optimum catalyst, the quantity of the hydrogenation component added must be balanced against the amount of acidity lost by its addition. A suggested mechanism of interaction between the hydrocarbon reactants and the two catalyst sites is as follows (60): the reactant is adsorbed on the acid site and ionized, then isomerized and cracked to form another adsorbed ion and an olefin. The olefin is either desorped and diffused through the gas phase to the hydrogenation site or continues to diffuse along the surface without being completely desorped.

Irrespective of the detailed fashion in which hydrocracking catalysts function, it is apparent that reaction kinetics play an important part in determining the nature of the hydrocracked product. Because the only function of the catalyst is to alter the kinetics of the reaction, the specific nature of the component making up the hydrocracking catalyst becomes of significant. Two particular features are worth considering. First, the inherent saturation activity of the hydrogenation constituent is important. It is possible to have considerably more hydrogenation

activity than is necessary merely to saturate the olefinic products and keep the catalyst free of the carbonaceous deposit. Excessive hydrogenation activity can result in the unnecessary saturation of aromatic rings present in the reactant which could, if retained, result in a higher octane number gasoline and reduced hydrogen consumptions. Metallic hydrogenation components such as platinum or nickel, tend to saturate aromatics more readily than oxides or sulfide catalyst, such as cobalt molybdate or tungsten oxide. If multiplering condensed aromatics are present in the reactant, it is desirable to saturate all but one ring during hydrocracking when gasoline is the desired product. Thus, the choice of hydrogenation component is dependent upon both the product desired and the nature of the charge.

A second consideration that arises from reaction kinetics and affects the choice of the hydrogenation component is the branched nature of the product. Hydrocracked products typically contain branched aliphatics in excess of equilibrium quantities, which is a situation that can arise only because of favorable reaction kinetics. If the isomerization activity of the catalyst were sufficiently great, the excess branched product would be equilibrated before leaving the reactor. Certain hydrogenation component, notably the noble metals, appear to possess an isomerization activity independent of that contributed by the cracking support upon which they may be distended. Thus, when highly branched products are desired, the choice of the hydrogenation component is also important. The nature of the cracking component can also affect the degree of branching in the products.

The component that makes up a hydrocracking catalyst determines not only the nature of the products but also such important factors as the process condition and the process cycle length. Activity and selectivity can be varied widely and, unlike some other processes, quite a large variety of catalysts are active and useful for hydrocracking, although virtually all incorporate the dual function of acidity and hydrogenation activity. The choice of a particular catalyst from this large group

depends upon the nature of the charge stock, the desired products and economics.

2.2.3.2 Behavior of Solid Catalysts

Yields and product properties in hydrocracking are influenced by the relationship between catalyst acidity and the hydrogenation-dehydrogenation activity of the dual function catalyst employed. Hydrocracking catalyst can be tailored to meet specific refining objectives. Sullivan et al. (61) employed both amorphous and crystalline catalysts of varying acidity and hydrogenation activity to examine their behavior at constant process condition for:

1. Production of both jet fuel and gasoline.

2. Production of gasoline as the major product.

Observation by these researchers were:

1. Most dual functional hydrocracking catalysts show an inverse relationship between C_5+ liquid and the F-1 clear octane number of the C_5 - C_6 products.

2. Preferential poisoning of either the acid sites or the remaining hydrogenation-dehydrogenation sites indicates that both the yields and octane number are related to the ratio of the hydrogenation to acidity provided by the catalyst. A high ratio favors high liquid yields; a low ratio favors high octane products.

3. Some modest changes in the relationship between C_5+ yield and light octane number occurs as catalyst temperature is increased.

4. With certain aged catalyst such as those containing faujasite, changes in catalyst geometry, brought about by plugging due to carbonaceous deposits may cause substantial deviation from above relationships.

2.2.4 Oil Soluble Organometallic Catalyst

Oil soluble organometallic catalysts have been deployed to hydrocrack Athabasca bitumen (62,63,64). The liquid phase hydrocracking of Athabasca bitumen by oil soluble carboxylates of nickel, cobalt, tin and iron was investigated at a concentration (based on the metal) of 100 ppm in the bitumen (62). The evaluation of the catalytic performance was conducted at reaction temperature of 673.15 K and 698.15 K and at initial hydrogen pressure of 6.89 MPa (1000 psig) and 10.33 MPa (1500 psig) using a residence time of one hour. When ranked on the basis of the highest percentage asphaltene and lowest percentage of hydrocarbon gas formation and coke yield, the catalytic metals were placed in the following order: Ni > Co > Sn = Fe = thermal hydrocracking. The activity of the nickel catalyst at a concentration of 100 ppm was judged to be sufficient enough to produce feedstocks for further hydrotreating. Using this catalyst at 673.15 K and 10.335 MPa (1500 psig) initial hydrogen pressure gave an asphaltene conversion of 57 % of the original asphaltene and a yield of cracked gases and volatiles of 2.3 wt. % of the bitumen. Increasing the temperature to 698 K increased the yield of the cracked gases to 16.7 % and the asphaltene conversion to 65 %, and resulted in reduced concentration of sulfur in both the asphaltene and maltene fraction. However the nitrogen and oxygen concentrations in the asphaltene increased, indicating the greater relative stability of the hetero compounds in the core of the asphaltenes. At 400 C°, on the basis of the % asphaltene conversion, it was found that nickel carboxylate and molybdenum acetylacetonate were essentially equivalent in catalyst activity and were the most active catalysts (63). These catalysts gave the lowest quality of hydrocracked liquid product compared to other catalysts as measured by the density and viscosity due to the effectiveness of these catalysts in converting the asphaltenes and high molecular weight polar compounds to pentane soluble liquids. At 425 C° these catalysts gave the best quality of hydrocracked liquid products due

to their superior capacity to upgrade the liquid products. Nickel and molybdenum had sufficient activity at a concentration of 100 ppm to be considered as a potential liquid phase catalyst that could be used without the need for catalyst recovery.

Athabasca bitumen was also hydrocracked in the presence of nickel and molybdenum naphthanates (64). Maintaining the nickel to molybdenum weight ratio constant at 1:1, the consequence of varying the total metal concentration in the bitumen from 50 to 300 ppm on the product quality was investigated at 698.15 K and 13.78 MPa (2000 psig) of hydrogen. The extent of asphaltene conversion decreased rapidly below 50 ppm of total catalyst metals and there was little merit in increasing the catalyst concentration above 100 ppm to achieve higher conversions.

2.2.5 Mechanism of Hydrocracking

The reactions occurring during hydrocracking have been studied by many authors (60,65-72). In general, the conclusion is that the mechanism of hydrocracking is similar to that of cracking with hydrogenation superimposed. Rapid hydrogenation of the olefinic products made during cracking prevents their readsorption on the catalyst, thus suppressing coke formation and maintaining cracking activity of the catalyst at a high level. This, coupled with a relatively high feed partial pressure, allows cracking to proceed rapidly at a lower temperature than is required in catalytic cracking alone and for a much longer process period without requiring regeneration of the catalyst.

With a conventional hydrocracking catalyst such as sulfided nickel supported on a silica-alumina, the isomerization of paraffins seems to be of little importance. As in catalytic cracking, quaternary paraffinic structures are not found in the hydrocracked product, and uncracked normal paraffins from the feedstock tend to retain their normal structure. Extensive splitting produces large amounts of low molecular weight paraffins ($C_3 - C_6$) with a much higher iso/normal ratio

than would be expected by the prevailing thermodynamic equilibria. From this, a primary reaction of paraffins appears to be extensive catalytic cracking followed by hydrogenation to form isoparaffins directly.

With a catalyst of much higher hydrogenation activity, such as platinum on silica-alumina, however, direct isomerization activity appears to be much greater. Isomerized charge stock has been noted in the product from hydrocracking a normal paraffin with this catalyst (73). A higher ratio of intermediate to low molecular weight paraffins was also found in the product from this catalyst. This indicates less secondary splitting, presumably also a consequence of the higher hydrogenation activity of the platinum component in more rapidly converting cracked products to more stable paraffins. This property is desirable for minimizing the ratio of gas to liquid products during hydrocracking thus leading to less hydrogen consumed in reaction of this type.

The lower activity of hydrogenating component such as nickel sulfide or tungsten sulfide can be advantageous, however, in maintaining the high iso/normal ratio of light paraffins made during hydrocracking. The use of more highly active hydrogenation components, such as metallic nickel and platinum of known hydroisomerization activity, can lead to lower iso/normal paraffin ratios more approaching thermodynamic equilibrium. When hydrocracking a pure normal paraffin , iso/normal light paraffin ratios even below the normal equilibrium value have been obtained during hydrocracking over metallic type catalyst, whereas much higher iso/normal paraffin ratio were obtained with the same catalysts after converting the metals to sulfides (74). Similar results were noted in a study of the hydroisomerization of pentene-1 over nickel and sulfided nickel supported on silica-alumina (74).

Olefins hydrocrack more readily than paraffins. From similarities in product distribution, however, the feeling is that the hydrocracking of paraffins and olefins proceeds through the same reaction intermediates.

Structure of the feedstock appears also to influence the degree of branching in the hydrocracked products. A multiring naphthene such as decalin hydrocracks more readily than the corresponding normal paraffin to give even higher iso/normal ratios of light paraffins and large yields of single ring naphthenic structures. The latter are resistant to further hydrocracking at normal process conditions and contain a higher than equilibrium ratio of methyl cylopentane to cyclohexane. For the production of high quality gasoline, probably the most important reaction in conventional hydrocracking is the partial hydrogenation of polycyclic aromatic rings, followed by rapid splitting of the saturated rings, to form substituted monocyclic aromatics. The substituent side chains resulting from this splitting are readily cleaved to form isoparaffins. With conventional hydrocracking catalysts, one ring of a polycyclic aromatic can be readily hydrogenated at the usual process conditions, whereas single aromatic rings are not readily hydrogenated. It is desirable to maintain such single ring aromatic structures unhydrogenated for their contribution to gasoline octane number and for minimum hydrogen consumption during hydrocracking. Here again, catalysts with excessive hydrogenation activity can be undesirably hydrogenate such structures and thus require excessive subsequent reforming for maximum gasoline octane number.

Although side chains of three or more carbon atoms are readily removed from an aromatic ring by catalytic cracking, shorter side chains have been considered as resistant to further change. However, in the hydrocracking of single ring aromatics containing four or more methyl groups over nickel sulfide on silica-alumina catalyst, it has been found that extensive conversion can be obtained under normal hydrocracking conditions at temperatures as low as 589 K, with removal of the methyl group largely as isobutane and with a high degree of retention of the aromatic rings (75). Similar results were also noted with silica-alumina alone but at a much lower reaction rate, emphasizing the effect of the hydrogen at-

mosphere and nickel sulfide hydrogenation component in maintaining the activity of silica-alumina. This reaction, called the *pairing* reaction, occurs by successive isomerization of a feed molecule adsorbed on the catalyst until a four carbon atom side chain is formed which can then readily be cracked off at the prevailing hydrocracking conditions. Small amounts of ethyl and propyl alkylated benzenes in the product from hydrocracking hexamethylbenzene confirm the side chain growth mechanism suggested. The absence of any substantial quantities of the materials in the product, however, suggests that the adsorbed species undergoing isomerization usually do not desorped from the catalyst before growing a sufficiently large side chain to be eliminated readily by cracking.

Aside from the hydrocarbon type structure discussed above, feedstocks to hydrocracking may also contain considerable quantities of sulfur, nitrogen and oxygen compounds. Under normal hydrocracking conditions, such materials are converted to hydrocarbons, with essentially complete removal of sulfur, nitrogen, and oxygen as hydrogen sulfide, ammonia and water, to yield a stable hydrocracked product.

In general, cyclic type feedstocks largely give cyclic type hydrocracked products and paraffinic type feedstocks give paraffinic type products. Thus the type of products made directly by hydrocracking is influenced to a significant extent by the type of feedstocks used in the process.

From the above discussions the mechanisms of hydrocracking can be summarized under three categories [76]

1. Mechanism for normal paraffins.

2. Mechanism for cycloparaffins and alkyl aromatics.

3. Mechanism for polycyclic aromatics.

Each category is discussed very briefly below

2.2.5.1 Mechanism for Normal Paraffins

Use of strong acidity/mild hydrogenation catalyst leads to:

1. Formation of normal olefins by dehydrogenation
2. Adsorption of normal olefin on acid sites to form carbonium ion.
3. Isomerization of carbonium ions to form stable tertiary ions/cracking to form a smaller ion and an olefin desorption as a normal olefin.
4. Isomerization/cracking or desorption of above formed tertiary ions.
5. Saturation by hydrogenation/hydrogen transfer, of above formed olefins.

Use of high hydrogenation activity catalyst leads to:

1. Isomerization of reactants (without cracking).
2. Hydrogenalysis (without isomerization).
3. Cyclization (in case of noble metal catalyst).

2.2.5.2 Mechanism for Cycloparaffins and Alkylaromatics

Use of strong acidity catalyst leads to:

1. Dealkylation by cracking (for alkylaromatics).
2. Isomerization (for cycloparaffins and alkyl benzene).
3. Alkyl transfer (for alkylaromatics).
4. Pairing to form different cyclic structures.
5. Cyclization of cracked long side chains.

Use of strong hydrogenation catalyst leads to:

1. Little or no isomerization.

2. Successive removal of short alkyl groups from the side chains by hydrogenolysis.

3. No cracking of primary ring structure.

2.2.5.3 Mechanism for Polycyclic Aromatics

Mechanism for polycylic aromatics is described below.

1. Partial hydrogenation of the compound.

2. Opening of one of the cycloparaffin rings to form alkyl side chain.

3. Alkyl transfer of the side chain to another reactant molecule.

4. Ring closure accompanied by hydrogenation.

5. Cracking of a central paraffin ring to give lower cyclic compounds.

2.3 Feedstock Characteristics

The different feedstocks for hydrotreating and hydrocracking such as heavy oils, petroleum resids, and synthetic crudes are complex mixtures of organic compounds and consequently are difficult to characterize. Petroleum resids and heavy oils contain a large number of compounds which have high molecular weights, high metal content, and numerous multifunctional groups. Coal liquids and synthetic crudes, including bitumen, have different amounts and types of functional groups and contain different metals. The most important heteroatoms present in hydrotreating feedstocks are sulfur, nitrogen and oxygen. The complex organic compounds in

these feedstocks can be grouped into three basic subclasses based on difference in solubilities: oil, resins and asphaltenes. The asphaltene fraction is precipitated out from the other fractions using solvents such as n-pentane. The oils and resins can be separated by difference in solubility in liquid propane or adsorption behavior on fuller's earth (77). The efficiency of the upgragrading process depends on the feed characteristics.

2.3.1 Atomic H/C Ratio

Petroleum resids and synthetic crude oils have an atomic hydrogen to carbon (H/C) ratio ranging from 1.6 to 1.3. The asphaltene fraction of petroleum resids has a H/C ratio of about 1.2.

2.3.2 Molecular Weight and Size

Takeuchi et. al (38) have given the molecular weight distribution for a petroleum resid and several characteristic compound subclasses from that resid. They reported average molecular molecular weight of the resid to be 1100. Sulfur containing compounds show nearly the same molecular weight distribution as that of the entire resid. Metal containing compounds, however, show a molecular weight distribution closer to that for the asphaltene fraction. Molecular size plays an important role in the hydrotreating and hydrocracking process.

2.3.3 Metal Compounds

Petroleum resids and synthetic crudes contain significant amount of nickel and vanadium, while coal liquids contain iron and tungsten. Nickel and vanadium content ranges from 10 to 120 ppm and 5 to 160 ppm. respectively. Most of the metals are concentrated in the resin and asphaltene fractions. Metal compounds can be classified as porphyrinic or nonporphynic with most metal compounds in

petroleum resids being porphyrinic, where metal atoms occupy the center location of the molecule. The structures of nonporphyrinic compounds are not well understood. The reactivity of nonporphyrinic metals exceeds that of porphyrinic metals (39).

2.3.4 Sulfur Compounds

Sulfur is the major heteroatom contained in petroleum and synthetic crudes and exists mostly in nonpolar or weakly aromatic compounds (78). Most of the sulfur exists in the aromatic fraction with progressively smaller amounts in the resin and asphaltene fraction. Coal liquids on the other hand contain smaller amount of sulfur because most of the sulfur is removed by hydrogenation in the liquefaction process.

2.3.5 Nitrogen and Oxygen Compounds

Both nitrogen and oxygen concentrations are low in petroleum resids. However feedstocks from synthetic crudes such as tar sand bitumen and oil shale kerogen show significantly higher contents of oxygen. Bitumen from Utah tar sand contains nitrogen up to 1.1 to 1.3 wt. %. Oxygen and nitrogen contents may reach as high as 3.8 and 0.8 wt. % in coal liquids respectively.

2.3.6 Asphaltenes

Asphaltenes are aggregates of compounds that contain polycylic aromatics and various functional groups. In addition, part of the aggregate shows a close packing tendency which imparts a crystalline like character to the aggregate. A hypothetical structure and reaction scheme for asphaltene particle is suggested (79). The proposed structure shows a section of closely packed aromatic disks containing several heteroatoms. The proposed reaction scheme initially breaks the asphaltene into smaller compounds with the removal of the metals followed by heteroatom removal

from smaller compounds. Major portion of heteroatoms and metals from the feedstock are concentrated in the asphaltenes. The molecular weight of asphaltenes ranges from several hundreds to nearly 5000, however agglomerates of asphaltenes may have molecular weight as high as 100000. The aggregate size ranges from about 20 to 1000 A.

2.3.7 Ramsbottom Carbon

Ramsbottom carbon residue is quantified as carbonaceous residue formed during evaporation and pyrolysis of an oil under given condition (80). Information on the quantity of Ramsbottom carbon residue, or a similar property known as Conradson carbon, provides some indication of relative coke forming tendency of the feedstock. In a sense, measurement of Ramsbottom carbon residue acts as a measurement of coke precursor in the hydrotreating and hydrocracking process.

2.4 Hydrodynamics of TPEB

2.4.1 Three phase Fluidization

2.4.1.1 Three phase System

Three phase fluidization involves a solid phase, a liquid phase and a gas phase. All the three phases could be reactants or the solid phase could act as a catalyst while the liquid and the gas phases are reactants. The liquid can either be in continuous flow or batch flow while the gas is in continuous flow. The flow of gas and liquid can be cocurrent upward, concurrent downward, countercurrent or crosscurrent. The flow of solid can be upward or downward. The gas may either be a continuous phase or discrete bubbles. The liquid may be a continuous phase, or film, or droplets. The solids can be a discrete phase in either a packed or suspended state.

The state of particle motion can be subdivided into three basic operating regimes (17):

1. The fixed regime

2. The expanded bed regime

3. The transport regime

The fixed bed regime exists when the drag force on the particle by the flow of a gas-liquid mixture is smaller than the effective weight of the particle. When, with the increase in gas and/or liquid velocity, the drag force counterbalances the effective weight of the particle, the bed is in a state of minimum fluidization which marks the onset of the expanded bed regime. With an increase in gas and/or liquid velocity beyond the minimum fluidization velocity, the bed transforms into the expanded bed regime until the gas or liquid velocity, relative to the solid particles, reaches the terminal velocity u_{tp} of the particle in the gas-liquid medium. At gas or liquid velocities above u_{tp}, the system enters the transport regime.

2.4.1.2 Operating Modes of Three phase Fluidized Beds

Three phase fluidized systems can be classified as follows:

1. **Three phase ebullieted:** an expanded bed regime with continuous liquid phase flowing concurrently upward with the gas, where the solids can be introduced either batch wise or continuously. For large or dense particles ($u_{tp} > 5.0$ cm/s) the solids can be charged and discharged independently of the liquid flow. In such a system the bed height is well-defined within the system. For small/light particles ($u_{tp} < 5.0$ cm/s) the charging and discharging of the solids usually depends on the liquid flow and in such a system the bed surface is ill defined. For both the modes, the bed expansion can be supported by the

liquid phase, the gas bubbles, or both. An expanded bed, with a continuous gas phase flowing cocurrently upwards with the liquid, and the particle bed mainly supported by the gas flow is called **three phase ebullieted bed (TPEB)**.

2. **Downward liquid flow mode:** in this mode the liquid phase is flowing downward countercurrent to the gas phase and the direction of bed expansion depends on the density difference of the particle and the continuous phase. In these systems the solids are continuously charged independent of the gas and liquid flow. When the liquid density exceeds the solid density and the liquid phase is continuous, the particle bed expands downward supported by the liquid flow; this mode is referred to as that of an inverse three phase fluidized bed. When the particle density exceeds the liquid density, the particle bed expands upwards supported by the gas bubbles. When the gas is in the continuous phase, the liquid density usually significantly exceeds the solid density and the liquid trickles down through an expanded bed of particles supported by the gas phase. This mode of operation is typical but not limited to that of the turbulent bed contacter.

3. **Batch liquid phase mode:** This is also an expanded bed with a batch liquid phase, with the solid charged and discharged batch wise. When the particle density exceeds the liquid density and the liquid is in the continuous phase, the expanded bed of particles is supported by the gas bubbles. When gas is the continuous phase, a bed of particles expand upward supported by the gas phase and the liquid phase exists as s film or droplets. Depending on the gas velocity, the axial solid concentration distribution may vary from an exponential decrease at low velocities to near uniform at high gas velocities.

4. **Cocurrent transport mode:** In this mode the continuous liquid phase flows concurrently upward with the gas and solids particles. The solid particles are mainly transported by the liquid phase. In slurry bubble column, where particles are usually charged or discharged continuously as a slurry, the bubbling gas phase is used to establish a uniform particle distribution.

5. **Countercurrent traansport mode:** in this situation the slurries flow downward relative to the upward flow of gas with either the liquid or gas as the continuous phase.

2.4.2 Description of TPEB

A three phase ebullieted bed consists of three phases; solid, liquid and gas. The solid phase is fluidized primarily by the gas. A schematic representation of a TPEB

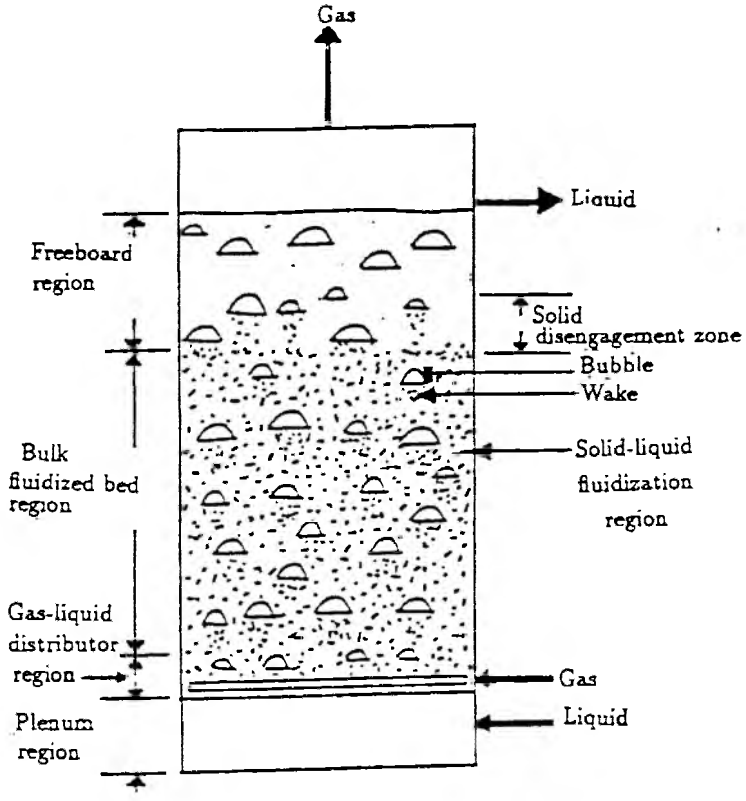

Figure 2.1. Schematic Representation of a Three Phase Ebullieted Bed.

is shown in Figure 2.1.

The liquid phase enters the bed from the plenum region, while the gas is injected through a gas distributor. The gas-liquid distributor region is characterized by the formation and growth of bubbles. The bulk fluidized bed region consists of a solid-liquid fluidized region, which surrounds the rising bubbles. The bubble wake is a liquid mass attached to the bubble which follows the bubble at the same velocity. The bubble wakes carry solid particles with them as they rise in the bed. The freeboard region is above the bulk fluidized region, where the bubble wakes shed solid particles into the surrounding liquid region. These shed particles settle down into the bulk fluidized region. The gas and liquid effluent flows out from the top of the bed.

2.4.3 Process Applications

The TPEB reactor was first used commercially in 1968 for hydrotreating petroleum residue in the H-Oil process developed by Hydrocarbon Research Inc. (51). Based on the similar technology, the LC Fining residue hydrocracking process was later developed. Several commercial reactors based on one of these processes are currently in operation in refineries in Canada, Kuwait and Mexico. The processing capacity in these refineries ranges from 18,500 to 60,000 bbl/day (17). The technical term *ebullieted bed* was first defined by P. W. Garbo in the patent of Johanson (68) to describe a gas-liquid contacting process in contrast to the common industrial term *fluidized bed* where particles are in *fluidization* induced by gas phase alone.

The energy crisis in 1973 brought renewed interest to the synthetic fuels area. Demonstration or semi demonstration process units using TPEB reactors were developed in the U.S. The H-Coal process was developed using the same technology as the H-Oil process and was operated at a coal feed rate of 500 ton/day.

Table 2.1. Applications of Three Phase Ebullieted Beds.

#	Application	Reference	Category*
1.	Sand filter cleaning	(81)	A
2.	Crystallization	(82)	A
3.	Hydrotreating and conversion of heavy petroleum and synthetic crude (H-Oil,LC Fining)	(83,84)	B
4.	Coal liquefaction (H-Coal)	(85,86,87)	
5.	Electrodes	(88,89)	B
6.	Methanation	(90)	B
7.	Production of zinc hydrosulfite	(91)	B
8.	Hydrogenation of heptane	(92)	B
9.	Hydrogenation of 1-heptene	(93)	B
10.	Calcium bisulfite production	(94)	B
11.	Methanol production	(95)	B
12.	Treatment of lactose wastewater	(96)	C
13.	Treatment of phenol wastewater	(97,98)	C
14.	Treatment of thiocynate wastewater	(99)	C
15.	Treatment of municipal sewage wastewater	(99)	C
16.	Treatment of phenol wastewater	(100,101)	C
17.	Treatment of gasification wastewater	(102)	
18.	Treatment of synthetic milk wastewater	(103)	C

Apart from the large scale applications of TPEB described above, there have been a number of small scale applications of TPEB. Fan (17) has grouped these examples according to physical, chemical and biochemical applications. These applications are tabulated in Table 2.1.

*

Category A: Physical system

Category B: Chemical system

Category C: Biochemical system

2.4.4 Advantages and Disadvantages of TPEB

The major advantages of the TPEB system over the fixed bed system are:

1. High reactant conversion for reaction kinetics favoring mixed flow pattern.
2. Ability to achieve significant temperature uniformity without external means.
3. Ease in heat supply and removal and high temperature controllablity.
4. Low intraparticle diffusion resistance and low external mass transfer resistance.
5. Ease in catalyst replacement and hence high controllablity of catalyst activity and minimum flow maldistribution.

The advantages of the fixed bed system over the TPEB system are:

1. Low micromixing, yielding small axial dispersion of the phases and high reactant conversion for reaction kinetics favoring plug flow pattern.
2. High controllablity over product selectivity for complex reaction.
3. Low solid attrition and consumption, hence permitting precious metal catalyst to be used for the reaction.

2.4.5 Hydrodynamics of TPEB

The hydrodynamics of the TPEB can be classified into two major areas (17):

1. General Bed Behavior.
2. Mechanics of bubbles and bubble wakes.

2.4.5.1 General Bed Behavior

2.4.5.1.1 Regions in a TPEB. Three distinct regions above the gas distributor are identifiable.

1. Gas-liquid distributor region: this is the region immediately above the gas-liquid distributor and includes initial bubble formation to the establishment of the final bubble size. The hydrodynamics of this region depends on the distributor design and the physical properties of the liquid-solid medium.

2. Bulk fluidized bed region: this region includes the main portion of the ebullieted bed, where the hydrodynamic behavior varies drastically with the operating conditions. However, for a given set of operating conditions, there is minimum axial transport property variation in this region.

3. Freeboard region: this region contains entrained particles from the bulk ebullieted region leading to a solid holdup profile, which decreases axially above the bed.

2.4.5.1.2 Pressure drop. The total vertical pressure gradient in the bed (static pressure gradient) is given by (104)

$$-dP/dZ = (\epsilon_s \rho_s + \epsilon_l \rho_l + \epsilon_g \rho_g)g \tag{2.3}$$

The dynamic pressure drop, defined as the total pressure drop corrected for the hydrostatic head of the liquid is given by (105)

$$-dP_d/dZ = \epsilon_s(\rho_s - \rho_l)g - \epsilon_g(\rho_l - \rho_g)g \tag{2.4}$$

The frictional pressure gradient, defined as the total pressure gradient corrected for the hydrostatic head of the gas-liquid two phase mixture is given by (91)

$$-dP_f/dZ = (1 - \epsilon)(\rho_s - \rho_f)g \tag{2.5}$$

where

ϵ_s, ϵ_l and ϵ_g are the solid, liquid and gas holdups in the bed respectively,

and

ρ_s, ρ_l and ρ_g are the solid, liquid and gas densities respectively.

Above equations permit evaluation of individual phase holdup from the pressure gradients measured experimentally . This has been verified by various researchers (106,107). The dynamic pressure distribution shows linear behavior in both bulk fluidized region and the freeboard region. Both the dynamic pressure and the dynamic pressure gradient decrease with increasing gas velocity (108).

2.4.5.1.3 Flow regimes. Three flow regimes can be identified in a TPEB.

1. Coalesced bubble regime:

   This flow regime is characterized by coalescing and breaking of bubbles to give wide distribution of bubble sizes across the crossection of the bed. The coalesced bubbles rise near the column center with high velocity and stir the bed violently. This regime predominates at low liquid and high gas velocities.

2. Dispersed bubble regime:

   In this regime, no bubble coalescence occurs and the bubbles are of uniform size across the crossection of the bed. This regime predominates at high liquid and low gas velocities or at high bed pressures.

3. Slugging regime:

   In this regime, the bubble occupy nearly the whole cross section of the column. This regime predominates in beds with small column diameters and when the gas rates are high.

In general the flow regimes are affected by the column diameter, phase properties, particle terminal velocity and bed pressure. Correlation for calculating the liquid

velocity for a transition from the coalesced to the dispersed regime, for a given particle terminal velocity have been deployed (109).

2.4.5.1.4 Incipient fluidization. For a given gas velocity, the minimum liquid velocity required to fluidize a bed of particles is known as the minimum fluidization velocity, u_{lmf} and can be determined by noting the change (decrease) in the bed dynamic pressure drop behavior, which occurs as the bed changes from a fixed bed to a fluidized bed.

Determination of minimum fluidization velocity (u_{lmf}) is difficult for beds of small/light particles. For large/heavy particles (u_{lmf}) decreases with an increase in the gas velocity and is independent of the initial bed height and column diameter. A correlation for (u_{lmf}) proposed by Song et al. (110) is given below.

$$\frac{u_{lmf}}{u_{lmfo}} = 1 - 376{u_g}^{.327}{\mu_l}^{.227}{d_e}^{.213}(\rho_s - \rho_l)^{-.423} \tag{2.6}$$

and u_{lmfo}, which is the minimum fluidization velocity of the liquid-solid system can be determined by correlation suggested by Wen and Yu (111)

$$Re_{mfo} = ((33.7)^2 + 0.0408Ar)^{.5} - 33.7 \tag{2.7}$$

where

$$Re_{mfo} = \frac{d_e u_{lmfo}\rho_l}{\mu_l} \tag{2.8}$$

and

$$Ar = \frac{{d_e}^3\rho_l(\rho_s - \rho_l)g}{{\mu_l}^2} \tag{2.9}$$

In equations 2.6 to 2.9

u_g is the gas superficial velocity,

μ_l is the liquid viscosity,

and

d_e is the equivalent particle diameter for a nonspherical particle given by diameter of a spherical particle of volume equivalent to that of the nonspherical particle.

Correlations for calculating minimum fluidization velocity for a mixed particle system are also available (112).

2.4.5.1.5 Phase holdups. The characteristics of phase holdups is discussed below.

1. Solid holdup:

   Several empirical correlations, available in literature, for calculating the solid holdup have been summarized by Muroyama and Fan (113). In the limit as the gas velocity approaches zero, a good solid holdup correlation should reduce to those for liquid-solid fluidized bed. A TPEB using small particles displays unique bed contraction-expansion characteristics. Upon initial introduction of the gas into the liquid-solid fluidized bed, contraction of the bed occurs instead of expansion. However on increasing the gas flow beyond a certain value, the bed starts expanding. The explanation for the contraction phenomenon that has received wide agreement is that some of the liquid which would otherwise support the solid particles is diverted to the solid deficient wake behind the gas bubbles. Where the wake flux is large relative to the remaining liquid flux, as is the case for small and/or light particles in viscous liquid, the resulting contraction effect usually overrides the expansion caused by the gas bubbles. However where the bubble wake flux is relatively small, as for large and/or heavy particles in nonviscous liquids the expansion effects tend to predominate. Thus beds with large particles expand on introduction of gas. Correlations for predicting this behavior have also been developed (114).

2. Gas holdup:

   The gas holdup varies significantly with flow regime and a unified correlation equation is difficult to establish. Several empirical correlations have been summarized by Muroyama and Fan (113), which can be applied for different operating conditions. As gas holdup behavior strongly depends on the flow regime, it is a strong function of particle and liquid properties. A decrease in liquid surface tension can dramatically increase gas holdup. Gas holdup in TPEB can be lower than that in a corresponding bubble column when the particles promote bubble coalescence and it can be higher than that in a corresponding bubble column when the particles break up gas bubbles. The gas holdup is inversely proportional to the bubble rise velocity in the bed and increases with bed pressure when other parameters are kept constant (115).

3. Liquid holdup:

   The liquid holdup increases with liquid velocity and decreases monotonically with increasing gas velocity (116). The liquid holdup increases with liquid viscosity and the trend is more pronounced for small particles (117). Change in liquid holdup depends on size/shape of the particles (117). Thus for 1 mm glass beads liquid holdup decreased whereas for 2.6 mm gravel particles, liquid holdup increased with surface tension. Several empirical correlations for calculating liquid holdups are available in literature (113).

4. Solid holdup in the freeboard region:

   The solid particles are drawn from the upper surface of the fluidized bed into the freeboard in the wake behind the bubble. Vortices containing particles are shed behind the wake in the free board. The particles in the shed vortices settle back into the bed, when the liquid velocity in the freeboard is less than the particle terminal velocity. The solid holdup in the freeboard region for given

operating conditions is higher for small/light particles than for the large/heavy particles. Furthermore the particle entrainment increases with an increase in any of the following; bubble size, bubble frequency, liquid velocity or gas velocity.

5. Gas holdup in the freeboard region:

   The gas holdup in the freeboard region decreases significantly with increasing liquid velocity. Furthermore gas holdup in the freeboard region is greater than that in the bulk fluidized region but smaller than that in a bubble column. Correlations for predicting gas holdup in the freeboard region have been proposed (117,118).

2.4.5.1.6 Effect of solid wettability. A bed of nonwettable particles always expands upon introducing gas in contrast to a bed of clean wettable beads, which contracts upon the initial introduction of gas (119). Beds of nonwettable 6 mm beads show greater expansion compared to those of wettable ones and the gas holdup is much lower than that for the wettable ones (120). This result may be due to adherence of the bubbles to the nonwettable solid particles due to the absence of liquid film on the solid particle. When bubbles adhere to the nonwettable particles, the apparent density of the particle bubble aggregates becomes less than that of the particle alone . The lesser apparent density leads to the greater bed expansion and less bubble breakage which results into lower gas holdup (66).

2.4.5.1.7 Effect of surface tension. Pure fluids that have low surface tension compared to water, initially form smaller bubbles that may undergo coalescence and increase in size. In TPEB the use of a low surface tension liquid like kerosene may eventually lead to a foaming where bed expansion rather than contraction takes place when gas is introduced (121,122).

Gas holdup in a surfactant solution depends on the molecular composition of the liquid, liquid velocity and distributor design but is not dependent upon equilibrium

surface tension nor on the surfactant concentration above a certain value (67). Surfactant reduces the bubble size by reducing the surface tension. They inhibit coalescence of bubbles by formation of an electrically charged monolayer at the gas-liquid interface. Further they increase drag on the gas bubble due to the surface tension gradient on the bubble surface, which results in a lower bubble rise velocity. All these effects lead to a higher gas holdup in presence of a surfactant. Behavior of fluidized beds under the influence of surfactants has been studied by various researchers (17).

2.4.5.1.8 Rheological behavior. The overall viscosity or the apparent viscosity depends on the viscosities of gas and the liquid phases, particle to particle interaction and bed expansion. It reflects the combined effect of frictional viscosity and kinetic viscosity of the system (123). The frictional effect can be defined as a shearing viscosity which depends on the bed voidage. The kinetic viscosity is contributed by the fluid turbulence and the particle kinetic energies which inherently reflect particle accelerations and interactions. Consequently, the apparent viscosity varies with the bed voidage and the degree of turbulence in the bed and hence the liquid and gas flow rates. In addition, a factor, such as particle size and density that affect bed expansion behavior, necessarily affects the bed reheology.

2.4.5.1.9 Effect of internals. The presence of internals in the system, such as draft tubes, heat exchangers and baffles, or geometric irregularities greatly increase the complexity of the transport phenomena.

2.4.5.2 Mechanics of bubbles and bubble wakes

Phase holdups and flow patterns in a TPEB are closely related to bubble and bubble wake flow characteristics.

2.4.5.2.1 Bubble geometry and motion. In low viscosity liquids such as water, bubbles are very irregular and oscillate unsteadily in a transition zone between ellipsoidal and spherical cap shapes. In viscous liquids under very quiscent conditions the formation of skirts whose thickness is about 100 microns have been experimentally observed (124). The skirt is a thin annular film of gas trailing behind the rim of a large spherical cap bubble.

For small bubbles, where only the surface tension forces dominate, the shape is approximately a sphere and the bubbles rise steadily in a rectilinear path. For intermediate size bubbles, the effect of both surface tension and inertia of liquid flowing around the bubble is important and the liquid viscosity and the presence of surface active contaminants influence the bubble dynamics. Large bubbles have an approximately spherical cap shape with an included angle of about 100° and a relatively flat base. These bubbles follow a rectilinear path with some rocking and, or base oscillations.

For small bubbles, the flow around the bubble can be described by the creeping flow approximation, or Stokes law, and the wake size is negligible. The secondary motion associated with intermediate size bubbles probably results from periodic shedding of vortices from the bubble wake. The bubble oscillations start with the onset of vortex shedding from the wake (17).

At low liquid velocities the bubble chord length distribution is normal whereas at higher liquid velocities the distribution is log-normal. Small bubble size is associated with a small variance, while a large mean bubble size is associated with large variance which increases with gas flow rate (125).

Increase in the liquid velocity decreases the bubble size (126). In the dispersed bubble regime the mean bubble size reaches a minimum near minimum fluidization conditions and then increases with an increase in liquid velocity (127). The bubble size decreases with an increase in bed pressure. At high pressure, when the particle

size is greater than the bubble size, the particle size effects on the prevailing bubble size become minimal yielding bubble size characteristics in the bed similar to those in the gas-liquid bubble column, under the same operating conditions (115).

2.4.5.2.2 Bubble coalescence and breakup. In the distributor region bubbles are formed and their initial size depends on the distributor design as well on the forces such as bouyancy, viscous drag, surface tension and inertia. As the bubble rises, coalescence or breakup may occur due to the interaction between the rising bubble and other bubbles, individual particles and the surrounding liquid-solid medium. Initial bubble size depends strongly on the type of gas distributor (128).

The bubble size increases and the size distribution broadens within a short distance from the distributor with an increase in the axial distance due to bubble coalescence (129). The bubble coalescence results into a decrease in bubble frequency within a short distance from the distributor. Furthermore as the bed porosity increases the coalescence rate decreases (126).

When two successive bubbles rise in a liquid-solid suspension, the latter accelerates due to the suction caused by a low pressure region immediately below the proceeding bubble (130). Bubble coalescence commonly occurs in the liquid-solid suspension acting as a pseudo-homogeneous medium of higher apparent viscosity and density than those of the liquid medium alone. However there is a limit to coalescence. Large bubbles may be deformed and rupture to form smaller bubbles by the turbulent eddies generated in the liquid-solid suspension.

Bubble breakup may also be attributed to horizontal entrainment, flattening, necking and disintegration of the latter bubbles affected by the turbulent shear and vortical flow near the edge of the preceeding bubble (130). Interaction between a bubble and individual particles can also lead to bubble breakup. Lee (131) proposed that bubble disintegrates when a particle with adequate inertia induces a hemispherical indentation on the bubble roof.

This approach leads to a critical Weber number of three beyond which the bubble will break. Fan (17) also indicated that the penetrated bubble should deform into a doughnut shape, with the central hole being the size of the particle, and the bubble height being estimated from the condition that the deformed bubble should have the same volume as the original bubble. In order for a single particle to break a bubble the particle diameter must be greater than the height of the deformed bubble. The subsequent bubble breakup is by the necking mechanism suggested by Boy (132).

Thus three markedly different collision phenomena between a single particle and a single bubble can be predicted:

1. A small/light particle is unable to penetrate and is ejected after collision.

2. A medium size particle is able to penetrate but is unable to break the bubble.

3. A large and heavy particle penetrates and subsequently breaks the bubble.

Multiparticle penetration induces an unstable bubbles and causes bubble breakup. The concept of bubble breakage by large/ heavy particles has been applied to TPEB to enhance the gas holdup by the use of floating bubble breakers in the bed. The optimum ratio of breaker volume to the total particle volume in the bed yielding minimum bubble size and hence the maximum gas holdup is found to be 0. 2 (133).

The competing tendencies of bubble coalescence and disintegration may result in an equilibrium bubble size distribution. Therefore the bubble size distribution for a deep bed is virtually independent of the initial size of bubbles immediately above the distributor.

2.4.5.2.3 Bubble rise velocity. The rise velocity of a single gas bubble inherently depends on its size and the following factors:

1. For small bubbles, the rise velocity is strongly dependent on the liquid properties such as surface tension and viscosity.

2. For large bubbles, the rise velocity is insensitive to the liquid properties as predicted by Davies-Taylor relationship (134).

The rise velocity increases with an increase in bed expansion, but the size and density of the particle apparently have little effect on the rise velocity.

For a multibubble system, bubble-bubble interaction plays a significant role in the resulting bubble rise velocity behavior. In the dispersed bubble and coalesced bubble regimes the bubble rise velocity distribution is narrow, and the variations in the mean and variance of the bubble rise velocity distribution are insensitive to the particle size used. In the slugging regime, the bubble rise velocity distribution shows a broad multimodal distribution (135).

2.4.5.2.4 Bubble wake structure. The bubble wake has been recognized as a key factor in explaining various phenomena such as solid mixing, particle entrainment into the freeboard and bed contraction upon the initial introduction of gas bubbles into liquid-solid fluidized bed. Wake geometry can be grouped into three types (17):

1. **Closed laminar/toroidal wakes:** which have been observed behind large spherical capped bubbles rising in various liquids or behind the corresponding circular cap bubble in two dimensional vessels. The closed laminar wake is hydrodynamically stable with a well-defined boundary and a toroidal vortex ring inside and exchanges no liquid with the external flow (136).

   The stability of the closed laminar wake is due to the viscous and/or wall effect. On keeping the bubble volume constant and decreasing the viscosity, or increasing the Reynolds number the flow in the wake becomes less stable and starts shedding vortices (transition to the open wake) (17). The actual shape

of the closed wake is somewhat elongated downward, but the dimensionless distance from the axis of symmetry to the stagnation ring is a constant 0.707.

2. **Turbulent wakes:** These wakes have been observed behind large bubbles rising in less viscous liquids. Open geometry appears to be more accurate in describing turbulent wakes. The internal structure of this bubble wake is characterized by the dynamic behavior of the vortices. This region includes two growing vortices, one is represented by a well established circulation and the other is just being formed (17). This region, denoted as a primary wake has nearly the same rise velocity as the bubble and thus plays a primary role in the various hydrodynamic/transport phenomena.

   The region beneath the primary wake demarcated by streams of external flow across the wake, includes shed vortices and is called the secondary wake. Lower concentration regions are observed immediately beneath the bubble base and around the vortex center. Higher concentration region occurs around the vortices, especially in the region where the two vortices intersect.

2.4.5.2.5 Wake instability. Initially, the wake consists of a closed laminar region of a toroidal vortex ring and a narrow tail following it. As the bubble accelerates and the wake grows in size by continuous accumulation of the material from outside, the symmetry of flow is perturbed and eventually some wake material is discharged

The mechanism of wake formation and shedding has been described in detail by Fan (17). Coppus (136) found that the vortex shedding rate slightly increased with bubble Reynolds number (Re_b). Tsuchiya and Fan (137) have reported the Strouhal number (Sr), which characterizes the vortex shedding, as a function of the bubble Reynolds number. Periodic alternate shedding of vortices was observed at

low Re_b and Sr was uniquely defined and monotonically increased for each particle size. At higher Re_b, shedding occurred in alternate and parallel shedding modes.

2.4.5.2.6 Wake boundary and size. At higher Re_b, for intermediate to large bubbles in liquid and/or liquid suspension with low inertia solid particles, the wake flow is unsteady but has a steady vortex shedding. Over the same Reynolds number range, but for larger inertial particles, the wake flow is still asymmetric shedding and the shed material has a larger scale vortical motion.

This region may result from either the high solid particles deviating from the liquid flow pattern and being expelled from the vortex region to the central wake region or the turbulent shear layer being dragged into the interior. For very large bubbles rising at high Re_b the wake flow is unsteady and has parallel wake shedding. Darton and Harrison (138) have proposed a correlation for estimating the height of the liquid wake.

2.4.5.2.7 Wake solid concentration. The variation in solid concentration between the wake and the surrounding medium and within the wake region itself results from the inability of the particle to follow exactly the flow path of the liquid elements. For a circulating flow pattern within the vortices of the primary wake, the larger inertial particles deviate from the liquid flow path, with the extent of deviation strongly depending on the particle size and density.

The circulating flow pattern brings about centrifugal forces which in turn tend to expel larger inertial particles out of the vortex towards the surrounding medium. Some particles, however, remain within the vortex and keep circulating because the surroundings are fully occupied with a high concentration of particles and because the tangential velocity is much greater than the radial velocity of the particle.

The particle flow is downward near the free shear layer and upward around the central axis of the wake. The upward flow of particles tends to penetrate very close to the bubble base. Nevertheless there is a local pressure maximum along the plane

parallel to but somewhat below the bubble base established by the liquid flow. The upward particle inertia must overcome the pressure gradient, drag force and the downward gravitational force in order to invade into the stagnant layer of low particle concentration. This is a possible mechanism to account for the formation and maintainence of the stable liquid wake (17). The near-wake region can be subdivided into four regions (17):

1. A stable liquid region that occurs immediately beneath the bubble base and has a negligible solids concentration.

2. A stable solid wake region that follows the liquid wake and includes part of the growing vortices and the turbulent region around the wake center line. This region is made up of a liquid-solid emulsion and is partitioned from the fluctuating wake region by a relatively low solid concentration layer.

3. A fluctuating solid wake region that is distinguished by a stream wise flow from the far wake region and which interacts with the external flow field.

4. A vortex shield region that has a low particle concentration and which resides outside the stable and fluctuating solid wake region.

For a single bubble system the shape of the solid holdup profile behind a single large bubble depends significantly on the average solids holdup in the liquid-solid fluidized region (ϵ_{sf}). At high ϵ_{sf} the wake behavior seems to be damped and the concentration difference between the wake and the liquid-solid solid fluidized region are limited to only a small region beneath the rising bubble. However, at low ϵ_{sf} the wake effect can extend to a very great depth beneath the bubble and both local regions of high and low solids holdup can be found.

In multiplebubble system , the depth beneath the bubble to which the wake effects extend is expected to be reduced drastically. Quantitatively the average

relative solid holdup x is near one for a high ϵ_{sf} and, in general decreases with a decrease in ϵ_{sf}. Locally, however the relative holdup can exceed unity to a significant degree. For small bubble system, the concentration difference in the wake is less pronounced. El-Temtamy and Epstein (139) have suggested a correlation for calculating the relative solid holdup x in the wake.

2.4.6 Flow Models

The development of flow models is essential to the quantitative description of the transport properties in the TPEB. The wake concept has provided a fundamental framework for a global treatment of the bed behavior. Some of the models available in the published literature have been described briefly below. The generalized wake model has been frequently used throughout this work.

2.4.6.1 Generalized Wake Model

The generalized wake model was proposed by Bhatia and Epstein (119). An important assumption is that the bed can be subdivided into a gas bubble region, a wake region and a liquid-solid (fluidized) region. The sum of the volume of these regions must equal the total volume, or in terms of fractions

$$\epsilon_g + \epsilon_l + \epsilon_s = 1 \tag{2.10}$$

Furthermore, it is assumed that:

1. The solids content in the wake can be an arbitrary value different from that in the liquid-solid fluidized region.

2. The wake rises at the same velocity as that of the bubble.

3. The Richardson-Zaki correlation (140) between solids holdup and liquid velocity applies in the liquid-solid fluidized region.

The model calculates the overall phase holdups and the bed porosity.

On the basis of the solid-free wake model, mathematical criterion of contraction-expansion behavior have been developed (i141,142). El-Temtamy and Epstein (114), based on the generalized wake model, developed a criterion for bed contraction that was further modified by Jean and Fan (143).

According to this, a critical value of x exists above which expansion and below which contraction would be expected when gas is introduced (143). Here x is the ratio of solid concentration in the bubble wake region to that in the liquid-solid region. This criterion indicates that a large k, which is the ratio of wake volume to bubble volume, a high bubble velocity, or a high liquid viscosity favors bed expansion.

2.4.6.2 Structural Wake Model

This model predicts the liquid holdup in a TPEB and the contraction/expansion of the bed on introducing gas in a liquid fluidized bed. Fan et al. (17), in proposing the structural wake model, assumed that the primary wake is responsible for the hydrodynamic phenomena such as bed contraction and solid mixing. They subdivided the primary wake into:

1. The confined turbulent wake region (CTW).

2. The shedding vortical wake region (SVW).

The CTW region includes the stable liquid layer and the chaotic turbulent region about the wake central axis. The CTW region was assumed to be an isolated region and treated in the same manner as the wake in the generalized wake model. The SVW region consists of vortices or vortical blobs on the diametrically opposite sides of the bubble and the spouting region in between.

It constantly sheds a certain volume of solid asymmetrically into the secondary wake and thus eventually into the liquid-solid fluidized region. It was further

presumed that this shedding of the old vortex is equal to the rate of formation of a new vortex.

2.4.6.3 Stagewise Partition Process Model

Developed by El-Temtamy and Epstein (144), this model predicts the particle entrainment height in the freeboard region. They postulated that in each stage the solid particles are carried upwards in the bubble wake, transferred to the surrounding liquid-solid region and settle in the liquid-solid region. The height of a stage in the model was assumed to be equivalent to the height of a wake shedding unit, and was defined as a distance traveled by a bubble during the time interval between the shedding of two successive wake cycles.

The model assumes a minimum concentration of the solid particle in the upper most stage and calculates the solid concentration in the subsequent stages, proceeding downwards, until the boundary between the bed and the freeboard region is reached. The product of the number of stages and the height of the stage gives the particle disengaging height. This model is described in more detail in Chapter 3.

2.4.6.4 Circulating Flow Model

Morooka et al. (145) found that the liquid phase flow pattern in a TPEB is similar to that in a bubble column where the liquid flows upward in the central region and downward in the peripheral region. They proposed a circulating flow model to simulate the lateral distribution of gas holdup and interstitial liquid velocity. The model predicts that the liquid velocity is a maximum at the axis and minimum near the wall and that the liquid velocity at the wall is not necessarily negative in a TPEB.

2.4.6.5 Other Flow Models

Jean and Fan (143) suggested a particle terminal velocity model which presumes that in addition to the usual bouyancy and drag forces on the particles, an interaction force must be considered, which accounts for the effect of the bubble to particle interaction. The model predicts gas holdup for a given gas and liquid velocity.

Bhaga and Weber (146,147) used the concept of relative velocity to develop equations describing the interelationship among the velocities of the dispersed phases (gas and solid) and the continuous phase (liquid). However this one dimensional flow model does not take into account the presence of the wake behind bubbles and the accompanying distribution of the liquid flow; hence it cannot predict initial bed contraction upon gas injection in a TPEB.

2.5 Selection of Process

2.5.1 Nature of Bitumen as Process Feed

Nature of bitumen and its response to upgrading process is discussed below.

1. Due to the heavy nature of the feed, efficient contact between feed, hydrogen and the catalyst is difficult.

2. Deep hydrogenation of the feed, to give upgraded products, is accompanied by release of heat.

3. Due to the presence of appreciable amount of polynuclear aromatics in the feed, the catalyst is susceptible to coke fouling, especially if the reactor is not isothermal. the reactor.

4. Analysis of bitumen (53) (derived from White Rocks deposits) indicates that the feed contains high amount of nitrogen and organometallic compounds (N -

1.1 to 1.3 wt. %, Ni - $\sim$ 0.8 ppm, V - 1.3 to 3.6 ppm, As - 2.2 ppm and S - 0.5 wt. %). These levels of poisons will degrade the catalyst very fast rendering it ineffective for the actual hydrocracking step.

5. The catalyst bed could get plugged due to

   (a) High levels of asphaltenes in the feed.

   (b) Carbon laydown during hydrocracking

   (c) Presence of sand, left over during bitumen extraction, in the feed

2.5.2 Features of H-Oil Process

The features of H-Oil process (51,57) are discussed below.

1. Because the reactor is maintained in a thorough ebullieted condition with the catalyst in a state of constant motion, an efficient contact between the feed, hydrogen and the catalyst is maintained facilitating efficient reaction kinetics.

2. The recycle product stream used for ebullieting the catalyst bed also serves to carry away the heat of exothermic reaction, thereby maintaining a near isothermal condition in the reactor. The cooling by recycle stream is very effective, eliminating the need for an elaborate quench system for reactor temperature control.

3. Due to better control on the reactor temperature and the inherent feature of the hydrocracking process (presence of hydrogen) the amount of coke formation is reduced, thereby allowing the the process to be operated at a lower hydrogen partial pressure.

4. The rapid poisoning of the catalyst due to organometallic compounds and nitrogen can be avoided by employing a two stage reactor where the organometal-

lic compounds and nitrogen are removed in the first stage using a catalyst with a high metal component.

5. Because the catalyst is in a state of continues motion, any fine particles (like sand), asphaltenes or carbon cannot plug the catalyst bed.

6. In the ebullieted state, the catalyst behaves much like a gas solid fluidized bed and can be made to flow into or out of the reactor. Catalyst can thus be added or withdrawn, while the unit is in operation, to maintain the catalyst activity constant at a desired level without shutting down the unit.

7. As an inherent advantage of an ebullieted bed reactor, there is no catalyst carryover in the products. Thus a step for separating the catalyst from the product, is not required.

8. Because there is a continues liquid phase, with a low pressure drop in the ebullieted bed, the velocity of the vapor phase relative to the liquid is much higher than that in the down flow fixed bed reactor. Consequently, in the conversion operation the distillates are rapidly removed as they are formed, tending to concentrate the heavy materials in the reactor and increasing the effective residence time of the heavy reactants.

9. The low pressure drop associated with the ebullieted bed system permits the use of smaller catalyst size than is practical in a fixed bed system. These smaller size catalysts are more effective than the usual 1/8 inch or larger catalyst particles.

The H-Oil process has been successfully used for upgrading bitumen derived from Athabasca tar sands (51). As mentioned earlier, inspection of the properties of the product indicates that though it is not in finished condition, it is ready for

use as synthetic crude. The distillate fractions need further processing to reduce the sulfur and nitrogen contents and to saturate the olefins.

The particular quality of the product result due to the mild hydrogenation condition employed, which reduces the hydrogen consumption in the heavy ends (which would often be burnt as fuel and would not need to be of high quality).

However on studying the composition of bitumen from Utah tar sands, it appears that the weight percent of sulfur in Utah bitumen is much lesser than Athabasca bitumen (0.5 wt. % max. against 4.9 wt. %), however the nitrogen content is much higher in Utah bitumen (1.1 to 1.3 wt. % against 0.45 wt. %).

This implies that if the HDN step in the first stage reactor is effective in reducing the nitrogen to a desired level, the products from processing Utah bitumen will contain low amounts of sulfur also and hence the products can be used as synthetic crude directly.

From the above discussions, it may be concluded that a hydrocracking process employing a TPEB two stage reactor system could be used effectively for upgrading the bitumen and bitumen derived liquids from Utah tar sands, to yield a synthetic quality crude.

2.5.3 Process Considerations

Simultaneous hydrotreating and hydrocracking is probably the most commonly considered application when processing in TPEB reactors. Processing of residues involves two general classes of chemical reactions.

The first set involves hydrogenation reaction and includes desulfurization, denitrogenation, hydrogenation of the products resulting from C-C bond cracking, and ring and olefin saturation. Rates of these reactions are favored by high pressure, low space velocity, higher catalyst activity and higher temperature.

The second set of reactions involves the cracking of the carbon-carbon bonds. These reactions are favored by higher temperature and lower space velocity. On

the other hand, pressure and catalyst activity are of lesser importance in these reactions and in the region of usual interest, equilibrium considerations have little effect.

The relationship between temperature and space velocity for each of these reaction types has been presented in form of a plot by Johnson et al. (57). Although, a sour Wcot Texas vacuum residue is chosen as feed for this figure, a similar set of curves could be constructed for any feedstock.

Percent desulfurization has been used to represent the effectiveness of hydrogenation, although percentage conversion of material boiling over 1248 K has been used to indicate the extent of C-C cracking. The plot represents constant conditions of pressure, catalyst activity and number of reactor stages.

Because pressure and catalyst activity will not have a large effect on cracking, although they are important for hydrogenation, both of these parameters if increased, will not change the conversion lines while this would shift the desulfurization lines upward. This plot can be used to select the operating point to get the required product slate.

Since the cracking reaction is more temperature sensitive than desulfurization, and because desulfurization will respond to other variables, there is a considerable freedom in controlling these factors independently. For example, a plant can be designed for any one level of desulfurization at a constant conversion. Similarly, one can change from a low conversion-high desulfurization operation to a high conversion operation by raising reactor temperature at constant space velocity.

The process yields predicted for a refinery processing 23000 BPD of vacuum residue using H-Oil process has been presented by Johnson et al. (57). Design conditions for some of the operations considered are shown by lettered points on a plot by them.

Particulars of each point are noted below (57):

1. **Point A:** (Desulfurization-low conversion) on Figure 2.2 could be selected for producing low sulfur fuel oil from a high sulfur vacuum residue. In this case the overall desulfurization is 76 % and 28 % of the 975 F° material is converted to lighter fraction. As the process yields show, because sufficient cracking takes place no cutter stock would be required if all of the 375 F° material were blended with the bottoms. This case would be attractive to a refiner having an outlet for low sulfur fuel oil.

2. **Point B :** (Low conversion-low desulfurization) achieves same conversion as was the case for point A, but at a much reduced hydrogen requirement and at a considerable saving in capital and operation requirement. A refiner who has limited hydrogen availability and who does not require a high order of desulfurization can operate at this point.

3. **Point C:** In this case the design criterion used is utilization of all available hydrogen to process all of the vacuum bottoms. Operating conditions at point C accomplish a moderate degree of 975+° F conversion (60 %) with a rather low order of desulfurization. These conditions result in a maximum degree of conversion per unit of hydrogen availability. The space velocity required for this case is actually higher than that for the low conversion-high desulfurization instance (point A). Reactor sized for point A operation is sufficient for point C.

4. **Point D:** In many instances the refiner may wish to maximize conversion of the 975 F° fraction. In this case the space velocity (and hence the reactor size) is fairly close to that of point A - the principal difference being the reactor temperature.

5. **Point E:** As an extension of point D, the fraction of the product boiling between 650 and 975 F° can be recycled to extinction. This will accomplish a high yield of 375-650 F° material which can be a feed stock to a light oil hydrocracker.

2.5.4 Proposed Process Conditions

From the extensive analytical data (53) for the properties of Utah tar sand bitumen following inferences can be drawn regarding the nature of the bitumen

1. High nitrogen content (1.1 wt. percent) and relatively low sulfur content (0.4 wt. percent).

2. Very heavy nature (IBP 460 F, 37.9 wt. %, between 650-1000 F and 55.9 wt. % in 1000 F+ range).

3. Very low H/C ratio (10.64/85.43 in 850 F+ fraction)

4. High proportion of saturated cyclic hydrocarbons (C_nH_2n, C_nH_{2n-2}, C_nH_{2n-4}, C_nH_{2n-6}).

5. High proportion of polynuclear aromatics.

6. Presence of oxygenated compounds (mainly carboxylic acids, total oxygen content 1,15 wt. %).

From the above observations, following approach is suggested for processing Utah tar sand bitumen

1. Due to the high amounts of heteroatoms in the feed, the processing should be carried in two stages

   (a) HDS, HDN and oxygen removal in the first stage.

   (b) Upgrading in the second stage.

2. As discussed earlier a TPEB is best suited for the process.

3. Due to the heavy nature of bitumen, an attempt should be towards upgrading bitumen to synthetic crude.

4. The upgraded products will require further processing to generate gasoline/diesel grade fuels. Thus the hydrocracking step in the second stage should concentrate on hydrogenation rather than extensive cracking. This will also limit the hydrogen consumption during the upgrading stage.

The above mentioned approach leads to proposition of following process conditions

1. Operate the first stage in the high desulfurization/high denitrogenation-low conversion mode (Point A in the plot), which would require high hydrogen pressure, low space velocity, high catalyst activity and high temperature.

2. Operate the second stage to maximize conversion of the 1000 F+ fraction (Point D in the plot). This would demand higher temperature than the first stage. To limit cracking, a catalyst with high hydrogenation activity and low acidity (Ni-silica alumina) is proposed.

2.5.4.1 Proposed Process Parameters

First Stage

1. Hydrogen pressure - 13.78-17.225 MPa (2000-2500 psi).

2. Reactor temperature - 700 K (800° F).

3. Space velocity - 1.0 to 0.5 vol. of oil/vol. of cat./hr.

4. Catalyst - Co-Mo-Alumina.

Second Stage

1. Hydrogen pressure - 13.78-17.225 MPa (2000-2500 psi).

2. Reactor temperature - 700-728 K (800-850° F.

3. Space velocity 1.0 to 0.5 vol. of oil/vol. of cat./hr.

4. Catalyst - Ni-Silica-Alumina.

2.5.5 Expected Product Distribution

The results of hydrocracking of Athabasca tar sand bitumen by H-Oil process (57) can be taken as a guideline to predict the distribution of products from hydrocracking of Utah tar sand bitumen.

As noted by Rapp and Driesen (51) the heteroatoms tend to concentrate in the heavy fractions after processing. As noted earlier, because Utah bitumen has much higher nitrogen content, an acceptable degree of denitrogenation of the bitumen in the first stage will lead acceptable reduction in sulfur.

However, because the nitrogen is concentrated in polynuclear aromatics, the expected HDN per pass in the first stage could be appreciably low. This implies that the recycle to feed ratio need to be to be low and a longer reactor length may be required to increase the residence time. Poisoning of the catalyst by heteroatoms and organometals will be severe, which may demand relatively frequent on-line replacement of the catalyst.

Because a high hydrogenation-low acidity catalyst is being used in the second stage, the C_2, C_3 and C_4 fractions produced will be negligible (2.5 wt. % for Athabasca bitumen). Most portion of the products would be in the 400-650 F boiling point range (40 to 45 wt. %). This portion could be used for jet fuel or as a feed to FCC unit for further processing.

There could be appreciably lower quantity of products boiling above 810 K (15 to 20 percent) with very low H/C ratio. This portion can be used for production of asphalt or electrode grade carbon. The portion boiling between 650-1000 F° (expected to be 20-25 wt. %) could be subjected to HDN and further hydrocracking.

3.1 Necessity and Basis for Scale Down

As noted in Chapter 2, TPEB reactors have been found appropriate for a number of applications such as hydrotreating and hydrocracking of heavy petroleum fractions, coal liquefaction, methanation, crystallization, production of zinc hydrosulfite, etc. (17). The H-Coal and the H-Oil processes for coal liquefaction and for the hydrocracking of heavy resids, respectively, (51) and the Exxon EDS process for coal liquefaction (18) used three phase reactors.

The lengths of commercial reactors, in three phase ebullieted bed process with pelleted catalysts, for the processing of heavy oils, bitumen and bitumen derived liquids are long due to the requirement of low space velocities. Even in the laboratory and pilot scale of development of H-Coal and Exxon EDS process, either large or multiple stage reactors were used. Typical size of an H-Oil hydrocracking TPEB reactor at commercial scale can be 4.0 m ID, 22.0 m long with wall thickness ranging upto 0.3 m. It would be useful to scale down the commercial scale unit, so that the process could be studied in the laboratory and the information extended to larger scales.

Maintaining constant phase holdups is the first significant step toward achieving complete hydrodynamic similarity. Bubble size, bubble rise velocity and bubble coalescence characteristics may be some of the other important hydrodynamic parameters. These aspects are covered in the succeeding chapters. After carefully studying the various hydrodynamic models in section 2.4.6 of Chapter 2, it can be inferred that the phase holdups are governed by the system parameters such as, diameter of the orifices on the distributor, d_o, the particle size, d_p, the reactor diameter, d_r, the liquid superficial velocity, u_l, the gas superficial velocity, u_g, the liquid viscosity, μ_l, the particle density, ρ_p, the liquid density, ρ_l, the gas density, ρ_g and the gas-liquid surface tension, σ. ρ_g, at lower bed pressure, is usually much lower than ρ_l and thus does not affect the phase holdups appreciably.

Hence the dependence of the phase holdups on ρ_g can be neglected at low bed pressure. However, at high bed pressure, ρ_g manifests its influence through the bubble rise velocity u_{br}, on the phase holdups. Thus ρ_g cannot be neglected at high bed pressure. Effect of bed pressure on phase holdups is covered in Chapter 7.

The reactor length, for laboratory scale studies, can be reduced by reducing the liquid superficial velocity. Consequently the catalyst size has to be reduced to achieve ebullietion in the reactor. It is important to ensure that with these changes, the value of the phase holdups are maintained the same in the commercial and the laboratory units. The basis for scaling down the commercial reactor would then be as follows.

1. Reduce the liquid superficial velocity u_l, which increases the solid holdup ϵ_s in the reactor.

2. Reduce the particle size, in the laboratory reactor, to readjust ϵ_s, so that it is same in both the reactors.

3. Adjust the other parameters, such as gas superficial velocity u_g, to get same liquid and gas holdups, ϵ_l and ϵ_g respectively, in the two reactors.

As u_l is reduced, for the same value of space velocity, the solid stagnant bed height reduces. This in turn reduces the reactor length.

A step by step procedure for scaling down the reactor is presented in section 3.3.2 below.

3.2 Calculation of Phase Holdups

3.2.1 Generalized Wake Model

Bhatia and Epstein (119) developed the generalized wake model for predicting phase holdups in three phase ebullieted beds. The model accounts for the presence of solid particles in the bubble wake. It is based on a material balance between the solids carried upward through the bubble wake and the solids settling in the liquid-solid region that surrounds the bubble.

The model requires values for the bubble rise velocity (relative to the surrounding liquid), u_{br}, the ratio of the solid holdup in the bubble wake to the solid holdup in the liquid-solid region, x, and the ratio of the wake volume to bubble volume, κ. These parameters must be calculated by independent methods. For a TPEB operating under atmospheric pressure, with bubbles in a plug flow mode, u_{br} can be calculated according to the following two procedures.

1. The coefficient of viscous drag on a single bubble due to the surrounding liquid C_{Db} is calculated from the correlations developed by Tadaki and Maeda (148).

$$\begin{aligned} C_{Db} &= 0.076(Re_b Mo^{0.23})^{1.82} \quad for\ 8Mo^{0.068} < Re_b Mo^{0.23} < 6 \\ C_{Db} &= 1.25(Re_b Mo^{0.23})^{0.21486} \quad for\ 6 < Re_b Mo^{0.23} < 16.5 \\ C_{Db} &= 2.6 \quad for\ 16.5 < Re_b Mo^{0.23} \end{aligned} \tag{3.1}$$

where,

Re_b, the bubble Reynold number, is given by

$$Re_b = \frac{\rho_l u_{tb} d_b}{\mu_l} \tag{3.2}$$

and

Mo, the Morton number, is given by

$$Mo = \frac{g\mu_l^4}{\sigma^3 \rho_l} \tag{3.3}$$

The diameter of the bubble required to calculate Re_b in Equation set 3.1 is determined from the correlation published by Kim et al. (117).

$$d_b = 0.142 u_l^{0.052} u_g^{0.248} \sigma^{0.034} \mu_l^{0.008} \tag{3.4}$$

C_{Db} is used to calculate the terminal velocity, u_{tb} of a single bubble rising through a liquid column. u_{br} is assumed to be equal to u_{tb} (149).

2. u_{br} can also be calculated from the correlation published by Kim et al.,(117).

$$u_{br} = 5.541 u_l^{0.065} u_g^{0.339} \mu_l^{0.025} \sigma^{0.179} \tag{3.5}$$

κ is obtained by using the procedure developed by Bhatia and Epstein (119).

$$\kappa = \left(0.61 + \frac{0.037}{\epsilon_g + 0.013}\right)(\epsilon_g + \epsilon_l)^3 \tag{3.6}$$

x is calculated using the equation developed by El-Temtamy and Epstein (133).

$$x = 1.0 - 0.877 ar \quad when \;\; ar < 1.14 \tag{3.7}$$

and

$$x = 0 \quad when \;\; ar \geq 1.14 \tag{3.8}$$

where,

$$ar = \frac{u_i}{\left(\frac{u_g}{\epsilon_g} - \frac{u_l}{\epsilon_l}\right)} \tag{3.9}$$

In these equations, u_i is the Richardson-Zaki intercept (Richardson and Zaki, (135)).

The following procedure is used in this study to determine the phase holdups, using the generalized wake model.

1. Define the values of the hydrodynamic parameters, such as u_l, u_g, μ_l, σ, ρ_p, ρ_l, d_p and d_r.

2. Assume a trail value for ϵ_l and ϵ_g.

3. Calculate the particle terminal velocity (u_{tp}) using following steps.

   (a) Assume a value for u_{tp}.

   (b) Calculate the particle Reynolds number, $(Re)_p$.

$$Re_p = \frac{u_{tp} d_p \rho_l}{\mu_l} \tag{3.10}$$

   (c) Calculate the coefficient of drag for the particle C_{Dp}, using the correlation given in Equation 3.11 (150).

$$C_{Db} = \frac{24}{Re_p} + \frac{6}{1 + Re_p^{0.5}} + 0.3 \tag{3.11}$$

   (d) Calculate u_{tp}, using Equation 3.12 (10).

$$u_{tp} = \left(\frac{(4 g d_p (\rho_p - \rho_l))}{3 C_{Dp} \rho_l} \right)^{0.5} \tag{3.12}$$

   (e) Compare the values of u_{tp} in step (b) and calculated in step (d). If the two values are not within a given tolerance, repeat steps (b) to (d), using the value of u_{tp}, calculated in step (d).

4. Calculate the particle Reynolds number from the value of u_{tp} determined in step 3 (d), using Equation 3.10.

5. Calculate the Richardson-Zaki intercept u_i (135).

$$u_i = u_{tp}(0.1^{(d_p/d_r)}) \tag{3.13}$$

6. Calculate the Richardson-Zaki exponent (135) n using the following correlations.

$$
\begin{aligned}
n &= 4.65 + 20(d_p/d_r) && for\ \ Re_p < 0.2 \\
n &= \left(\frac{4.4 + 18(d_p/d_r)}{Re_p^{0.03}}\right) && for\ \ 0.2 \leq Re_p < 1.0 \\
n &= \left(\frac{4.4 + 18(d_p/d_r)}{Re_p^{0.1}}\right) && for\ \ 1.0 \leq Re_p < 200 \\
n &= \left(\frac{4.4}{Re_p^{0.1}}\right) && for\ \ 200 \leq Re_p < 500 \\
n &= 2.4 && for\ \ Re_p \geq 500
\end{aligned}
\tag{3.14, 3.15}
$$

7. Calculate κ using Equation 3.6.

8. Calculate x using Equations 3.7 to 3.9.

9. Calculate the wake volume ϵ_k, using Equation 3.16.

$$\epsilon_k = \kappa \epsilon_g \tag{3.16}$$

10. Calculate $\epsilon_{lf}^{"}$, the liquid holdup in the liquid-solid region.

$$\epsilon_{lf}^{"} = \left(\frac{u_l - v_g \epsilon_k (1-x)}{u_i (1 - \epsilon_g - \epsilon_k)}\right)^{1/n} \tag{3.17}$$

Because

$$v_g \epsilon_k = \frac{u_g \kappa \epsilon_g}{\epsilon_g} = \kappa u_g \tag{3.18}$$

Equation 3.16 becomes

$$\epsilon_{lf}^{'''} = \left(\frac{u_l - \kappa u_g (1-x)}{u_i (1 - \epsilon_g - \epsilon_k)} \right)^{1/n} \tag{3.19}$$

11. Calculate v_g, using Equation 3.20.

$$v_g = \frac{u_l + u_g + \epsilon_{lf}^{''}(1 - \epsilon_g - \epsilon_k) u_{br}}{(1 - \epsilon_s)} \tag{3.20}$$

12. Calculate ϵ_{lt1} from Equation 3.21

$$\epsilon_{lt1} = \epsilon_k (1-x) + \epsilon_{lf}^{''}(1 - \epsilon_g - \epsilon_k + x\epsilon_k) \tag{3.21}$$

13. Calculate ϵ_{lt}, using Equation 3.22.

$$\epsilon_{lt} = \frac{(\epsilon_l + \epsilon_{lt1})}{2} \tag{3.22}$$

14. Calculate ϵ_{gt}, using Equation 3.23.

$$\epsilon_{gt} = \frac{u_g}{v_g} \tag{3.23}$$

15. If values of ϵ_{lt} and ϵ_{gt} calculated in step 13 and 14 are not equal to the values of ϵ_l and ϵ_g, within a given tolerance, make

$$\epsilon_l = \epsilon_{lt} \tag{3.24}$$

and

$$\epsilon_g = \epsilon_{gt} \tag{3.25}$$

and repeat steps 1 to 15.

otherwise

ϵ_{lt} and ϵ_{gt} give the value of the liquid and gas holdup in the TPEB.

The computer code for the generalized wake model is presented in Appendix A.

3.2.2 Validation of Generalized Wake Model

The holdup values predicted by the above model are compared to the experimental values obtained by Armstrong (120) in Table 3.1. For entries 1-4 in Table 3.1, Equations 3.1 to 3.4 are used for the calculation of u_{br} and for entries 5-10, Equation 3.5 is used for u_{br} determination. It is observed from Table 3.1 that the holdups are predicted to within 10% by the above approach. It should be noted that the correlation for d_b obtained by Kim et al. (117) (Equation 3.4) was for a two dimensional system with a rectangular column, whereas, the Richardson-Zaki correlations (135), used in the above formulation for the calculation of phase holdups were developed for columns with circular crossections. Armstrong's (120) data were also obtained using a circular column. The discrepancy between the model calculations and the experiments could be attributed to the different geometry used. Thus, the procedure developed above performs well in predicting phase holdups in three phase ebullieted beds and is used for the formulating and validating the similarity criteria for scaling down commercial units to laboratory scale.

Table 3.1. Validation of the Generalized Wake Model

#	d_p (m)	u_l (m/s)	u_g (m/s)	$(\epsilon_l)_{cal}$ $(-)$	$(\epsilon_l)_{exp}$ $(-)$	$(\epsilon_g)_{cal}$ $(-)$	$(\epsilon_g)_{exp}$ $(-)$
1	0.005	0.092	0.033	0.552	0.577	0.041	0.038
2	0.005	0.092	0.059	0.540	0.558	0.069	0.067
3	0.005	0.092	0.089	0.525	0.535	0.102	0.098
4	0.005	0.092	0.178	0.482	0.529	0.191	0.126
5	0.003	0.056	0.119	0.508	0.504	0.066	0.051
6	0.003	0.056	0.148	0.503	0.543	0.077	0.051
7	0.003	0.056	0.178	0.498	0.527	0.087	0.069
8	0.005	0.067	0.089	0.456	0.512	0.054	0.054
9	0.005	0.067	0.119	0.474	0.504	0.066	0.067
10	0.005	0.067	0.178	0.466	0.509	0.087	0.088

Note: Holdups in entries 1-4 have been calculated using u_{br} correlations given by Tadaki and Maeda (148); holdups in entries 5-10 have been calculated by u_{br} correlation given by Kim et al. (117)

$\rho_p = 2489.0\ kg/m^3$ $\qquad$ $\rho_l = 1000.0\ kg/m^3$
$\mu_l = 0.00131\ kg/m-s$ $\qquad$ $\sigma = 0.0727\ N/m$
$d_r = 0.2413\ m$

3.3 Similarity Criteria

In this section, a similarity criterion is developed, whereby, the holdups in the commercial and laboratory scale reactor would be identical by manipulating all the parameters mentioned in section 3.1 above.

Appropriate scaling down of commercial reactors involves reducing the length of the reactors keeping the space velocities unchanged and ensuring identical hydrodynamic properties in commercial and laboratory units. In order to reduce the reactor length, the liquid velocity has to be reduced. To achieve ebullietion at this liquid velocity, the particle size has to be reduced. The reduction in superficial liquid velocity and particle size has to be achieved in such a manner that the important hydrodynamic parameters remain unchanged. It is recognized here that there may be hydrodynamic parameters, other than phase holdups that influence the process.

Therefore as a first step toward complete hydrodynamic similarity, this chapter considers the similarity of phase holdups which are important hydrodynamic parameters. Consideration to the kinetic rate constant is given in Chapter 9.

After the scale down, particle elutriation in the scaled down reactor, due to the small size of the particles, must be considered. The particle disengaging height should be sufficient to ensure catalyst retention in the reactor. Furthermore, the particle size should not be reduced to such an extent that all particles are elutriated irrespective of the length of the disengaging section. These aspects are incorporated into the scale down procedure by using the stagewise partition process model (144).

The stagewise partition process model and the procedure to calculate the particle disengaging height, using the model, are described below.

3.3.1 Stagewise Partion Process Model

Page and Harrison (151) suggested that the wake formation and shedding were the main mechanism for particle entrainment and de-entrainment in the transition

region and the freeboard. Consequently, the wake shedding frequency plays a prominent role in the axial variation of the solid holdup.

El-Temtamy and Epstein (144) developed a stagewise partition process model for solids entrainment in the freeboard region. They postulated that in each stage, the solid particles are carried upwards in the bubble wake, transferred to the surrounding liquid-solid region, and settled in the liquid-solid region. The height of a stage in the model is assumed to be equivalent to a wake shedding unit, defined as the distance traveled by a bubble during the time interval between the shedding of two successive wake fragments. The stages are numbered from the top of the freeboard region to the surface of the fluidized bed, so that stage N is located between stage N-1 above and stage N+1 below.

A solid balance around stage N gives Equation 3.26.

$$(1-\epsilon_g-\kappa\epsilon_g)(-v_{lf}\epsilon_{lf})_{N-1}+u_g\kappa x(\epsilon_{sf})_{N+1}= u_g\kappa x(\epsilon_{sf})_N+(1-\epsilon_g-\kappa\epsilon_g)(-v_{sf}\epsilon_{lf})_N \tag{3.26}$$

where v_{sf} = Solid linear velocity in the liquid-solid fluidized region.

It is then assumed that v_{sf} is the vectorial difference between the liquid velocity in this region and the velocity of the liquid relative to the solid in the same region (152). v_{sf} can be expressed as

$$v_{sf}=\frac{u_l-u_g\kappa[1-x(\epsilon_{sf})_N]}{(1-\epsilon_g-\kappa\epsilon_g)[1-(\epsilon_{sf})_N]}-u_i(1-(\epsilon_{sf})_N)^{n-1} \tag{3.27}$$

The solid holdup for stage N, obtained by summing up the solids contained in both the wake and liquid-solid fluidized region, is given by Equation 3.28.

$$(\epsilon_s)_N=\kappa\epsilon_g x(\epsilon_{sf})_N+(1-\epsilon_g-\kappa\epsilon_g)((\epsilon_{sf})_N \tag{3.28}$$

Solving Equation 3.26, 3.27 and 3.28 gives solution for ϵ_s in each of the stage. The height of a stage, or wake shedding unit, is

CHAPTER 3

SIMILITUDE STUDIES IN THREE PHASE EBULLIETED BED REACTORS

This chapter deals with the development of hydrodynamic scale down criteria for nonreacting and reacting TPEB reactor systems. The necessity for scaling down the reactor for laboratory kinetic studies is first highlighted and the basis for scale down laid down. The hydrodynamic parameters, on which the phase holdups depend, are identified. Through extensive similitude studies on these parameters, similarity criteria that ensure identical holdups in the commercial and laboratory units with nonreacting systems are identified, which requires the equality of six dimensionless numbers. These criteria are validated using the generalized wake model.

It is found that it is impractical to establish all the parameters in the set of dimensionless numbers at the desired values, without changing the identity of the system. Therefore, a method to achieve similarity by varying a minimum number of parameters, such as liquid and gas superficial velocities and particle size, is developed, by carrying out a rigorous functional analysis on the equations of the generalized wake model. This results in a set of two conditions, which when satisfied, yielded practically equal holdups in the two reactors.

To understand the methodology followed throughout the chapter, the generalized wake model and the stagewise partition process model are explained.

$$HWU = \frac{(u_g/\epsilon_g)}{\nu} = \left(\frac{u_g/\epsilon_g}{(u_g/\epsilon_g - u_l/\epsilon_l)}\right)\left(\frac{d_b}{Sr}\right) \tag{3.29}$$

where,

ν is the wake shedding frequency,

d_b is the effective bubble diameter,

and

Sr, the Strouhal number, defined as

$$Sr = \frac{d_b \nu}{(u_g/\epsilon_g - u_l/\epsilon_l)} \tag{3.30}$$

In the calculations for stage 1, it is necessary to assume a small, but a nonzero value for solid holdup $(\epsilon_s)_1$ and zero for the term $(-v_{sf})_0$. Proceeding downwards, $(\epsilon_s)_N$ is calculated for each stage until, it equals or exceeds the solid holdup in the main three phase region.

The procedure to find the particle disengaging height, used in this study, is as follows.

1. Calculate the values of κ, x, u_i, ϵ_g and ϵ_l for given set of parameters, using the generalized wake model.

2. Assume a value of $(\epsilon_s)_N = 0.0005$.

3. Calculate $(\epsilon_{sf})_N$, using Equation 3.31.

$$(\epsilon_s)_N = \left(\frac{(\epsilon_s)}{(\kappa x \epsilon_g (1 - \epsilon_g - \kappa \epsilon_g))}\right) \tag{3.31}$$

4. Calculate $(v_{sf})_N$, using Equation 3.32.

$$(v_{sf})_N = \frac{u_l - u_g\kappa(1 - x(\epsilon_{sf})_N)}{(1 - \epsilon_g - \kappa\epsilon_g)(1 - (\epsilon_{sf})_N)} - u_i(1 - (\epsilon_{sf})_N)^{(n-1)} \tag{3.32}$$

5. Calculate $(\epsilon_{sf})_{N+1}$, using Equation 3.33.

$$(\epsilon_{sf})_{N+1} = \frac{(\kappa x u_g(\epsilon_{sf})_n - (1 - \epsilon_g - \kappa\epsilon_g)((v_{sf})_N(\epsilon_{sf})_N) + (1 - \epsilon_g - \kappa\epsilon_g)(d_N))}{(\kappa x u_g)} \tag{3.33}$$

where

$d_N = 0$ for N = 1.

and for N > 1, d_N is given by Equation 3.36.

6. Calculate $(\epsilon_s)_{N+1}$, using Equation 3.34.

$$(\epsilon_s)_{N+1} = (\kappa x\epsilon_g(\epsilon_{sf})_{N+1}) + ((1 - \epsilon_g - \kappa\epsilon_g)(\epsilon_{sf})_{N+1}) \tag{3.34}$$

7. If

$$(\epsilon_s)_{N+1} < \epsilon_s \tag{3.35}$$

(a) Calculate d_N, using Equation 3.36.

$$d_N = (v_{sf})_N(\epsilon_{sf})_N \tag{3.36}$$

(b) Make

$$(\epsilon_{sf})_N = (\epsilon_{sf})_{N+1} \tag{3.37}$$

and

repeat steps 1 to 7, by increasing N in steps of one, until

$$(\epsilon_s)_{N+1} > \epsilon_s \tag{3.38}$$

8. Calculate the effective size of the bubble d_b, using the bubble model suggested in Chapter 4.

9. Calculate the terminal velocity of the bubble $(u_t)_b$, using the following steps

   (a) Assume $u_{tb} = 1$.

   (b) Calculate the bubble Reynold number Re_b.

$$Re_b = \frac{u_{tb} d_b \rho_l)}{\mu_l} \tag{3.39}$$

   (c) Calculate the coefficient of drag on the bubble C_{Db}, using Equation 3.40.

$$C_{Db} = \frac{24}{Re_b} + \left(\frac{6}{(1 + {Re_b}^{1/2})}\right) + 0.3 \tag{3.40}$$

   (d) Calculate u_{tb}, using Equation 3.41.

$$u_{tb} = \left(\frac{(4 g d_b(\rho_l - \rho_g))}{(3 C_{Db} \rho_l)}\right)^{1/2} \tag{3.41}$$

   (e) If u_{tb}, calculated in step 9(d) does not compare with the value of $(u_t)_b$ in step 9(b), within a certain tolerance, repeat steps 9(b) to 9(d), using the values of u_{tb}, calculated in step 9(d).

10. Calculate bubble Reynolds number Re_b, using Equation 3.35.

11. Calculate the Strouhal number Sr, using the correlation suggested by Tsuchiya and Fan (153).

$$Sr_b = \frac{1}{2420 Re_b^{-1.02} + 0.776} \tag{3.42}$$

12. Calculate the particle disengaging height tdh, using Equation 3.43.

$$tdh = N \left(\frac{(u_g/\epsilon_g)}{(u_g/\epsilon_g - u_l/\epsilon_l)} \right) \left(\frac{d_b}{Sr} \right) \tag{3.43}$$

3.3.2 Development of Similarity Criteria

As mentioned in section 3,1, the following functional relationships are satisfied.

$$\epsilon_l = f(d_r, d_p, \rho_p, \rho_l, \mu_l, \sigma, u_l, u_g, g, k, x, n, \nu) \tag{3.44}$$

and,

$$\epsilon_g = f(d_r, d_o, d_b, \rho_p, \rho_l, \mu_l, \sigma, u_l, u_g, g, k, x, n, \nu) \tag{3.45}$$

Due to the weak dependence of ϵ_g on the reactor diameter, d_r, it can be eliminated from the above relationships. When the size of the bubbles is governed by bubble coalescence, the bubble diameter, d_b becomes practically independent of the orifice diameter, d_o. Hence, the functional dependence of ϵ_g on d_o has also been neglected at this stage. In the present analysis, d_b is assumed to be a function of the basic system parameters. In practice, it may additionally depend on factors such as the particle diameter d_p, the concentration of impurities and system pressure. In such cases, d_b can be retained as a system parameter in the dimensional analysis and eliminated at a later stage.

By dimensional analysis, following equations are obtained for the phase holdups. The details of the dimensional analysis is presented in Appendix F.

$$\epsilon_l, \epsilon_g = f\left[(\frac{u_l}{u_g}), (\frac{\rho_l}{\rho_r}), (\frac{d_r}{d_p}), (\frac{\rho_l u_l d_p}{\mu_l}), (\frac{u_l^2}{g d_p}), (\frac{u_l^2 d_p \rho_l}{\sigma})\right] \tag{3.46}$$

or

$$\epsilon_l, \epsilon_g = f\left[(\frac{u_l}{u_g}), (\frac{\rho_l}{\rho_p}), (\frac{d_r}{d_p}), (Re_p), (Fr_p), (We_p)\right] \tag{3.47}$$

The dimensionless numbers, Re_p, Fr_p and We_p can be combined to derive a dimensionless number independent of d_p, the Morton number, Mo.

$$\frac{We_p^3}{Re_p^4} \times \frac{1}{Fr_p} = \frac{g\mu^4}{\sigma^3 \rho_l} = Mo \tag{3.48}$$

For similarity, only three out of the four of the above dimensionless numbers (Re_p, Fr_p, We_p and Mo) have to be the same for the commercial and the laboratory units. Hence for an overall similarity of phase holdups between the commercial and laboratory units, the following criteria must be satisfied. The laboratory and the commercial reactors are represented by the subscript 'm' and 'p' respectively.

$$(Re_p)_p = (Re_p)_m \tag{3.49}$$

$$(Fr_p)_p = (Fr_p)_m \tag{3.50}$$

$$(Mo)_p = (Mo)_m \tag{3.51}$$

$$(u_l/u_g)_p = (u_l/u_g)_m \tag{3.52}$$

$$(\rho_l/\rho_p)_p = (\rho_l/\rho_p)_m \tag{3.53}$$

$$(d_r/d_p)_p = (d_r/d_p)_m \tag{3.54}$$

3.3.3 Verification of the Similarity Criteria

The similarity criterion established above is verified by calculating the phase holdups for hypothetical commercial and laboratory systems assuming that the

dimensions and system parameters for the commercial reactor are known. Generalized wake model, described earlier, is then used to calculate the phase holdups in the laboratory system and these values are compared with the phase holdups of the commercial system to validate the similarity criterion. The steps involved in the scaledown procedure are enumerated below:

1. From the known values of the system parameters for the commercial reactor, calculate phase holdups, using the generalized wake model, and calculate all the relevant dimensionless numbers.

2. Select a $(d_p)_m$, which is smaller than $(d_p)_p$ and a value for ρ_l.

3. Calculate $(u_l)_m$, from the condition,

$$(Fr_p)_p = (Fr_p)_m$$

4. Calculate $(\mu_l)_m$ from the criterion,

$$(Re_p)_p = (Re_p)_m$$

5. Determine $(\sigma)_m$ from the equation,

$$(Mo)_p = (Mo)_m$$

6. Evaluate $(u_g)_m$ from the condition,

$$(u_l/u_g)_p = (u_l/u_g)_m$$

7. Calculate $(\rho_p)_m$ from,

$$(\rho_l/\rho_p)_p = (\rho_l/\rho_p)_m$$

8. Finally, find the reactor diameter $(d_r)_m$ using the condition,

$$(d_r/d_p)_p = (d_r/d_p)_m$$

The dependence of the phase holdups ϵ_l and ϵ_g on the reactor diameter d_r is not significant; hence, in a practical situation, if $(d_r)_m$, from the above calculation becomes very small, the above condition can be relaxed to arrive at a practical solution without affecting the phase holdups to a great extent. In fact, wall effects on the particles can be minimized by increasing the diameter of the laboratory reactor.

9. The liquid velocity, $(u_l)_m$ calculated from the above procedure is used to determine the volume of the catalyst for a particular value of space velocity (vol. of catalyst/vol. of feed - hr). The height of the expanded bed is then calculated from the stagnant bed height and the value of ϵ_s.

10. The disengaging height is calculated using the stagewise partition model. The total length of the laboratory reactor is then the sum of the expanded bed height and the disengaging height. In practice, an allowance for mechanical accessories must also be made.

11. If the length of the reactor so calculated is impractically large then the above procedure (steps 1-10) is repeated with a smaller value of $(d_p)_m$. However, it must be ascertained that this reduction in $(d_p)_m$ does not lead to excessively large disengaging heights.

The procedure outlined above is used to arrive at the dimensions and values of the system parameters for the laboratory scale unit using assumed values of the system parameters for a commercial unit. The equality of the phase holdups is then verified by applying the generalized wake model. The results are presented in Table 3.2.

The parameters for both the commercial and the laboratory scale units are hypothetical and have been used simply to illustrate the similarity concept. In Table 3.2, entry #1 ($d_p = 0.0026m.$) can be interpreted as representing the commercial unit. The dimensions of the reactor and the values of the system parameters for subsequent entries in Table 3.2 are arrived at by similarity analysis detailed above and can be interpreted as parameters for scaled down units. The values of the relevant dimensionless numbers used in the calculations are also listed in Table 3.2. It can be seen from the table that the analysis yields absolutely identical values of the phase holdups in each of the cases. It should be kept in mind that the only hydrodynamic parameters that are being considered in the above similarity analysis are phase holdups. Two other important hydrodynamic parameters, bubble size and bubble rise velocity will be considered in the following section.

3.4 A Practical Procedure for Scale Down

The parameters used in the previous section verification are hypothetical. However, in a practical situation, it may not be possible to vary all the system parameters independently to the extent manifested in Table 3.2. For example, the surface tension (σ) can be changed to the desired level by adding an appropriate amount of surfactant; however, this may not effect the necessary change in the liquid viscosity (μ_l). Some other property will have to be changed (temperature, concentration) to achieve the desired value of viscosity. Such a change would alter the reaction chemistry which implies that the previously established similarity criteria can be used only for nonreacting systems. For reacting systems it is mandatory to use the same reactants in the two systems which requires that the parameters, ρ_l, μ_l, ρ_g, and σ after scale down remain unchanged and leaves only d_r, d_p, u_l and u_g for manipulation. This section is concerned with the development

Table 3.2. General Similarity: Six Dimensionless Groups Held Constant

#	d_p (m)	d_r (m)	ρ_p (kg/m^3)	ρ_l (kg/m^3)	σ (N/m)	μ_l $(kg/m.s)$	u_l (m/s)	u_g (m/s)	ϵ_s $(-)$	ϵ_l $(-)$	ϵ_g $(-)$
1.	.0010	.150	2300	1000	.0728	.00100	.0200	.02074	.487	.494	.019
2.	.0012	.180	2254	980	.1020	.00129	.0219	.02271	.487	.494	.019
3.	.0013	.195	2208	960	.1180	.00142	.0228	.02364	.487	.494	.019
4.	.0017	.255	2507	1090	.2290	.00242	.0261	.02706	.487	.494	.019
5.	.0026	.390	2645	1150	.5660	.00482	.0323	.03439	.487	.494	.019

$Re_p = 20.0$

$Fr_p = 0.04077$

$M_o = 2.5426 \times 10^{-11}$

$u_g/u_l = 1.037$

$d_s/d_l = 2.3$

of criteria which lead to the desired similarity between holdups in the two reactor system by the manipulation of the above four parameters.

Equations (3.17) and (3.20) can be rearranged to give the following equations:

$$\epsilon''_{lf} = \left(\frac{(u_l - u_g \kappa(1-x))}{u_i(1-\epsilon_g - \epsilon_k)} \right)^{1/n} \tag{3.55}$$

$$\epsilon_g = \frac{v_g(\epsilon_l + \epsilon_g)}{[u_l + u_g + \epsilon''_{lf}(1-\epsilon_g - \epsilon_k)]u_{br}} \tag{3.56}$$

and since

$$v_g = f(\epsilon, u_{br}) \tag{3.57}$$

we have;

$$\epsilon_g = f(u_l, u_g, \epsilon''_{lf}, \epsilon_l, \epsilon_g, \epsilon_k, u_{br}) \tag{3.58}$$

Equation 3.6 and 3.16 imply that

$$\epsilon_k = f(\epsilon_l, \epsilon_g) \tag{3.59}$$

Thus, if the holdups are identical and if ϵ''_{lf} and u_{br} are the same in the commercial and the laboratory units, then, $\epsilon_g = f(u_l, u_g)$. Thus, one of the important considerations is that,

$$(u_{br})_p = (u_{br})_m \tag{3.60}$$

At this stage, it should be noted that there is a close relationship between u_{br} and d_b. In fact, Kim et al. (117), presented a single valued correlation between u_{br} and d_b. Thus, when the bubble rise velocities in the commercial and laboratory units are equal, the bubble sizes will also be equal or close to being equal, provided the flow regimes are the same in the commercial and laboratory units. Hence the practical similarity procedure, by allowing the phase holdups, the bubble size and bubble rise velocity to be equal for the laboratory and commercial units, is a step

closer to complete hydrodynamic similarity than the general similarity procedure discussed earlier.

Equation 3.55 indicates that

$$\epsilon_{lf}'' = f(u_l, u_g, \kappa, x, u_i, \epsilon_g, \epsilon_k, n) \tag{3.61}$$

From Equations 3.6 to 3.9 and ( ), we have

$$\epsilon_{lf}'' = f(u_l, u_g, u_i, n, \epsilon_g, \epsilon_l) \tag{3.62}$$

When the holdups are identical, Equation 3.61 reduces to,

$$\epsilon_{lf}'' = f(u_l, u_g, u_i, n) \tag{3.63}$$

However,

$$u_i \text{ and } n = f(d_p, \mu_l, \rho_p, \rho_l). \tag{3.64}$$

Thus, if the parameters μ_l, ρ_l and ρ_p are defined for the two systems (same catalyst and fluid systems), and if $(d_p)_p$ and $(d_p)_m$ are known, then u_i and n for the laboratory unit can be determined. With this information and with u_{br} being identical for the two systems, Equations 3.55 and 3.56 can be solved to obtain the values of $(u_l)_m$ and $(u_g)_m$ for identical holdups between the commercial and laboratory systems.

Combining Equations 3.17 and 3.20 we have,

$$\epsilon_l = \epsilon_k(1-x) + \left(\frac{u_l - \kappa u_g(1-x)}{u_i(1-\epsilon_g-\epsilon_k)}\right)^{1/n}(1-\epsilon_g-\epsilon_k+x\epsilon_k) \tag{3.65}$$

It is found that in the generalized wake model, the value of x does not affect the phase holdups appreciably. If x is chosen to be equal to zero in the above equation, then

$$\epsilon_l \simeq \epsilon_k + \left(\frac{u_l - \kappa u_g}{u_i(1-\epsilon_g-\epsilon_k)}\right)^{1/n}(1-\epsilon_g-\epsilon_k) \tag{3.66}$$

When the holdups, ϵ_l and ϵ_g are identical, then $(\epsilon_k)_p = (\epsilon_k)_m$. This yields the simplified similarity condition.

$$\left(\frac{(u_l - \kappa u_g)}{u_i(1-\epsilon_g-\kappa\epsilon_g)}\right)_p^{1/n} = \left(\frac{(u_l - \kappa u_g)}{u_i(1-\epsilon_g-\kappa\epsilon_g)}\right)_m^{1/n} \tag{3.67}$$

Again, by keeping u_{br} the same for the commercial and the laboratory units, Equations 3.55, 3.56 and 3.67 can be solved simultaneously for the values of $(u_l)_m$ and $(u_g)_m$. Thus, Equations 3.60 and 3.67 constitute a set of reduced similarity criteria for the three phase ebullieted bed systems, requiring manipulation of a minimum number of parameters.

These conditions consider changes only in four easily adjusted parameters; d_p, d_r, u_l and u_g. Using these conditions, for a given set of values of the system parameters for a commercial unit, and for a certain choice of d_p for the laboratory unit, the values of u_l and u_g for the laboratory, can be calculated to give identical holdups. As noted earlier, d_r does not influence the phase holdups significantly. The results of these calculations are presented in Table 3.3. In each of the entries, the larger diameter particle represents the commercial unit and the smaller diameter particle the laboratory unit. Given the parameters for the commercial unit and a value for $(d_p)_m$, u_l and u_g for the laboratory system are calculated using the simplified similarity criteria. The phase holdups are calculated using the generalized wake model. It is observed from Table 3.3, that the holdups are almost identical for the commercial and the laboratory units in each of the entries. Thus, the reduced set of criteria are an effective means for scaling down a commercial three phase ebullieted bed reactor to laboratory scale.

Table 3.3. Practical Similarity: Two Reduced Similarity Criteria Satisfied

	commercial					laboratory				
#	d_p (m)	u_l (m/s)	u_g (m/s)	ϵ_l $(-)$	ϵ_g $(-)$	d_p (m)	u_l (m/s)	u_g (m/s)	ϵ_l $(-)$	ϵ_g $(-)$
1	0.005	0.075	0.122	0.497	0.067	0.003	0.056	0.119	0.508	0.066
2	0.005	0.075	0.153	0.492	0.078	0.003	0.056	0.148	0.503	0.077
3	0.005	0.075	0.183	0.487	0.089	0.003	0.053	0.178	0.486	0.087
4	0.005	0.067	0.178	0.466	0.087	0.003	0.047	0.173	0.463	0.085
5	0.005	0.067	0.089	0.479	0.054	0.003	0.047	0.086	0.475	0.053
6	0.005	0.067	0.119	0.474	0.066	0.003	0.047	0.115	0.471	0.064

Values of other parameters

$\rho_p = 2489.0\ kg/m^3$ $\qquad$ $\rho_l = 1000.0\ kg/m^3$
$\mu_l = 0.00131\ kg/m - s$ $\qquad$ $\sigma = 0.0727\ N/m$
$d_r = 0.2413\ m$

3.5 Summary

1. The scaledown of a TPEB commercial reactor is necessary to study the hydrotreating and hydrocracking process in the laboratory.

2. The similarity criteria, which requires the equality of six dimensionless numbers, ensures identical phase holdups in the laboratory reactor and the large scale reactor with nonreacting systems.

3. The reduced similarity criteria ensures equality in phase holdups of the laboratory and the commercial reactor with reacting system maintaining the chemical identity of the process same in both the reactors.

4. The reduction in reactor length achieved by using the reduced similarity criteria depends on the degree of reduction in particle size d_p and the change in liquid hourly space velocity S_v.

CHAPTER 4

A MODEL FOR THE PREDICTION OF BUBBLE SIZE

Accurate predictions of bubble sizes in gas-liquid systems are required for the evaluation of the hydrodynamic parameters and estimation of transport coefficients. As noted in Chapter 3, the bubble rise velocity is a key parameter in the determination of hydrodynamic parameters such as liquid and gas holdups, and is governed by the bubble size. This has a further implication in three phase gas-liquid-solid systems under high pressure conditions, where bubble coalescence is minimal (154).

In this chapter, a new model for the prediction of volumes of bubbles generated from a single orifice in two phase gas-liquid systems has been developed based on a rigorous bubble closure mechanism. The interaction between the primary bubble and subsequent bubbles formed at the orifice has been incorporated into the model at high gas flow rates. The distance traveled by the bubble from the orifice before it detaches is also calculated by the model. This has been validated by comparison with the available experimental data and it is found that this model represents an improvement over previous models.

4.1 Introduction

Ramakrishna et al. (155) developed a model for computing the volumes of gas bubbles emanating from a single submerged orifice. This analysis has been the primary reference on this topic since the time it was published (150,156). The model of Ramakrishna et al. (155) is based on a force balance around the bubble and makes

an important assumption that the bubble detaches from the spout (connecting it to the orifice) after its base has covered a distance equal to r_E, which is the radius of the bubble at a stage when it detaches from the orifice. In a separate study (157), it was assumed that this distance was equal to the diameter of the orifice. In the model presented in this chapter, the above assumptions are not required. The model developed is for bubble formation from a single orifice under constant gas flow conditions with the liquid being in the stagnant mode.

4.2 Previous Work

Ramakrishna et al. (155) consider two stages in the formation of the bubble, the expansion and the detachment stages. In the expansion stage the bubble expands, but remains attached to the lip of the orifice. In the subsequent detachment stage, the bubble remains in contact with the orifice through a cylindrical spout, though the base of the bubble moves away from the orifice. The bubble detaches from the spout after it has traversed a distance equal to its radius (r_E) at the end of the expansion stage. During the detachment stage, the bubble is filled at the rate of constant gas flow, Q. The final volume of the bubble is given by the sum of the volumes of the two stages.

The force balance employed by Ramakrishna et al. (155) considered forces due to buoyancy, viscous drag, surface tension and inertia. The volume of the bubble, V_E, at the end of the expansion stage is calculated using Equation 4.1.

$$V_E^{5/3} = \frac{11}{192\pi(3/4\pi)^{2/3}g}Q^2 + \frac{3}{2(3/4\pi)^{1/3}g} \times \frac{\mu_l Q V_E^{1/3}}{\rho_l} + \frac{\pi d_o \sigma V_E^{2/3}}{g\rho_l} \qquad (4.1)$$

In the above development, the density of the gas has been considered negligible compared to the density of the liquid.

Equation 4.2 was obtained for the detachment stage by using a dynamic force balance to describe the motion of the bubble.

$$(V_E + Qt)(11\rho_l/16)(dv/dt) + v(11\rho_l/16)Q$$
$$+6\pi(3/4\pi)^{1/3}(V_E + Qt)^{1/3}\mu_l v =$$
$$(V_E + Qt)\rho_l g - \frac{3\mu_l Q}{2(3/4\pi)^{1/3}(V_E + Qt)^{1/3}} -$$
$$\frac{Q^2(11\rho_l/16)(V_E + Qt)^{-2/3}}{12\pi(3/4\pi)^{2/3}} - \pi d_o \sigma cos\alpha \tag{4.2}$$

If Equation 4.2 is integrated twice with respect to t, the distance, x, traveled by the bubble from the orifice as a function of time is obtained.

$$y = \frac{B}{2Q(A+1)}(V^2 - V_E^2) - \left(\frac{C}{AQ}\right)(V - V_E)$$
$$-\frac{3G}{2Q(A-1/3)}(V^{2/3} - V_E^{2/3}) - \frac{3E}{Q(A-2/3)}(V^{1/3} - V_E^{1/3})$$
$$-\frac{1}{Q(-A+1)}(V^{-A+1} - V_E^{-A+1})$$
$$\times \left[\frac{B}{A+1}V_E^{A+1} - \left(\frac{C}{A}\right)V_E^A - \frac{G}{A-1/3}V_E^{A-1/3} - \frac{E}{A-2/3}V_E^{A-2/3}\right] \tag{4.3}$$

where, V is the instantaneous volume of the rising bubble. The parameters A, B, C, E and G are the same as those used by Ramakrishna et al. (155) and are given below:

$$A = 1 + \frac{96\pi(1.25)r_E\mu_l}{11\rho_l Q} \tag{4.4}$$

$$B = \frac{16g}{11Q} \tag{4.5}$$

$$C = \frac{16\pi d_o \sigma cos\alpha}{11\rho_l Q} \tag{4.6}$$

$$E = \frac{Q}{12\pi(3/4\pi)^{2/3}} \tag{4.7}$$

$$G = \frac{24\mu_l}{11\rho_l(3/4\pi)^{1/3}} \tag{4.8}$$

The *key* assumption by Ramakrishna et al. (155) is that the bubble travels a distance equal to its radius, r_E, at the end of the first stage before it detaches from

the spout. Ramakrishna et al. (155) set x in Equation 4.3 equal to r_E, solved the equation for V and obtained the final volume, V_T, of the bubble.

$$V_T = V = V_E + Q \times t \tag{4.9}$$

This technique predicts reasonably accurate bubble volumes for high gas flow rates but considerably higher volumes for lower flow rates.

4.3 Model Formulation

4.3.1 Bubble Formation at Low Gas Flow Rates

In this study, a different approach is used to estimate times for bubble closure in the second stage. Consider the growth of the bubble as shown in Figure 4.1. As the bubble grows, the angle that the center of the bubble makes with the edge of

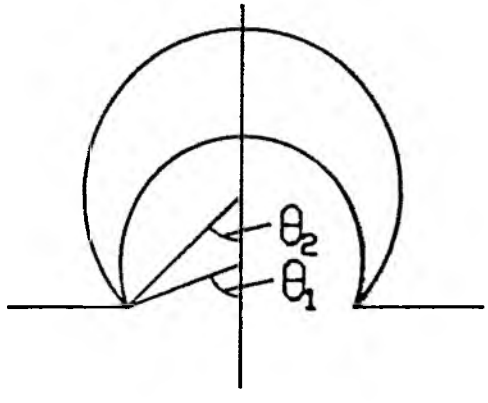

Figure 4.1. Variation in θ in the Bubble Expansion Stage.

the orifice, θ, decreases. Thus, θ_1 is greater than θ_2 (Figure 4.1). If this angle is θ_E when the bubble detaches from the orifice (at the end of the first stage), then the time of bubble closure can be calculated using the rate at which this angle changes with time.

Consider the bubble accelerating during the second stage with the frame of reference attached to its center as shown in Figure 4.2. By applying a force equal and opposite to that experienced by the center of mass of the accelerating bubble at the origin of the frame of reference, the frame of reference becomes an inertial frame of reference. The fact that in this frame of reference, the resultant force on the center of mass of the bubble is zero, implies one of the following:

1. the forces on the individual bubble elements, though nonzero, cancel to yield a zero resultant force at the center of mass; or

2. the forces on the individual elements are zero.

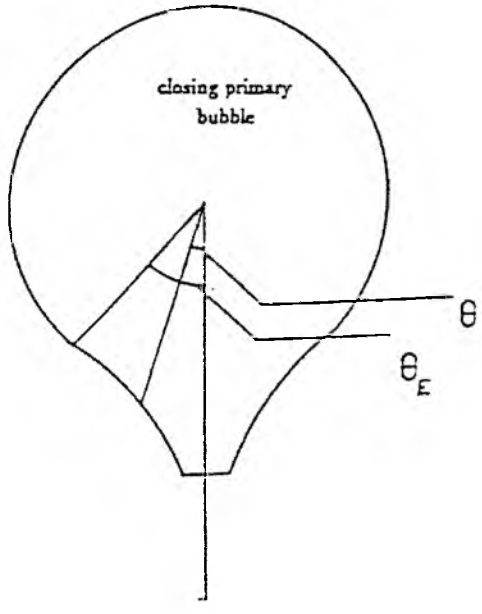

Figure 4.2. Spout as Seen by an Observer Outside the Bubble.

Implication one is not valid because, in the stationary frame of reference outside the bubble, the center of mass of the bubble is accelerating which means that the forces on the individual bubble elements do not cancel. This means that the individual forces on the elements are zero in the inertial frame of reference. Thus for an observer situated at the center of mass of the bubble in the inertial frame of reference, the bubble grows in a symmetrical fashion and closes at a constant rate given by $d\theta_E/dt$. An observer outside the bubble in a stationary frame of reference, sees a spout emerging from the bubble as shown in Figure 4.2.

Once V_E is calculated by Equation 4.1, then the radius of the bubble r_E can be computed using the expression for the volume of a truncated sphere (158).

$$r_E = \left[\frac{3}{4\pi}\left\{V_E + \frac{1}{3}\pi(r_E - (r_E^2 - r_0^2)^{1/2})^2\,(2r_E + (r_E^2 - r_0^2)^{1/2})\right\}\right]^{1/3} \tag{4.10}$$

This nonlinear, implicit equation can be solved for r_E by successive substitution. If the radius of the orifice r_0 is known, then the angle θ_E can be determined from:

$$\theta_E = arcsin(r_0/r_E) \tag{4.11}$$

The rate of bubble closure is calculated by considering the time required to form the bubble just before its detachment, in the first stage.

$$\frac{d\theta_E}{dt} = \frac{(2\pi - 2\theta_E)}{(V_E/Q)} \tag{4.12}$$

Once θ_E and $d\theta_E/dt$ are known , the time of closure t_c can be calculated by Equation 4.13.

$$t_c = \frac{\theta_E}{(d\theta_E/dt)} \tag{4.13}$$

The additional volume, V_A, in the second stage is calculated by taking into account the constriction of the throat of the spout during the expansion stage. V_A is given by:

$$V_A = \frac{Q}{r_0^2}\int_0^{t_c}(r_i sin\theta_i)^2 dt \tag{4.14}$$

where $r_i sin\theta_i$ represents the instanteneous radius of the throat.

Equation 4.14 is integrated numerically to obtain the additional volume entering the bubble in the second stage. The instantaneous volume of the rising bubble, V, used in Equation 4.3 to calculate y, is determined by using the changing time, t, as the upper limit of integration in Equation 4.14. r_i in Equation 4.14 is evaluated by using V in place of V_E in Equation 4.10. In fact, Equations 4.10 and 4.14 are solved simultaneously, iteratively for r_i and V. The total volume of the bubble, V_T, is determined by the addition of the volumes from the two stages of bubble growth.

$$V_T = V_E + V_A \tag{4.15}$$

This formulation holds as long as the primary bubble that detaches from the orifice is not interfered with by the rapid growth of a secondary bubble. This is generally true for low gas velocities. The flow rate at which this interference occurs is determined by a complex interaction between the parameters involved (ρ_l, d_o, μ_l, σ, etc.). In general, higher liquid viscosities and higher gas flow rates promote this interaction.

4.3.2 Bubble Formation at Medium Flow Rates

At higher flow rates, before the initial primary bubble has a chance to close and detach from the spout, the next bubble (secondary bubble) that forms at the orifice grows sufficiently fast to interfere with the primary bubble. When this happens, the growth of the primary bubble in the second stage is influenced by the growth of the secondary bubble and its *merger* with the primary bubble. This phenomenon is taken into account by the following stepwise procedure.

1. The time of closure of the primary bubble (t_c) is calculated.

2. The distance traveled by the the primary bubble (x) in time t_c is determined using Equation 4.3. The volume V in this equation is set equal to V_T calculated

from Equation 4.15. The growth of the secondary bubble in the same time period is also evaluated. The parameter of interest in this growth is h (Figure 4.3 and 4.4). Initially, the secondary bubble is a truncated hemisphere (Figure 4.3) and when h is greater than r_0, it transforms into a truncated sphere (Figure 4.4). The volume of a truncated hemisphere is given by (158):

$$V_s = \frac{1}{6}\pi h(3r_0^2 + h^2) \tag{4.16}$$

where,

$$V_s = Qt_c - V_A \tag{4.17}$$

Equation 4.17 results from the assumption that the difference between the constant flow rate Q at the orifice and the instantaneous flow rate into the primary bubble gives the flow rate into the secondary bubble during its forma-

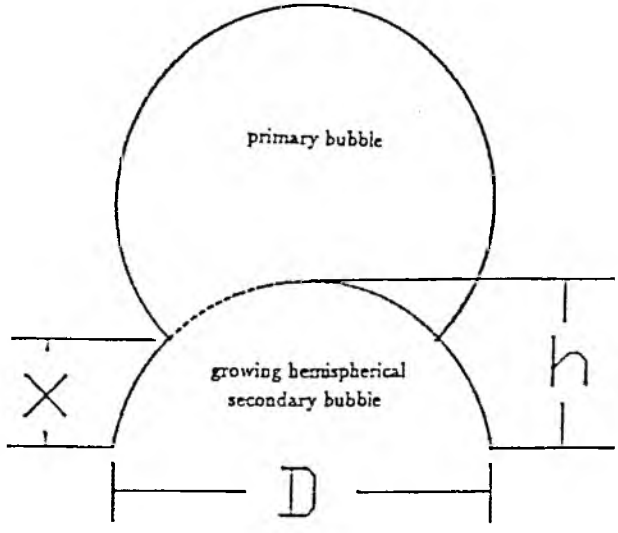

Figure 4.3. Interference Between the Hemispherical Secondary Bubble and the Primary Bubble at Medium Flow Rate.

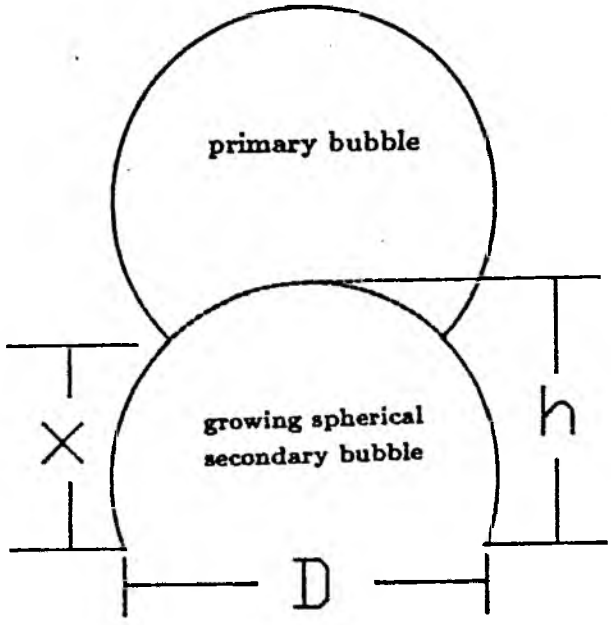

Figure 4.4. Interference Between the Spherical Secondary Bubble and the Primary Bubble at Medium Flow Rate.

tion and growth. h can then be calculated by combining Equations 4.16 and 4.17.

When the secondary bubble grows into a spherical segment, V_s is substituted into Equation 4.10 in place of V_E to calculate the radius r of the spherical segment. h is then related to r by the equation for a truncated sphere (158).

$$h = 2r - (r^2 - r_0)^{1/2} \tag{4.18}$$

3. If h is greater than y, then the secondary bubble interferes with the primary bubble before it closes and detaches from the spout.

4. When this is known to occur, there is a dynamic interaction between the growths of the primary and the secondary bubbles and the bubble closure equations developed earlier no longer apply. During this dynamic interaction,

it is assumed that half the flow enters the primary bubble and the other half into the secondary bubble for the calculations of h and y. The time of this interference (t_i) is calculated by considering the rise of two hypothetical interfaces; the bottom of the rising primary bubble and the top of the growing secondary bubble. This situation is depicted in Figure 4.5. The time of interference is calculated by considering the time for which h remains greater than y. As additional gas enters the primary bubble, its velocity increases and after a period of time, the bottom of the primary bubble rises above the top of the growing secondary bubble ($y = h$ in Figure 4.5). At this point the interaction between the two bubbles ceases and the primary bubble pulls away. Due to this interference, the gas that enters the primary bubble and the secondary bubble during the period of interference actually results in

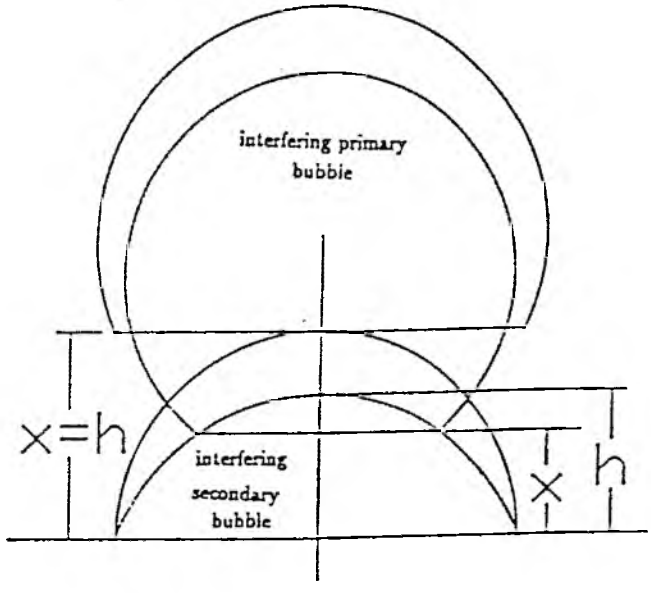

Figure 4.5. Illustration of the Interference Concept: Interference when $y < h$ and End of Interference when $y \geq h$.

expanding the primary bubble.

5. Once this interference ends, the primary bubble begins to close and the additional volume of gas, V_A, entering the bubble during its closure is calculated as described previously (Equation 4.14).

6. Thus the total volume of the bubble is given by:

$$V_T = V_E + Qt_i + V_A \tag{4.19}$$

7. In the range of these flow rates, the secondary bubble *does not* grow to the size V_E in time t_i, and remains in contact with the orifice at all times.

The first contact between the primary and the secondary bubbles takes place in a matter of microseconds ($<< t_c$), after which the secondary bubble is not a separate entity. It becomes a part of the feeding spout for the primary bubble and is difficult to observe visually, even with high speed photography (Datta et al. (159) and Davidson and Schüler (160)). The growth concepts for the secondary bubble described above, are intended to calculate the interference time. In the photographs presented by Davidson and Schüler (160) (Figure 3 in that reference, frames 3, 4 and 5) it can be observed that the volume of the bubble attached to a spout (after the end of interference) is considerably greater than the volume of the bubble, V_E, at the time of detachment from the orifice. This could be due to the merger of the secondary bubble with the primary bubble. The presence of the secondary bubble is also noticed from the fact that before the start of bubble closure, the spout assumed the shape of an inverted bell and its overall diameter is larger than the orifice diameter. The neck closure phenomenon is also observed clearly in Figure 3, frame 2 of Davidson and Schüler (160).

4.3.3 Bubble Formation at High Flow Rates

When the gas flow rates are very high, the secondary bubble grows sufficiently (i.e., attains volume V_E) to detach from the orifice and merges with the primary bubble (Figure 4.6). The force balance on the secondary bubble dictates this detachment of the secondary bubble. The detached secondary bubble with volume V_E becomes part of the primary bubble. The following procedure is used for the calculation of bubble volumes at high flow rates:

1. If the secondary bubble is known to interfere with the primary bubble, its volume is monitored by the procedure outlined in Section 4.3.2 (step 4).

2. If the volume of the secondary bubble exceeds V_E, then the secondary bubble detaches and merges into the primary bubble.

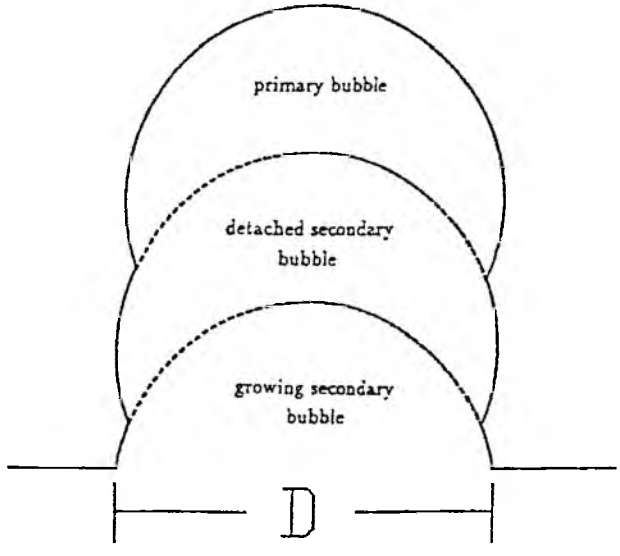

Figure 4.6. Bubble Assembly at High Flow Rates.

3. The distance that the lower tip of this merged bubble assembly (refer to Figure 4.6) travels from the orifice in a given time is calculated. In the same time period, the growth of a new secondary bubble at the orifice is recorded. If there is interference, the volume of the new secondary bubble is again monitored as in subsection 4.3.2 (step 2). If it does not exceed its detachment volume, V_E, the contribution of this bubble to the volume of the bubble assembly is calculated by procedure outlined in subsection 4.3.2 (step 4). If the volume of the secondary bubble does exceed V_E, then step 2 in this section is repeated.

4. This calculation sequence is repeated until the assembly of bubbles no longer indicates interference by subsequent growing secondary bubbles.

5. As this assembly pulls away, the volume V_A, entering the bubble assembly during the closure time is added to obtain the final volume, V_T.

The fact that the volume of the bubble before the start of bubble closure is several times V_E is observed in Figure 10, frames 8, 9, 10, 11 and 12 in the reference by Davidson and Schüler (160) and confirms the merger of several secondary bubbles with the primary bubble before detachment. The flow rate for this experiment was 2.6×10^{-5} m^3/s and this falls into high rate classification as shown in the Results Section.

4.3.4 Bubble Formation Under High Pressure

The bubble model formulated by Ramakrishna et al. (155), and presented in Section 4.2 is based on the assumption, that the gas density ρ_g is negligible compared to the liquid density ρ_l and can therefore be neglected in the derivation. This is true at low pressures. However, this assumption cannot be made for the formation of the bubble at high pressure, where ρ_g increases and therefore cannot be neglected. The effect of high pressure, on the bubble formation, can

be introduced by including ρ_g in the development presented in Section 4.2. The equations of Section 4.2 have been modified to include ρ_g along with the force due to gas momentum and the derivation is presented in details in Appendix G. The formulation in Appendix G has been used to determine the bubble diameter for laboratory reactor design in Section 7.8.

4.4 Results and Discussion

The computer codes for the proposed model are presented in Appendix B. The predictions of the above model are compared with the experimental results from Datta et al. (159) and from Davidson and Schüler (160). The comparison of the experimental results from Datta et al. (159) with the model predictions is presented in Table 4.1. The bubble volumes predicted by Ramakrishna et al. (155) are also included in the table. As can be seen from Table 4.1, the experimental values were obtained over a wide range of values of the parameters, μ_l, σ, ρ_l and Q. The calculation for the bubble volume must take into account primary and secondary bubble interference, which depends on the interaction of these parameters. In general, bubble interaction is significant for high liquid viscosities and high flow rates. For higher orifice diameters this transition from no interference to interference occurs at lower viscosities than for lower orifice diameters.

The reasons for the above observations are easily explained. At higher flow rates, the secondary bubble grows at a rapid rate and interferes with the primary bubble before it closes. The closure of the primary bubble is not affected to the same degree by the increased flow rates. The viscosity effect is due to the fact that the velocity of the rising primary bubble is reduced in high viscosity fluids due to increased drag. This limits the distance that the primary bubble travels from the orifice and creates the possibility of interference with the secondary bubble. When

Table 4.1. Comparison of the Calculated Bubble Volumes with the Experimental Values (159)

μ	σ	ρ_l	Q	Bubble volume, $m^3 \times 10^{-6}$			x	r_E
N s/m^2	N/m	kg/m^3	m^3/s $\times 10^6$	Expt.	Calcd.	Ref. [2]	m	m
				D = 0.036 cm				
.0012	.0728	999.4	0.00810	0.0072	0.0087	0.0107	.00043	0.126
.0154	.0683	1170	0.00787	0.0070	0.0072	0.0077	.00042	0.117
.0235	.0676	1185	0.00787	0.0070	0.0070	0.0077	.00044	0.116
.0497	.0664	1210	0.00765	0.0068	0.0069	0.0075	.0041	0.115
.1108	.0657	1220	0.00765	0.0068	0.0070	0.0074	0.00040	0.114
				D = 0.141 cm				
.0012	.0728	999.4	0.06083	0.0294	0.0365	0.0611	0.136	0.199
.0154	.0683	1170	0.05208	0.0250	0.0303	0.0319	0.140	0.185
.0235	.0676	1185	0.05104	0.0245	0.0290	0.0312	0.138	0.183
.0497	.0664	1210	0.04812	0.0231	0.0286	0.0311	0.135	0.182
.1108	.0657	1220	0.04583	0.0220	0.0291	0.0301	0.128	0.180
				D = 0.388 cm				
.0012	.0728	999.4	0.20500	0.0984	0.1080	0.2072	0.145	0.283
.0154	.0683	1170	0.18120	0.0870	0.0883	0.9653	0.135	0.265
.0235	.0676	1185	0.18120	0.0870	0.0865	0.0916	0.120	0.263
.0497	.0664	1210	0.17170	0.0850	0.0856	0.0876	0.146	0.261
.1108	.0657	1220	0.17500	0.0840	0.0839	0.0865	0.169	0.260

the orifice diameter is large, the closing angle is large, making t_c longer and hence the interference phenomena are observed for lower viscosities.

As the orifice diameter increases, it requires larger flow rates for interference between primary and secondary bubbles. This is because for smaller orifice diameters, the secondary bubble front (h) grows at a faster rate than for larger orifice diameters at a given flow rate. It is seen from Table 4.1 that the proposed model predicts the bubble volumes much more accurately than the previous model of Ramakrishna, et al. (155). This is particularly evident for lower flow rates for each of the orifice diameters studied. In Tables 4.1 and 4.2, x denotes the distance traveled by the bubble or the bubble assembly before it finally pulls away from the spout. This can be compared to r_E, the radius of the bubble at the end of the expansion stage. It is clear that at lower flow rates, x is much lower than r_E. Ramakrishna et al. (155) assumed that $x = r_E$ and thus overestimated the bubble volumes at lower flow rates. Tsuge and Hibino (157) assumed that x was equal to the diameter of the orifice. Though their formulation is for variable pressure in the plenum chamber, it can be seen that this assumption is reasonable at lower orifice diameters. In fact, this observation holds for all but the largest of the orifice diameters (0.00388 m). The flow rates noted in Table 4.1 are not sufficiently high to generate multiple secondary bubbles and it is not necessary to consider secondary bubble formation and their detachment at high flow rates.

The predictions of the model are compared to the experimental results from Davidson and Schüler (160) and calculations from Ramakrishna et al. (155) in Table 4.2. In most instances, the proposed model predicts bubble volumes more accurately than the previous model.

It can be observed from Table 4.2 that the experimental bubble volumes for the two systems with $d_o = 0.004$ m, $\mu_l = 0.001$ N s/m^2, $\rho_l = 1000$ kg/m^3, $\sigma = 0.0727$ N/m and $d_o = 0.004$ m, $\mu_l = 0.00099$ N s/m^2, $\rho_l = 810$ kg/m^3, $\sigma = 0.0271$ N/m are

Table 4.2. Comparision of the Calculated Bubble Volumes with the Experimental Values (160) for High Flow Rates

σ (dyn/cm)	ρ_l (g/cc)	Q (cc/sec)	Bubble volume (cc) Expt.	Calcd.	Ref. [2]	x (cm)	r_E (cm)	n_{sb} (#)
			$D = 0.0668$ cm $\mu = 0.01$ poise					
72.7	1.000	0.5	0.0260	0.0211	0.0333	0.066	0.155	-
		1.0	0.0365	0.0270	0.0481	0.065	0.157	-
		1.5	0.0365	0.0320	0.0632	0.065	0.159	-
		2.0	0.0500	0.0390	0.0789	0.065	0.160	-
		2.5	0.0680	0.0420	0.0952	0.066	0.165	-
			$D = 0.0668$ cm $\mu = 0.0099$ poise					
27.1	0.810	0.5	0.009	0.013	0.0215	0.06	0.121	-
		1.0	0.0200	0.017	0.0350	0.061	0.125	-
			$D = 0.4$ cm $\mu = 0.01$ poise					
72.7	1.000	5.0	0.2000	0.315	0.3106	0.35	0.290	1
		10.0	0.4200	0.471	0.5210	0.36	0.300	2
		20.0	0.9000	0.823	0.9897	0.382	0.328	3
		30.0	1.3000	1.2500	1.5068	0.404	0.357	4
			$D = 0.4$ cm $\mu = 0.0099$ poise					
27.1	0.810	5.0	0.2000	0.233	0.2306	0.365	0.239	2
		10.0	0.4200	0.426	0.4348	0.348	0.257	4
		20.0	0.8500	0.812	0.9007	0.367	0.297	6
		30.0	1.1500	1.300	1.4173	0.386	0.333	7

equal for $Q = 5 \times 10^{-6} \mathrm{m}^3/\mathrm{s}$. As observed by bubble volumes at other flow rates, at lower σ, the bubble volumes decrease. Thus there may have been an experimental discrepancy at the lower flow rate for the system with $\sigma = 0.0727$ N/m. Davidson and Schüler (8) report experimental difficulties with some of their measurements at high gas flow rates.

It should be noted that at these high rates, x is close to r_E and the predictions of Ramakrishna et al. (155) are also very good. The number of secondary bubbles with volume V_E, which merge into the primary bubble to form the final bubble assembly is also listed in Table 4.2. There are a considerable number of secondary bubbles generated at high flow rates (1×10^{-5} to 3×10^{-5} m^3/s), as can be seen from Table 4.2. As the flow rates increase further, the number of secondary bubbles increase and add to the volume of the primary bubble. At a certain stage, the volume of the primary bubble will be so large that it will form a continuous gas column through the liquid. Thus, the model has a potential for predicting jet formation in two phase gas liquid bubble columns.

The above observations are consistent with the classification of bubble formation regimes postulated by Tsuge (161). At constant flow condition, Tsuge (9) classified the bubble formation into three ranges based on the flow rate number N_w.

$$N_w = (Bo)(Fr)^{0.5}$$

where,

$$Bo = \frac{\rho_l d_o^{\,2} g}{\sigma}$$

$$Fr = \frac{u^2}{d_o g}$$

1. When N_w is small, uniform bubbles are formed.

2. For intermediate values of N_w, the bubble volume increases with increase in N_w.

3. When N_w increases further, the bubbles break down after detachment at the orifice and distributions of bubble volume are produced.

Based on the above scheme, the formation of bubbles considered by the present model can be explained in the following manner.

When N_w is small, the primary bubble escapes without interfering with the subsequently formed bubble. Because Q is low, V_E and V_A do not increase significantly with increase in Q. This results in a slow increase in V_T with Q leading to nearly uniform bubble sizes at low N_w. For intermediate values of N_w, the primary bubble interferes only with the first secondary bubble. In this situation, the secondary bubble does not grow to the size V_E in time t_i, thus remaining in contact with the orifice at all times. The portion of the secondary bubble that contributes to the total volume of the bubble, V_T, depends on the flow rate and thus N_w. Consequently, V_T increases with increase in N_w. At even higher values of N_w, more than one secondary bubble interfere with the primary bubble to contribute to the total bubble volume. The bubble breakage at different stages of this interference may result in a bubble size distribution. However, factors influencing bubble breakage are complex and are not considered in the present model.

In general, bubbles are closely approximated by spheres if surface tension and/or viscous forces are more important than the inertial force. Because the bubble is anchored at the orifice and not freely rising, the inertial force is relatively small. Thus the deformation of the bubble from the spherical shape is small. However, at high gas flow rates, the bubble grows rapidly which results in a high slip velocity between the bubble and the surrounding liquid. This could deform the bubble from a spherical to an ellipsoidal shape, increasing the drag on the bubble. Consequently, the bubble rises slowly leading to a higher V_T. It can be observed from Table 4.2 that at high Q, the model in general, underpredicts the bubble volume. Thus considering the bubble deformation would improve bubble volume predictions.

4.5 Conclusions

The volume of the bubble formed at the orifice in two phase, gas-liquid systems is an important parameter in several applications. In this chapter, a model has been developed for the prediction of the bubble volume at a single orifice in gas-liquid systems. The concept of the bubble closure mechanism has been introduced and the bubble closure time is calculated in a rigorous fashion.

It was noted in these studies that the interaction between the primary bubble, which is in the process of detachment from the spout and the secondary bubble, which is being formed simultaneously at the orifice must be taken into account as the flow rate increases. At even higher flow rates, the formation of entire secondary bubbles (with volume V_E), their detachment and their merger into the primary bubble have to be taken into account. The number of these secondary bubbles is also calculated by the model. The degree of these interactions increases as the liquid viscosity and gas flow rates increase and as the orifice diameter decreases. These interaction phenomena seem to be supported by bubble formation photographs for medium to high flow rates.

The model predicts bubble volumes accurately over a wide range of parameters affecting bubble formation. It calculates the actual distance traveled by the bubble before it eventually pulls away from the spout and thus provides a verification for earlier *assumptions* made about the detachment distance. The assumption that the detachment distance is equal to the orifice diameter seems appropriate for all but very large orifice diameters as demonstrated by the model calculations. For low flow rates, the assumption that the detachment distance is equal to the radius of the bubble at the end of the expansion stage, overpredicts the bubble volumes. The same assumption applied to high flow rates is reasonably good.

4.6 Summary

1. The new concepts of bubble closure and coalescence of the primary bubble with the successive secondary bubbles were effectively used to formulate a bubble model to predict the volume of bubbles formed at an orifice in a two phase system.

2. The bubble model applies to bubble formation in nonviscous as well as viscous liquids over a wide range of fluid properties.

3. The bubble model, for the first time, determines the distance traveled by the bubble from the orifice before detachment.

4. The dependence of bubble volume on the fluid properties such as liquid density ρ_l, liquid viscosity μ_l and surface tension σ were explained by means of the model.

5. The bubble model can be used to approximate the size of the bubble in a high pressure TPEB, where the bubble coalescence is minimum.

CHAPTER 5

CORRELATIONS FOR EFFECTIVE BUBBLE RISE VELOCITY

The gas holdup predicted by the generaliZed wake model is very sensitive to the value of the bubble rise velocity u_{br} (19). The value of u_{br} must be estimated independently for the model. Thus a means of predicting u_{br} in a three phase ebullieted bed would be useful.

In this chapter the equations in the generaliZed wake model are manipulated to give the best value of u_{br}, which when substituted back into the model, give values of phase holdups close to the experimentally observed values. Correlations are then obtained for the effective bubble rise velocity, at atmospheric pressure, with size of the particle, liquid and gas superficial velocities, liquid viscosity and surface tension as variables. The forms of the correlations are explained by evoking various hydrodynamic phenomena for three phase ebullieted beds such as flow regimes and their transitions, flow transition liquid velocity, solid wettability, behavior of bubbles, apparent bed viscosity and the effect of solid particles.

The correlations, at atmospheric pressure, are then modified by introducing a pressure coefficient which is calculated by considering the effect of gas density and therefore the bed pressure, on the bubble rise velocity. These modified correlations may be used to predict values of bubble rise velocity at higher pressure. The performance and trends of the modified correlations are checked by drift flux vs. gas holdup plots.

The three phase systems for which the correlations are developed consist of a wide variety of materials, such as glass beads or cylindrical catalyst particles as

solid phases, water or kerosene as liquid phases and air, nitrogen or helium as gas phases. The flow regimes are of industrial significance. The solid particles range in size from 1.0 - 5.0 mm.

5.1 Introduction

As noted in Chapter 3, the generalized wake model requires the values of the bubble rise velocity relative to the surrounding solid-liquid fluidized region, u_{br}, the ratio of the solid holdup in the bubble wake to the solid holdup in the solid-liquid region, x, and the ratio of the wake volume to the bubble volume, κ. These parameters must be calculated by independent methods. The model predicts the phase holdups in the three phase ebullieted bed, for a given value of the liquid superficial velocity, u_l, gas superficial velocity, u_g and other system parameters (such as particle size, d_p, reactor diameter, d_r, liquid viscosity, μ_l, particle density, ρ_p, liquid density, ρ_l, and surface tension, σ) and for the independently calculated values of u_{br}, x and κ.

The model is relatively insensitive to the values of x, especially for heavy or large solid particles (19,119). However the gas holdup ϵ_g predicted by the model is very sensitive to the value of u_{br} (19). It is observed, that for a given value of the linear liquid velocity v_l, ϵ_g increases as u_{br} decreases. This also follows from Equation 5.1

$$\epsilon_g = u_g/(u_{br} + v_l) \tag{5.1}$$

It is therefore important that the value of u_{br} be accurately predicted to exploit the full potential of the generalized wake model in the design of three phase ebullieted beds.

5.2 Prevailing Methodology for Predicting u_{br}

A number of different approaches have been used to predict the value of u_{br}.

1. Bhatia and Epstein (119) used empirical equations for a two phase gas-liquid system to predict u_{br}.

   (a) For large diameter columns ($d_r > 100$ mm.), where slugging is not applicable, Equation 5.2, as proposed by Towell et al. (162), was used to compute u_{br}.

   $$u_{br} = u_{tb} + 2u_g \tag{5.2}$$

   Here u_{tb} is the terminal velocity of a single bubble in a stagnant liquid.

   (b) For small diameter columns ($d_r < 100$ mm.) two distinct flow regimes were considered:

      i. For the bubble flow regime, Equation 5.3, suggested by Bhatia (163), was recommended for the computation of u_{br}

      $$u_{br} = \frac{u_{tb}(tanh(0.25\epsilon_g)^{-0.33})^{0.5}}{\left(\frac{\epsilon_l}{\epsilon_l + \epsilon_g}\right)} \tag{5.3}$$

      ii. For the slug flow regime, Equation 5.4, as originally proposed by Nicklin (164), was recommended for the computation of u_{br}

      $$u_{br} = \frac{0.2(u_l + u_g) + 0.35(gd_r)^{0.5}}{\left(\frac{\epsilon_l}{\epsilon_l + \epsilon_g}\right)} \tag{5.4}$$

   In Equation 5.3, u_{tb} must be calculated from an estimate of the average bubble diameter d_b in the bubble swarm.

2. Vasalos et al. (19) tested the validity of using a correlation suggested by Kim et al. (117) to estimate u_{br}.

$$u_{br} = 5.541 u_l^{0.065} u_g^{0.339} \mu_l^{0.025} \rho_l^{0.179} \tag{5.5}$$

When this value of u_{br} was used in the generalized wake model, the model predicted gas holdups that were lower than the experimentally observed values. Therefore they concluded that Equation 5.5 overestimated the value of u_{br} for the generalized wake model.

3. Sastry et al. (149) suggested the following procedure to determine u_{br}:

The coefficient of viscous drag on a single bubble, due to the surrounding liquid, is obtained by using the correlations given by Tadaki and Maeda (165):

$$\begin{aligned} C_{Db} &= 0.076(Re_b Mo^{0.23})^{1.82} \quad for \ 8Mo^{0.068} < Re_b Mo^{0.23} < 6 \\ C_{Db} &= 1.25(Re_b Mo^{0.23})^{0.26} \quad for \ 6 < Re_b Mo^{0.23} < 16.5 \\ C_{Db} &= 2.6 \quad for \ 16.5 < Re_b Mo^{0.23} \end{aligned} \tag{5.6}$$

where,

Re_b, the bubble Reynolds number, is given by

$$Re_b = \frac{\rho_l u_{tb} d_b}{\mu_l} \tag{5.7}$$

Mo, the Morton number, is given by

$$Mo = \frac{g\mu_l^4}{\sigma^3 \rho_l} \tag{5.8}$$

The value of C_{Db} is used to calculate u_{tb}. u_{br} is then assumed to be equal to u_{tb}. The use of the above procedure requires an estimate of d_b. Furthermore, the assumption that u_{tb} is equal to u_{br} may not be appropriate. Thus in many of the formulations for estimating u_{br}, u_{tb} is the parameter that has to be determined first. An estimate of d_b is required to calculate u_{tb} and may have

to be determined experimentally. However, relating the behavior of a single bubble rising through a liquid column directly to the behavior of multiple bubbles rising in a three phase solid-liquid-gas system may not be appropriate because :

1. bubble rise phenomena in liquids are different from the bubble rise phenomena in solid-liquid-gas systems; and,

2. in a multibubble three phase system, bubble to bubble and bubble to solid particle interactions must be considered.

As mentioned earlier, the generalized wake model is based on a material balance between the solids carried upwards in the wakes of the bubbles rising across the crossection of the column and the solids settling in the liquid-solid region that surrounds the rising bubbles. Accordingly, u_{br} represents the *effective* bubble rise velocity across the crossection of the column and not the velocity of a single bubble rising at a particular location in the column.

A correlation such as the one given in Equation 5.5 may estimate the effective u_{br} fairly accurately for the plug flow case where all bubbles rise upward across the crossection of the column, because the correlation is based on experimental values of the bubble rise velocity, measured at a single location in the column for rising bubbles. However, for the backmix case, where bubbles are known to flow upward at the center of the column and downward near the column walls (19), the net bubble flux, which takes into account backmixing, must be considered. Thus for backmix flow, equating u_{br} to u_{tb} or even to an average upward bubble rise velocity, as given by Equation 5.5, may not represent the variation of the bubble flux across the column crossection and could overestimate the magnitude of u_{br}.

5.3 Determination of Effective Bubble Rise Velocity

As discussed in the previous section, u_{br} in the generalized wake model should represent the effective bubble rise velocity in three phase ebullieted beds. The terminology *effective* becomes more applicable for a bed with backmixing. In this section the procedure used to estimate effective u_{br} is discussed below.

5.3.1 Calculation of the Effective Bubble Rise Velocity

Equations noted in Chapter 3 are used to compute the optimum value of the effective bubble rise velocity u_{br}, for a given set of values of u_l, u_g, d_p, d_r, μ_l, ρ_p, ρ_l and σ and the experimentally observed phase holdups ϵ_{g_e} and ϵ_{l_e}.

The procedure is as follows:

1. Determine the values of κ and x using Equations 3.6 - 3.9 from the known values of the experimental liquid holdup ϵ_{l_e}, the experimental gas holdup ϵ_{g_e} and the particle properties.

2. Calculate v_g from Equation 5.9.

$$v_g = \frac{u_g}{\epsilon_{g_e}} \tag{5.9}$$

3. Solve Equations 3.17 and 3.21 for ϵ''_{lf} by successive substitution.

4. Calculate u_{br} using Equation 5.10.

$$u_{br} = \frac{(v_g(\epsilon_l + \epsilon_g) - u_l - u_g)}{\epsilon''_{lf}(1 - \epsilon_g - \epsilon_\kappa)} \tag{5.10}$$

The computer codes for the procedure are presented in Appendix C. u_{br} calculated by the above procedure, along with values of the system parameters, yields the values of ϵ_g and ϵ_l which are close to ϵ_{g_e} and ϵ_{l_e} respectively, when used in the

generalized wake model described in Chapter 3. It should be noted that the above procedure yields the effective value of u_{br}. This indirectly accounts for the effect of backmixing and the variation of u_{br} in the radial direction.

Values of u_{br} are determined for a number of experimentally observed phase holdups, using the above procedure. u_{br} is calculated for a system consisting of glass beads, water and air, using the experimental data published by Armstrong (120) and for a system of catalyst particles, kerosene or water and helium or nitrogen using the experimental data obtained by Vasalos et al. (19). The experimental conditions for all the three phase systems considered are presented in Table 5.1.

The values of u_{br} are plotted against u_g with u_l as a parameter to illustrate the trends of u_{br} and to determine the values of u_l at which u_{br} changes abruptly. The abrupt changes in u_{br} are then related to the flow transition from one regime to another. Furthermore, the value of u_{br} is used to construct u_{br} correlations, with u_l, u_g, d_p, μ_l and σ as the variables.

The correlation for u_{br} given in Equation 5.5 was derived by Kim et al. (117) for glass beads-air and a wide variety of liquids (including water) which gave a broad range of values of μ_l and σ. Armstrong (120) used solid particles of the same size as those used by Kim et al. (117). However, because Armstrong used only water as the liquid phase, there was no variation in μ_l and σ in his experimental data.

In the absence of variations in μ_l and σ in Armstrong's data (120), the values of the exponents on μ_l and σ, in the correlations developed herein for u_{br} for the glass beads-water-air system, are assumed to be the same as those proposed by Kim et al. (117) (Equation 5.5). Furthermore, because the degree of backmixing depends on u_g and u_l and not on μ_l and σ, retaining identical exponents on μ_l and σ in the correlations for u_{br} is reasonable. However, the value of exponent on σ in the correlation for u_{br}, for the catalyst-liquid-gas system is modified to account for the higher wettability of the catalyst particles compared to glass beads.

Table 5.1. Details of Three Phase Systems

Phase	Parameter	Three phase systems*		
		System 1	System 2	System 3
	d_r	0.2413	0.15	0.15
	pressure	atmospheric	atmospheric	atmospheric
Solid	Shape	Spherical	Cylindrical	Cylindrical
		d_s = 0.001, 0.003, 0.005	d_c = 0.0016, $\frac{l}{d_c}$ = 3	d_c = 0.0016, $\frac{l}{d_c}$ = 3
	d_p	0.001, 0.003, 0.005	0.00264	0.00264
	ρ_p	for d_p=0.001, ρ_p=2961.62 for d_p=0.003, ρ_p=2496.10 for d_p=0.005, ρ_p=2489.68	1630.0	1630.0
	n	Richardson-Zaki correlation	3.3 (experimental)	3.3 (experimental)
Liquid	ρ_l	1000.0	990.0	790.0
	μ_l	0.0013	0.001	0.00139
	σ	0.0727	0.0755	0.0286
	u_l	0 - 0.1261	0 - 0.06096	0 - 0.06096
Gas	u_g	0 - 0.2224	0 - 0.06096	0 - 0.07620

*
System 1: Glass beads-water-air (120)
System 2: Catalyst-water-nitrogen (19)
System 2: Catalyst-kerosene-helium (19)

5.4 Results

5.4.1 Correlations

Correlations for u_{br} are developed for the following three phase systems.

1. Glass beads - Water - Air system, Armstrong (120).

2. Catalyst - Water - Nitrogen system, Vasalos et al. (19).

3. Catalyst - Kerosene - Helium system, Vasalos et al. (19).

The values of u_{br} calculated by the procedure described earlier are subjected to a nonlinear regression analysis using the Levenberg-Marquartdt (166) algorithm to determine the values of exponents for the u_{br} correlations.

The general form of the correlation for u_{br} is given in Equation 5.11. Values of the various exponents and u_{tr} are given in Table 5.2.

$$u_{br} = K {d_p}^a {u_l}^b {u_g}^c {\mu_l}^d \sigma^e \tag{5.11}$$

The correlations are formulated with the particle size d_p and the flow regime as parameters. For large d_p ($\geq$ 0.0025 m.), where both the coalescing bubble regime and the dispersed bubble regime are observed, two correlations have been developed: one for each regime (parameter sets I(a) and I(b) in Table 5.2), along with the identification of the value of u_{tr}.

For small d_p ($<$ 0.0025 m.), where only the coalescing bubble regime in conjunction with bed contraction upon introduction of gas is observed, two correlations have been developed, one for the bed contraction stage (parameter set II(a) in Table 5.2) and the other for the bed expansion stage (parameter set II(b) in Table II). Separate correlations (parameter sets III(a), III(b), IV(a), IV(b) and IV(c) in Table 5.2) for catalyst particles are developed to account for the higher wettability of the catalyst particles.

Table 5.2. Ranges and Parameters for Correlations

System	u_{tr}		Range			Exponents						Set #
	d_p	u_{tr}	d_p	u_l	u_g	K	a	b	c	d	e	
Glass Beads -Water -Air	0.003 0.005	0.0572 0.0674	0.0025 to 0.005	u_{lmf} - u_{tr}	0.059 < u_g < 0.178	0.0180	-0.7544	-0.4219	0.0569	0.025	0.175	I(a)
				u_{tr} - 0.1261	0.0330 < u_g < 0.238	0.1204	-0.4111	-0.8027	0.6621	0.025	0.175	I(b)
	0.001	-	0.001 to 0.0025	< 0.095	0.0593 < u_g < 0.090	0.00008	-0.7544	-0.9584	-0.7860	0.025	0.175	II(a)
				0.095 < u_l < 0.117	0.0593 < u_g < 0.238	0.01003	-0.7544	-0.5558	0.7714	0.025	0.175	II(b)
Catalyst -Water -Nitrogen	0.0264	0.0572	0.0025 to 0.005	$\leq u_{tr}$	0.015 < u_g < 0.061	0.0051	-0.7544	-0.4219	0.0569	0.025	0.5	III(a)
				u_{tr} - 0.061	0.015 < u_g < 0.061	0.1041	-0.4111	-.8027	0.6621	0.025	0.5	III(b)
Catalyst -Kerosene -Hellum	0.0264	0.0572	0.0025 to 0.005	$\leq u_{tr}$	0.015 < u_g $\leq$ 0.046	0.0026	-0.7544	-0.4219	0.0569	0.025	0.5	IV(a)
				$\leq u_{tr}$	0.046 < u_g $\leq$ 0.061	0.0051	-0.7544	-0.4219	0.0569	0.025	0.5	IV(b)
				u_{tr} - 0.06	0.015 < u_g $\leq$ 0.061	0.1041	-0.4111	-0.8027	0.6621	0.025	0.5	IV(c)

5.4.2 Observations and Discussion

5.4.2.1. Oservations

u_{br} versus u_g with u_l as a parameter for the glass beads - water - air system, is plotted in Figures 5.1, 5.2 and 5.3, with d_p = 0.005 m, 0.003 m and 0.001 m, respectively.

The following observations can be made from these graphs.

1. For a constant u_g, u_{br} decreases as u_l increases.

2. At very low values of u_g (u_g approaching zero), u_{br} decreases rapidly as u_g increases.

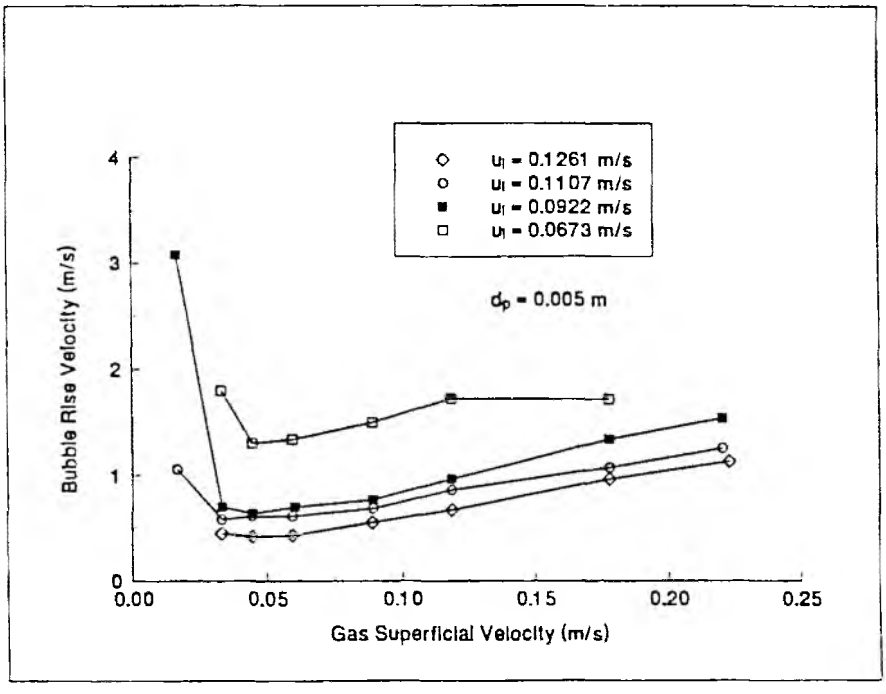

Figure 5.1. Bubble Rise Velocity vs. Gas Superficial Velocity

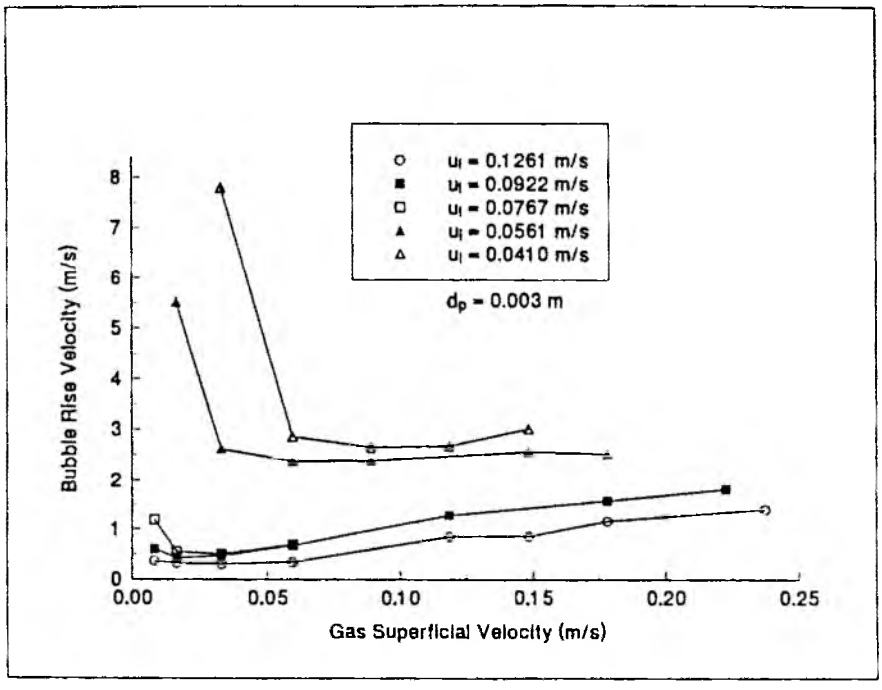

Figure 5.2. Bubble Rise Velocity vs. Gas Superficial Velocity

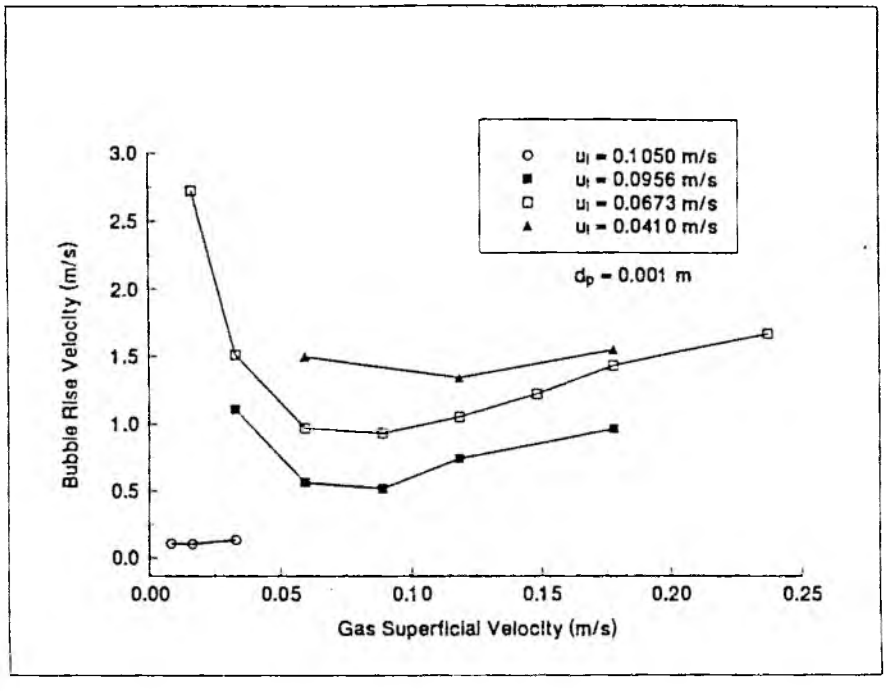

Figure 5.3. Bubble Rise Velocity vs. Gas Superficial Velocity

3. u_{br} decreases initially for $d_p = 0.005$ m and 0.003 m, at a constant u_l. After the initial decrease, u_{br} increases slowly as u_g increases. For $u_l < u_{tr}$, the value of u_g at which the minimum value of u_{br} occurs decreases with the increase in value of u_l. However for $u_l > u_{tr}$, the value of u_g at which minimum u_{br} occurs essentially remains constant.

4. For $d_p = 0.005$ m and 0.003 m and for a constant value of u_g, at a certain value of $u_l (= u_{tr})$, u_{br} decreases significantly as u_l increases.

5. For $d_p = 0.001$ m and at a constant u_l, u_{br} initially decreases and then increases as u_g increases.

5.4.2.2. Discussion

The hydrodynamic behavior of three phase ebullieted beds is discussed in this section. Furthermore, an attempt is made to explain the reasons for the sign and magnitude of the exponents on the various parameters in the correlations and the trends in the graphs.

1. Three flow regimes, based on bubble flow behavior, can be identified in a three phase ebullieted bed (17); the coalescing bubble regime, the dispersed bubble regime and the slugging regime. In the coalescing bubble regime, the bubbles tend to coalesce and both the bubble size and the effective bubble rise velocity u_{br} are comparatively large. The coalescing bubble regime predominates at low liquid and high gas velocities. In the dispersed bubble regime, limited bubble coalescence occurs and the bubble size and therefore u_{br} are small. The dispersed bubble regime predominates at high liquid velocities and at low and intermediate gas velocities. High gas rates may lead to a flow transition towards a slugging regime. The flow regimes can be mapped on a plot of u_l vs u_g, as done by Muroyama and Fan (113). A liquid superficial transition

velocity is observed in such a plot for a given system and different values of u_g. For u_l greater than u_{tr}, the flow is in a dispersed bubble regime and for u_l less than u_{tr} the flow changes to a coalesced bubble regime. The significance of superficial liquid velocity for transition, u_{tr}, is discussed below:

(a) The decrease in u_{br} with increase in u_l for a constant u_g is due to a transition to less coalescing and more dispersed flow, which leads to smaller bubbles. Smaller bubble size leads to a reduced bouyancy and consequently to a lower u_{br}. At the transition value of u_l $(= u_{tr})$, u_{br} is reduced significantly. The reduction of u_{br} can be attributed to the transition from a coalescing bubble regime to a dispersed bubble regime. As noted earlier the dispersed bubble regime is characterized by smaller bubbles and therefore a lower u_{br}. The value of u_l at which the reduction in u_{br} takes place, is the superficial liquid transition velocity, u_{tr}. It can be further noted from Figures 5.1 - 5.3 that for $u_l < u_{tr}$ and a constant u_g, u_{br} decreases continuously with an increase in u_l, indicating that the flow tends to become relatively more dispersed. The values of u_{tr}, in Table 5.2, represent the limits on u_l between which the correlations apply, since each correlation is applicable for a particular flow regime. Kim et al. (117) worked with a similar system and in the same ranges of gas and liquid superficial velocities as Armstrong (120) and observed the transition between coalescing and dispersed bubble regimes (167). Vasalos et al. (19), whose experimental data have been correlated in this work, also observed the same flow regimes during their experiments.

(b) Fan et al. (17) have indicated that at a given u_l and u_g, the particle properties profoundly affect the prevailing flow regimes. The terminal velocity of the fluidized particles, u_{tp}, affects u_{tr}. An increase in particle size increases u_{tr} for a low u_{tp}, however, for a high u_{tp}, the opposite trend is observed. That

is, for the glass beads considered in the correlations in parameter sets I(a) II(a), u_{tp} is in the low range (0.05 - 0.06 m/sec). Consequently, the value of u_{tr} for d_p = 0.003 m (0.0561 m/sec) is lower than the value of u_{tr} for d_p = 0.005 m (0.0674 m/sec).

2. Particle penetration alone could be adequate to account for bubble breakup in a three phase fluidized bed, because the bubbles are impinged from all sides by the solid particles (109). Fan (17) found the critical particle size for the glass beads - water - air system to be 0.0022 m by assuming particle penetration to be a sufficient condition. This matched closely with the experimentally observed value of 0.0025 m (117). Particles smaller than 0.0025 m promote bubble coalescence while particles greater than 0.0025 m promote bubble disintegration. This justifies the formulation of two separate correlations for u_{br}; parameter sets I(a) and I(b) for d_p greater than 0.0025 m and parameter sets II(a) and II(b) for d_p less than 0.0025 m.

3. The sign and magnitude of the value of the exponent a on d_p in various correlations, are discussed below:

   (a) Larger particles tend to reduce bubble coalescence. Reduced bubble coalescence leads to relatively smaller bubbles, a lower u_{br} and hence a higher ϵ_g (168,169,170) Even in a coalescing bubble regime, larger particle size tends to reduce coalescence and decrease u_{br}. This observation supports the negative sign of the exponent, a, on d_p in the correlations given by parameter sets I(a), III(a), IV(a) and IV(b), which apply for large particles with $d_p \geq 0.0025$ m in the coalescing bubble regime.

   (b) When the size of the bubbles in a three phase ebullieted bed is large compared to the particle size, the fluid medium surrounding the bubble can be assumed to act as a pseudo homogeneous medium of higher apparent viscosity

and density than those of the liquid medium alone (17,135). Kim et al. (117) formulated a correlation for the average diameter of the bubble d_b, with u_l, u_g, μ_l and σ as the parameters.

$$d_b = 0.142 u_l^{0.052} u_g^{0.248} \rho_l^{0.034} \mu_l^{0.008} \tag{5.12}$$

Although the experiments carried out by Kim et al. (117) were in a two-dimensional column, the range of values of u_l, u_g, μ_l and σ were the same as those used by Armstrong (120) in a circular column. It can then be concluded that Equation 5.12 would predict the order of magnitude of d_b to a fair degree of accuracy for Armstrong's experimental system. Based on Equation 5.10, d_b is of the order of 0.02 m to 0.03 m for the range of parameters considered by the correlations in the parameter sets II(a) and II(b). Therefore, with d_p less than 0.0025 m the concept of a psuedo homogeneous medium having the appropriate apparent properties can be evoked with these correlations. A formulation for the apparent viscosity μ_{app} of a solid-liquid mixture suggested by Rigby et al. (171), is presented in Equation 5.13, for 0.0012 m $\leq d_p \leq$ 0.00775 m

$$\mu_{app} = .0199(u_l/u_{lmf})^{-2.9} \tag{5.13}$$

This equation indicates that μ_{app} is proportional to d_p. Thus, as d_p decreases, the apparent viscosity of the psuedo homogeneous medium decreases, leading to a reduction in the viscous drag on the bubbles and consequently to an increase in u_{br}. This accounts for the the negative sign on the exponent, a, on d_p for the correlations given in parameter sets II(a) and II(b).

4. In general, for Glass bead-Water-Air systems with $d_p > 0.0025$ m, as u_g increases at a constant u_l, ϵ_s decreases, whereas ϵ_g increases. As ϵ_g, increases,

more liquid is diverted to the solid-liquid region leading to an increase in the liquid holdup in the liquid-solid region, ϵ''_{lf}. Furthermore, the bubble to particle interaction is greater in the coalesced bubble regime than in the dispersed bubble regime. The effect of the changes in ϵ_s, ϵ_g and ϵ''_{lf} and the phase interactions on u_{br} is discussed below:

(a) At low u_g, the gas holdup ϵ_g increases rapidly with an increase in u_g (120) leading to a rapid decrease in v_g. This rapid decline is also observed when v_g is calculated from Equation 5.14.

$$v_g = u_g/\epsilon_{ge} \tag{5.14}$$

It then follows from Equation 5.3 that for low values of u_g, u_{br} should decrease rapidly with u_g.

(b) At medium values of u_g, although ϵ_g increases, the rate of increase of ϵ_g decreases (120) leading to a lower rate of decrease of v_g and consequently leading to a lower rate of decrease in u_{br} as observed in Figures 5.1 and 5.2.

(c) It should be noted that in Figures 5.1 and 5.2, u_{br} increases with u_g after the minimum. It can therefore be inferred from Equation 5.14 that after the minimum, the rate of increase of ϵ_g with respect to u_g is lower than that before the minimum and that u_{br} becomes a stronger function of u_g, d_b and bed porosity rather than ϵ_g. There is a significant bubble to solid interaction in a coalescing bubble regime ($u_l < u_{tr}$) and u_{br} is dependent on the state (porosity) of the bed. As u_l increases, the bed porosity increases which leads to a more rapid passage of the bubbles through the bed. This could explain why, for $u_l < u_{tr}$, the value of u_g at which the minimum value of u_{br} occurs, decreases with an increase in value of u_l.

However, in a dispersed bubble regime ($u_l > u_{tr}$) there is no appreciable bubble to solid interaction and therefore u_{br} is less dependent upon the bed porosity and therefore on u_l. This could be the reason why, for $u_l > u_{tr}$, the value of u_g, at which the minimum value of u_{br} occurs, essentially remains the same (eg. $u_g = 0.033$ m/sec in Figure 5.1 and $u_g = 0.0165$ m/sec in Figure 5.2)

(d) Armstrong (120) observed that the bed contracted appreciably on the introduction of gas for the bed with $d_p = 0.001$ m. and $u_l \leq 0.0956$ m/sec. However, the bed expanded as the gas flow rate was increased. This contraction and subsequent expansion of small particle size beds led to an initial increase in μ_{app} (and therefore an initial decrease in u_{br}) followed by a decrease in μ_{app} (and therefore an increase in u_{br}) of the bed with an increase in u_g. Similar observations were made in the studies by Song and Fan (172), where μ_{app}, for a glass bead - water - air system with $d_p = 0.0015$ m., increased initially and then decreased with an increase in u_g. These observations explain why, in Figure 5.3, for $d_p = 0.001$ m., u_{br} decreases initially and then increases with an increase in u_g.

5. The effect of surface tension σ on u_{br} is discussed below:

(a) It is observed that beds of nonwettable beads exhibit greater expansion compared to those of wettable beads and the gas holdup is much lower for the wettable solids. These observations may be due to the adherence of the bubbles to the nonwettable solid particles. When bubbles adhere to the particles, the apparent density of the particle-bubble aggregate becomes less than that of the particle (9). The smaller apparent density leads to greater bed expansion and reduced bubble breakup and hence to a lower ϵ_g and higher u_{br}.

The tendency for bubbles to adhere more to the less wettable particles is related to the work of adhesion W_a, which is defined as the energy required to

separate a liquid from a solid per unit interfacial area. The work of adhesion (173) is given by

$$W_a = \sigma(1 + cos\theta_c) \tag{5.15}$$

where θ_c is the contact angle.

The wettability of the solid is higher for smaller values of θ_c. This means that W_a is higher for more wettable particles. A higher value of W_a implies a greater probability that a liquid film will be present on the solid surface. The presence of the liquid film makes the bubble bouyant thereby reducing the tendency of the bubbles to adhere to the solid. As the catalyst particles are more wettable than glass beads, for the reasons mentioned above, one can expect smaller bubble size, a lower u_{br} and therefore a higher ϵ_g for a system which contains catalyst particles as opposed to glass beads. This accounts for the different values of the exponent, e, on σ in parameter sets I(a) and I(b), and in the parameter sets III(a), III(b), IV(a), IV(b) and IV(c).The higher value of the exponent on σ in parameter sets III(a), III(b), IV(a), IV(b) and IV(c) implies that u_{br} for catalyst - water/kerosene - nitrogen/helium systems is lower than u_{br} for glass beads - water - air systems, other parameters being the same. Furthermore, Vasalos et al. (19) observed a high degree of foaming for the catalyst - kerosene - helium system which led to a lower u_{br}. Since foaming can be related primarily to the surface tension σ, the higher values of exponent, e, in parameter sets IV(a), IV(b) and IV(c) could partially be attributed to the foaming phenomenon.

5.4.3 Performance of the Correlations

The experimentally observed gas holdups ϵ_{ge} are compared to those calculated by substituting u_{br} obtained from the correlations into the generalized wake model (ϵ_{gc}) in Figures 5.4-5.7.

1. A plot of ϵ_{ge} versus ϵ_{gc}, for the glass beads - water - air system with $d_p = 0.005$ m., using parameter sets I(a) and I(b), is presented in Figure 5.4.

2. A plot of ϵ_{ge} versus ϵ_{gc}, for the glass beads - water - air system with $d_p = 0.003$ m., using parameter sets I(a) and I(b), is presented in Figure 5.5.

3. A plot of ϵ_{ge} versus ϵ_{gc}, for the glass beads - water - air system with $d_p = 0.001$ m., using parameter sets II(a) and II(b), is presented in Figure 5.6.

4. A plot of ϵ_{ge} versus ϵ_{gc}, for the catalyst - water/kerosene - nitrogen/helium system with $d_p = 0.00264$ m., using parameter sets III(a), III(b), IV(a), IV(b) and IV(c), is presented in Figure 5.7.

It is noted from Figure 5.4 and 5.5 that at high and medium values of u_g, the experimental and calculated gas holdups are reasonably close, but at lower values of u_g they differ appreciably.

This difference in ϵ_{ge} and ϵ_{gc} at lower values of u_g is explained as follows:

1. It is observed in Figures 5.1 through 5.3 that for low values of u_g, u_{br} decreased rapidly with an increase in u_g, but at higher values of u_g, u_{br} increased gradually with increase in u_g. Such a trend for u_{br} would be difficult to represent by a single correlation. This implies that there should be two separate correlations, one for the decreasing portion of the curve and a second for the increasing portion of the curve. However, this would lead to too many correlations. We have therefore carried out a nonlinear regression analysis

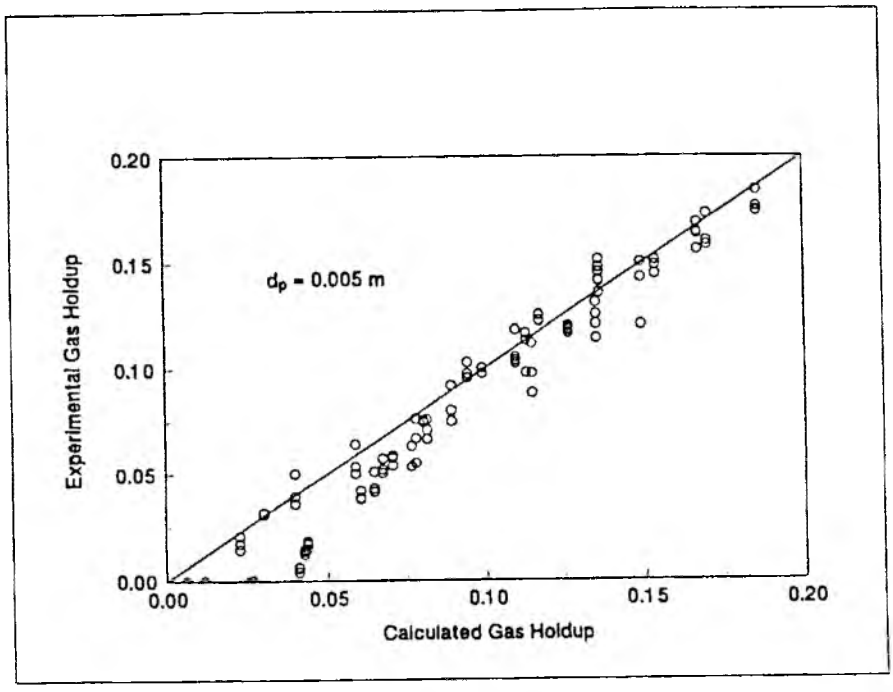

Figure 5.4. Experimental Gas Holdup vs. Calculated Gas Holdup

only over those regions of the graphs where a particular trend (decreasing or increasing) persists over an appreciable range. For Figures 5.1 and 5.2, the correlations were obtained for the region where u_{br} increased with u_g. Thus the correlations in parameter sets I(a) and I(b) do not account for the initial rapid decrease in u_{br} and this leads to the observed discrepancy in gas holdups at lower values of u_{br}. This approach is reasonable because three phase ebullieted reactors are usually operated at high ϵ_g and therefore the reactor performance and concomitantly, the correlations at lower ϵ_g (and therefore at lower u_g) is less important.

It can be observed that the fit in Figure 5.6 (d_p = 0.001 m.) is not as good as those in Figures 5.4 and 5.5 (d_p = 0.005 m. and 0.003 m.). This can be attributed

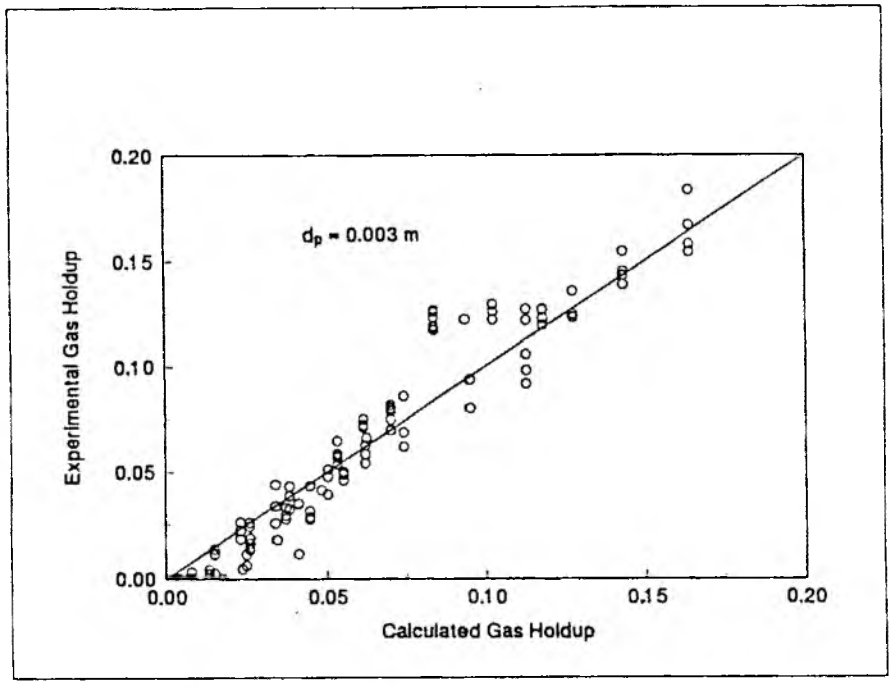

Figure 5.5. Experimental Gas Holdup vs. Calculated Gas Holdup

to the apparent variations in the experimental values of ϵ_g, for the same values of u_l and u_g.

For the catalyst systems (Figure 5.7), the experimental and calculated phase holdups are in a reasonablely good agreement.

It should be emphasized here that the constant k, in the correlations, varies among the correlations and includes the effect of other parameters, such as liquid and gas density, liquid contamination, column diameter, distributor type and orifice size on u_{br} in each specific setup, for which the correlations are formulated. This implies that the correlations are system specific and may not apply *exactly* for other systems with different configurations. In such cases, the correlations developed in this paper can be used as guidelines to estimate the value of u_{br} and phase holdups for a different configuration.

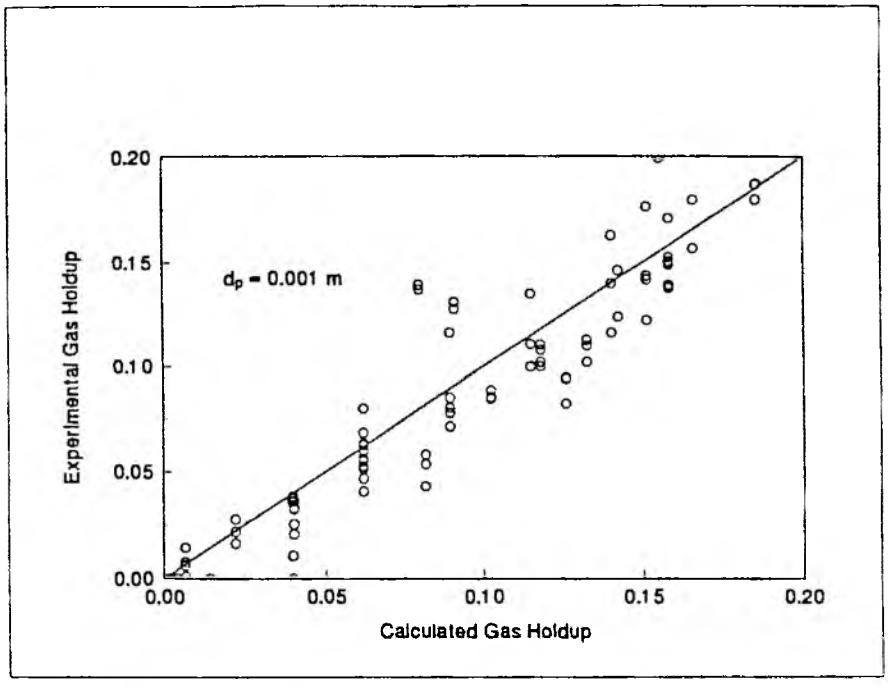

Figure 5.6. Experimental Gas Holdup vs. Calculated Gas Holdup

5.4.4 Conclusions

1. The gas holdup in a three phase ebullieted bed is inversely dependent on the effective bubble rise velocity u_{br} for a fixed set of parameters.

2. The equations for the generalized wake model can be used to determine the value of u_{br} for a known set of system parameters and experimentally observed phase holdups. When this value of u_{br} is substituted in the generalized wake model, the model predicts phase holdups close to the experimental phase holdups.

3. The plot of u_{br} versus u_g with u_l as a parameter indicates that u_{br} decreases with an increase in u_l. Furthermore, a transition value of u_l at which u_{br}

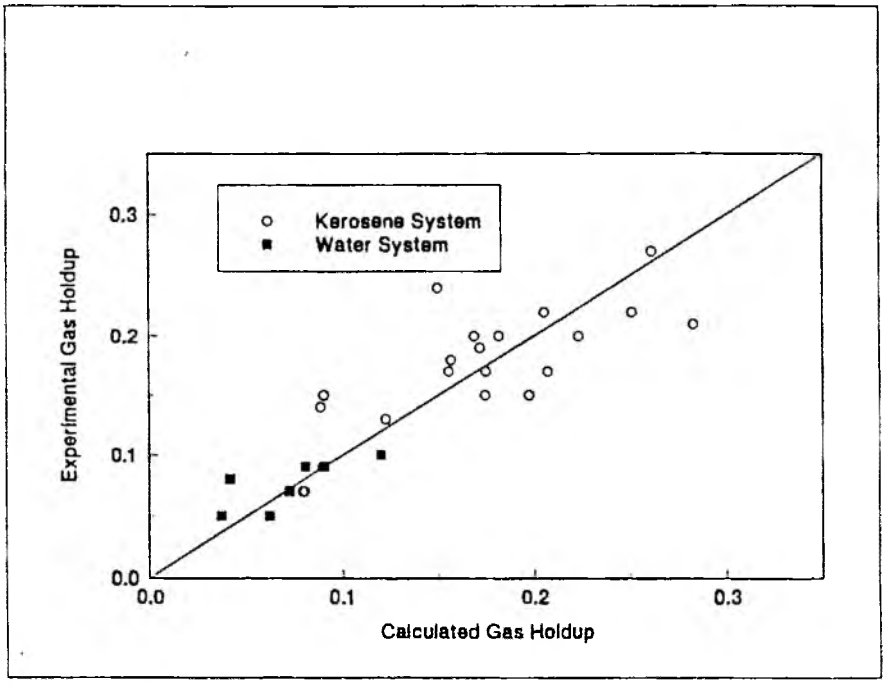

Figure 5.7. Experimental Gas Holdup vs. Calculated Gas Holdup

decreases significantly is observed indicating a transition from a coalesced bubble regime to a dispersed bubble regime.

4. The predicted values of u_{br} can be fitted by a correlation with u_l, u_g, d_p, μ_l and σ as the parameters. Such correlations can be used to predict the *effective* u_{br} directly from the basic system parameters without need to estimate bubble diameters d_b, by means of correlations or experimental data.

5. The forms of correlations support the following previously observed hydrodynamic behavior of three phase ebullieted beds.

   (a) At constant u_g, above a critical value of d_p, as u_l exceeds u_{tr}, the flow changes from a coalescing bubble regime to a dispersed bubble regime. (b)

At constant u_g, below a critical value of d_p, the flow is in a coalesced bubble regime, however, it undergoes a transition to a less coalescing and a more dispersive nature, as u_l increases. (c) The concept of psuedo homogeneous medium can be applied rigorously for a system with small d_p and relatively large d_b. u_{br} increases as d_p decreases for such a system with the values of other parameters held constant. (d) In general, high u_l and low u_g increase bubble dispersion, while low u_l and high u_g promote bubble coalescence. (e) Solid wettability influences u_{br} and hence ϵ_g. Lower wettability promotes bubble growth, greater bed expansion and greater u_{br}. (f) Greater solid wettability leads to a stronger dependence of u_{br} on σ.

5.5 Prediction of u_{br} at High Pressure

In the above sections correlations for the effective bubble rise velocity in a TPEB reactor, operating at atmospheric pressure, have been developed. Many of the process applications of a TPEB reactor are at pressures higher than the atmospheric pressure. The expected operating pressure for hydrotreating/hydrocracking of bitumen related liquids is around 13.78 MPa (2000 psi). Pressure has an appreciable effect on the bubble behavior (115) and therefore on the effective bubble rise velocity. It is therefore essential to modify the correlations to incorporate the effect of pressure.

5.5.1 Drift Flux

5.5.1.1. Concept of Drift Flux

In accounting for the interaction between two phases in a gas-liquid or liquid-solid systems, the interaction is usually assumed to depend upon the relative

motion between the two phases, rather than upon the absolute velocity of each phase. Under this premise, two approaches have been used to describe the phase interaction: one correlates the relative, or slip, velocity as a function of the phase holdups (167) and the other correlates the drift velocity or the drift flux as a function of phase holdups (174). While the two approaches have similarities and are interconvertible, a major conceptual difference exists: the relative velocity refers to the slower moving phase velocity and the drift velocity refers to a volumetric mean velocity of both the phases (17).

The drift flux represents the volumetric flux of a component relative to a surface moving at the average velocity of the phase mixture (174). For the gas phase, in a two phase system, the drift flux is given by Equation 5.16.

$$q_{df}^{"} = \epsilon_g^{"} \left(v_g^{"} - \frac{(Q_l^{"} + Q_g^{"})}{A_r} \right) \tag{5.16}$$

where

$q_{df}^{"}$ = drift flux of the gas phase in a two phase system.

$\epsilon_g^{"}$ = gas holdup in the two phase system.

$v_g^{"}$ = linear gas velocity in a two phase system.

$Q_l^{"}$ = volumetric flow rate of the liquid phase through the column, in a two phase system.

$Q_g^{"}$ = volumetric flow rate of the gas phase through the column, in a two phase system.

A_r = crossection area of the column.

The concept of drift flux in the gas-liquid systems has been extended to the solid-liquid-gas system (17,135). Thus, for a three phase system Equation 5.16 becomes

$$q_{df} = \epsilon_g \left(\frac{u_g}{\epsilon_g} - (u_l + u_g) \right) \tag{5.17}$$

Assuming uniform bubble size distribution in the bed

$$u_{br} = \left(\frac{u_g}{\epsilon_g} - \frac{u_l}{\epsilon_l}\right) \tag{5.18}$$

Equation 5.17 can then be rewritten as

$$\begin{aligned} \frac{q_{df}}{\epsilon_g} &= \frac{u_g}{\epsilon_g} - (u_l + u_g) \\ &= u_{br} + u_l\left(\frac{1-\epsilon_l}{\epsilon_l}\right) - u_g \end{aligned} \tag{5.19}$$

and

$$q_{df} = \epsilon_g\left(u_{br} + u_l(\frac{1-\epsilon_l}{\epsilon_l}) - u_g\right) \tag{5.20}$$

5.5.2 Behavior of Drift Flux

The relation between the drift flux q_{df} and the gas holdup ϵ_g in three phase system has been studied by various researchers (116,141,174). In the dispersed bubble regime, the drift flux can be correlated (116) (in SI units) by

$$q_{df} = 0.18\epsilon_g \tag{5.21}$$

However, in the coalesced bubble regime, it is difficult to correlate q_{df} as an explicit function of ϵ_g. The linearly correlated q_{df} values for the dispersed bubble regime in kerosene with fines are significantly lower than those in glass beads-water-air system (25, Darton and Harrison). The drift flux in the coal char slurry system lies mainly in the transition regime, and shows wide variation depending on u_l. Thus for a given value of ϵ_g, the drift flux is lower at higher u_l.

The relationship of gas drift flux and gas holdup, with variation in pressure, has been studied for ambient and high temperature three phase systems (18). The cold system consisted of nitrogen, heptane, and raw coal as the three phases and was

operated at ambient temperature, with pressure ranging from ambient to 520 KPa. The high temperature system consisted of coal, hydrocarbon and hydrogen as the three phases and was operated at 723 K and 17 MPa.

This study indicated that the drift flux mainly lies in the transition region, and shows a wide variation depending on the pressure. Thus for a given value of ϵ_g the drift flux is lower at higher pressure. It can therefore be inferred that the plot of q_{df} vs ϵ_g can be used to determine the flow regimes in a TPEB reactor, since the boundaries between the various flow regimes have a typical characteristics. Further conclusions that can be drawn from these studies (18,116) are:

For a three phase system operating under ambient pressure

1. At low u_l, the flow is in a coalescing bubble regime with q_{df} increasing appreciably with ϵ_g.

2. As u_l increases, the flow enters the transition regime with the slope of q_{df} vs ϵ_g curve decreasing with increasing u_l.

3. At higher values of u_l, the flow would enter the dispersed bubble regime and the q_{df} vs ϵ_g curve would lie below the dispersed bubble regime boundary.

It should be noted that the changes in the flow regimes with change in u_l match with the trends noted in section 5.4.2.1 above.

For a three phase system operating at constant u_l

1. At a low bed pressure, the flow is in a coalesced bubble regime with q_{df} changing appreciably with ϵ_g.

2. As the bed pressure increases, the flow enters the transition regime with the slope of q_{df} vs ϵ_g curve decreasing with increase in pressure.

3. At high pressures, the flow enters the dispersed bubble regime and the slope of q_{df} vs ϵ_g decreases appreciably.

As mentioned earlier, in this section, the u_{br} correlations at atmospheric bed pressure are modified to incorporate the effect of higher pressure. These modified u_{br} correlations are used in the generalized wake model, to forecast the gas holdups at higher pressure. The drift flux is calculated separately for the corresponding values of gas holdup and u_{br}, using Equation 5.20. The results are then checked for their validity, by plotting the drift flux vs gas holdup and examining the trends and the shapes of these plots against the expected behavior of the bed under high pressure noted above.

5.6 Effect of Bed Pressure on the Bubble Behavior

The behavior of the bubble in multiphase systems, under varying pressure, can be considered in two stages: bubble formation and bubble ascent.

5.6.1 Bubble Formation

The change in bed pressure affects the phase properties such as ρ_l, ρ_g, μ_l and σ, which in turn affects the volume of the bubble during its formation at the orifice. This aspect has been discussed in details in subsection 4.3.4 of Chapter 4.

5.6.2 Bubble Ascent

Pressure seems to affect the behavior of bubbles as they rise through multiphase systems. Behavior of the bubbles under high pressure (up to 15 MPa) in air-water system has been studied by Idogawa et al. (115). Their observations are noted below.

1. At atmospheric pressure, the bubble size had a broad distribution, with many sizes being formed. The distribution narrowed as the pressure rose, and the bubble size decreased, becoming almost uniform.

2. At atmospheric pressure, the cross-sectional average gas holdup and the bubble size varied greatly, depending on the type of gas distributor used, but this effect diminished as the pressure was increased.

3. At high pressure coalescence of bubbles was not observed in the axial direction, except near the gas distributor.

4. As the pressure was increased the gas holdup increased.

Considering the above observations and the phenomena of bubble formation, at the orifice, at high pressure, we can infer that:

1. As the pressure increases the volume of bubble formed at the orifice increases.

2. As the pressure increases the density of gas increases. This increases the inertia of the bubble. Thus, the bubble coalescence during its ascent decreases. This leads to a reduced bubble growth and therefore a uniform and smaller bubble size (compared to a situation where coalescence is promoted, at lower pressure).

3. Smaller bubble size leads to reduced bouyancy and hence reduced bubble rise velocity.

4. The reduced bubble rise velocity leads to an higher gas holdup, at higher pressure.

Three phase systems, under varying pressure show similar behavior, as the two phase systems (116). As the pressure increases, the gas holdup increases and the flow proceeds from the coalesced bubble regime towards the dispersed flow regime,

indicating reduced bubble coalescence at high pressure (174). The inference that the bubble rise velocity reduces with the increase in pressure has been used to modify the u_{br} correlations in the following section. Further, the effect of particle size on the reduction in bubble coalescence, at high pressure, is also discussed there.

5.7 Effect of Pressure on u_{br}

5.7.1 Pressure Coefficient

Zuber and Finlay (175) have correlated the effect of gas density on the drift velocity, in a two phase air-water system, through Equation 5.22.

$$\begin{aligned} \frac{q_{df}}{\epsilon_g} &= \left(\frac{u_g}{\epsilon_g} - (u_l + u_g)\right) \\ &= A_1 \left(\sigma g \frac{(\rho_l - \rho_g)}{{\rho_g}^2}\right)^{1/4} \end{aligned} \tag{5.22}$$

where A_1 is a characteristic constant for the system and includes the effect of u_l, u_g, d_p, μ_l, d_o and d_r. Equation 5.22 assumes that the bubble size and velocity is controlled by the surface tension and the gas kinetic energy at the distributor.

Equation 5.22 can be rewritten as

$$\frac{q_{df}}{\epsilon_g} = A_1 \left(g \frac{(\rho_l - \rho_g)}{{\rho_g}^2}\right)^f \sigma^f \tag{5.23}$$

where $A_1 = A_1(u_l, u_g, d_p, \mu_l, d_o, d_r)$. and

f = 1/4 for the system used by Zuber and Finlay (175).

Though the effective bubble rise velocity, u_{br}, is not analogous to the drift velocity, q_{df}/ϵ_g, there is a similarity between the two. The drift velocity is the relative velocity of the bubble with respect to the surface moving at the average velocity of the phase mixture, while the effective bubble rise velocity is the relative

velocity of the bubble with respect to the velocity of the liquid-solid region. This similarity can be then extended to predict the effect of gas density on u_{br} according to the following equation.

$$u_{br} = A_2 \left(g \frac{(\rho_l - \rho_g)}{{\rho_g}^2} \right)^e \sigma^e \tag{5.24}$$

where $A_2 = A_2(u_l, u_g, d_p, \mu_l, d_o, d_r)$

From the form of correlation for u_{br} given in Equation 5.11, we have

$$u_{br} = K {d_p}^a {u_l}^b {u_g}^c {\mu_l}^d \sigma^e$$

which implies

$$u_{br} = K_1 \left(g \frac{(\rho_l - \rho_g)}{{\rho_g}^2} \right)^e {d_p}^a {u_l}^b {u_g}^c {\mu_l}^d \sigma^e \tag{5.25}$$

where K_1 is termed as the pressure coefficient and is given by

$$K_1 = \frac{K}{\left(g \frac{((\rho_l)_a - (\rho_g)_a)}{{(\rho_g)_a}^2} \right)^e} \tag{5.26}$$

where subscript a denotes phase property at atmospheric pressure.

It should be noted that in the above formulation the drift velocity is not equated with u_{br}, but Equation 5.22 has been used as a guideline to incorporate the effect of liquid and gas density on u_{br}.

The liquid and gas density increases with bed pressure and therefore Equation 5.25 indirectly incorporates the effect of pressure on u_{br}. Since the liquid density ρ_l is not as sensitive to pressure as the gas density, Equation 5.26 implies that u_{br} decreases with increase in ρ_g or increase in bed pressure. These implications are in concurrence with the discussions on effect of pressure on u_{br} in section 5.6.

Table 5.3. Calculated Values of K_1

Set #	System	d_p (m)	ρ_l $(kg/m^3$	ρ_g $(kg/m^3$	K	K_1
I(a)	Glass beads-water-	.0025 to	1000	1.225	.0180	3.825×10^{-3}
I(b)	air	.005	1000	1.225	.1204	2.558×10^{-2}
II(a)	Glass beads-water-	.001 to	1000	1.225	.00008	1.594×10^{-5}
II(b)	air	.0025	1000	1.225	0.01003	2.976×10^{-3}
III(a)	Catalyst-water-	.0025 to	990	1.064	.0051	5.483×10^{-5}
III(b)	nitrogen	.005	990	1.064	.1041	1.119×10^{-3}
IV(a)	Catalyst-	.0025	790	0.169	0.0026	4.888×10^{-6}
IV(b)	kerosene-	to	790	0.169	0.0051	9.776×10^{-6}
IV(c)	helium	.005	790	0.169	0.1041	1.998×10^{-4}

For set numbers refer Table 5.1.
ρ_g calculated at 288.15 K and 101.3 KPa.

5.7.2 Determination of Pressure Coefficient

The procedure for determining the values of pressure coefficient K_1 is described below and the values of K_1 are presented in Table 5.3.

1. Select the appropriate u_{br} correlation from Table 5.2. for a TPEB operating at atmospheric pressure. The form of the correlations is given in Equation 5.27.

$$u_{br} = K {d_p}^a {u_l}^b {u_g}^c {\mu_l}^d{}_a \sigma^e \tag{5.27}$$

2. Calculate the pressure coefficient K_1 from Equation 5.28.

$$K_1 = \frac{K}{\left(g \frac{(\rho_l)_a - (\rho_g)_a}{{(\rho_g)_a}^2} \right)^e} \tag{5.28}$$

3. Include the pressure factor K_1 in the correlation for u_{br}, to generate the modified u_{br} correlation, whose form is represented by Equation 5.29.

$$u_{br} = K_1 \left(g \frac{(\rho_l - \rho_g)}{{\rho_g}^2} \right)^e {d_p}^a {u_l}^b {u_g}^c {\mu_l}^d \sigma^e \tag{5.29}$$

Equation 5.29 applies for all the values of bed pressure, including the atmospheric pressure.

The values of K_1 for various three phase systems, covered in Table 5.1., determined by the above procedure, are given in Table 5.3.

5.8 Performance of the Modified u_{br} Correlations

The procedure for modifying the u_{br} correlation, to incorporate the effect of pressure, has been developed by assuming that the effect of change in gas density

on the effective bubble rise velocity is similar to that on the gas drift velocity. The procedure used to modify the u_{br} correlations could be best validated by experiments. As mentioned in section 5.5.2, q_{df} vs. ϵ_g relation follows a particular trend, depending on the flow regime and responds to the change in the liquid superficial velocity and the bed pressure in a typical fashion. Since at this stage no experimental evidence is available, the performance of the modified u_{br} correlations has been studied by an indirect method mentioned below.

5.8.1 Performance Under Varying u_l Condition

To study the response of the TPEB operating at atmospheric pressure and varying u_l, u_{br} was calculated for different values of u_l using the modified u_{br} correlations. The gas holdup was determined by using these values of u_{br} in the generalized wake model. Under these conditions ρ_g is constant, implying that the calculations for ϵ_g are made for a TPEB operating under constant pressure and varying u_l. q_{df} was calculated for the corresponding values of ϵ_g, u_{br} and u_l using Equation 5.20 and plotted against ϵ_g with u_l as a parameter.

5.8.2 Performance Under Varying Bed Pressure Condition

The value of u_{br} for different bed pressures was determined using the modified u_{br} correlations. The gas holdup was calculated using these values of u_{br} in the generalized wake model. Values of ρ_g at various pressures were calculated using the Redlich-Kwong (176) equation of state. The values of q_{df} were plotted against corresponding values of ϵ_g, with pressure (indirectly ρ_g) as the parameter, to study the response of the TPEB system to variation in bed pressure.

The result of the above procedures are shown and discussed in the following section.

5.8.3 Results and Observation

The plot of drift flux q_{df} vs. ϵ_g, resulting from the above procedure, are presented in Figures 5.8 through 5.11.

1. Figure 5.8: For Glass beads-Water-Air system with $d_p = 0.005$ m. and operating at atmospheric pressure and varying u_l.

2. Figure 5.9: For Glass beads-Water-Air system with $d_p = 0.005$ m. and operating at constant u_l and varying bed pressure.

3. Figure 5.10: For Glass beads-Water-Air system with $d_p = 0.001$ m. and operating at constant u_l and varying bed pressure.

4. Figure 5.11: For Catalyst-Kerosene-Helium system with $d_p = 0.00265$ m. and operating at constant u_l and varying bed pressure.

Following observations are made from the above graphs.

1. The flow in Figure 5.8 changes from coalescing bubble flow towards dispersed bubble flow, with increase in u_l.

2. The flow in Figure 5.9 changes from coalescing bubble flow to dispersed bubble flow, after passing through the transition flow region, with increase in bed pressure.

3. The flow in Figure 5.10 changes from coalescing bubble flow towards dispersed bubble flow after passing through the transition flow regime, with increase in pressure. At lower pressures, the flow shows a change towards the churn turbulent regime, with increase in ϵ_g, and therefore u_l. This is indicated by the change in direction of the plot. Similar trends are seen in other studies (18,19,116,125).

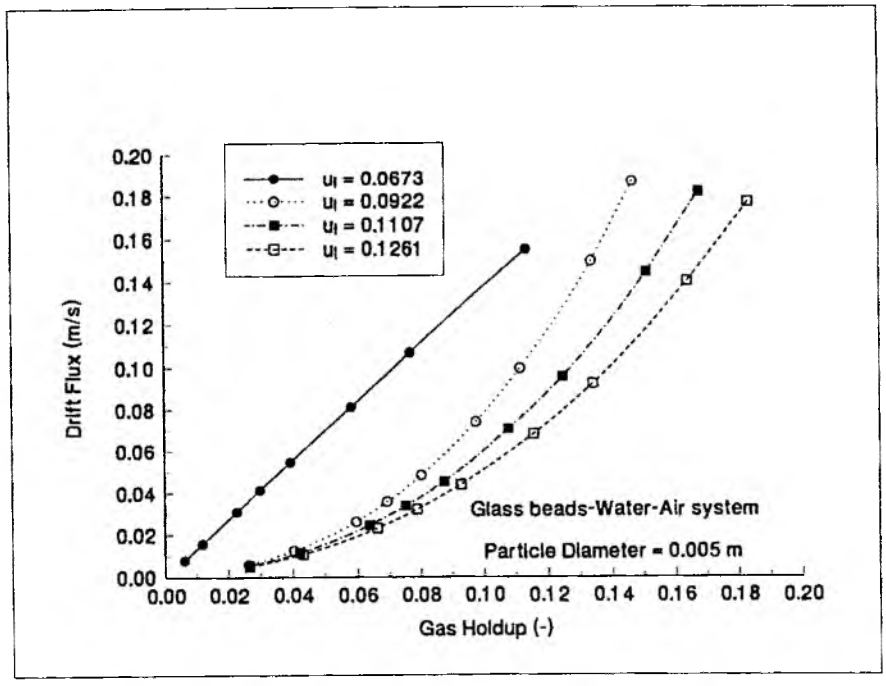

Figure 5.8. Drift Flux vs. Gas Holdup, at Ambient Pressure and Varying u_l.

4. The flow in Figure 5.11 changes from coalescing bubble flow to dispersed bubble flow much faster (w.r.t. pressure) than that in Figure 5.9, implying that systems with wettable solids and hydrocarbons which have a foaming tendency, as liquid phase, change towards dispersed flow, with increasing pressure, faster than systems with non wettable solids like glass beads or nonfoaming liquids like water.

5.8.4 Conclusions

1. The observations regarding the effect of gas density on the drift flux can be extended to modify the u_{br} correlations to incorporate the effect of bed pressure. This led to the introduction of a pressure coefficient K_1 in the modified correlations.

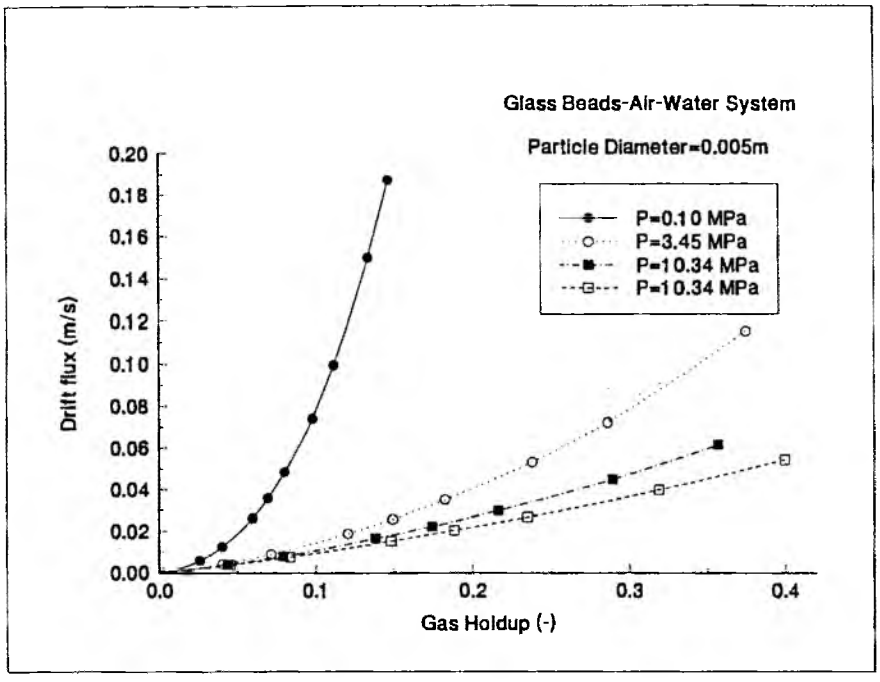

Figure 5.9. Drift Flux vs. Gas Holdup, at u_l = .092 m/s, with Varying Pressure.

2. The plots of drift flux vs. gas holdup can be used to study the response of a TPEB to change in superficial liquid velocity or bed pressure.

3. The behavior of a TPEB under varying superficial liquid velocity or varying bed pressure conditions, predicted by using the modified u_{br} correlations in the generalized wake model is similar to that observed experimentally.

4. For a given gas holdup, the drift flux decreases with increase in liquid superficial velocity and the flow regime changes from coalescing bubble regime to dispersed bubble regime.

5. For a given gas holdup, the drift flux decreases with increasing bed pressure and the flow regime changes from coalescing bubble regime to dispersed bubble

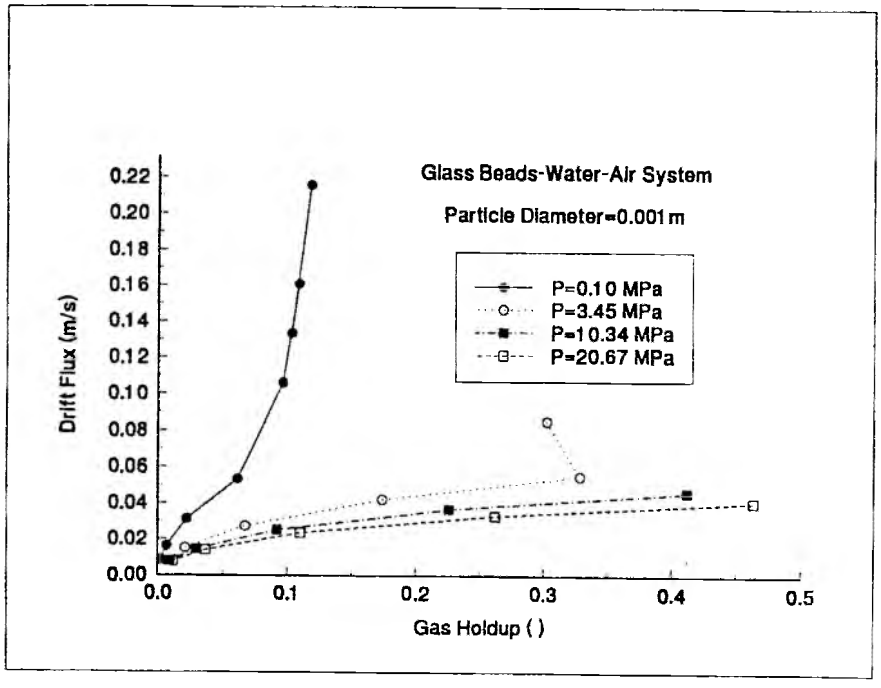

Figure 5.10. Drift Flux vs. Gas Holdup, at u_l = .067 m/s, with Varying Pressure.

regime.

6. The shape of the plot for bed pressure equal to 0.101 MPa. in Figure 5.10 can be explained on the following basis. TPEB with $d_p < 0.0025$ m. is known to contract on injection of gas and expand later as the gas superficial velocity u_g is increased. ϵ_g is inversely proportional to u_{br} and q_{df} is a function of ϵ_g and u_{br}. The bed starts contracting when u_g is small and, as noted in item 5.4.2..2.4(a), u_{br} decreases rapidly. This results in a rapid increase of ϵ_g with u_g and correspondingly q_{df} increase rapidly with ϵ_g. As u_g increases the rate of contraction reduces leading to a reduction in rate of decrease of u_{br} with u_g as seen from Figure 5.3. Accordingly the rate of increase of ϵ_g with u_g and rate of increase of q_{df} with ϵ_g decreases as seen from Figure 5.10. As u_g increases

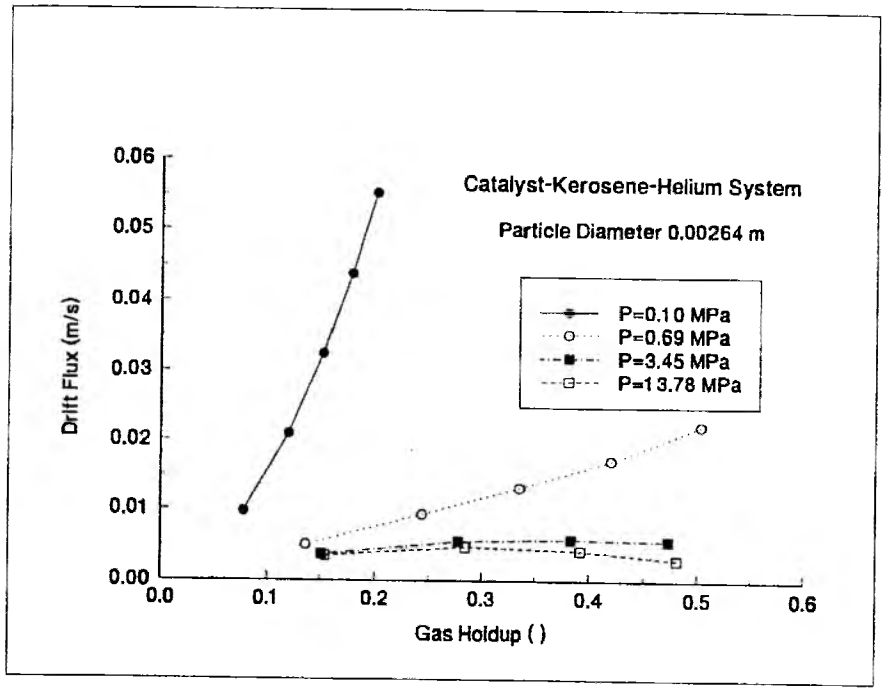

Figure 5.11. Drift Flux vs. Gas Holdup, at u_l = .061 m/s, with Varying Pressure.

further the bed begins to expand and u_{br} increases as indicated by Figure 5.3 leading to a decrease in ϵ_g. At this stage, when the contracting bed changes to an expanding bed, q_{df} increases whereas ϵ_g decreases due to the increase in u_{br} thereby changing the direction of the plot in Figure 5.10. As the bed continues to expand both q_{df} and ϵ_g increase monotonically with u_g as also indicated by later portion of the plot.

5.9 Summary

1. The concept of effective bubble rise velocity considers the bubble rise flux across the crossection of the reactor rather than the bubble rise velocity at a

single location in the reactor.

2. The proposed u_{br} correlations cover wide variety of materials and flow regimes of industrial significance.

3. The values of phase holdups determined by substituting the values of u_{br}, calculated from the correlations, in the generalized wake model, match with the experimental observed values in a TPEB.

4. The correlations developed in this studies are system specific and depend on system configuration such as distributor type. The procedure formulated to generate the correlations can be used to generate similar correlations for any other system, once the hydrodynamic data are available for that system.

5. The correlations consider the effect of particle diameter d_p, in addition to the effect of other fluid properties and flow conditions on u_{br}.

6. The plots of bubble rise velocity u_{br} vs. gas superficial velocity u_g identify the liquid transition velocity u_{tr} at which the transition of flow regimes occurs.

7. The correlations were categorized according to the type of three phase system, particle diameter d_p, liquid superficial velocity u_l and gas superficial velocity u_g and takes

8. The forms of the correlations were explained by addressing various hydrodynamic phenomena for three phase ebullietion.

9. The concept of drift flux was used to study the response of a TPEB to varying liquid superficial velocity u_l and bed pressure P.

10. The u_{br} correlations were modified to include the effect of bed pressure by extending the observations regarding the effect of gas density ρ_g on drift flux.

This led to the introduction of the pressure coefficient K_1 in the modified correlations.

11. The values of u_{br} determined by the modified correlations when used in the generalized wake model, predicted the behavior of a TPEB under varying liquid superficial velocity u_l or varying bed pressure P, similar to that observed experimentally.

CHAPTER 6

DETERMINATION OF PHYSICAL PROPERTIES OF BITUMEN AND BITUMEN FRACTIONS

A knowledge of the physical properties, such as density, viscosity and surface tension, of bitumen and bitumen fractions is useful for recovery and processing operations. Experimental determination of the values of these properties at high temperatures and high pressures is difficult because of the limitations of conventional laboratory equipments and thermal instability of the material. An extrapolative correlative scheme has been developed to predict the values of these properties, at various temperatures and pressures, using the petroleum fraction approach and the Watson characterization factor as a single parameter.

The low temperature SIMDIS data were curve fitted and extrapolated to the high temperature region, by matching the specific gravity, correlated from the extrapolated curve, with the experimentally determined specific gravity of the mixture. Properties such as critical temperature, critical pressure, acentric factor, molecular weight, density and reduced density of the fractions were then determined from the extrapolated SIMDIS curve.

Experimentally determined values of viscosity of bitumen fractions, at various temperatures were correlated with modified reduced density as one of the parameters. A new mixing rule was developed to predict the viscosity of the mixture using the Arrhenius equation and the standard deviation for the reduced density. This accounted for the wide variation in the viscosity of the individual fractions. The pressure coefficient that incorporated the effect of pressure on viscosity was

also determined. Finally, the surface tension of the fractions and the mixture was determined using the parachor value concept.

6.1 Physical Properties and their Significance

The practical scale down procedure identifies two conditions (equations 3.60 and 3.67) which need to be satisfied, to achieve the scale down of three phase ebullieted bed reactor, with variation of minimum number of process parameters.

To apply Equations 3.60 ana 3.67, values of the following physical properties of the fluid phases at high temperatures (698-750 K) and high pressures (13.5 MPa-20.0 MPa) are necessary for the reasons mentioned below:

1. Surface tension between gas and liquid phase to determine bubble rise velocity u_{br}.

2. Viscosity of liquid phase to determine u_{br} and particle terminal velocity u_{tp}.

3. Density of liquid phase to determine u_{br}, u_{tp} and finally the liquid holdup ϵ_l.

4. Density of gas phase to determine u_{br} and gas holdup ϵ_g.

In this chapter a correlative predictive procedure is developed to determine the values of physical properties of bitumen and bitumen fractions at high temperature and high pressure, from the SIMIDS data and experimentally measured values of some of the properties at low temperature.

6.2 Introduction

A knowledge of the values of physical properties of bitumen, such as density, viscosity and surface tension is required for various applications. Some of the applications are

1. Recovery process design.

2. Refining process design.

3. Kinetic modeling.

4. Equipment design.

5. Process control.

Refining processes such as hydrocracking and hydrotreating of bitumen are carried out at high temperature (673-773 K) and high pressure (13.5 MPa-20.0 MPa). An estimate of the physical properties of bitumen and its associated products, at high temperature and high pressure, is necessary to design these processes. Mehrotra et al. (177-182) have published extensive literature on the properties of Athabasca bitumen. Their studies includes determination of the properties up to 473 K and pressure of 10 MPa. Experimental determination of viscosities and surface tensions of bitumen at high temperature and high pressure is restricted by the limitation of conventional laboratory equipments and bitumen thermal instability. Many specialized instruments, such as Jacobs viscometer (183), JEFRI high pressure fluid viscometer (184) and ARC/AOSTRA viscometer (185) have been designed to measure viscosities of heavy hydrocarbons at low and medium temperatures. These specialized equipments are described in detail below.

In this chapter a correlative predictive procedure is developed to determine the values of physical properties of bitumen and bitumen fractions at high temperature and high pressure, from the simulated distillation (SIMDIS) data and experimentally measured values of some of the properties at low temperature.

The predictive procedure takes into consideration the physical changes, such as phase transformation, with temperature. However the procedure does not consider

the thermal instability at high temperatures. However, in the presence of high pressure hydrogen, the thermal instability at high temperature is reduced. Therefore for process with high pressure hydrogen the predictive procedure is expected to predict the values of physical properties close to the actual values.

6.3 Experimental Methods for Determining Viscosity and Surface Tension

Experimental determination of viscosity and surface tension of bitumen and bitumen fractions at high temperature and high pressure cannot be achieved in conventional laboratory equipments.

6.3.1 Viscosity Measurements

Variety of devices and techniques exist for determining viscosity of low viscosity liquid under relative mild condition. Devices using linear flow conditions (flow between parallel plates) have disadvantages such as controlling and analysing edge effects and difficulty of instumentation. Rotational viscometers are relatively more versatile and can be adapted for wide ranges of temperatures and pressures. For high pressures, special seals are required and in some cases a magnetic coupling is used to rotate the cylinder. At extremes of temperature and pressure, the viscosity range of a given instrument becomes somewhat restricted owing to mechanical considerations (186). Though small sample, typically 10-15 ml. may be required for simple commercial versions, specialized versions may require large sample volumes. In a cylinder type rotational viscometer, the gap between the cylinder and the casing, the shear rate is not constant, which complicates interpretation of non-Newtonian behavior (187).

Some of these drawbacks are solved in a cone-and-plate viscometer. The principal advantages of this instrument are its ability to rigorously define non-Newtonian

behavior and extremely small sample size required. In the sheared space, the shear rate is constant and reaches steady state in a fraction of a second. This results in measurements being made with limited viscous heating. Thus the viscosity-shear-rate-time profiles are readily determined without approximations. Excessive rotational speeds could throw the lighter fluids from the gap between the cone and plate; however such a situation is unlikely to be encountered with heavy fluids such as bitumen and bitumen fractions

Tube flow viscometers, in practice, experience entrance effects as the fluid enters the tubing (188). If the viscometer is well designed, the entrance pressure loss will be a small fraction of the total pressure loss over the tubing. If dissolved gases are present, enough back pressure has to be mentained to avoid flashing at the exit.

The main types of commercial viscometer are: rotational viscometers-controlled speed (shear rate) and controlled torque (shear stress) types and tube viscometers-controlled ram/screw speed (shear rate) and controlled pressure (shear stress) types. The most common design is the speed controlled viscometer where the shear rate is fixed and the resulting shear stress is measured. Such commercial viscometers may not be appropriate for the measurements of bitumen and heavy oil viscosities (186). A study by the Alberta Research Council on commercial available apparatus revealed that at high pressure, capillary tube and rolling ball viscometers tended to plug, causing an inconsistency in the measurements (185). Three of the specialized instruments designed by Jacobs (183,184,185) are described briefly.

The ARC/AOSTRA viscometer has the following features:

- Leak free operation at high temperature and high pressure.
- A mechanism capable of producing pressure variations that are independent of the vapor pressures of the compounds contained within the pressure vessel.

- A means of heating and maintaining constant temperature throughout the apparatus.
- A mechanism for mixing a known quantity of additives in with the bitumen or heavy oil, to produce a mixture of a constant compositions throughout the apparatus.
- A positive displacement piston pump that eliminates the need for the apparatus to be pressurized with an inert hydraulic fluid.

The JEFRI high pressure fluid viscometer is designed specifically to measure the viscosity of high pressure single phase fluids and has the following features:

- Constant volume, controlled flow, high pressure pump.
- Sensitive pressure differential cell.
- Uniform temperature air bath.
- Long, narrow capillary tube with consistent geometer.

The Jacobs viscometer consists of a gear pump, a mixing cell and a Contraves DC viscometer with the following features:

- Temperature range of 20 - 300° C.
- Pressure range of atmospheric - 13.8 MPa.
- Viscosity range of 3.5 - 1.5 x 10^6 mPa.s.
- Specific gravity range of 0.75 - 1.1.

6.3.2 Surface Tension Measurements

The most common techniques used to measure liquid vapor tensions for bituminous systems include ring tensiometery, the Wilhemy plate method, and the maximum bubble pressure method (186). The maximum bubble pressure method is a dynamic method limited to aqueousvapor tensions and is ideally suited to the measurement of surfactant content in aqueous production systems from the hot water process (189). The Wilhelmy plate method is somewhat more accurate, since unlike ring tensiometery it causes less disturbance of the surface during the measurement. The method is also more amenable to temperature scans involving bitumen and time dependence of the surface tension (190).

6.4 Available Laboratory Data and their Limitations

In the present studies, the kinematic viscosity could be experimentally determined only in lower temperature range and atmospheric pressure. The values of viscosity and surface tension at higher temperatures were calculated by a predictive method. Due to the limitations on the simulated distillation equipment, the fractionation of bitumen can be carried up to 911 K. The available distillation curve therefore covered only the low temperature region and the high temperature distillation curve had to be extrapolated.

ectionExperimental Data

6.4.1 Simulated Distillation Data

The simulated distillation data are presented in Table 6.1.

Table 6.1. Simulated Distillation Data for Whiterock Bitumen

Temperature K (R)	wt. % Distilled
322.22 (612)	5.0
381.11 (718)	10.0
423.89 (795)	15.0
456.11 (853)	20.0
472.78 (883)	25.0
486.11 (907)	30.0
533.89 (993)	40.0
537.78 (1000)	44.1

IBP: 510.93 K (919.67 R)

Specific Gravity: 0.985

6.4.2 Viscosity Data

The viscosity μ_l, of a liquid reflects the resistance it offers to either the flow and its own deformation, or to the flow of material through it such as settling solids. Newtonian fluids are characterized by the behaviour where the stress is propotionate to the deforming stress. For a Newtonian fluid, contained between two parallel plates seperated by a distance d_v, and with a area A_v, the steady force F_v experienced by the plates, when the plates are pulled at a steady velocity V_v is given by

$$\frac{F_v}{A_v} = \mu_l \frac{V_v}{d_v} \tag{6.1}$$

For a rotational viscometer:

the shearing stress is given by

$$\tau_v = \frac{F_v}{A_v} \tag{6.2}$$

and

the shearing strain is given by

$$\lambda_v = \frac{V_v}{d_v} \tag{6.3}$$

For a cone and plate rotational viscometer, the viscosity is given by Equation 6.4 (186)

$$\mu_l = (\frac{3\tau_r}{2\pi {R_v}^3})/(\frac{\lambda_r}{\alpha_v}) \tag{6.4}$$

Equation 6.4 implies that for a constant ω, α and R

$$\mu_l \propto \tau_r$$

or

$$\mu_l \propto \theta_r$$

where

θ_r is the deflection of the counter-acting spring.

Viscosity of bitumen and bitumen fracions were measured for a temperature range between 298.15 K to 348.15 K, using Brookefield Dial Reading Viscometer,

manufactured by Brookfiekd Engineering Laboratories, Inc. The Brookfield Viscometer rotates a sensing element in the fluid and measures the torque necessary to overcome the viscous resistance to the induced movement. This is accomplished by driving the immersed element, which is called a spindle, through a beryllium copper spring. The degree to which the spring is wound, indicated by the pointer, is proportionate to the viscosity of the fluid.

Bitumen from Whiterocks tar sand was extracted by solvent extraction using toulene as the solvent. The solvent from mother liquor was removed by vaccum distillation first using a rotavap and then distilling under high vaccum. The bitumen fractions were got by further distilling the bitumen under vacuum conditions.

The viscosity measurement data for Whiterocks bitumen fractions is presented in Table 6.2 and the viscosity data for Whiterocks native bitumen is presented in Table 6.3.

Table 6.2. Experimental Data for Viscosity of Whiterock Bitumen Fractions

#	Temperature C	Average Viscosity (mPa.s)	
		Fraction 1*	Fraction 2*
1	298.15	21.36	298.12
2.	310.85	12.08	160.21
3.	321.95	8.24	97.56
4.	333.15	5.48	60.10
5.	344.25	-	40.32
6.	345.45	3.89	-

*
weight % of fraction 1 = 10.17 %.
weight % of fraction 2 = 4.372 %.

Table 6.3. Experimental Data for Viscosity of Whiterock Bitumen

#	Temperature K	Viscosity (mPa.s)
1.	322.581	36900.0
2.	333.330	12500.0
3.	343.640	4900.0
4.	353.36	2100.0
5.	363.64	900.0

6.5 Procedure for Predicting the Density

6.5.1 Petroleum Fraction Approach

The introduction of *undefined* mixtures, also commonly known as *fractions*, has tremendously simplified the characterization of petroleum. Petroleum fraction up to C5 are considered as the *defined* compounds, but all the heavier compounds are grouped into petroleum *fractions*. *Defined* compounds are the identifiable chemical substances such as hydrogen, methane, benzene, phenol. As the carbon number of identifiable chemical substances rises rapidly, the concept of *defined* compounds becomes unmanageable. The normal practice is to break a wide petroleum cut in several narrower cuts or fractions. Each fraction should have a narrow boiling range so that it can be treated as a single pseudocomponent that has only one boiling point, equal to the average boiling point of the fraction (78). This approach is generally used for boiling points above 317.15 K (the normal boiling point of n-pentane, usually the heaviest identified *defined compound* is 370.05 K, (191). The enormous simplification introduced by the use of fractions has been very successful for paraffinic crude oils. In such cases the fractions are characterized

by a single parameter: the average boiling point. For crudes with relatively high level of naphthenes, however, the one parameter characterization is no longer very successful. A second parameter, which is a measure of stuctural difference, is needed to differentiate between naphthenes and paraffins. The second parameter is the specific gravity of the fractions or alternatively the Watson characterization factor (192).

6.5.2 Watson Characterization Factor

Watson Characterization factor K_w is given by Equation 6.1.

$$K_w = \frac{T_b^{1/3}}{s_{gm}} \tag{6.5}$$

where T_b is the average normal boiling point of the cut in degree Rankines and s_g is the specific gravity of the cut at 60° F/60° F.

The use of K_w has made it possible to account for naphthenes and even aromatics in the petroleum fractions. However, most of the thermodynamic correlations are based on the properties of paraffinic/naphthenic crudes. The correlation for aromatic crude works best when the level of aromatics is relatively small. The aromaticity of liquids is commonly a measure of K_w. Crude oil fractions have a K_w of about 12, while heavy paraffins have K_w in excess of 13. The K_w of naphthenes goes down approximately to 11. Coal liquids, which are much more aromatic than petroleum crude have fractions with K_w less than 10 and even below 9.

It is observed that the Watson characterization factor K_w remains essentially constant for all the fractions of a mixture and is equal to the Watson characterization factor of the mixture (78). Thus, if the Watson characterization factor for a wide cut K_w and the mean boiling point of the individual fraction T_{bf} is known,

the specific gravity of the individual fraction s_{gf} can be determined by Equation 6.6.

$$s_{gf} = \frac{T_b^{1/3}}{K_w} \tag{6.6}$$

6.5.3 Extrapolation of the Low Temperature Distillation Curve

The low temperature distillation curve was extrapolated to high temperature region by the following procedure:

1. For the low temperature region, the weight percent distilled was plotted against the end boiling point, and the plot was fitted in equation, by nonlinear regression analysis using Levenberg-Marquardt (166) algorithm.

2. An equation for the higher temperature region of the simulated distillation curve (the extrapolated portion of the curve) was assumed and was plotted along with the low temperature curve on the percent weight fraction vs. end boiling point plot.

3. The total curve was divided into 10 equal weight fractions.

4. The mean boiling point T_{bm} of the mixture was approximated by taking the average of the initial normal boiling point and end normal boiling point of the mixture.

5. The Watson characterization factor K_w of the mixture was determined using Equation 6.5.

6. From the correlations for petroleum fractions mentioned in the suceeding section, following parameters, for each of the bitumen fractions, were estimated.

   (a) Mean boiling point, T_{bf} (from equation 6.7)

(b) Specific gravity, s_{gf} (from equation 6.6)

(c) Critical temperature, T_{cf} (from equation 6.8)

(d) Acentric factor, ω_f (from equation 6.10)

(e) Molecular weight, MW_f (from equation 6.11)

(f) Mole percent, mf_f (from equation 6.12)

7. From the correlations for mixing the fractions, mentioned in suceeding section, the values of the following parameters for the mixture (bitumen) were estimated.

   (a) Specific gravity, s_{gm} (from equation 6.13)

   (b) Critical temperature, T_{cm} (from equation 6.15)

   (c) Critical pressure, P_{cm} (from equation 6.23)

   (d) Acentric factor, ω_m (from equation 6.24)

   (e) Molecular weight, MW_m (from equation 6.14)

8. The difference $\Delta(s_{gm})$, in the calculated value of specific gravity of bitumen $(s_{gm})_{cal}$ and the experimentally determined value of specific gravity $(s_{gm})_{exp}$ was determined.

9. The equation of the extropolated curve was varied and steps 1 to 6 were repeated.

10. The equation of best fit extrapolated curve was the one for which the difference in the specific gravities $\Delta(s_{gm})$, calculated in step 8 was the minimum.

11. The best fit curve was plotted and divided into 10 equal weight fractions.

12. Steps 1 - 5 were repeated for the best fit curve.

6.5.4 Prediction of Density

The density of the bitumen fractions and bitumen was calculated in the following manner:

1. Density of a fraction at 60° F and saturation pressure was calculated by Equation 6.25.

2. Density of a fraction at higher temperatures was calculated by Equation 6.26 (Riedel, (193)).

3. Density of a fraction at high temperature and high pressure was calculated using correlation suggested by Chuch-Pransnitz, 1967 given by Equation 6.28.

6.6 Correlations for Physical Properties

6.6.1 Mean Boiling Point

The mean boiling point of the fraction was determined using Equation 6.7.

$$t_{mb} = \frac{(t_{ib} + t_{eb})}{2} \tag{6.7}$$

where

t_{mb} = mean boiling point

t_{ib} = initial boiling point

t_{eb} = end boiling point

6.6.2 Critical Temperature of the Fraction

The critical temperature of the fraction was determined using following correlation (191).

$$T_{cf} = 24.2787(T_{bf})^{0.58848}(s_{gf})^{0.3596} \tag{6.8}$$

where

T_{cf} = critical temperature of the fraction (R)

T_{bf} = average boiling point of the fraction (R)

6.6.3 Critical Pressure of the Fraction

The critical pressure of the fraction was determined using following correlation (191).

$$log(P_{cf}) = 9.0874 - 2.15833log(T_{bf}) + 3.35417log(s_{gf}) + 5.64019(log(s_{gf}))^2 \quad (6.9)$$

where

P_{cf} = critical pressure of the fraction (psia)

6.6.4 Acentric Factor of the Fraction

The acentric factor of the fraction was determined using following correlation (193).

$$\omega_f = [-ln(P_{cf}/14.696) - 5.671485 + (5.809839/T_{rf}) + 0.867513ln(T_{rf}) - 0.1383536(T_{rf})^6]/[12.439604 - (12.755971/T_{rf}) - 9.654169ln(T_{rf}) + 0.316367(T_{rf})^6] \quad (6.10)$$

where

ω_f = acentric factor of the fraction

$T_{rf} = (T_{bf}/T_{cf})$ = reduced temperature of the fraction

6.6.5 Molecular Weight of the Fraction

The molecular weight of the fraction was determined using following correlation (194).

$$MW_f = 4.5673x10^{-5}(T_{bf}{}^{2.1962}(s_{gf})^{-1.0164} \quad (6.11)$$

where

MW_f = molecular weight of the fraction

6.6.6 Mole Fraction

The mole fraction was calculated using Equation 6.12.

$$mf_f(i) = \frac{[w_{ff}(i)/MW_f(i)]}{\sum_{i=1}^{n}[w_{ff}(i)/MW_f(i)]} \tag{6.12}$$

where

$mf_f(i)$ = mole fraction of the i^{th} fraction

$w_{ff}(i)$ = weight fraction of the i^{th} fraction

and

n = number of fractions

6.6.7 Specific Gravity of the Mixture

The specific gravity of the mixture was calculated using Equation 6.13.

$$s_{gm} = \frac{1}{\sum_{i=1}^{n}[w_{ff}(i)/s_{gf}(i)]} \tag{6.13}$$

where

s_{gm} = specific gravity of the mixture

6.6.8 Molecular Weight of the Mixture

The molecular weight of mixture was calculated using Equation 6.14.

$$MW_m = \frac{1}{\sum_{i=1}^{n}(w_{ff}(i)/MW_f(i))} \tag{6.14}$$

where

MW_m = molecular weight of the mixture

6.6.9 Critical Temperature of the Mixture

The critical temperature of the mixture was determined using following correlation (195).

$$T_{cm} = \sum_{i=1}^{n}\sum_{j=1}^{n}\phi_i\phi_j T_{cij} \tag{6.15}$$

$$T_{cij} = 8\left\{\frac{(v_{ci}{}^{1/3}v_{cj}{}^{1/3})^{1/2}}{(v_{ci}{}^{1/3}+v_{cj}{}^{1/3})}\right\}^3 (T_{ci}T_{cj})^{1/2} \tag{6.16}$$

$$\phi_i = \frac{(mf_f(i)v_{ci})}{(\sum_{j=1}^{n} mf_f(j)v_{cj})} \tag{6.17}$$

where

T_{cm} = critical temperature of the mixture (R)

T_{ci} = critical temperature of i^{th} component (R)

ϕ_{ij} = critical volume fraction of i^{th} component.

v_{ci} = critical volume of i^{th} component given by Equation 6.18

$$v_{ci} = 1/\rho_{ci} \tag{6.18}$$

and ρ_{cf}, the critial density, is calculated by the correlation suggested by Watson (192).

$$\rho_{cf} = \rho_{r,f}\left(\frac{\rho_{ref,f}}{\rho_{r,ref,f}}\right) \tag{6.19}$$

where

ρ_{rf} = reduced density.

$\rho_{ref,f}$ = density of fraction at 60° F, (gm/cc).

and $\rho_{ref,f}$ is given by Equation 6.20, (gm/cc).

$$\rho_{ref,f} = 0.999024 s_{gf} \tag{6.20}$$

and $\rho_{r,ref}$, the reduced density at 60° F, is calculated from Equation 6.21 given by Riedel, 1954.

$$\rho_{r,ref} = 1 + 0.85(1 - T_r f) + (1.6916 + 0.9846\omega_f)(1 - T_r f)^{1/3} \tag{6.21}$$

where

$$T_{rf} = (459.67 + 60)/T_{cf} \tag{6.22}$$

6.6.10 Critical Pressure of the Mixture

The critical pressure of the mixture was determined using following correlation (78).

$$\frac{1}{P_{cm}} = T_{cm} \sum_{i=1}^{n} m f_f(i) \left(\frac{T_{cf}(i)}{P_{cf}(i)}\right) \tag{6.23}$$

where

P_{cf} = critical pressure of the i$^{\text{th}}$ component (psia)

P_{cm} = critical pressure of the mixture (psia)

6.6.11 Acentric Factor of the Mixture

The acentric factor of the mixture was determined using following correlation (196).

$$\omega_m = \sum_{i}^{n} m f_f(i) \omega_f(i) \tag{6.24}$$

where

$\omega_f(i)$ = acentric factor of the i$^{\text{th}}$ component

ω_m = acentric factor of the mixture

6.6.12 Density of the Fraction at 60° F

The density of the fraction at 60° F was calculated using Equation 6.25.

$$\rho_{60,f} = 0.99902 s_{gf} \tag{6.25}$$

where $\rho_{60,f}$ = density of the fraction at 60° F

6.6.13 Density of Fraction at High Temperature

The density of the fraction at high temperature was determined using following correlation (193)

$$\begin{aligned} \rho_{ht,rf} &= \frac{(\rho_{ht,f})}{(\rho_{cf})} \\ &= 1 + 0.85(1 - T_{rf}) + (1.6916 + 0.9846\omega_f)(1 - T_{rf})^{1/3} \end{aligned} \tag{6.26}$$

where

$\rho_{ht,rf}$ = reduced density of the fraction at high temperature.

$\rho_{ht,f}$ = density of fraction at high temperature (gm/cc)

ρ_{rf} = reduced density (density/critical density)

T_{rf} = reduced temperature (T_{bf}/T_{cf}) and

ω_f = acentric factor of the fraction

The critical density of the fraction ρ_{cf} is determined from the value of s_{gf} at 60° F/60° F via. the Watson relationship given by Equation 6.27 (192), where $\rho_{ref,f}$ is the density of fraction at 60° F, $\rho_{r,ref,f}$ is obtained from Equation 6.26 such that T_{rf} is equal to ($519.67/T_{cf}$) and $\rho_{r,f}$ is equal to 1.

$$\rho_{cf} = \rho_{rf}\left(\frac{\rho_{ref,f}}{\rho_{r,ref,f}}\right) \tag{6.27}$$

6.6.14 Density of the Fraction at High Temperature and High Pressure

The density of the fraction at high temperature and high pressure was determined using following correlation (195).

$$(\frac{\rho_{hthp,f}}{\rho_{ht,f}}) = 1 + 9\beta(P - P_{sf})^{1/9} \tag{6.28}$$

where

$\rho_{hthp,f}$ = density of the fraction at high temperature and high pressure (gm/cc).

P = pressure (psia).

P_{sf} is the saturation pressure of the fraction given by Equation 6.29, originally suggested by Riedel, 1954.

and

β is a factor defined by Equation 6.35

$$lnP_{rsf} = A_3 - B_1/T_{rf} - ClnT_{rf} + DT_{rf}{}^6 \tag{6.29}$$

where

$$P_{rsf} = P_{sf}/P_{cf} \tag{6.30}$$

$$A_3 = 5.671485 + 12.439604\omega_f \tag{6.31}$$

$$B_1 = 5.809839 + 12.755971\omega_f \tag{6.32}$$

$$C_7 = 0.867513 + 9.654169\omega_f \tag{6.33}$$

$$D = 0.1383536 + 0.316367\omega_f \tag{6.34}$$

$$\begin{aligned}\beta &= (v_{cf}/RT_{cf})(1 - 0.89{\omega_f}^{1/2})exp(6.9547 - 76.2853T_{rf} + \\ &\quad 191.306{T_{rf}}^2 - 203.5472{T_{rf}}^3 + 82.7631{T_{rf}}^4)\end{aligned} \tag{6.35}$$

where v_{cf} = critical volume of the fraction (ft^3/lbm) calculated from Equation 6.18.

6.7 Procedure for Predicting Viscosity

6.7.1 Trends of Viscocity of Petroleum Fractions

Plots of the kinematic viscosity vs. temperature for Penna Crude fractions and California crude fractions have been presented by Maxwell (197). It can be observed from these graphs that the kinematic viscosity of each of the fractions, though different, follows a similar trend in change with temperature. It can therefore be assumed that the kinematic viscosity of various fractions of petroleum or petroleum like material (bitumen) can be represented by a common correlation, for that particular material. The kinmatic viscosity of coal derived liquids fractions have also been represented by a common correlation (78). This principle has been applied to formulate the correlation for kinematic viscosity of bitumen fractions at various temperatures.

6.7.2 Methodology for Predicting Viscosity of Bitumen Fractions

For coal derived liquids the procedure used to predict the viscosity is the correlation used by Hwang et al. (198), which is an application of corresponding state

concept to liquid viscosity (78). A similar correlation was originally developed by Abbott and Kaufmann (199) by analysing a large amount of experimental data on defined compounds. This correlation is applicable from the freezing point to the critical point and has the general form:

$$\begin{aligned} \ln \nu_{rf} &= ln(\frac{\nu_f}{\nu_{cf}}) \\ &= A_4(\rho_{rf} - 1) + B_2(\rho_{rf} - 1)^{7/2} \\ &\quad + \sum_j^5 C_j[exp(\rho_{rf} - 1)^{((j+1)/2)} - 1] \end{aligned} \tag{6.36}$$

where

ν_{rf} = reduced kinematic viscosity of the fraction

ν_f = kinematic viscosity of the fraction (cSt)

ρ_{rf} = reduced density of the fraction (gm/cc)

and ρ_{rf} is given by Equation 6.26

and for coal derived liquid fraction:

$$A_4 = 3.71104{\omega_f}^2 \tag{6.37}$$

$$B_2 = 0.25121 - 0.65882\omega_f \tag{6.38}$$

$$C_2 = C_3 = 0 \tag{6.39}$$

$$C_4 = 1.27195x10^{-2} \tag{6.40}$$

$$C_5 = -2.411x10^{-4}\omega_f \tag{6.41}$$

$$C_6 = 2.33529x10^{-7}{\omega_f}^2 \tag{6.42}$$

and by extending the correlation suggested by Uyehara and Watson (200)

$$\nu_{cf} = 61.154x10^{-4}(\frac{{T_{cf}}^{5/6}}{{MW_{\omega f}}^{1/2}})(\frac{RZ_{cf}}{P_{cf}})^{1/3} \tag{6.43}$$

In Equation 6.43, T_{cf} is in K and P_{cf} is in atm. where Z_{cf}, the critical compressibility factor, is given by Equation 6.44 suggested by Lydersen et al. (201).

$$Z_{cf} = \frac{1}{(3.41 + 1.28\omega_f)} \tag{6.44}$$

In the original correlation for kinematic viscosity of liquid n-alkanes, proposed by Abbot and Kaufmann (199), the reduced density of liquid n-Alkane was given by Equation 6.45

$$\nu_{rf} = 1.85 - 0.85(\frac{T_f}{T_{cf}}) + (0.53 + 0.2a_k)(1 - (\frac{T_f}{T_{cf}}))^{1/3} \tag{6.45}$$

where

$$a_{kf} = 5.808 + 4.93\omega_f \tag{6.46}$$

From the above discussions, it is clear that

$$\nu_f = f(\rho_{rf}) \tag{6.47}$$

and

$$\nu_{rf} = f(T_f, T_{cf}, \omega_f) \tag{6.48}$$

For bitumen fractions the following procedure was used to generate equations similar to Equation 6.36 and Equation 6.45. The dynamic viscosity of the first and the second fraction of Whiterock native bitumen (μ_f), at various temperatures, was determined experimentally as described in section 'Experimental data'. The kinematic viscosity of the fraction (ν_f) was determined by Equation 6.49

$$\nu_f = \mu_f / \rho_{ht,f} \tag{6.49}$$

where $\rho_{ht,f}$ was calculated using Equation 6.26.

The kinematic viscosity of these two fractions were then simalteneously fitted in two correlations given in Equation 6.50 and Equation 6.51 by nonlinear regression analysis using the Levenberg-Marquardt (166) algorithm.

$$\begin{aligned} ln(\nu_{rf}) = ln(\frac{\nu_{ht,f}}{\nu_{cf}}) &= L \\ &= 0.507222(\rho_{rf,mod})^{2.756673} \end{aligned} \tag{6.50}$$

where $\rho_{rf,mod}$ = modified reduced density given by Equation 6.51.

$$\rho_{rf,mod} = 1.85 - 3.95(T_f/T_{cf}) + (0.53 + 0.2a_{kf})(1 - (T_f/T_{cf}))^{1/3} \tag{6.51}$$

and

a_{kf} is given by Equation 6.46.

The kinematic viscosity ($\nu_{ht,f}$) and the dynamic viscosity ($\mu_{ht,f}$) at various temperatures was then determined by Equations 6.52 and 6.53 respectively.

$$\nu_{ht,f} = \nu_{cf} e^{L} \tag{6.52}$$

and

$$\mu_{ht,f} = \nu_{ht,f} \rho_{ht,f} \tag{6.53}$$

6.7.3 Formulation of a Mixing Rule

No single blending method for computing the viscosity of mixtures has been found applicable to all types of mixture. The procedure used for coal derived liquid fractions by Tsonopoulos et al. (78) was the Kendall-Monroe (202) method for ideal solutions given by Equation 6.54

$$\mu_m = \left(\sum_i^n m f_f(i) \mu_f(i)^{1/3}\right)^3 \tag{6.54}$$

where μ_m is the viscosity of the mixture and μ_f is the viscosity of the fraction.

A more frequently used concept, in the petroleum industry, is the concept of Blending Index. To predict the viscosity of a blend of two or more fractions at any given temperature, the Blending Index of each fraction is determined from its viscosity at that temperature, using the chart for the Blending Index vs. Temperature (197). The Blending Index of the individual fractions is additive by volume fractions and the resulting sum may be converted to the viscosity of the mixture by refering to the blending chart again.

The concepts of ideal solutions as well as the Blending Index were applied to calculate the viscosity of bitumen from the viscosities of bitumen fractions. These values, when compared with the experimental values of viscosity of bitumen at

same temperatures, were not found to be satisfactory. This identified a need to formulate a new mixing rule. The poor agreement could be attributed to the very wide difference in the viscosity of the first and the last fraction of bitumen. At 323 K the experimental value of viscosity of the first fraction is 7.76 mPa.s, while the predicted value of viscosity of the tenth fraction is 2.06×10^{17} mPa.s.

Arrhenius (203) suggested an empirical formula for calculating the viscosity of a mixture of two components, which is given in Equation 6.55

$$log(\mu_m) = x_{vf} log(\mu_1) + (1 - x_{vf}) log(\mu_2) \tag{6.55}$$

where

x_{vf} = volume fraction of the first fraction

μ_m = dynamic viscosity of the mixture

and

μ_1, μ_2 = dynamic viscosity of fraction one and fraction two respectively.

This logorithmic formula holds fairly well for mixtures containing upto about 0.1 volume fraction of one component, but fails to represent the viscosity of a mixture over the entire range from $x = 0$ to $x = 1$ (204). Since the distillation curve for bitumen was divided into 10% weight fractions the Arrhenius correlation was used to generate the mixing rule.

To account for the wide difference in the viscosities of the individual bitumen fraction at any temperature, the concept of standard deviation ρ_{std} of $\rho_{rf,mod}$ was introduced.

ρ_{std} was calculated by Equation 6.56

$$\rho_{std} = \left\{ \frac{\left(\rho_{rf,mod} - \left(\rho_{rf,mod}\right)_{avg}\right)^2}{(n-1)} \right\}^{0.5} \tag{6.56}$$

where $\left(\rho_{rf,mod}\right)_{avg}$ is the average of $\rho_{rf,mod}$ given by Equation 6.57

$$(\rho_{rf,mod})_{avg} = \sum_{i}^{n} \frac{\rho_{rf,mod}}{n} \tag{6.57}$$

and n is the number of fractions.

$\rho_{rf,mod}$ is calculated from Equation 6.51.

The various values of ρ_{std} at different temperatures were fitted in a correlation by nonlinear regression analysis using Levenberg-Marquardt (166) algorithm, to generate C_m, a coefficient, which when applied to Equation 6.55, as explained below, yielded values of viscosity of bitumen close to the experimentally observed values, at the same temperature. C_m was found to satisfy Equation 6.58

$$C_m = 0.12455(\rho_{std}{}^{-9.339631}) \tag{6.58}$$

The procedure to apply the mixing rule is as follows:

1. Calculate the viscosity of the individual bitumen fraction as described in Subsection 6.8.2.

2. Calculate ρ_{std} from Equation 6.56 and C_m from Equation 6.58.

3. Calculate $M_1 = \log(\mu_m)$ from Equation 6.55.

4. Calculate μ_m by Equation 6.59.

$$\mu_m = exp(C_m M_1) \tag{6.59}$$

The performance of this procrdure is presented in Section 6.7.

6.8 Incorporation of Pressure Effect on Viscosity

6.8.1 Correlation for Pressure Effects

In this work the effect of pressure on the dynamic viscosity of the fraction was estimated by the correlation of Kouzel (205) given in Equation 6.60.

$$log(\frac{\mu_{hp,f}}{\mu_{0,f}}) = \frac{(P - 14.696)(0.0239 + 0.01638\mu_0{}^{0.278})}{1000} \tag{6.60}$$

where $\mu_{hp,f}$ = dynamic viscosity of fraction at pressure P

and μ_0 = dynamic viscosity of fraction at atmosphere pressure.

The kinetic viscosity of the fraction at high pressure was calculated by dividing $\mu_{hp,f}$ by the density of the fraction at that pressure, calculated by Equation 6.28.

The kinematic viscosity of the mixture at high pressure was then calculated by applying the proposed mixing rule to the viscosities of the individual fractions, at that pressure.

6.8.2 Pressure Coefficient for Viscosity β_T

The Alberta Research Council has fitted the viscosity behavior of bitumen with pressure, in a correlation (Equation 6.61), which is consistent with molecular physics (185)

$$\frac{\mu}{\mu_o} = exp(\beta_T P) \tag{6.61}$$

where μ = dynamic viscosity (mPa.s) at high pressure P

μ_o = dynamic viscosity (mPa.s) at atmospheric pressure and

β_T = pressure coefficient for viscosity $(\text{MPa})^{-1}$ at pressure P.

Using the values of μ_m at various pressures, predicted by the predictive procedure noted above, the values of predicted pressure coefficient β_{Tp} at a given temperature were determined using Equation 6.61.

6.9 Prediction of Surface Tension

Since the *molecular* structure of petroleum or coal derived liquids is generally not known, a group contribution procedure such as that of Quayle (206) for defined compounds cannot be used to predict parachor values (P*) of hydrocarbons. Thus a more emperical correlation based on the normal boiling point and the specific gravity, is needed for such predictions (78). One such approach is to predict the parachor value directly from the normal boiling point and specific gravity. Following an approach similar to that presented by Nokay (207), the following correlation has been developed for predicting P*/M for a wide variety of hydrocarbons including coal derived liquids (78).

$$(\frac{P^*}{MW})_f = 1.6652(T_{bf})^{0.05873}(s_{gf})^{-0.64927} \tag{6.62}$$

where $(P^*/MW)_f$ = ratio of parachor factor to molecular weight of fraction.

One of the most frequently used correlation for the surface tension of mixture is the one proposed by Weinang and Katz (208), which reletes the mixture surface tension to the component parachors and mixture properties by

$$\sigma_m = \sum_i^n \left\{ P_i^* \left(\frac{x_i \rho_l}{MW_l} - \frac{y_i \rho_v}{MW_v} \right) \right\}^4 \tag{6.63}$$

where

x_i = mole fraction of the i^{th} component in the liquid phase

y_i = mole fraction of the i^{th} component in the vapor phase

σ_m = surface tension of the mixture

ρ_l and ρ_v are the mass density of the liquid and vapor phases

MW_l and MW_v are the molecular weights of the liquid and vapor phases

and

P_i^* is the parachor value of the i^{th} component calculated from Equation 6.62.

Tsonopoulos et al. (78) observed no difference in the average deviation in the predicted surface tension value calculated from Equation 6.63, with the assumption that the vapor phase consisted along with hydrogen the coal derived liquid vapors or consisted pure hydrogen. This was due to the very low hydrogen solubility in the liquid phase and the small quantity of coal derived liquids in the vapor phase.

Since the mean boiling points of the bitumen fractions are high and the solubility of hydrogen in bitumen is low, in the surface tension calculation, it was assumed that the vapor phase consisted only pure hydrogen while the liquid phase consisted only pure bitumen fractions.

The density of hydrogen at various temperatures and pressures were calculated using Redlich-Kwong equation of state (176)

$$V_g - b = \frac{RT}{P} - \frac{a_{Rk}(V_g - b_{RK})}{T^{1/2}PV_g(V_g + b_{RK})} \tag{6.64}$$

where

V_g = volume of gas

R = gas constant

P = pressure of gas

$$a_{RK} = \frac{0.42748R^2T_c^{2.5}}{P_c} \tag{6.65}$$

and

$$b_{RK} = \frac{0.08664RT_c}{P_c} \tag{6.66}$$

where T_c = critical temperature of the gas and

P_c = critical pressure of the gas

The parachor value for hydrogen was approximated by a value of 15.0 which is the structural contribution of H atom to parachor value (150).

To calculate the surface tension at high temperature and high pressure, the value of densities of liquid phase and hydrogen at that temperature and pressure were used in Equation 6.63.

6.10 Results

The computer code for the correlative procedure is presented in Appendix D.

6.10.1 Simulated Distillation Curve Extrapolation

The curve that fitted the low temperature range simulated distillation data was a parabola described by Equation 6.67.

$$W_b = \frac{(t_b - IBP)^2}{4G_1} \tag{6.67}$$

where

W_b = total wt. % of bitumen distilled at temperature t_b (° F) G_1 = constant for a parabola

IBP = initial boiling point of bitumen = 460° F

The calculated value for 'G' is presented in Table 6.4. It was assumed that the extrapolated curve was an inverted parabola. With the following equation

$$t_{be} = V_1 - \mid (-4d_e(w_{be} - 100)^{1/2} \mid \tag{6.68}$$

where w_{be} = wt. % of bitumen distilled in the extrapolated region at temperature t_{be} (° F)

Table 6.4. Values of Parameter 'G_1' at Various Temperatures

#	Temperature t_b K	Distilled w_b wt. %	'G_1'
1.	595.37	5.0	1155.2
2.	654.26	10.0	1664.1
3.	697.04	15.0	1870.42
4.	729.26	20.0	1930.61
5.	745.93	25.0	1789.29
6.	759.26	30.0	1665.08
7.	807.04	40.0	1775.56
8.	810.93	44.1	1653.06

Average value of 'G_1' (for # 2–8) = 1764.02

and V_1 = value of vortex of the inverted parabola in the extrapolated region

$$d_e = -\frac{(x_1 - V_1)^2}{4(y_1 - 100)} \tag{6.69}$$

where y_1 = value of weight % distilled where the inverted parabola starts

and x_1 = value of temperature (F) at which the inverted parabola starts value for which

is given by Equation 6.70.

$$x_1 = 2 \mid (1764.016 y_1)^{0.5} \mid +460 \tag{6.70}$$

The shape of the inverted parabola was changed by varying the values of V_1 and y_1. For the different values of V_1 and y_1, the values of various parameter mentioned

in step 6 and step 7 of Subsection 6.6.3 were calculated. The difference $\Delta(s_{gm})$ between the calculated value of specific gravity $(s_{gm})_{cal}$ and experimental value of specific gravity $(s_{gm})_{exp}$ for various values of V_1 and y_1 are shown in Table 6.5. By studying Table 6.5, it can be concluded that the values of V_1 and y_1 for the best fit of the extrapolated curve, where $\Delta(s_{gm})$ is the minimum are

$y_1 = 72.5$ wt %

$V_1 = 1600°$ F

Therefore the simulated distillation curve for Whiterocks bitumen is described by the following equations

Table 6.5. Values of ΔS_{gm} for Various Values of V_1

#	y_1 wt %	V_1 (K)	$\Delta S_{gm} = S_{gm_{cal}} - S_{gm_{exp}}$
1.	77.4	1732.29	-0.011958
2.	77.4	1650.00	-0.0048878
3.	77.4	1800.00	-0.017612
4.	75.0	1732.29	-0.0115277
5.	80.0	1732.29	-0.013
6.	77.4	1600.00	-0.0004816
7.	75.0	1600.00	-0.00022775
8.	**72.5**	**1600.00**	**-0.0002106**
9.	77.4	1850.00	-0.0216981
10.	80.0	1600.00	-0.001295
11.	80.0	1850.00	-0.0229326
12.	72.5	1850.00	-0.020622
13.	70.0	1850.00	-0.02108
14.	65.0	1850.00	-0.0185416
15.	60.0	1850.00	-0.0177211
16.	55.0	1850.00	-0.016229
17.	55.0	1800.00	-0.012724
18.	55.0	1750.00	-0.009155
19.	55.0	1700.00	-0.00552
20.	55.0	1650.00	-0.001817
21.	55.0	1600.00	-0.001956

Table 6.5. Values of ΔS_{gm} for Various Values of V_1

#	y_1 wt %	V_1 (K)	$\Delta S_{gm} = S_{gm_{cal}} - S_{gm_{exp}}$
1.	77.4	1732.29	-0.011958
2.	77.4	1650.00	-0.0048878
3.	77.4	1800.00	-0.017612
4.	75.0	1732.29	-0.0115277
5.	80.0	1732.29	-0.013
6.	77.4	1600.00	-0.0004816
7.	75.0	1600.00	-0.00022775
8.	**72.5**	**1600.00**	**-0.0002106**
9.	77.4	1850.00	-0.0216981
10.	80.0	1600.00	-0.001295
11.	80.0	1850.00	-0.0229326
12.	72.5	1850.00	-0.020622
13.	70.0	1850.00	-0.02108
14.	65.0	1850.00	-0.0185416
15.	60.0	1850.00	-0.0177211
16.	55.0	1850.00	-0.016229
17.	55.0	1800.00	-0.012724
18.	55.0	1750.00	-0.009155
19.	55.0	1700.00	-0.00552
20.	55.0	1650.00	-0.001817
21.	55.0	1600.00	-0.001956

in step 6 and step 7 of Subsection 6.6.3 were calculated. The difference $\Delta(s_{gm})$ between the calculated value of specific gravity $(s_{gm})_{cal}$ and experimental value of specific gravity $(s_{gm})_{exp}$ for various values of V_1 and y_1 are shown in Table 6.5. By studying Table 6.5, it can be concluded that the values of V_1 and y_1 for the best fit of the extrapolated curve, where $\Delta(s_{gm})$ is the minimum are

$y_1 = 72.5$ wt %

$V_1 = 1600°$ F

Therefore the simulated distillation curve for Whiterocks bitumen is described by the following equations

For 0 %≤ $w_b \leq$ 72.5 %

$$t_b = (7056.064 w_b)^{1/2} + 460 \tag{6.71}$$

and for 72.5 % < $w_b \leq$ 100 %

$$t_b = 1600 - \{|\ (20480.46(w_b - 100))\ |\}^{1/2} \tag{6.72}$$

where w_b = weight percent of bitumen distilled at temperature t_b (F)

These equations are plotted in Figure 6.1.

The predicted value of various parameters for 10 fractions of Whiterock bitume calculated from the best fit curve and procedure mentioned in item 6 of subsection 6.4.6 are presented in Table 6.6. indent Predicted molecular weight of bitumen =

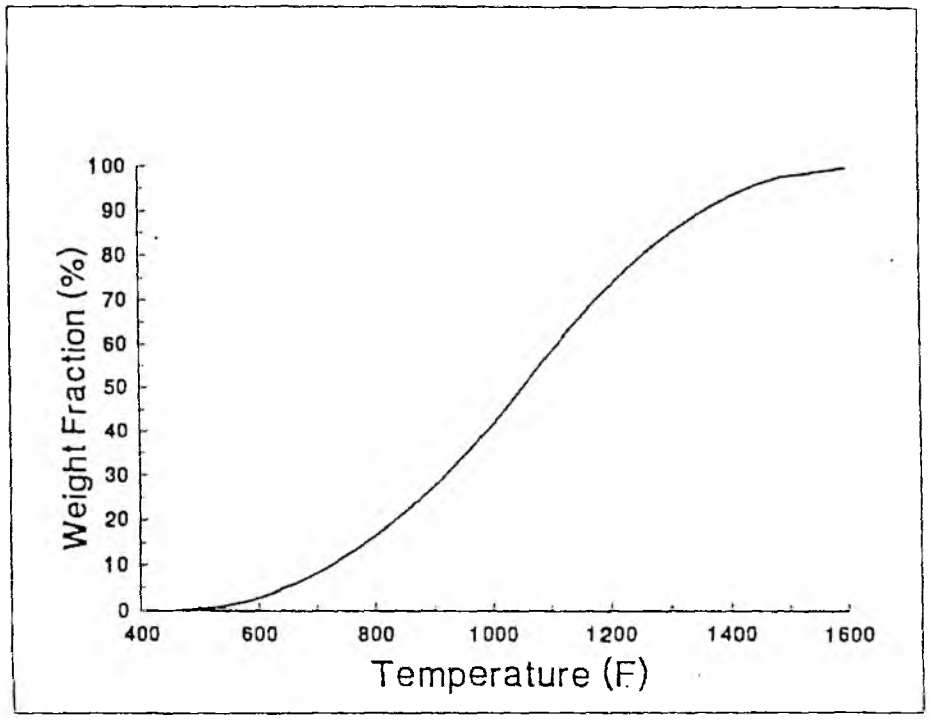

Figure 6.1. Extrapolated Distillation Curve for Whiterocks Bitumen

Table 6.6. Predicted Values of Parameters of the Fractions of Whiterocks Bitumen

Fraction no.	T_{bf} (K)	T_{cf} (K)	P_{cf} (MPa)	MW_f	mf_f
1.	584.72	772.72	1.700	226.38	0.1799
2.	689.07	868.04	1.394	307.12	0.1326
3.	743.08	915.71	1.279	353.33	0.1153
4.	786.31	953.12	1.200	392.45	0.1038
5.	823.49	984.84	1.143	427.63	0.0953
6.	857.48	1013.46	1.095	460.98	0.0884
7.	891.60	1041.86	1.051	495.64	0.0822
8.	931.26	1074.48	1.006	537.36	0.0758
9.	980.82	1114.67	0.956	591.69	0.0688
10.	1078.56	1190.69	0.875	703.44	0.0579

Predicted molecular weight of bitumen = 407.34

Predicted Watson charecterization factor of bitumen = 11.5947

Table 6.7. Predicted and Extrapolated Viscosity of Whiterocks Bitumen and Bitumen Fractions

#	Temperature K	Viscosity (mPa.s)				
		Whiterock Bitumen		Fraction 1	Fraction 5	Fraction 10
		Extrapolated	Predicted	0-10 wt. %	50-60 wt. %	90-100 wt. %
1.	333.15	15015.4	12677.3	5.61	26585.0	5.90×10^{16}
2.	344.26	4273.27	4485.10	3.88	14166.7	1.69×10^{16}
3.	366.48	746.77	752.75	1.98	4256.12	1.49×10^{15}
4.	422.04	75.50	33.24	0.52	290.21	4.93×10^{12}
5.	477.59	24.48	5.50	0.211	30.73	2.71×10^{10}
6.	533.15	12.56	2.04	0.125	4.93	2.45×10^{8}
7.	588.71	8.09	1.23	0.098	1.17	3.62×10^{6}
8.	644.26	5.92	1.25	-	0.40	86272.4
9.	699.82	4.69	0.79	-	0.187	3290.79
10.	755.37	3.92	0.52	-	0.117	198.60

6.10.2 Viscosity Predictions

The predicted and extrapolated experimental values of viscosities for native bitumen and bitumen fractions at various temperatures and atmospheric pressure are presented in Table 6.7. The extrapolated experimental values were obtained by fitting the experimental data for viscosity of Whiterocks bitumen in temperature range from 321.15 K to 398.15 K in a correlation by non regression analysis using Lavenberg-Marquardt (166) alogorithm. The correlation is given in Equation 6.73

$$\mu_{ext,m} = exp(13.686193(\frac{100}{T_f})^{1.048743}) \tag{6.73}$$

Table 6.8 presents the predicted values of viscosity of Whiterocks bitumen and bitumen fractions at various pressures and fixed temperature.

Predicted values of surface tension for Whiterocks bitumen-hydrogen system are presented in Table 6.9.

Table 6.10 presents the predicted values of β_{Tp} for Whiterock bitumen along with the values of β_T for Athabasca bitumen (186).

The results for viscosity prediction are presented in graphical form in following Figures 6.2 - 6.7.

6.11 Observations and Discussions

Due to the limitation of the laboratory equipments, it is not possible to validate the predicted values of viscosity in the high temperature-high pressure region by experimental data. In spite of these limitation an attempt is made to speculate the reasons for the trends of the values of the viscosity got from the predictive method.

1. It is recommended that for the *defined* compound approach, the variation in the boiling point within the selected fractions should be as small as possible,

Table 6.8. Predicted Values of Viscosities of Whiterocks Bitumen and Bitumen Fractions at Different Pressures

#	Temperature K (R)	Pressure (MPa)	Viscosity (mPa.s)			Pressure coeff. β_T MPa^{-1}
			Whiterocks bitumen	Fraction 1 0-10 wt. %	Fraction 5 50-60 wt. %	
1.	338.71 (609.68)	0.1013	7441.71	4.653	19361.1	—
		3.4474	9506.87	4.915	26433.3	0.07104
		6.8947	12235.50	5.200	30430.6	0.07212
		10.3420	15747.40	5.503	50209.0	0.07248
		13.7895	20267.20	5.822	69198.6	0.07266
		17.2369	26084.40	5.160	95370.1	0.07276
		20.6842	33571.20	6.518	131440.0	0.07283
2.	422.04 (759.67)	0.1013	33.24	0.520	290.21	—
		3.4474	35.84	0.542	325.66	0.02185
		6.8947	38.73	0.566	366.72	0.02217
		10.3420	41.85	0.591	412.96	0.02227
		13.7895	45.22	0.617	465.03	0.02232
		17.2369	48.86	0.644	523.66	0.02235
		20.6842	52.79	0.673	589.68	0.02236
3.	477.59 (859.67)	0.1013	5.50	0.211	30.73	—
		3.4474	5.82	0.220	33.09	0.01640
		6.8947	6.17	0.229	35.72	0.01660
		10.3420	6.53	0.238	38.55	0.01660
		13.7895	6.92	0.248	41.61	0.01660
		17.2369	7.33	0.258	44.92	0.01666
		20.6842	7.77	0.268	48.48	0.01670
4.	533.15 (959.67)	0.1013	2.04	0.125	4.93	—
		3.4474	2.15	0.129	5.21	0.01429
		6.8947	2.26	0.134	5.52	0.01485
		10.3420	2.38	0.140	5.84	0.01491
		13.7895	2.50	0.145	6.18	0.01475
		17.2369	2.63	0.151	6.54	0.01474
		20.6842	2.76	0.157	6.92	0.01461
5.	588.71 (1059.67)	0.1013	1.23	0.098	1.17	—
		3.4474	1.29	0.101	1.22	0.01382
		6.8947	1.35	0.105	1.28	0.01350
		10.3420	1.42	0.109	1.34	0.01388
		13.7895	1.49	0.113	1.41	0.01390
		17.2369	1.56	0.117	1.48	0.01379
		20.6842	1.64	0.122	1.55	0.01391

Table 6.9. Predicted Values of Surface Tension of Whiterocks Bitumen-Hydrogen System

#	Temperature K	Pressure (MPa)	Surface Tension (dynes/cm)
1.	363.65	0.1013	36.75
2.	363.65	10.342	33.87
3.	588.71	10.342	18.93

Table 6.10. Values of Pressure Coefficient at Various Temperatures

#	Temperature K (R)	β_{Tp} (predicted) for Whiterock bitumen (1/MPa)	β_T (literature) for Athabasca bitumen (1/MPa)
1.	338.71	0.0713	0.035
2.	422.04	0.0219	0.021
3.	477.59	0.0164	0.016
4.	533.15	0.0142	-
5.	588.71	0.0135	-

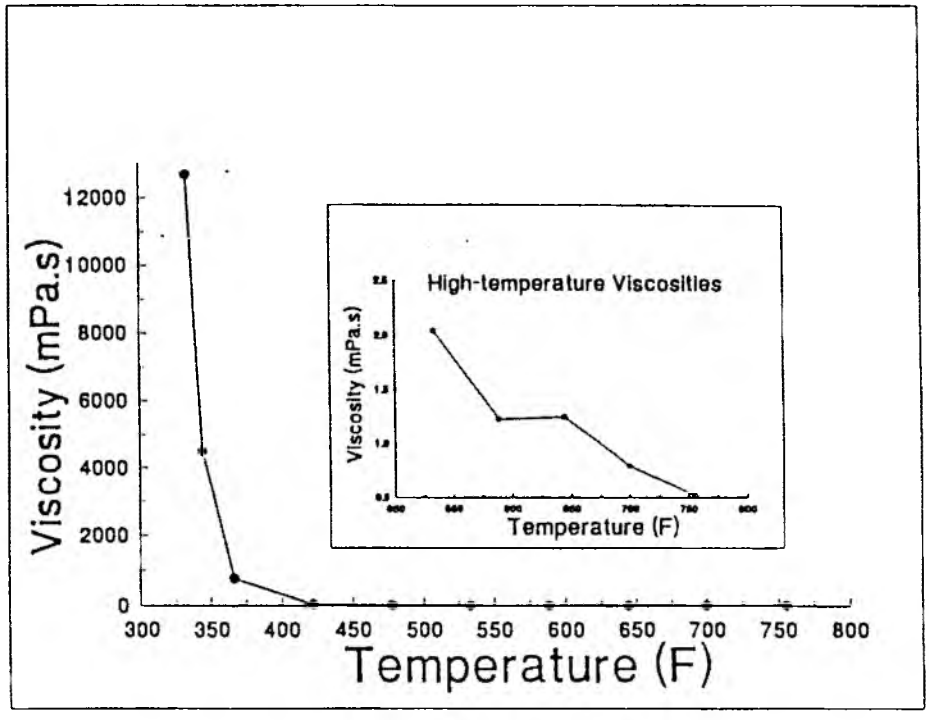

Figure 6.2. Predicted Viscosity of Whiterocks Bitumen vs. Temperature

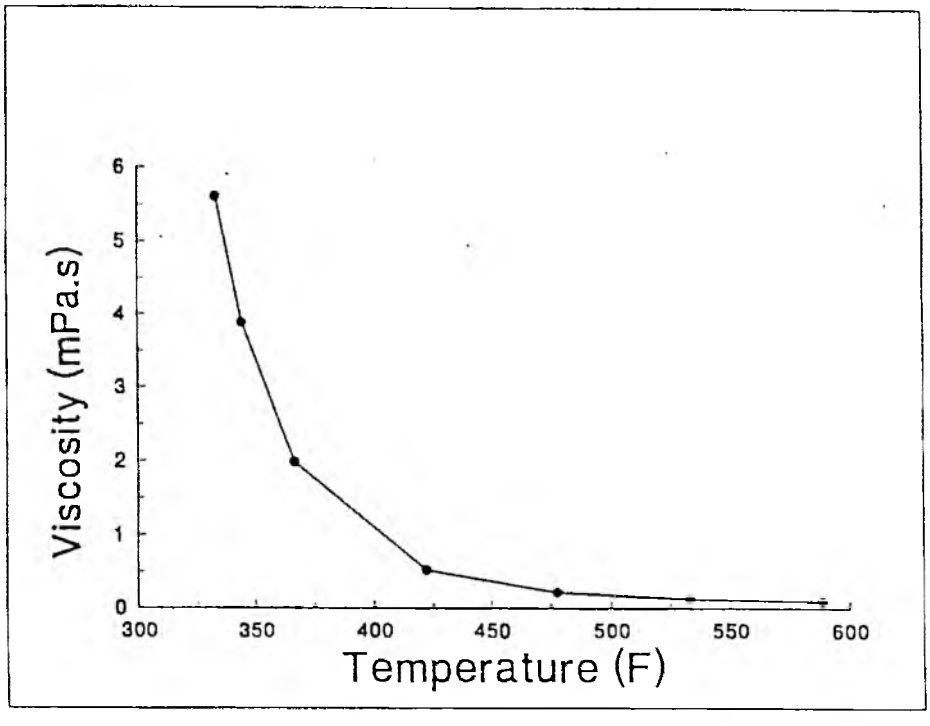

Figure 6.3. Predicted Viscosity of Bitumen Fraction 1 vs. Temperature

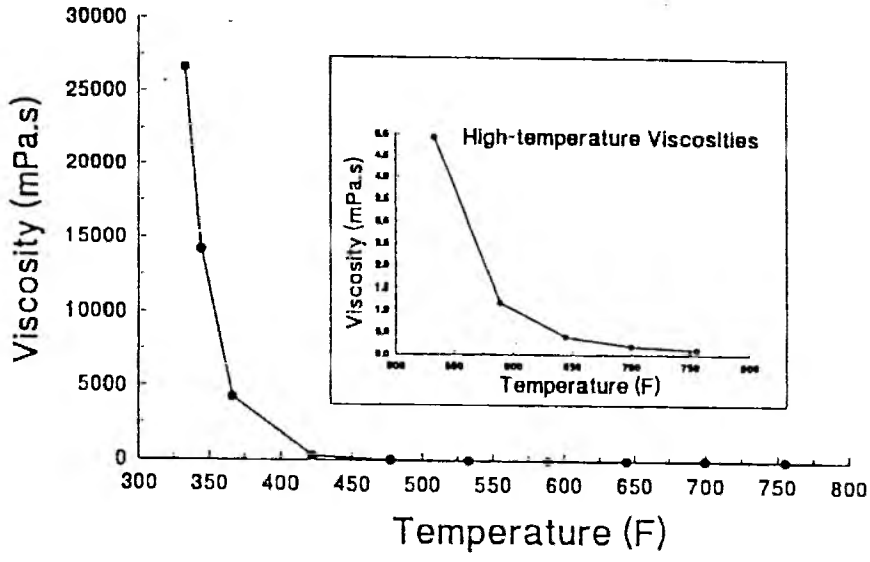

Figure 6.4. Predicted Viscosity of Bitumen Fraction 5 vs. Temperature

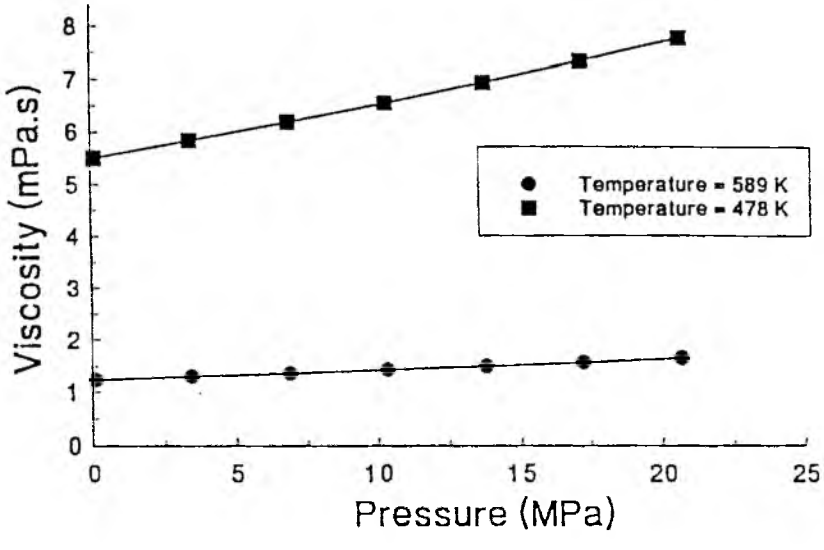

Figure 6.5. Predicted Viscosity of Whiterocks Bitumen vs. Pressure

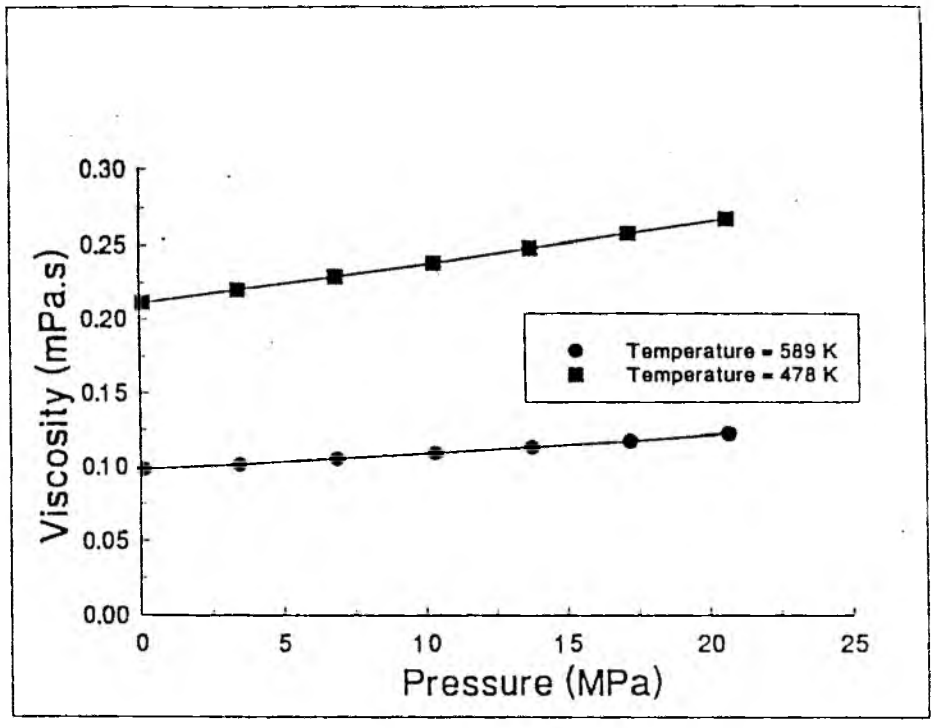

Figure 6.6. Predicted Viscosity of Bitumen Fraction 1 vs. Pressure

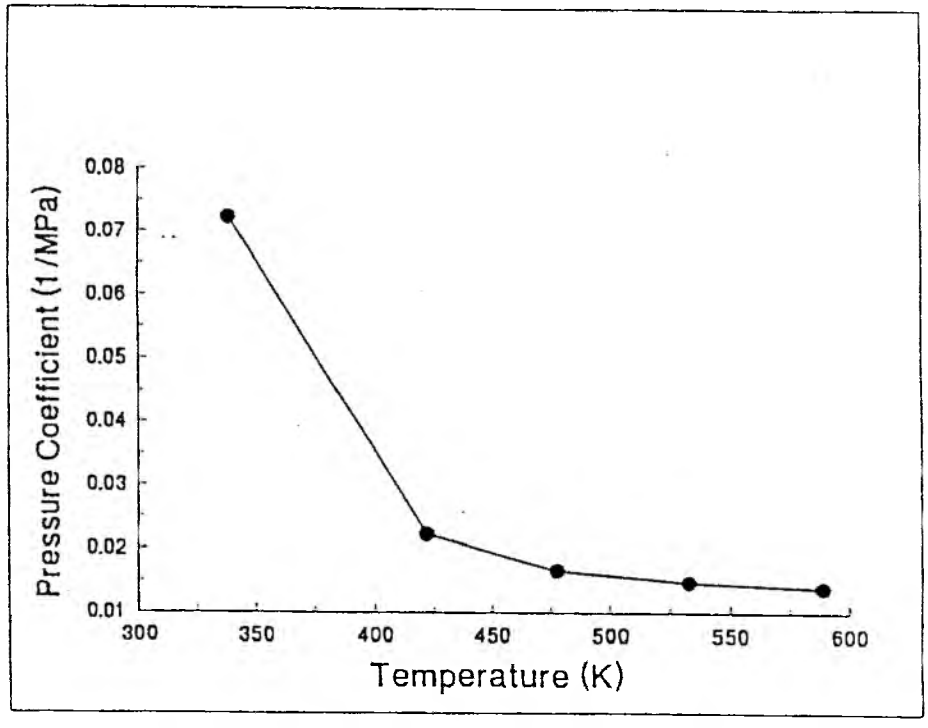

Figure 6.7. Pressure Coefficient vs. Temperature

so that each of the fractions can be treated as a psuedocomponent. From the shape of the predicted distillation curve in Figure 6.1 it can be concluded that:

- This recommendation is satisfied approximately for the low and the highest temperature region, where the rate of distillation with respect to the temperature is appreciably low.
- However this recommendation applies very well for the middle section of the curve, where the rate of distillation is high.

It should be observed that major portion of the bitumen distillation occurs in the middle section of the curve and hence the *fractions* approach applies very well to the overall curve.

2. The values of the Watson Characterization factor for bitumen K_{wm} calculated from the predictive method is 11.5. This value agrees well with the naphthenic nature of the bitumen (210) and the expected range of the value for naphthenic feed (78).

3. An attempt was made to apply the petroleum fraction liquid viscosity correlation (209) to predict the viscosities of bitumen. However, the solution became unstable for the low values of API gravity of bitumen. This agrees with the findings of Hwang and Tsonopoulos, (198), who concluded that this correlation cannot be applied in the low API gravity region of the K_w/API plane.

4. It was assumed that a parabola, instead of a second (or higher) degree polynomial, represented the extrapolated SIMDIS curve. Representing the extrapolated curve by a second degree polynomial would involve three variables, different permutations of the values of which would lead to different possible shapes of the extrapolated curve. By considering the parabolic shape, the

number of variables were reduced to two (vortex and 'G') thereby making the curve fitting process simpler and more decisive.

5. It can be observed from Figure 6.2 that the viscosity vs. temperature curve for bitumen decreases very rapidly up to 425 K and then flattens out at higher temperatures. This behavior could be explained on the basis that around 450 K the viscosity of the lower fractions is appreciably low and the contribution of these fractions to the viscosity of the mixture is negligible compared to the contribution of the heavier fractions. The heavier fractions primarily consist of heavy asphaltenes whose boiling point is high. Due to the high boiling point of the heavy fractions, the bitumen undergoes relatively slower phase change with temperature beyond 450 K, leading to a slower decrease in viscosity.

6. The predictive procedure takes into consideration the physical changes of bitumen with temperature. However the correlations for the extrapolated values are derived from the values of viscosity determined experimentally in the low temperature region, where the physical changes are minimal. The extrapolative method therefore does not take into account the physical changes of the bitumen at higher temperatures. Thus, as observed from Table 6.7, beyond 422 K the extrapolated values of viscosity are higher than the predicted value.

7. Though the viscosity of the higher fractions is much higher than that of the lower fractions, the viscosity of the total mixture is more close to the viscosity of the lower fractions. This indicates that the lower fractions effectively behave as solvents reducing the viscosity of the higher fractions, without changing the chemical identity of the higher fractions.

8. From Table 6.7 it can be observed that the predicted viscosity of bitumen decreases monotonically with temperature up to 588.71 K then spikes up locally around 644.26 K, after which it again decreases monotonically up to 755.37 K. It can be also observed here that the first bitumen fraction boils off around 644.26 K and therefore its contribution to the viscosity of the mixture at this temperature is negligible. Thus, around 644.26 K the solvent effect of the first fraction becomes negligible leading a local increase in viscosity of bitumen. After the local spike the physical changes due to rise in temperature dominate leading to a further monotonic decrease in viscosity of bitumen between 644.26 K and 755.37 K.

9. Figure 6.5 indicates that the rate of increase in viscosity of bitumen with pressure is higher at lower temperatures. Similarly Figures 6.5 and 6.6 indicate that the rate of increase of viscosity with pressure for bitumen is higher than that for the first fraction. It can be therefore concluded that the rate of increase in viscosity with pressure is proportional to the viscosity of the material. This conclusion can be supported by the following explanation. As the pressure increases the molecular distance in the liquid decreases leading to an increase in the intermolecular forces of attraction. The rate of increase in the attractive forces is proportional to the molecular weight of the molecules. The increase in intermolecular forces leads to a increased shear stress in the liquid, resulting in a higher viscosity. This means that the rate of increase in the intermolecular forces with pressure for bitumen is higher than that for the lighter bitumen fractions leading to a faster increase in the viscosity of heavier material, with pressure.

6.12 Conclusions

1. A new procedure for extrapolating low temperature SIMDIS curve to high temperature region, where data may not be available due to limitations of laboratory equipments, was devised.

2. A new predictive method was formulated to predict the characteristic parameters, viscosity and surface tension, of bitumen and bitumen fractions, at high temperature and high pressure.

3. A new mixing rule was suggested to mix the viscosities of the individual fractions, to yield the viscosity of the mixture, for cases where the viscosities of individual fractions vary appreciably from each other.

4. The viscosity of bitumen and its fractions increase with pressure and the rate of increase is proportional to the value of viscosity.

5. The trends of the predicted values of viscosities in the high temperature-high pressure region were explained in terms of the physical changesand intermolecular forces.

6. The extrapolative method for SIMDIS curve, the predictive method for viscosity and the mixing rule together form a general methodology which may be applied to predict the viscosities of heavy hydrocarbons, especially in presence of high pressure hydrogen.

6.13 Summary

1. Conventional laboratory equipments cannot be used to determine viscosity and surface tension of hydrocarbons at high temperatures and high pressures.

2. A extrapolative method was formulated to predict the shape of the SIMDIS curve, for bitumen, in the high temperature region, since total elutriation of bitumen cannot be achieved in a SIMDIS column.

3. The values of the characteristic parameters of bitumen fractions and bitumen were predicted using mean boiling point as a single characterization factor.

4. A predictive correlative procedure was developed to predict the values of physical properties of bitumen fractions and bitumen at high temperatures and high pressures.

5. The values of viscosity predicted by this procedure match with the experimentally determined values of viscosity in the low and medium temperature ranges. Viscosity data in the high temperature region are necessary to validate and tune the predictions of the procedure in this region.

6. A new mixing rule was proposed to predict the viscosity of mixtures, when the viscosity of individual components of the mixture vary by a order of magnitude.

CHAPTER 7

REACTOR SCALE-DOWN

In this chapter the various criteria, correlations and procedures, developed in the previous chapters, have been applied to carry out the hydrodynamic design of the laboratory reactor. This reactor can be used to carry out process development studies on hydrotreating or hydrocracking of bitumen and bitumen derived liquids. The scale down criteria, developed in Chapter 3, have been rigorously applied. The modified u_{br} correlations have been used to calculate phase holdups, in the reactor, through the generalized wake model. The plots for the drift flux vs. the gas holdup, noted in Chapter 3, have been used to study the flow regimes in the reactor. The bubble model, presented in Chapter 4, has been used to calculate the bubble size in the reactor. The procedure to calculate the properties of bitumen at high temperature and high pressure, developed in Chapter 6, has also been used in the design.

The effect of the recirculation ratio, the liquid axial dispersion coefficient and the diffusion coefficient have been considered during the hydrodynamic design. A method of scaling up the gas distributor has also been suggested.

Finally, the mechanical design for the reactor has been carried out, as per ASME code, and presented in form of a data sheet.

7.1 Introduction

The scale-down procedure would be applied in two situations:

1. Consider an existing TPEB commercial reactor, for which process conditions such as temperature, pressure, feed quality, recycle ratio and hydrodynamic parameters such as liquid and gas superficial velocities, catalyst size and shape, reactor size and grid configuration are known. This information could be used to determine the phase-holdups in the commercial reactor and to design a laboratory reactor, using the scale-down procedure. The laboratory reactor can then be used to study the process and improve its performance, for a number of process variations in the commercial reactor such as

   (a) Different catalyst (type and size).

   (b) Different process conditions (temperature, pressure, space velocity and feed quality).

   (c) Different grid design (orifice size, layout, construction).

   (d) Different phase holdups.

   The results of the above studies, in the laboratory reactor, can then be easily extrapolated to predict the performance of the process at the large scale.

2. Consider a situation where an existing TPEB is to be employed for processing a new feed (e.g. tar sands bitumen). In such a case, the laboratory reactor could be designed for the process and hydrodynamic conditions expected in the commercial reactor. The results of the kinetic, hydrodynamic and transport studies in the laboratory reactor can then be used to design a new commercial reactor and operate the process, at commercial scale, under similar process and hydrodynamic conditions.

In this chapter, the application of the scale-down procedure is demonstrated for the second situation.

7.2 Algorithm to Calculate $(u_l)_m$ and $(u_g)_m$

The steps enumerated below have been used to calculate the values of the liquid and gas superficial velocities in the laboratory (model) reactor, so that the scale-down requirements are satisfied, *provided* the bubble rise velocity in both the reactors are the same. The procedure for adjusting the bubble rise velocity in the laboratory reactor is covered in Section 7.5.

1. The scale down requirements are

$$(\epsilon_l)_m = (\epsilon_l)_p \tag{7.1}$$

$$(\epsilon_g)_m = (\epsilon_g)_p \tag{7.2}$$

2. Since

$$\epsilon_\kappa = f(\epsilon_l, \epsilon_g) \tag{7.3}$$

It follows from Equation 7.1 and 7.2 that

$$(\epsilon_\kappa)_m = (\epsilon_\kappa)_p \tag{7.4}$$

3. Define the value of $(d_p)_m$, initialize the values of $(u_l)_m$ and $(u_g)_m$ and set

$$(u_{br})_m = (u_{br})_p$$

4. Calculate x_m and $(u_i)_m$ from Equations 3.7, 3.8 and 3.13..

5. Since from Equation 3.21.

$$\epsilon_l = \epsilon_\kappa(1-x) + \epsilon_{lf}{}''(1-\epsilon_g-\epsilon_\kappa+x\epsilon_\kappa)$$

we have

$$\epsilon_{lf}{}'' = \frac{(\epsilon_l - \epsilon_\kappa(1-x))}{(1-\epsilon_g-\epsilon_\kappa+x\epsilon_\kappa)} \tag{7.5}$$

Calculate $(\epsilon_{lf}{}'')_m$ from Equation 7.5.

6. From Equation 3.17

$$\epsilon_{lf}{}'' = \left(\frac{u_l - v_g\epsilon_\kappa(1-x)}{u_i(1-\epsilon_g-\epsilon_\kappa)}\right)^{1/n}$$

since

$$v_g\epsilon_\kappa = \kappa u_g$$

$$u_l = u_i(1-\epsilon_g-\epsilon_\kappa)(\epsilon_{lf}{}'')^n + \kappa u_g(1-x) \tag{7.6}$$

Calculate $(u_l)_m$ from Equation 7.6.

7. Calculate $(v_g)_m$ from Equation 3.20.

8. Calculate $(u_g)_m$ from Equation 7.7.

$$(u_g)_m = (v_g)_m(\epsilon_g)_m \tag{7.7}$$

9. Compare values of $(u_l)_m$ and $(u_g)_m$, calculated in steps 6 and 8, with the previous values of $(u_l)_m$ and $(u_g)_m$. If the values do not compare within a given tolerance (0.1 %), repeat steps 4-8.

10. Calculate

$$(Coeff)_p = \left(\frac{(u_l - \kappa u_g)}{u_i(1 - \epsilon_g - \kappa\epsilon_g)}\right)_p^{1/n} \tag{7.8}$$

$$(Coeff)_m = \left(\frac{(u_l - \kappa u_g)}{u_i(1 - \epsilon_g - \kappa\epsilon_g)}\right)_m^{1/n} \tag{7.9}$$

7.3 Selection of Correlation for u_{br}

The correlations for bubble rise velocity u_{br} have been presented in Chapter 5. Furthermore, the effect of the bed pressure has been incorporated by introducing the pressure coefficient.

Since the properties and the nature of bitumen at high temperature are close to that of kerosene at room temperature, as indicated in Table 7.1, the *modified* correlations for u_{br}, presented for set III(a) and III(b) in Table 5.2 along with

Table 7.1. Physical Properties of Bitumen and Kerosene

#	Liquid	Density ρ_l	Viscosity μ_l	Surface Tension σ
1.	Bitumen 700 K (note 1)	729.22	0.00079	0.0139
2.	Kerosene 298 K (note 2)	790.00	0.00139	0.0286

Notes:

1. Values of properties determined by the predictive correlative method presented in Chapter 6.
2. Values from Table 5.1.

the corresponding values of K_1 given in Table 5.3, are used for hydrodynamic calculations of laboratory reactor with $(d_p)_m$ between 0.0025 m. and 0.005 m.

In the absence of a correlation for u_{br} for $d_p \leq 0.0025$ m. for catalyst-kerosene-helium system, the correlations presented of set IV(a), IV(b) and IV(c) in Table 5.2 along with corresponding values of K_1 in Table 5.3 may be used, after modifications suggested in subsection 7.4.2, for the design of the laboratory reactor, when $(d_p)_m <$ 0.0025 m.

7.4 Limits on Reduction of Particle Size

One of the requirements for the hydrodynamic scale down to be successful is that the flow regimes and the bubble rise velocity in the two reactors should be the same. In Chapter 5 the behavior of a TPEB with respect to pressure, for various particle sizes, has been studied by plotting the drift flux versus the gas holdup. From these plots (Figure 5.11) the following observations have been made:

1. For the catalyst-kerosene-helium system, with $d_p \geq 0.0025$ m., the bed operates in a coalesced bubble regime at lower pressure, but transforms into the dispersed bubble regime at higher pressure.

   However for a TPEB with wettable solid particles, such as alumina supported catalyst and hydrocarbons, such as bitumen, the flow may transform into the dispersed bubble regime at a much lower pressure. This type of behavior was also observed by Tarmy et al. (18).

2. For glass beads-water-air system, with $d_p < 0.0025$ m., the bed operates in a coalesced bubble regime at lower pressure and continues to operate in the coalesced bubble regime even at fairly high pressure (20.6 MPa). A very high pressure would be required to change the bed into a dispersed bubble regime.

A commercial reactor would have $(d_p)_p \geq 0.0025$ m. Vasalos et al. ( ), in the H-Coal studies used catalyst with effective diameter equal to 0.0026 m. Larger d_p is preferred to increase the life of the catalyst which is affected by particle attrition and breakup. Larger $(d_p)_p$ also leads to a lower bubble rise velocities in the reactor which could enhance the gas-liquid mass transfer.

From the above considerations following assumptions can be made regarding the hydrodynamic regimes of the TPEB:

1. For $d_p \geq 0.0025$ m, the commercial reactor would be operated in the dispersed bubble regime at high pressures and will remain in the dispersed regime as long as $(d_p)_m$ is ≥ 0.0025 m. In such a case the correlations given by set IV(a), IV(b) and IV(c) in Table 5.2, along with corresponding values of K_1, from Table 5.3, can be used to calculate the values of u_{br}.

2. It was concluded in Chapter 5, that wettability of solid particles affect u_{br}. Accordingly the exponent on σ was modified for the correlations for u_{br} for Catalyst-Kerosene-Helium system. Since the modified u_{br} correlations generated in Chapter 5, for $d_p < 0.0025$ m, cover Glass beads-Water-Air system, they need to be modified for applying to a catalyst-bitumen-hydrogen system. Thus the exponent on σ for the correlations in set II(a) and 1I(b) of Table 5.2 may be changed from 0.175 to 0.5 as was done for systems with $d_p > 0.0025$ m. With these modifications, the equations for u_{br}, for catalyst-bitumen-hydrogen system, with $d_p < 0.0025$ m become:

   For $0 < u_l < 0.095$ m and $0 < u_g < 0.09$ m

$$u_{br} = 9.9\text{x}10^{-7} \left(\frac{(\rho_l - \rho_g)^{0.5} g^{0.5}}{\rho_g} \right) d_p{}^{-0.7544} u_l{}^{-0.9584} u_g{}^{-0.7860} \mu^{0.025} \sigma^{0.5} \qquad (7.10)$$

   and for $u_l \geq 0.095$ m. and $u_g \geq 0.09$ m.

$$u_{br} = 1.24\text{x}10^{-4} \left(\frac{(\rho_l - \rho_g)^{0.5} g^{0.5}}{\rho_g} \right) d_p{}^{-0.7544} u_l{}^{-0.5558} u_g{}^{0.7714} \mu^{0.025} \sigma^{0.5} \qquad (7.11)$$

In the present studies $(d_p)_p$ is assumed to equal to 0.005 m. and and two values are considered for $(d_p)_m$ [0.0026 m. and 0.001 m.].

7.5 Adjusting the Bubble Rise Velocity

In Section 7.2, the values of the liquid and gas superficial velocities $(u_l)_m$ and $(u_g)_m$ are calculated based on the restriction that

$$(u_{br})_m = (u_{br})_p$$

Since

$$u_{br} = f(d_p, u_l, u_g, \mu_l, \sigma, \rho_l, \rho_g) \qquad (7.12)$$

The value of u_{br} can be modified by adjusting the ρ_{g_m}. This will not alter the process because of the following reason.

The hydrotreating/hydrocracking process for bitumen is expected to operate under a large excess of hydrogen, than that consumed by the process. The expected amount of hydrogen consumed is 2.91 %, by volume, of the total hydrogen fed for TPEB ebullietion, when the gas holdup is around 0.2 (ie. 3400 % excess). This implies that the concentration of Hydrogen and therefore the kinetics of the process will not alter much, if $(\rho_g)_m$ is increased by adding about 10%, by volume, of nitrogen or butane to the hydrogen feed. This will result in 3000% excess hydrogen, which is still in great excess.

The procedure to calculate the volume of nitrogen or butane to be mixed is given below.

1. Calculate the value of $(u_{br})_m$ from an appropriate u_{br} correlation using values of $(u_l)_m$ and $(u_g)_m$, determined in Section 7.2 above.

   Here

$$(u_{br})_m = f((d_p)_m, (u_l)_m, (u_g)_m, (\mu_l)_p, (\rho_l)_p, (\rho_g)_p) \tag{7.13}$$

   Note that $(u_{br})_m$ **will not be equal to** $(u_{br})_p$ at this stage.

2. Calculate the value of the density of gas $(\rho_g)_{reqd}$ so that

$$(u_{br})_{mod} = (u_{br})_p \tag{7.14}$$

   where

$$(u_{br})_{mod} = f((d_p)_m, (u_l)_m, (u_g)_m, \mu_p, (\rho_l)_p, (\rho_g)_{reqd}) \tag{7.15}$$

   $(\rho_g)_{reqd}$ will be greater than $(\rho_g)_p$

3. The higher value of the gas density $(\rho_g)_{reqd}$ is achieved by mixing an inert and heavier gas like nitrogen or butane with the incoming H_2 feed. The volume percent of N_2 to be mixed is calculated by Equation 7.16.

$$(Vol)_{N_2} = \frac{((\rho_g)_{reqd} - (\rho_g)_p)}{((\rho_{N_2} - (\rho_g)_p)} \tag{7.16}$$

   where the densities are calculated at the appropriate temperature and pressure.

4. To maintain similar kinetics in both the reactors the total pressure of the laboratory reactor is adjusted, so that the partial pressure of H_2 in the gas feed, after adding N_2/C_4H_10, is equal to the bed pressure of the commercial reactor.

Another method of adjusting (increasing) the gas density in the laboratory reactor is to increase the pressure in the reactor. The pressure P_{reqd} required to reach the gas density $(\rho_g)_{reqd}$, determined above, can be calculated by using the Redwich-Kwong equation of state.

The behavior of the reactor is envisaged to be as follows. When the laboratory reactor is operated at the same pressure as the large scale reactor, $(u_{br})_m$ will be greater than $(u_{br})_p$. As the pressure is increased $(u_{br})_m$ will decrease until $(u_{br})_m = (u_{br})_p$ at pressure equal to P_{reqd}.

The following method is suggested to modify $(u_{br})_m$.

1. If P_{reqd} is not very much greater than P_p then operate the laboratory reactor at P_{reqd}.

2. If P_{reqd} is very much greater than P_p then the following extrapolative method could be used:

   (a) Study the process by operating the laboratory reactor at pressure equal and greater than P_p.

   (b) Plot the value of the process parameter being studied (e.g. kinetic coefficient) vs. pressure.

   (c) Extrapolate the value of the parameter to pressure equal to P_{reqd}

7.6 Recycle Reactor

In the H-Oil process a portion of the effluent stream from the reactor is cooled in a cooler and returned to the reactor after mixing with the fresh feed. This stream is termed as the recirculation stream and the reactor operates in a recycle mode. The recycle stream serves the following purposes:

1. Since the recirculation stream is cooled externally, it serves to carry away the exothermic heat of reaction from the reactor.

2. By recirculating the effluent back into the reactor, the uncoverted products are exposed to the process conditions and the catalyst repetatively, leading to better conversions. This in effect reduces the length of the reactor. Thus the length of a TPEB reactor with a recirculation stream is less than that with a once through flow. The proportion of recirculation is adjusted according to the degree of conversion desired.

3. If only the fresh feed stream is used to ebulliete the catalyst, the proportion of fresh feed contacting the catalyst will be very high. This will lead to a very long reactor for the low values of space velocities needed for the process. By recirculating the effluent, the proportion of fresh feed contacting the catalyst is reduced. This in effect leads to a reduction in space velocity and the reactor length.

A recycle reactor with homogeneous reaction can be described by Equation 7.17 (211). The schematic of the recycle reactor is given in Figure 7.1.

$$V_R/Q_f = C_f(R_r + 1)\int_{C_1}^{C_e} \frac{1}{rr} dc \tag{7.17}$$

C_1 is given by Equation 7.16.

$$C_1 = \frac{C_f + R_r C_e}{R_r + 1} \tag{7.18}$$

The assumption in deriving Equation 7.15 is that the effective volumetric flow rate of the product Q_e (flow rate out of the reactor minus the recirculation flow rate) is equal to the fresh feed rate Q_f into the reactor.

In Equation 7.15, the ratio of V/Q_f represents the reciprocal of the space velocity in the reactor. Thus Equation 7.15 can be rewritten as:

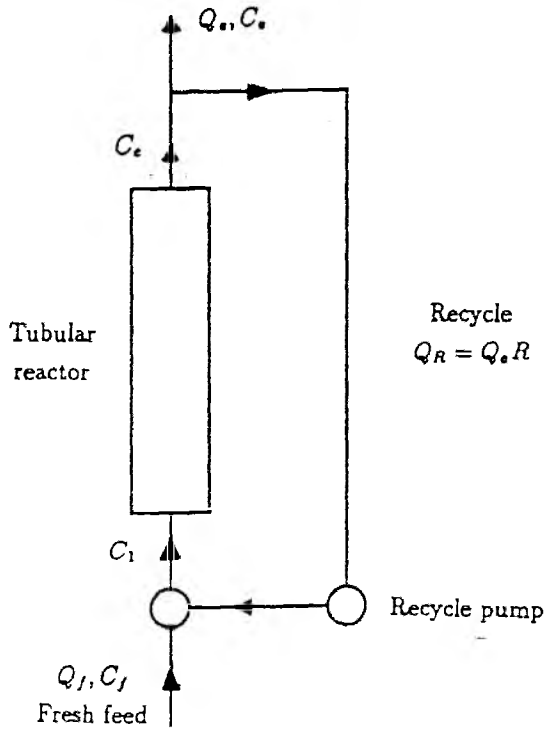

Figure 7.1. Schematic of a Recycle Reactor

$$1/S_v = C_f(R_r + 1)\int_{C_1}^{C_e} \frac{1}{rr} dc1 \tag{7.19}$$

where S_v is the liquid hourly space velocity in the reactor.

If rr is represented by

$$rr = R_1 f(c1) \tag{7.20}$$

where R_1 = reaction rate constant.

then Equation 7.17 becomes

$$1/S_v = \frac{C_f(R_r + 1)}{R_1}\int_{C_1}^{C_e} \frac{1}{f(c1)} dc1 \tag{7.21}$$

or

$$\frac{R_1}{S_v} = C_f(R_r + 1)\int_{C_1}^{C_e} \frac{1}{f(c1)} dc1 \tag{7.22}$$

Equation 7.19 implies that, for a fixed values of C_f, C_1 and R_r, S_v should be varied proportionally, with K_1 to get same C_e. This may be represented by Equation 7.23.

$$S_v \propto R_1 \tag{7.23}$$

The value of S_v can be changed by varying Q_f, while keeping C_f constant. This ensures that the value of C_1, represented by Equation 7.18, remains constant.

Since the phase holdups in both the reactors are the same, the value of the integral, in Equation 7.22, for the two reactors may be same. This implies that the value of the proportionality constant in Equation 7.23 is same for both the reactors.

7.7 Effect of Particle Size Reduction

The effect of reducing the catalyst particle size in the laboratory reactor could have the following effects on the process.

1. Change in liquid dispersion coefficient
2. Change in intraparticle diffusion coefficient

Each of these aspects is discussed below.

7.7.1 Change in Liquid Dispersion Coefficient

Muroyama et al. (212) have developed correlations for axial mixing in a TPEB. The correlation applicable for dispersed bubble regime in SI units is reproduced in Equation 7.24.

$$\frac{d_r u_l}{\epsilon_l E_{zl}} = 26\left(\frac{d_p}{d_r}\right)^{1/2} \tag{7.24}$$

where E_{zl} = liquid axial dispersion coefficient.

Equation 7.22 indicates that E_{zl} is lower for the laboratory reactor than for the commercial reactor, because of the relatively lower value of $(d_p)_m$, $(d_r)_m$ and $(u_l)_m$.

The lower value of $(E_{zl})_m$ implies that the liquid residence time per unit volume of the laboratory reactor is higher, leading to enhanced reaction kinetics by increasing the value of R_1. To ensure that the change in the liquid dispersion coefficient does not affect the reaction kinetics between the two reactors, one could then increase the space velocity by using Equation 7.21. Due to the lack of knowledge of the effect of axial dispersion coefficient on the reaction kinetics of hydrotreating/hydrocracking of bitumen related feeds in a TPEB. It is assumed that the rate constant R_1 is inversely proportional to the axial dispersion coefficient. In such a case the following proportionality holds.

$$(R_1)_m \propto (1/E_{zl})_m \tag{7.25}$$

$$(R_1)_p \propto (1/E_{zl})_p \tag{7.26}$$

or

$$\frac{(R_1)_m}{(R_1)_p} = \frac{(E_{zl})_p}{(E_{zl})_m} \tag{7.27}$$

and from Equation 7.23 we have

$$\frac{(S_v)_m}{(S_v)_p} = \frac{(E_{zl})_p}{(E_{zl})_m} \tag{7.28}$$

It should be pointed out again that Equation 7.28 is an approximation and is used only to size the laboratory reactor.

The liquid Peclet number is defined as

$$P_e = \frac{u_l L}{\epsilon_l E_{zl}} \tag{7.29}$$

where L = characteristic length; the expanded bed height for a TPEB.

During the EDS coal liquefaction studies Tarmy et al. (18) observed that the coal conversion increased with increase in P_e (or decrease in E_{zl}) at lower values of P_e (< 20). This indicated that the rate of conversion is mass transfer controlled at low values of P_e.

However at higher values of P_e (≥ 20), the coal conversion remained almost constant with increase in P_e, indicating that the reactor performance is not mass transfer controlled at high P_e. Due to the low values of axial liquid dispersion coefficient $(E_{zl})_m$ (and hence high values of P_e, resulting in the laboratory reactor performance may not be mass transfer limited but diffusion limited. In such a case, it may not be necessary to adjust $(S_v)_m$ to counter the effect of lower values of E_{zl} in the laboratory reactor.

7.7.2 Change in Diffusion Coefficient

If the performance of the laboratory reactor is diffusion controlled, then the rate constant will depend on the surface area of the catalyst available for diffusion into the catalyst particle. The ratio of the surface area of the catalyst available to the liquid per unit volume of the catalyst in the two reactors is given by

$$\frac{(A_s)_m}{(A_s)_p} = \frac{(d_p)_p}{(d_p)_m} \tag{7.30}$$

where

A_s = catalyst surface area available for diffusion per unit volume of the catalyst.

Assuming that the rate constant is proportional to the surface area available for diffusion, Equation 7.30 implies that

$$\frac{(R_1)_m}{(R_1)_p} = \frac{(d_p)_p}{(d_p)_m} \tag{7.31}$$

This relationship was verified by Kato et al. (213), who found that for small catalyst sizes (< 1 mm.), where the hydrodesulfurization was diffusion controlled, a first order rate constant varied as the reciprocal of the size of the catalyst.

From Equation 7.23, we have

$$\frac{(S_v)_m}{(S_v)_p} = \frac{(d_p)_p}{(d_p)_m} \tag{7.32}$$

Since the hydrotreating and hydrocracking of bitumen and bitumen derived liquids is expected to be diffusion limited rather than mass transfer limited (due to the ebullieted nature of TPEB and low axial liquid diffusion coefficient) the value of the space velocity for the laboratory reactor $(S_v)_m$ was calculated using Equation 7.32 rather than equation 7.28. However, during the actual use of the laboratory reactor, if the process is found to be mass transfer limited, then Equation 7.26 can be used to estimate $(S_v)_m$. In the course of the design calculations, it was found that

$$\frac{(E_{zl})_p}{(E_{zl})_m} < \frac{(d_p)_p}{(d_p)_m} \tag{7.33}$$

and hence the value of $(S_v)_m$ calculated by Equation 7.32 would be smaller than that calculated by Equation 7.28. This leads to a longer laboratory reactor and therefore a conservative sizing.

7.8 Calculation of the Bubble Diameter

As noted in Chapter 3, the stagewise-partition model requires the value of the bubble diameter in the bed as one of the parameter. The diameter of the bubble d_b

for this purpose was calculated by using the bubble model, developed in Chapter 4, after incorporating the effect of bed pressure on the liquid density, gas density, liquid viscosity, surface tension, and the bubble formation at the orifice, in the bubble model. The liquid and gas properties at high pressure were calculated using the procedure developed in Chapter 6.

For the commercial reactor, $(d_b)_p$ is calculated by assuming that $(Q)_p$, the volumetric flow of gas through the orifice, which is the same as $(Q)_m$, and the density of gas equal to $(\rho_g)_p$. For the laboratory reactor, $(d_b)_m$ is calculated with the volumetric flow through the orifice equal to $(Q)_m$ and the density of gas equal to ρ_{reqd} (also refer Section 7.15 - Scale up procedure for gas distributor).

Though the bubble model applies for gas-liquid system, it has been used as an approximation for a three phase system. This approach is reasonable because, for multiphase beds operating under high pressure, the coalescence and disintegration of bubbles is minimal. This leads to a uniform bubble size distribution throughout the bed (115). Further, high pressure leads to a dispersed flow regime in the TPEB reactor, minimizing the bubble to bubble interaction (18). It can therefore be expected that, for a TPEB operating under high pressure, the size of the bubbles does not change appreciably as it rises through the reactor and can be approximated by the size of the bubble just before it detaches from the orifice. Since at this stage there is no published model or correlation to predict the bubble size at the *orifice* in a TPEB, the bubble model for two phase system was used.

7.9 Algorithm to Calculate $(u_l)_p$ and $(u_g)_p$

The algorithm used to calculate the liquid and gas superficial velocities $(u_l)_p$ and $(u_g)_p$ respectively required to achieve a desired liquid and gas holdups $(\epsilon_l)_p$ and $(\epsilon_g)_p$,

in the commercial reactor, for a given values for the hydrodynamic properties, is described below.

1. Define the desired value of $(\epsilon_l)_p$ and $(\epsilon_g)_p$.
2. Assume a value of $(u_l)_p$.
3. Set $(u_g)_p$=0.
4. Calculate ϵ_l using the procedure given in Chapter 3. Since $(u_g)_p$ is set equal to zero, ϵ_g will be equal to zero at this stage.
5. If $(\epsilon_l)_p$ calculated in step 4 is not equal to the value defined in step 1, change the value of $(u_l)_p$ and repeat steps 3 to 5, until the equality is satisfied.
6. Now assume a value for $(u_g)_p > 0$.
7. Calculate $(\epsilon_l)_p$ and $(\epsilon_g)_p$ for the $(u_l)_p$ calculated in step 5 and $(u_g)_p$ assumed in step 6, using the procedure given in Chapter 3.
8. If $(\epsilon_l)_p$ and $(\epsilon_g)_p$ calculated in step 7 above are not equal to the values defined in step 1, change the value of $(u_l)_p$ and $(u_g)_p$ and repeat step 7, until the equality is satisfied.

7.10 Hydrodynamic Design

In this section, a step by step procedure for scaling down the commercial reactor in situation 2 (as detailed in Section 7.1) is presented. The flow chart showing the steps followed for the hydrodynamic design is presented in Figure 7.2. The procedure can be divided into two portions.

1. Establishing the parameters for the commercial reactor.

2. Scaling down the commercial reactor.

In the first portion, the hydrodynamic parameters (liquid and gas superficial velocity) to operate the commercial reactor at the desired values of phase holdups are calculated. Then in the second portion, the scale down procedure is applied to calculate the operating conditions in the laboratory reactor and for sizing this reactor.

7.10.1 Commercial Reactor

1. Define the processing capacity of the reactor $(Q_D)_p$.

2. Define the operating conditions in the reactor.

3. Define the diameter of the reactor $(d_r)_p$.

4. Calculate the phase properties enumerated below.

   (a) Solid phase: $(d_p)_p$ and $(\rho_p)_p$.

   where

   (a) In the case of nonspherical particles $(d_p)_p$ is the effective diameter, which is equal to the diameter of a spherical particle which has the same volume as the nonspherical particle.

   (b) In case of porous solid particle $(\rho_p)_p$ is the effective density of the particle, which is the density of the particle filled with the liquid phase.

   (b) Liquid phase: $(\rho_l)_p$, $(\mu_l)_p$ and $(\sigma)_p$.

   For bitumen these properties can be calculated using the procedure noted in Chapter 6.

   (c) Gas phase: $(\rho_g)_p$.

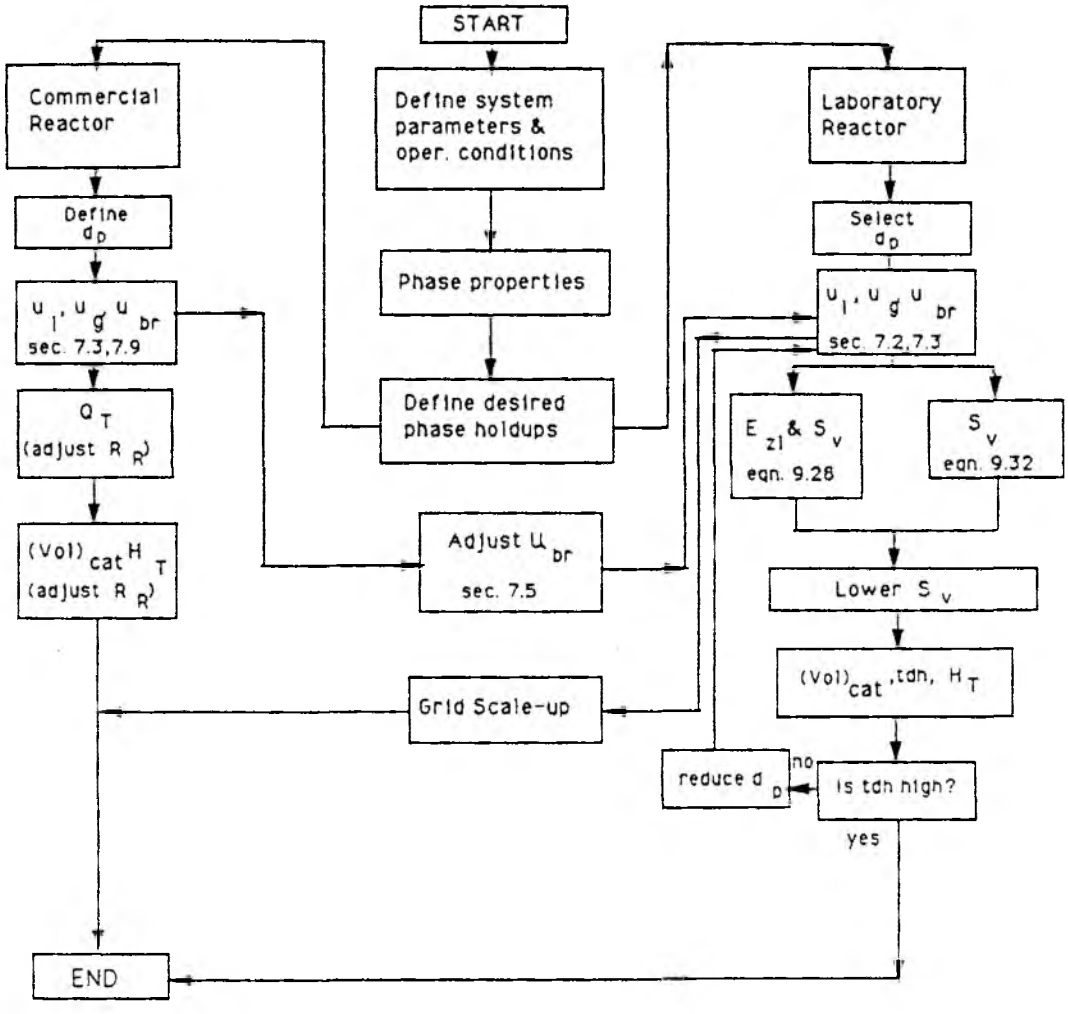

Figure 7.2. Flow Chart for Hydrodynamic Design

The gas density can be calculated using an appropriate equation of state such as Redwich-Kwong equation.

5. Define the values of the desired phase holdups in the reactor $(\epsilon_l)_p$ and $(\epsilon_g)_p$.

6. Use the algorithm given in Section 7.9 above, to calculate $(u_l)_p$ and $(u_g)_p$ required to achieve the phase holdups defined in item 5. The value of $(u_{br})_p$ for this purpose can be calculated using the modified (u_{br}) correlation noted in Section 7.3 above.

7. Define a recycle ratio $(R_r)_p$.

8. Calculate the volume flow rate $(Q_T)_p$, through the reactor, using Equation 7.34.

$$(Q_T)_p = \frac{\pi (d_r)_p^{\,2} (u_l)_p}{4} \tag{7.34}$$

9. Calculate the fresh feed rate $(Q_f)_p$, through the reactor, using Equation 7.35.

$$(Q_f)_p = \frac{(Q_T)_p}{(R_r)_p} \tag{7.35}$$

10. Check for the processing capacity, assuming $(Q_f)_p = (Q_e)_p$. If the processing capacity does not match with the required processing capacity $(Q_D)_p$ change the value of $(d_r)_p$ and repeat steps 6 to 10 until the required processing capacity is achieved. The processing capacity can also be adjusted by changing the recycle ratio. However this may lead to an excessive reactor length, which has to be monitored if $(R_r)_p$ is changed (refer step 18 below).

11. For a given value of liquid hourly space velocity $(Sv)_p$, calculate the volume of the catalyst in the reactor using Equations 7.36.

$$(Vol_{cat})_p = \frac{3600\pi(d_r)_p{}^2(u_l)_p}{4(R_r)_p(S_v)_p} \tag{7.36}$$

where

$(Vol_{cat})_p$ = volume of the catalyst in the commercial reactor.

$(S_v)_p$ = liquid hourly space velocity in the commercial reactor.

12. Calculate the stagnant bed height $(H_s)_p$ using Equation 7.37.

$$(H_s)_p = \frac{3600(u_l)_p}{(R_r)_p(S_v)_p} \tag{7.37}$$

13. Calculate the expanded bed height $(H_e)_p$ by using Equation 7.38.

$$(H_e)_p = \frac{(H_s)_p}{(\epsilon_s)_p} \tag{7.38}$$

14. For the given grid configuration, calculate the diameter of the bubble $(d_b)_p$ in the reactor by the procedure noted in Section 7.8 above.

15. Calculate the particle disengaging height $(tdh)_p$ in the reactor using the procedure described in Chapter 3 (144).

16. Assume an additional length $(ah)_p$ above the particle disengaging height to account for reactor mechanical components (viz. nozzles etc.). Here the effluent consists of a mixture of the gas and liquid phase, while the solid phase is retained in the reactor, by properly sizing the particle disengaging height. The separation between the gas and the liquid phase can be carried out in high and low pressure separators, before the liquid is recirculated back to the reactor.

17. Calculate the total height of the reactor by Equation 7.39.

$$(H_t)_p = 1.1\{(H_e)_p + (tdh)_p\} \tag{7.39}$$

where

$$(ah)_p = 0.1\{(H_e)_p + (tdh)_p\} \tag{7.40}$$

18. If $(H_t)_p$ is excessive, it can be reduced by either increasing $(d_r)_p$ or increasing $(R_r)_p$. In such a case steps 5 to 16 have to be repeated for the new value of $(d_r)_p$ or $(R_r)_p$.

7.10.2 Laboratory Reactor

1. The following equalities hold for the laboratory reactor.

   (a) $(\epsilon_l)_p = (\epsilon_l)_m$

   (b) $(\epsilon_g)_p = (\epsilon_g)_m$

   (c) $(R_r)_p = (R_r)_m$

   (d) $(\rho_p)_p = (\rho_p)_m$

   (e) $(\rho_l)_p = (\rho_l)_m$

   (f) $(\sigma)_p = (\sigma)_m$

   (g) $(\rho_g)_p = (\rho_g)_m$

   However the value of $(\rho_g)_m$ may be modified to adjust the value of $(u_{br})_m$ by using the procedure noted in Section 7.5 above.

2. Select a value for the diameter of the particle $(d_p)_m$.

3. Calculate the value of $(u_l)_m$ and $(u_g)_m$, using the algorithm noted in Section 7.2 above.

4. Calculate the liquid axial dispersion coefficient for the commercial and the laboratory reactors $(E_{zl})_p$ and $(E_{zl})_m$ respectively, using Equation 7.24.

5. Calculate $(S_v)_m$ for the laboratory reactor using Equation 7.28.

6. Calculate $(S_v)_m$ for the laboratory reactor using Equation 7.32.

7. Select the lower of the two values for $(S_v)_m$ from steps 5 and 6.

8. Calculate $(Q_T)_m$, $(Q_f)_m$, $(Vol_{cat})_m$, $(H_s)_m$, $(H_e)_m$, $(d_b)_m$, $(tdh)_m$, $(ah)_m$ and $(H_t)_m$ using the procedure described in steps 8 to 15 in section 7.10.1, using the values of parameters for the laboratory reactor and using Equation 7.41 to calculate $(ah)_m$.

$$(ah)_m = 0.05\{((H_e)_m + (tdh)_m\} \tag{7.41}$$

9. Calculate the value of $(\rho_g)_{reqd}$, using the procedure described in step 1(c) in Section 7.5, so that

$$(u_{br})_m = (u_{br})_p$$

10. Calculate P_{reqd}, the pressure required in the laboratory reactor to make

$$(u_{br})_m = (u_{br})_p$$

using the procedure described in step 2 of Section 7.5.

11. If P_{reqd} is not very different from $(P)_p$ (the pressure in the commercial reactor), the laboratory reactor can be designed for pressure rating equal to P_{reqd}. However if P_{reqd} is appreciably high, than the extrapolative procedure described in step 2(b) of Section 7.5 may be used.

12. An alternative method of adjusting $(u_{br})_m$ is to mix heavy gas such as nitrogen or butane with the hydrogen feed, to increase ρ_g. The method is described in step 1 of Section 7.5. The volume fraction of the heavy gas is calculated using Equation 7.16. Adjust the total pressure of the reactor so that the partial pressure of H_2 in the gas feed, after adding N_2 is equal to the bed pressure of the commercial reactor.

7.11 Sample Calculations

The computer code for TPEB reactor scale-down is presented in Appendix E. A set of sample calculations for the hydrodynamic design is presented in Appendix H.

A summary of the hydrodynamic calculations for various values of $(\epsilon_l)_p$ and $(\epsilon_g)_p$, is presented in Tables 7.2 and 7.3 for two values (0.0026 m. and 0.001 m.) of the catalyst particle diameters.

7.12 Mechanical Design of Laboratory Reactor

7.12.1 Introduction

After sizing the laboratory reactor for hydrodynamic similarity, the mechanical design of the reactor is undertaken in this section. The design conditions and the values of design parameters have been selected on the following basis.

Table 7.2. Summary of Hydrodynamic Design

Phase holdup		Commercial reactor				Laboratory reactor			
ϵ_l ( )	ϵ_g ( )	$u_l x 10^2$ (m/s)	$u_g x 10^2$ (m/s)	$(Vol)_{cat}$ (m^3)	H_l (m)	$u_l x 10^2$ (m/s)	$u_g x 10^2$ (m/s)	$(Vol)_{cat}$ (m^3)	H_l (m)
.34	.20 - .30	1.15 - 1.29	.72 - 1.20	6.50 - 7.29	19.97 - 28.51	.48 - .55	.33 - .55	.031 - .037	4.10 - 6.09
.35	.20 - .30	1.23 - 1.38	.75 - 1.25	6.98 - 7.83	21.89 - 31.54	.52 - .60	.34 - .58	.034 - .040	4.54 - 6.81
.36	.20 - .30	1.32 - 1.48	.78 - 1.29	7.46 - 8.37	23.91 - 34.58	.56 - .65	.35 - .60	.037 - .043	5.01 - 7.54
.37	.20 - .30	1.40 - 1.58	.80 - 1.34	7.95 - 8.96	26.01 - 38.16	.60 - .70	.37 - .62	.040 - .047	5.52 - 8.40
.38	.20 - .30	1.50 - 1.69	.83 - 1.39	8.48 - 9.56	28.44 - 42.01	.65 - .76	.38 - .65	.043 - .052	6.10 - 9.36

$(d_p)_p$ = 0.005 m. $(d_p)_m$ = 0.0026 m.
$(d_b)_p$ and $(d_b)_m$ = 0.00289 to 0.00347 m.
P_{reqd} = 31.8 MPa (4615 psi.) to 32.93 MPa (4780 psi.).
$(Vol)_{N_2}$ = 9.02 to 9.55 vol. %.
$(Vol)_{C_4H_{10}}$ = 3.46 to 3.67 vol. %.
Adjusted total pressure for N_2 mixing = 14.14 MPa. (2052 psi.).
Adjusted total pressure for C_4H_{10} mixing = 13.91 MPa. (2019 psi.).
$(S_v)_p$ = 1.0.
$(S_v)_m$ = 1.92.

Table 7.3. Summary of Hydrodynamic Design

Phase holdup		Commercial reactor				Laboratory reactor			
ϵ_l ( )	ϵ_g ( )	$u_l \times 10^2$ (m/s)	$u_g \times 10^2$ (m/s)	$(Vol)_{cat}$ (m^3)	H_t (m)	$u_l \times 10^2$ (m/s)	$u_g \times 10^2$ (m/s)	$(Vol)_{cat}$ (m^3)	H_t (m)
.34	.20 - .30	1.15 - 1.29	.72 - 1.20	6.50 - 7.29	19.97 - 28.51	.22 - .26	.17 - .29	.006 - .007	0.73 - 1.11
.35	.20 - .30	1.23 - 1.38	.75 - 1.25	6.98 - 7.83	21.89 - 31.54	.24 - .29	.18 - .30	.006 - .007	0.81 - 1.25
.36	.20 - .30	1.32 - 1.48	.78 - 1.29	7.46 - 8.37	23.91 - 34.58	.26 - .31	.19 - .31	.007 - .008	.90 - 1.40
.37	.20 - .30	1.40 - 1.58	.80 - 1.34	7.95 - 8.96	26.01 - 38.16	.28 - .34	.19 - .33	.007 - .009	1.00 - 1.57
.38	.20 - .30	1.50 - 1.69	.83 - 1.39	8.48 - 9.56	28.44 - 42.01	.31 - .37	.20 - .35	.008 - .009	1.11 - 1.76

$(d_p)_p$ = 0.005 m. $(d_p)_m$ = 0.001 m.
$(d_b)_p$ and $(d_b)_m$ = 0.00254 to 0.00317 m.
P_{reqd} = 100.84 MPa (14635 psi.) to 109.17 MPa (15845 psi.).
$(Vol)_{N_2}$ = 33.89 to 35.98 vol. %.
$(Vol)_{C_4H_{10}}$ = 13.91 to 14.98 vol. %.
Adjusted total pressure for N_2 mixing = 15.16 MPa. (2201 psi.).
Adjusted total pressure for C_4H_{10} mixing = 14.03 MPa. (2034 psi.).
$(S_v)_p$ = 1.0.
$(S_v)_m$ = 1.92.

1. The design temperature is based on the expected operating conditions mentioned in Chapter 1.

2. The design pressure is greater than the normal operating pressure, so as to facilitate the use of the extrapolative method mentioned in Section 7.5 above. This may be necessary to adjust the bubble rise velocity by increasing the pressure.

3. The reactor is expected to operate under near isothermal conditions, due to the ebullieted nature of the process, and therefore the temperature gradient along the axis of the reactor is assumed to be negligible for the mechanical design.

4. It is recognized that, to study the actual kinetics of catalytic hydrotreating or hydrocracking, it is necessary to bring the process to the operating conditions (high temperature and pressure) before it contacts the catalyst. This is to avoid any catalytic effect during the start-up or transient period which may not be that important during the initial steady state kinetic studies. The catalyst will therefore be charged into the reactor through a lock-hopper system only after the feed reaches the operating conditions. This will be achieved by initially recirculating only the liquid and gas in the reactor, in the absence of the solid catalyst.

5. Since the recirculating stream is cooled before entering the reactor there will be a temperature difference between the gas-liquid inlet nozzle and the reactor. The temperature differential will depend on the extent to which the recirculating stream is cooled, recirculation ratio and the preheat temperatures of the inlet fresh liquid feed and hydrogen stream. Thus the gas-liquid nozzle will

have to be rechecked for thermal stresses when the operating parameters for the overall hydrotreating/hydrocracking system are finalized.

7.12.2 Design Codes

The reactor has been designed as per ASME Section VIII Division 9 (214) with requirements of part UHA (Requirements for pressure vessels constructed of high alloy steel.) being mandatory. Though detailed design calculations are not included here, the design has been also been checked for the following aspects.

1. Shell for internal pressure ((214) part UG, UA, UW).
2. Heads for internal pressure ((214) part UG, UA, UW).
3. Nozzles for reinforcements ((214) part UG, UW).
4. Flanges for special construction ((214) part UA, Appendix 1).

The gas and liquid distributers have been designed as per methods suggested by Richardson (215) and Litz (216).

7.13 Material Selection

The material of construction for the laboratory reactor has to be resistant to hydrogen. Hydrogen under various pressure and temperature conditions migrates through steel. For carbon steel, this has the effect of decarborizing the steel and forming methane gas, which does not continue to migrate through the steel, but continues to build up pressure. This attack occurs at the grain boundaries and makes the steel brittle and prone to cracking. Hydrogen attack of the vessel is not prevented by the corrosion resistant layer of high alloy which is not attacked but penetrated by hydrogen. Due to the high cost of many of the high alloy

steels, commercial reactors are fabricated of lower alloys containing chromium and molybdenum (eg. 2.25 % Cr-1 % Mo steel) and cladded with stainless steel plates (eg. 18 % Cr-8 % Ni), which are resistant to hydrogen penetration. Multi-layered wall constructions and hot-cold wall constructions have commonly been used for thick walled reactors. Typical dimensions of an industrial reactor with a TPEB (viz. H-Oil reactor) would be 21.65 m (71 ft) long, 4.0 m ID with wall thickness ranging up to 0.305 m (12 in.). Such large sized rectors can be successfully fabricated in cladded or multilayered construction. Due to the small diameter of the laboratory reactor (app. 0.15 m.), it will be difficult to carry out efficient internal cladding and therefore the material of construction is selected to be complete stainless steel with minimum allowable tensile strength of 141.25 MPa (20500 ksi) at 755 K. The material specifications for various components are presented in Table 7.4.

Table 7.4. Material Specifications

Material	Specification	Allowable Stress	Reference
plate	SA-240 type 304	141.25 MPa (20.5 ksi)	(217)
forging	SA-182 grade F304	141.25 MPa (20.5 ksi)	(218)
bolting	SA-193 grade 2H	137.8 MPa (20.0 ksi)	(219)
nuts	SA-194 2H	137.8 (20.0 psi)	(220)
pipe	SA-312 TP304	141.25 (20.5 ksi)	(221)
gasket	stainless steel	y=26000, m=6.5	(214)

7.14 Data Sheet and Material Specifications

A brief pressure vessel data sheet and material specification for the laboratory reactor is presented below.

Laboratory Reactor Data Sheet

1. Dimension of vessel: 0.1778 m ID x 4.44 m. lg.
2. Working pressure: 27.56 MPa (4000 psi.).
3. Working temperature: 755 K (900° F).
4. Design code: ASME Section VIII Division 1.
5. Construction: All welded.
6. Corrosion allowance: Nil.

7.15 Scale-up Procedure for Gas Distributor

One of the purpose of the similitude study is to be able to study the effect of grid configuration on the hydrotreating/hydrocracking process and to be able to scale-up the grid configuration for the large-scale design. Such a scale-up procedure is suggested below.

One of the requirements for the kinetics and hydrodynamics in both the reactors to be similar is that the bubble size in the two reactors should be equal. The volume of a bubble formed at a single orifice, before detaching from the orifice, in a gas-liquid system, is given by Equation ( ), which is reproduced below.

$$(V_E)^{5/3} = \frac{11}{192\pi\left(\frac{3}{4\pi}\right)^{2/3} g} Q^2 + \frac{3}{2\left(\frac{3}{4\pi}\right)^{1/3} g}\left(\frac{\mu_l Q {V_E}^{1/3}}{\rho_l}\right) + \frac{\pi D \sigma {V_E}^{2/3}}{g\rho_l}$$

The effect of gas density is neglected here. Though V_E represents the volume of a bubble, before detachment from a single orifice, and that too in a gas-liquid

system, as a first approximation, it has been used here to calculate the final volume of a bubble in a multiorifice system in a three-phase system. The assumption that V_E is approximately equal to V_T hold true if Q is small. V_T is the final volume of the bubble as it detaches from the liquid spout. In such a case, the growth of the primary bubble through coalescence with the secondary bubble is not appreciable. The value of Q can be restricted by adjusting the number of holes in the gas distributor.

Thus

$$V_E{}^{5/3} = A_B Q^2 + B_B V_E{}^{1/3} Q + C_B D V_E{}^{2/3} \tag{7.42}$$

where

$$A_B = \frac{11}{192\pi(\frac{3}{4\pi})^{2/3} g} \tag{7.43}$$

$$B_B = \frac{3}{2(\frac{3}{4\pi})^{1/3} g}(\frac{\mu_l}{\rho_l} \tag{7.44}$$

$$C_B = \frac{\pi\sigma}{g\rho_l} \tag{7.45}$$

Since

$$(\mu_l)_p = (\mu_l)_m \tag{7.46}$$

and

$$(\sigma_l)_p = (\sigma_l)_m \tag{7.47}$$

we have

$$(A_B)_m = (A_B)_p \tag{7.48}$$

$$(B_B)_m = (B_B)_p \tag{7.49}$$

and

$$(C_B)_m = (C_B)_p \tag{7.50}$$

If we maintain the size of the orifice same in both the reactors,

i.e.,

$$(D)_m = (D)_p \tag{7.51}$$

to have

$$(V_E)_m = (V_E)_p \tag{7.52}$$

the following equality should be fulfilled

$$\begin{gathered}(A_B)_m {Q_m}^2 + (B_B)_m {(V_E)_m}^{1/3} Q_m + (C_B)_m D_m {(V_E)_m}^{2/3} \\ = \\ (A_B)_p {Q_p}^2 + (B_B)_p {(V_E)_p}^{1/3} Q_p + (C_B)_p D_p {(V_E)_m}^{2/3}\end{gathered} \tag{7.53}$$

If

$$(Q)_m = (Q)_p \tag{7.54}$$

along with the equalities mentioned in Equations 7.46 to 7.48 are satisfied, the equality in Equation 7.46 is automatically fulfilled for all values of V_E.

Thus, if Equation 7.49 and Equation 7.52 are satisfied the volume of the bubbles in both the reactors could be *approximately* equal.

Assuming that the gas distributor is so designed that the rearranging resistance upstream of the distributor is much smaller than the resistance to flow across individual orifice, which ensures uniform flow across the distributor, we have

$$Q = \frac{\pi {d_r}^2 u_g}{4N} \tag{7.55}$$

where

N = number of orifices in the gas distributor.

Equation 7.47 implies that

$$\frac{\pi {(d_r)_p}^2 {(u_g)_p}^2}{4N_p} = \frac{\pi {(d_r)_m}^2 {(u_g)_m}^2}{4N_m} \tag{7.56}$$

and therefore

$$N_p = \frac{{(d_r)_p}^2 (u_g)_p N_m}{{(d_r)_m}^2 (u_g)_m} \tag{7.57}$$

Thus Equation 7.55 facilitates the calculation of number of orifices in the gas distributor, of the commercial reactor, so as to keep the bubble sizes in both the reactors are close to each other.

Sample calculations for determining N_p and the orifice spacing L are presented in Appendix H.

7.16 Summary

1. The reduction in reactor length by using the scale-down procedure can be 5 to 20 times, depending on the particle size used in the scaled-down reactor.

2. An attempt is made to adjust the space velocity in the laboratory reactor to achieve mass transfer, at the catalyst surface, similar to that in the commercial reactor by considering the degree of reduction of particle size d_p during the scale-down.

3. A method is proposed to scale-up the gas distributor so that the bubble characteristics in the scale-up reactor would be similar to those in the laboratory reactor.

4. The bubble rise velocity u_{br} in the laboratory reactor was adjusted by mixing a heavier gas such as nitrogen or butane with the hydrogen feed.

5. The procedure for scale down can be used in a reverse manner for scale-up or design of a commercial reactor. This implies that the data collected from the laboratory reactor can be used to design a new commercial reactor. Further, the field data from an existing commercial TPEB reactor, along with the procedure, correlations and model developed in this study can be used to improve the performance of the existing reactor.

CHAPTER 8

CONCLUSIONS AND RECOMMENDATIONS

8.1 Conclusions

The conclusions drawn from this study are noted below.

1. The new concept of bubble closure and coalescence of the primary bubble with the successive secondary bubbles was used to estimate the size of the bubbles in a high pressure TPEB reactor.

2. Correlations for effective bubble rise velocity in a high pressure TPEB reactor were developed by using hydrodynamic data for phase holdup in a TPEB and by extending the observations regarding the effect of gas density on drift flux.

3. A new mixing rule was formulated to predict the viscosity of a mixture, where the viscosity of the individual components of the mixture vary by a order of magnitude.

4. A procedure for scaling down a commercial scale TPEB reactor to a laboratory scale was proposed. This procedure ensured equality of phase holdups and bubble rise velocity in the two reactors, without changing the chemical identity of the process. The laboratory scale reactor can be used to carry out process development studies on hydrotreating and hydrocracking of heavy petroleum residues, bitumen and bitumen derived liquids.

8.2 Recommendations

1. The proposed bubble model predicts the volume of bubbles formed under constant flow conditions. The concept of bubble closure and bubble coalescence can be used to formulate a model to predict volumes of bubbles formed under varying plenum pressure.

2. The liquid motion induced around the bubble by the rapid formation and rise of the bubble at high gas flow should be taken into consideration to improve the prediction of the model at high gas flow.

3. To improve the prediction of the actual size of the bubbles in a TPEB reactor the following phenomena should be considered in the bubble model

   (a) Bubble to bubble interaction at the distributor and in the bed.

   (b) Bubble to particle interaction at the distributor and in the bed.

   However at high pressure the size of the bubble is expected to be small due to reduced bubble coalescence which will lead to lesser bubble breakage by particle impingement. This aspect should be considered before modifying the bubble model to be applicable to a high pressure TPEB.

4. The potential of the proposed bubble model can be extended to identify the gas flow conditions under which a jet rather than discreate bubbles could be formed at the orifice.

5. Measurements of gas axial dispersion in a TPEB reactor operating at atmospheric pressure and high pressure are needed to improve the u_{br} correlations. However the gas dispersion studies should be conducted in the same system used to generate the hydrodynamic data for the initial formulation of the correlations.

6. Experimental data for the physical properties of bitumen fractions and bitumen at high temperatures (beyond 373 K) are needed to improve the correlations in the predictive method. Special laboratory equipments and experimental techniques should be developed for this purpose.

7. The predictive method does not take into account the thermal cracking of bitumen at high temperatures. This simplification is applied on the presumption that, under the presence of high pressure hydrogen , the thermal cracking of bitumen is reduced.

   The predictive method can be improved by considering the effect of thermal cracking.

8. The predictive method does not consider the solubility of hydrogen in the liquid phase for the prediction of surface tension. Consideration of the vapor-liquid equilibria and hydrogen solubility will improve the surface tension predictions. However, determination of interaction parameters needed to apply vapor-liquid equilibria must be accurate, which may be difficult for this complicated multicomponent system.

   Otherwise, wrong values of interaction parameters may lead to results less accurate than the results got by neglecting the solubility of the phase as done in the present studies.

9. The proposed scale-down procedure ensures similar phase holdups and bubble rise velocity in the two reactor. A attempt was made to achieve similar mass transfer at the catalyst surface in the two reactors. However the transport phenomena at the bubble surface as well as between and inside the catalyst particles have to be studied in more details. This will enhance the application

of the scale-down procedure to study the process kinetics in the laboratory reactor.

APPENDIX A

GENERALIZED WAKE MODEL: COMPUTER CODE

```
c             program simi.f
c             this program calculates holdups for similitude
c             studies using generalized wake model and gives
c             results presented in tables 3.1, 3.2 and 3.3
c
c             dp    - equivalent catalyst particle dia.     (M)
c             densp - catalyst density.                     (KG/M3)
c             densl - liquid density.                       (KG/M3)
c             st    - liquid surface tension.               (N/M)
c             vis   - liquid viscosity.                     (KG/M-S)
c             t     - system temperature.                   (K)
c             p     - pressure.                             (KG/M-S2)
c             g     - gravitational acceleration.           (M/S2)
c             dr    - reactor diameter.                     (M)
c             sv    - space velocity.                       (1/HR)
c             ul    - superficial liquid velocity.          (M/S)
c             ug    - superficial gas velocity.             (M/S)
c             hl    - liquid holdup.                        (-)
c             hg    - gas holdup.                           (-)
c             hs    - solid holdup.                         (-)
c             utp   - particle terminal velocity in liquid. (M/S)
c             ui    - Richardson-Zaki intercept.            (M/S)
c             errg  - allowable error on gas holdup         (-)
c             bh    - bed height.                           (M)
c             be    - bed expansion.                        (%)
c             utb   - bubble terminal vel. in liquid        (M/S)
c
c
c             intializatoin

c
c             read the  parameters
c
      open(12,file='scale')
c      print*,'enter,dp,dr,densp,densl,st,vis,ul,ug'
c      read*,dp,dr,densp,densl,st,vis,ul,ug
c      print*,'INPUT VALUE OF ind'
c      print*,'INPUT ind=1 for entry # 1-4 in Table 3.1'
c      print*,'INPUT ind=2 for entry # 5-10 in Table 3.2'
c      read*, ind
      j=1
45    if(j .ne. 2)then
      densp=2489.
      densl=900.
```

```
      st=.0727
      vis=.00131
      dr=.2413
      if(j .eq. 1)then
      write(12,*)'START OF TABLE 3.1.'
      write(12,*)
      open(10,file='simidata1')
      l=10
      else
      write(12,*)'START OF TABLE 3.3'
      write(12,*)
      open(10,file='simidata3')
      l=12
      end if
      else
      write(12,*)'STRART OF TABLE 3.2'
      write(12,*)
      open(10,file='simidata2')
      l=5
      end if
      rewind(10)
      do 50 i=1,1
      if(j .ne. 2)then
      read(10,*)nr,dp,ul,ug
      else
      read(10,*)nr,dp,dr,densp,densl,st,vis,ul,ug
      end if
      if(j .eq. 1)then
      if(nr .le. 4)then
      ind=1
      else
      ind=2
      end if
      else
      ind=2
      end if
      hl=.5
      hg=.05
      errg=.001
      if(ind .eq. 1)then
      db=0.142*(ul**0.052)*(ug**0.248)*(vis**0.008)*(st**0.034)
      utbt=1
12    reb=(utbt*densl*db)/(visc)
      amob=(9.81*(vis**4))/((st**3)*densl)
      fac=reb*(amob**0.23)
      if(fac .lt. 6)then
      cdb=0.076*(fac**1.82)
      else if(fac .ge. 6 .and. fac .lt. 16.5)then
      cdb=1.25*(fac**0.26)
      else if(fac .ge. 16.5)then
      cdb=2.6
      else
      end if
      utb=(sqrt(((4./3.)*(9.81)*(db)*(densp-densl))/(cdb*densl)))
      if(abs(utbt-utb) .ge. 0.001)then
      utbt=utb
      go to 12
      else
      end if
      else if(ind .eq. 2)then
      utb=5.541*(ul**(-0.065))*(ug**0.339)*(vis**0.025)*(st**0.179)
      else
      end if
```

```
c
c
c             computations
c             calculation of minimum fluidization liquid
c             superficial velocity ulmf
      remfo = (sqrt(((33.7)**2.) + (0.0408)*(ar)) - 33.7)
      ulmfo = (remfo*vis)/(dp*densl)
      ulmf = (ulmfo*(1.-(376.*(ug**0.327)*(vis**0.227)
     +       *(dp**0.213)/((densp - densl)**(0.423)))))
c
c
c             calculation of particle terminal velocity
c
5     r = ((0.61 + (0.037/(hg + 0.013)))*((hg + hl)**3))
      utpt = 1.
10    rept = (utpt*dp*densl)/vis
      cd = (24./rept)+(6./(1. + sqrt(rept))) + .3
      utp=(sqrt(((4./3.)*(9.81)*(dp)*(densp-densl))/(cd*densl)))
      if(abs(utpt-utp) .ge. .001)then
      utpt = utp
      go to 10
      else
      end if
      if(dp .gt. .0026) then
      utp=.7*utp
      else
      end if
      utpp=utp
      ui = utp*(0.1**(dp/dr))
c
c             calculation of Richardson-Zaki exponent
c
15      rep = ((utp*dp*densl)/(vis))
      if(rep .lt. 0.2)then
      s = 4.65 + 20.*(dp/dr)
      else if (rep .ge. 0.2 .and. rep .lt. 1)then
      s = (4.4 + 18.*(dp/dr))/(rep**.03)
      else if (rep .ge. 1. .and. rep .lt. 200.)then
      s = (4.4 + 18.*(dp/dr))/(rep**.1)
      else if (rep .ge. 200. .and. rep .lt. 500)then
      s = (4.4/(rep**0.1))
      else
      s = 2.4
      end if
c
c
c             calculation of solid,liquid and gas holdups
c
11    a = (ui/((ug/hg) - (ul/hl)))
      if(abs(a) .lt. 1.14)then
      x = 1- 0.877*(ui/((ug/hg) - (ul/hl)))
      else
      x = 0
      end if
      vgl = utb
      hkt = r*hg
      hlft=((ul-((r*ug)*(1.-x)))/(utp*(1.-hg-hkt)))**(1./s)
      vgt=(ul+ug+(hlft*(1.-hg-hkt)*(vgl)))/(hg+hl)
      hlt=hkt*(1.-x) + hlft*(1.- hg-hkt +(x*hkt))
      hlt1=hlt
      hlt = (hlt + hl)/2.
      hgt=(ug/vgt)
      hgavg=hgt
      hst=1. - hlt - hgavg
      p1=hl - hlt
      p2=hg -hgavg
```

```
      if(abs(p1) .ge. errg .or. abs(p2) .ge. errg)then
      hl=hlt
      hg=hgavg
      go to 5
      else
      hl=hltl
      hg=hgavg
      hs=1. - hl - hg
      end if
c     Calculating the coefficient for practicle scale-down
c
      chn=((ul-r*ug)/(ui*(1.-hg-hkt)))**(1/s)
c
       write(12,*)'ind=',ind,' nr=',nr,' hl=',hl,' hg=',hg,' chn=',chn,
     + ' utb=',utb
50     continue
c      400      continue
       write(12,*)'-------------------------------------------------'
       write(12,*)
       write(12,*)
       j=j+1
       if(j .le. 3)then
       go to 45
       else
       end if
       stop
       end
```

APPENDIX B

COMPUTER CODES FOR THE BUBBLE MODEL

```
c     program bub1.f for single bubble diameter at an orifice in
c     two phase system at low and medium flow when only single
c     secondary, which is a hemisphere merges with the primary.
      double precision do,densl,densg,st,vis,ql,ro,ve,vel,
     +re,rel,vex,the,dthedt,delt,delvd,v
     +,h,hl,g,t,y,a2,b2,c2,e2,g2,tc,velo,z,zz,x
     +,ao,difft,we,rin,diffthe,thein,yl,ains,qins
     +,vins,vic
      open(12,file='bub1')
      print*,'input do(cm),densl(gm/cm3),densg(gm/cm3),st(dyn/cm),vis(P)
     +,ql(cm3/sec),volbubexp(cm3)'
      read*,do,densl,densg,st,vis,ql,volbubexp
      f=1.
      ro=do/2
c
c     Inputing the estimate of ve
c
      ve=1.
c
c     Calculating volume ve of bubble at the end of expansion stage
c
5     vel=(.1019366/(densl-densg))*(((.024179897*vis*ql)*(
     +  1./((ve**.333333))))+(.031416*f*do*st
     +  )+((.000473878*(.6875*
     +  densl+densg)*(ql**2))/(ve**.666666)))
      if(ve-vel .ge. 1.D-12)then
      i=i+1
      if(i .ge. 50)then
      print*,'no. of iteration i exceeded 50'
      stop
      else
      end if
      ve=(ve+vel)/2.
      go to 5
      else
      end if
      ve=vel
      rt=((.237318*ve)**.333333)
c
c     Calculating the radius of bubble re at end of expansion stage
c
      re=1
15    rel=((.2387318*(ve+1.0472*((re-(sqrt((re**2.)
     +  -(ro**2.))))**2.)*(2.*re+(sqrt((re**
     +  2.)-(ro**2.))))))**.333333)
      if(abs(rel-re) .ge. 1.D-12)then
      l=l+1
      if(l .ge. 1500)then
```

```
      print*,'no. of iteration l exceeded 1500'
      stop
      end if
      re=rel
      go to 15
      else
      end if
      re=rel
c
c     Calculating theta
c
      the=asin(ro/re)
c
c     Calculating the angular closing velocity of bubble
c
      delthe=-the
      dthedt=-(3.1416-the)*(ql/ve)
c
c     Calculating the bubble closing time
c
      delt=delthe/dthedt
c
c     Calculating the initial area of bubble throat
c
      ao=3.1416*(ro**2.)
      difft=0
      we=dthedt
      vins=ve
      rin=re
c
c     Increamenting time in steps
c
18    difft=difft+(.01*delt)
c
c     Noting time elasped at any instant
c
      t=difft
c
c     Calculating angle closed
c
      diffthe=we*difft
c
c     Calculating instanteneous angle theta - yet to close
c
      thein=-the+diffthe
      yl=rin*sin(thein)
c
c     Calculating the instanteneous area of throat
c
      ains=3.1416*(yl**2.)
c
c     Calculating instanteneous flow rate through the
c     constricting throat
      qins=(ql/2.)*(ains/(ao+ains))
c
c     Calculating instateneous volume of bubble
      vins=vins+(qins*.01*delt)
      if(difft .lt. delt)then
      go to 18
      else
c
c     Volume of bubble immediately after closure
c
```

```
      vic=vins
      end if
c
c     Calculating flow into primary and secondary if
c     secondary was formed
c
      delvd=(ql*.5)*delt
      v=ve+delvd
      t=delt
      vex=ve
c
c     Calculating volume of secondary
c
      vl=(ql/2.)*t
c
c     Calculating radius of secondary when it is smaller
c     than an hemisphere
c
      vmark=2.0944*(ro**3.)
      if(vl .gt. vmark)then

      m=1
      else
      end if
      rl=re
25    if(m .eq. 1)then
26    rll=((.2387318*(vl+1.0472*((rl-(sqrt(
     +  (rl**2.)-(ro**2.))))**2.)*(2.*rl+(sqrt
     +  ((rl**2.)-(ro**2.)))))**.333333)
      j2=0
      if(abs(rll-rl) .ge. 1.D-12)then
      j2=j2+1
      if(j2 .ge. 50)then
      print*,'no. of iterartion j2 exceeded 50'
      stop
      else
      end if
      rl=rll
      go to 26
      else
      end if
      rl=rll
c
c     Calculating height h of the secondary bubble
c
      hl=abs(sqrt((rl**2.)-(ro**2.)))
      h=2.*rl-hl
      if(c .ge. 2)then
      ql=2.*ql
      else
      end if
c
c
      else
      t=delt
c      rl=re
27    hl=((.6366182*(.5*ql))/(ro**2.))*(t-((
     +  .5236*(h**3.))/(.5*ql)))
      print*,'hl=',hl
      j2=0
      if(abs(h-hl) .ge. 1.D-12)then
      j2=j2+1
```

```
      print*,'j2=',j2
      if(j2 .ge. 50)then
      print*,'no. of iterartion j2 exceeded 50'
      stop
      else
      end if
      h=hl
      go to 27
      else
      end if
      h=hl
      end if
c
c     Calculating the approximation factor for the
c     bubble when it is growing
c
      g=((v+ve)/(2.*ve))
c
c     Handling the single primary bubble formation,
c     when there is no coalescence between secondary
c
      if(c .lt. 2)then
      t=0
      vex=ve
c      vx=ve
     else
     end if
c
c     Calculating factors for detachment stage
c
      y=(((re**4.)*cos(the))/(2.*ro*t*(ql/2.)))*
     +  (cos(the)*(the-((2.*ro*(ql/2.)*t)/((re**
     +  4.)*cos(the))))-cos(the))
      a2=1.+((11.69335*g*(vex**.333333)*vis)/
     + ((ql/2.)*(.6875*densl+densg)))
      b2=(((densl-densg)*981.)/((ql/2.)*(.6875*
     +  densl+densg)))
      c2=((3.1416*do*st*f)/((ql/2.)*(.6875*
     +  densl+densg)))
      e2=.0689277*(ql/2.)
      g2=((2.4179897*vis)/((.6875*densl+
     +  densg)))
      tc=vex+(.5*ql*t)
      velo=(((b2/(a2+1.))*((tc
     +  )-((ve/tc)**(a2))*ve))-((c2/(a2
     +  ))*((1.)-((ve/tc)**
     +  (a2))))-((g2/(a2-.333333))*
     +  ((tc**(-.333333))-((ve/tc)**(a2
     +  ))*(ve**(-.333333))))-((e2/(a2-.666666))*((tc**(-
     +  .666666))-((ve/tc)**(a2))*(ve**(-.666666)))))
      z=tc
c
c      Calculating the distance traveled by bubble
c      during the detachment stage
c
40    zz=(b2/(2*(ql/2.)*(a2+1.)))*((z**2)-(ve**2))-
     +  (c2/(a2*(ql/2.)))*(z-ve)-((3.*g2)/(2.*(ql/2.)*(a2
     +  -.333333)))*((z**.666666)-(ve**.666666))
     +  -((3.*e2)/((ql/2.)*(a2-.666666)))*((z**.333333
     +  )-(ve**.333333))
      x=zz
      if(x .lt. 0.)then
      xin=(1./((ql/2.)*(1.-a2)))*((z**(1.-a2))-(ve**(1.
     +  -a2)))*((b2/(a2+1.))*(ve**(a2+1.))-((c2/a2)*(
     +  ve**a2))-((g2/(a2-.333333))*(ve**(a2-.333333)))
     +  -((e2/(a2-.666666))*(ve**(a2-.666666))))
```

```
      x=x-xin
      else
      end if
      if(c .ge. 2)then
c
c     Making half flow enter the primary and half into secondary
c
      if(m .eq. 1)then
      q1=q1/2.
      else
      end if
      else
      end if
      if(c .ge. 2)then
      go to 80
      else
      end if
      x1=(velo/2)*delt
      if(x .gt. h)then
c
c     Checking whether there is coalescence between primary
c     and first secondary
c
      c=1
      write(12,*)'NO COALESCENCE'
      write(12,*)'ve=',ve
      write(12,*)'vic=',vic
      write(12,*)'dthedt=',dthedt
      stop
      else
      c=2
      write(12,*)'COALESCENCE'
      end if
      if(c .ge. 2)then
c
c     Monitoring the growth of secondary
c
60    if(m .eq. 1)then
      t=1.*delt
      else
      t=.1*delt
      end if
      v1=(q1/2)*t
      vx=ve
      c=3
c
c     Going to statement 25 to calculate the radius of
c     the hemispherical bubble
c
      if(m .eq. 1)then
      go to 26
      else
      go to 27
      end if
c
c     Checking the distance between the boundaries of the
c     primary and secondary
c
80    if(h-x .ge. (x/10000.))then
      is1=is1+1
      if(is1 .ge. 10000)then
      print*,'no. of iterations is1 exceeded 10000'
      stop
      else
```

```
c
c     Increamenting time in smaller steps to monitor the stage
c     where primary and secondary seperate
c
      t=t+(.05*delt)
c
c     For better accuracy shortening the step
c
c      t=t+(.0005*delt)
      if(m .eq. 1)then
      go to 26
      else
      go to 27
      end if
c      go to 25
      end if
      else
      tm1=t
      write(12,*)'time for first collision tm1=',t
      write(12,*)'delt=',delt
      vadd=(ql/2.)*tm1
      vfinal=vic+vadd
      write(12,*)'diameter of orifice (cm)=',do
      write(12,*)'density of liquid (gm/cm3)=',densl
      write(12,*)'density of gas (gm/cm3)=',densg
      write(12,*)'surface tension (dyn/cm)=',st
      write(12,*)'viscosity of liquid (P)=',vis
      write(12,*)'flow rate at orifice (cm3/sec)=',ql
      write(12,*)'final vol. of bubble vfinal=',vfinal
      write(12,*)'experimental vol. of bubble=',volbubexp
      write(12,*)'vol. of bubble in expansion stage ve=',ve
      write(12,*)'radius of bubble in expansion stage re=',re
      write(12,*)'distance for detachment x=',x
      write(12,*)'height of secondary h=',h
      write(12,*)'total time for formation of bubble tm1=',tm1
      write(12,*)'time for closing of primary delt=',delt
      end if
      else
      end if
      stop
      end
```

```
c     program bub2.f for single bubble diameter at an orifice in
c     two phase system at high flow rate when multiple
c     secondaries merge.
      double precision do,densl,densg,st,vis,ql,ro,ve,vel,
     +re,rel,vex,the,dthedt,delt,delvd,b,v
     +,h,hl,g,t,y,a2,b2,c2,e2,g2,tc,velo,z,zz,rll,x
     +,tml,vp,rp,res,vs,vls,ts,
     + a2s,tcs,zzs,xs,xins,gs,hs,v
     +,ao,difft,we,rin,diffthe,thein,yl,ains,qins
     +,vins,vic
      open(12,file='bub2')
      f=1.
      fl=1.
      f2=1.
      print*,'input do(cm),densl(gm/cm3),densg(gm/cm3),st(dyn/cm),vis(P)
     +,ql(cm3/sec),volbubexp(cm3)'
      read*,do,densl,densg,st,vis,ql,volbubexp
      b=1.
      re=1.
      ro=do/2
c
c     Inputing the estimate of ve
c
      ve=1.
5     vel=(.1019366/(densl-densg))*(((.024179897*vis*ql)*(
     +  b/((ve**.333333))))+(.031416*f*do*st
     +  )+((.000473878*(.6875*
     +  densl+densg)*(ql**2))/(ve**.666666)))
      if(ve-vel .ge. 1.D-12)then
      i=i+1
      if(i .ge. 50)then
      print*,'no. of iteration i exceeded 50'
      stop
      else
      end if
      ve=(ve+vel)/2.
      go to 5
      else
      end if
      ve=vel
      rt=b*((.237318*ve)**.333333)
c
c     Calculating the radius of bubble re at end of expansion
c     stage
c
      re=1.
15    rel=((.2387318*(ve+1.0472*((re-(sqrt((re**2.)
     +  -(ro**2.))))**2.)*(2.*re+(sqrt((re**
     +  2.)-(ro**2.))))))**.333333)
      if(abs(rel-re) .ge. 1.D-12)then
      l=l+1
      if(l .ge. 1500)then
      print*,'no. of iteration l exceeded 50'
      stop
      end if
      re=rel
      go to 15
      else
      end if
      re=rel
c
c     Calculating theta
c
      the=asin(ro/re)
c
```

```
c     Calculating the angular closing velocity of bubble
c
      delthe=-the
      dthedt=-(3.1416-the)*(ql/ve)
c
c     Calculating the bubble closing time
c
      delt=delthe/dthedt
c
c     Calculating the initial area of the bubble throat
c
      ao=3.1416*(ro**2.)
      difft=0
      we=dthedt
      vins=ve
      rin=ro
c
c     Increamenting time in steps
c
18    difft=difft+(.01*delt)
c
c     Calculating the angle closed
c
      diffthe=we*difft
c
c     Calculating instanteneous theta - yet to close
c
      thein=the-diffthe
      y1=rin*sin(thein)
c
c     Calculating instanteneous area of throat
c
      ains=3.1416*(y1**2.)
c
c     Calculating instanteneous flow rate through the
c     constricting throat
c
      qins=(ql/2.)*(ains/(ao+ains))
c
c     Calculating instanteneous volume of bubble
c
      vins=vins+(qins*.01*delt)
      ravg=ravg+(y1*.01*delt)
      if(difft .le. delt)then
      go to 18
      else
      davg=2.*(ravg/delt)
c
c     Volume of bubble immediately after closing
c
      vic=vins
      end if
      delvd=(ql*.5)*delt
c      vet=(4.18888*(re**3.)-1.0472*((re-(rd**.5))
c     +  **2.)*(2.*re+(rd**.5)))
      v=ve+delvd
      t=delt
      vex=ve
c
c     Calculating volume of secondary
c
      v1=(ql/2.)*t
c
c     Approximating height of secondary
c
      h=(.2387318*v1)**(.333333)
```

```
c
c     Bypassing multi-bubble dynamics for first pass
c
      go to 35
      rl=re
c
c     Handling multi-bubble phenomena
c
c     Calculating height of truncated sphere
c
25    hl=((.6366182*(.5*ql))/(ro**2.))*(t-((
     +  .5236*(h**3.))/(.5*ql)))
      j2=0
      if(abs(hl-h) .ge. 1.D-12)then
      j2=j2+1
      if(j2 .ge. 50)then
      print*,'no. of iterations exceeded 50'
      stop
      else
      end if
      h=hl
      go to 25
      else
      if(hl .ge. .3*ro)then
      rl=ro
28    vl=2.1*(.666666)*3.1416*(ro**3.)
      t=(2*vl)/ql
c
c     Checking whether the secondary has grown beyond
c     ve (this is for both loops, (1) loop coming
c     through statement 25 and (2) loop starting
c     at statement 30
c
30    if(vl .ge. ve)then
      d=1
      res=1.
c
c     Registering number of secondary merging the primary
c
      is=is+1
      vp=(is+1)*ve
c
c     Calculating radius of bubble when its shape is
c     below an hemisphere
c
32    rp=((.2387318*(vp+1.0472*((res-(sqrt((res**2.)-
     + (ro**2.))))**2.)*(2.*res+(sqrt((res**2.)-(ro**
     + 2.))))))**.333333)
      if(abs(rp-res) .ge. 1.D-12)then
      ls=ls+1
      if(ls .ge. 1500)then
      print*,'no. of iterartions ls exceeded 1500'
      stop
      end if
      res=rp
      go to 32
      else
      end if
      vs=vp+(vic-ve)
c
c     Recording closing time of primary bubble for
c     multi bubble phenomena
c
      ts=delt
c
c     Calculating volume entering multi bubble assembly
```

```
c     before the merged secondary closes
c
      vls=(ql/2)*ts
33    rlls=(.2387318*vls)**(.333333)
      hs=2.*rlls
c
c     Calculating the approximate factor for subsequent
c     secondaries - in multi bubble phenomena
c
      gs=((vs+ve)/(2.*ve))
c
c     Calculating 'a' for the rising assembly - in
c     multi bubble phenomena
c
      a2s=1.+((11.69335*gs*(vp**.333333)*vis)/((ql
     + /2.)*(.6875*densl+densg)))
c
c     Monitoring the volume of rising assembly
c     as half the flow enters the assembly
c
      tcs=vp+(ql/2)*ts
c
c     Calculating the distance travelled by assembly
c
      zzs=(b2/(2.*(ql/2.)*(a2s+1.)))*((tcs**2)-(vp
     + **2.))-(c2/(a2s*(ql/2.)))*(tcs-vp)-((3.*g2)
     + /(2.*(ql/2.)*(a2s-.333333)))*((tcs**.666666)
     + -(vp**.666666))-((3.*e2)/((ql/2.)*(a2s-.666666
     + )))*((tcs**.333333)-(vp**.333333))
      xs=zzs
      xsl=xs
      if(xs .lt. 0.)then
      xins=(1./((ql/2.)*(1.-a2s)))*((tcs**(1.-a2s))-
     + (ve**(1.-a2s)))*((b2/(a2s+1.))*(ve**(a2s+1.))
     + -((c2/a2s)*(ve**a2s))-((g2/(a2s-.333333))*(
     +  ve**(a2s-.333333)))-
     + ((e2/(a2s-.666666))*(ve**(a2s-.666666))))
      xs=xs-xins
      xs2=xs
      else
      end if
      if(xs .ge. hs)then
      cs=1
      write(12,*)'hs=',hs
      write(12,*)'xs=',xs
      write(12,*)'no. coelescense after growth'
      vfinal=vs
      write(12,*)'vfinal=',vfinal
      write(12,*)'is=',is,'x=',x,'re=',re
      write(12,*)'dthedt=',dthedt
      stop
      else
      cs=2
c
c     Restarting monitoring the growth of primary
c
      h=0
      vex=vp
      go to 60
      end if
      else
      end if
      rll=(.2387318*vl)**(.333333)
      hrl=abs(sqrt((rll**2.)-(ro**2.)))
      h=2*rll-hrl
      hl=h
```

```
      h=f2*h
      go to 35
      else
      end if
      end if
      h=hl
c
c     Calculating the approximation factor for the bubble
c     when it is growing
c
35    g=((v+ve)/(2.*ve))
c
c     Handling the single primary bubble formation in first
c     pass
c
      if(c .lt. 2)then
      t=delt
      vx=ve
      else
      end if
c
c     Calculating factors for detachment stage for first pass
c
      y=(((re**4.)*cos(the))/(2.*ro*t*(ql/2.)))*
     +  (cos(the)*(the-((2.*ro*(ql/2.)*t)/((re**
     +  4.)*cos(the))))-cos(the))
      a2=1.+((11.69335*g*(vex**.333333)*vis)/
     + ((ql/2.)*(.6875*densl+densg)))
      b2=(((densl-densg)*981.)/((ql/2.)*(.6875*
     +  densl+densg)))
      c2=((3.1416*davg*st*f)/((ql/2.)*(.6875*
     +  densl+densg)))
      e2=.0689277*(ql/2.)
      g2=((2.4179897*vis)/((.6875*densl+
     +  densg)))
      tc=vex+(ql/2.)*t
      velo=(((b2/(a2+1.))*((tc
     +  )-((ve/tc)**(a2))*ve))-((c2/(a2
     +  ))*((1.)-((ve/tc)**
     +  (a2))))-((g2/(a2-.333333))*
     +  ((tc**(-.333333))-((ve/tc)**(a2
     +  ))*(ve**(-.333333))))-((e2/(a2-.666666))*((tc**(-
     +  .666666))-((ve/tc)**(a2))*(ve**(-.666666)))))
      z=tc
40    zz=(b2/(2*(ql/2.)*(a2+1.)))*((z**2)-(vex**2))-
     +  (c2/(a2*(ql/2.)))*(z-vex)-((3.*g2)/(2.*(ql/2.)*(a2
     +  -.333333)))*((z**.666666)-(vex**.666666))
     +  -((3.*e2)/((ql/2.)*(a2-.666666)))*((z**.333333
     +  )-(vex**.333333))
      x=zz
      if(x .lt. 0.)then
      xin=(1./((ql/2.)*(1.-a2)))*((z**(1.-a2))-(vex**(1.
     +  -a2)))*((b2/(a2+1.))*(vex**(a2+1.))-((c2/a2)*(
     +  vex**a2))-((g2/(a2-.333333))*(vex**(a2-.333333)))
     +  -((e2/(a2-.666666))*(vex**(a2-.666666))))
      x=x-xin
      else
      end if
      if(c .ge. 2)then
      go to 80
      else
      end if
c      xl=(velo/2)*delt
      if(x .gt. h)then
c
c     Checking whether there is coalescence between primary
```

```
c     and secondary
c
      c=1
      print*,'x=',x,'h=',h
      write(12,*)'NO COALESCENCE'
      write(12,*)'ve=',ve
      write(12,*)'vic=',vic
      write(12,*)'dthedt=',dthedt
      stop
      else
      c=2
      write(12,*)'COALESCENCE'
      h=0
      end if
c
c     Monitoring the growth of subsequent secondary
c     multi bubble
c
      if(c .ge. 2)then
c
c     Increamenting time for multi bubble coalescence
c
60    t=.01*delt
c
c     Calculating the volume of gas that has entered
c     the secondary since its growth
c
61    vl=((ql/2)*t)
      vx=ve
      c=3
c
c     Checking if secondary has grown above a
c     hemisphere or not
c
70    if(h .ge. .3*ro)then
c
c     Going to statement 30 because the bubble is
c     below hemisphere
c
      go to 30
      else
c
c     Going to statement 25 because the bubble is
c     above an hemisphere ie. truncated sphere
c
      go to 25
      end if
c
c     Checking the distance between the boundaries of primary
c     and secondary
c
80    if(h-x .ge. (x/10000.))then
      isl=isl+1
      if(isl .ge. 10000)then
      print*,'no. of iterations isl exceeded 10000'
      stop
      else
c
c     Increamenting the value of 't' to be used
c     in statement 61
c
      t=t+(.1*delt)
      go to 61
      end if
      else
      tml=t
```

```
vfinal=ve*(is+1)+(ql*tml)+(vic-ve)
vfinal1=ve*(is+1)+2*vl+(vic-ve)
vefull=ve*(is+1)
vsecondary=ql*tml
vclosing=(vic-ve)
write(12,*)'diameter of orifice (cm)=',do
write(12,*)'density of liquid (gm/cm3)=',densl
write(12,*)'density of gas (gm/cm3)=',densg
write(12,*)'surface tension (dyn/cm)=',st
write(12,*)'viscosity of liquid (P)=',vis
write(12,*)'flow rate at orifice (cm3/sec)=',ql
write(12,*)'final vol. of bubble vfinal=',vfinal
write(12,*)'experimental vol. of bubble=',volbubexp
write(12,*)'vol. of bubble in expansion stage ve=',ve
write(12,*)'radius of bubble in expansion stage re=',re
write(12,*)'distance for detachment x=',x
write(12,*)'height of secondary h=',h
write(12,*)'no. of secondary entering primary is=',is
write(12,*)'total time for formation of bubble tml=',tml
write(12,*)'time for closing of primary delt=',delt
end if
else
end if
stop
end
```

APPENDIX C

DETERMINING BUBBLE RISE VELOCITY IN THREE PHASE EBULLIETED BED COMPUTER CODE

```
c             program ubr.f
c             this program calculates the optimum bubble rise
c             velocity for calculation of ubr correlation
c
c
c             dp    - equivalent catalyst particle dia.      (M)
c             densp - catalyst density.                      (KG/M3)
c             densl - liquid density.                        (KG/M3)
c             st    - liquid surface tension.                (N/M)
c             vis   - liquid viscosity.                      (KG/M-S)
c             t     - system temperature.                    (K)
c             p     - pressure.                              (KG/M-S2)
c             g     - gravitational acceleration.            (M/S2)
c             dr    - reactor diameter.                      (M)
c             ul    - superficial liquid velocity.           (M/S)
c             ug    - superficial gas velocity.              (M/S)
c             hl    - liquid holdup.                         (-)
c             hg    - gas holdup.                            (-)
c             hs    - solid holdup.                          (-)
c             utp   - particle terminal velocity in liquid.  (M/S)
c             ui    - Richardson-Zaki intercept.             (M/S)
c             errg  - allowable error on gas holdup          (-)
c             utb   - bubble rise velocity                   (M/S)
c
c
c             intializatoin

c
c             read the  parameters
c
c
      print*,'Which data to be read'
      print*,'Input data=1, for Armstrong data with dp=5 mm.'
      print*,'Input data=2, for Armstrong data with dp=3 mm.'
      print*,'Input data=3, for Armstrong data with dp=1 mm.'
      print*,'Input data=4, for Armstrong data with dp=.5 mm.'
      print*,'Input data=5, for H-coal data,with cat.-water-N2'
      print*,'Input data=6, for H-coal data,with cat.-kerosene-helium'
      read*,data
      if(data .eq. 1)then
      open(10,file = 'dta5',status='old')
      rewind(10)
      else if(data .eq. 2)then
      open(10,file = 'dta3',status='old')
```

```
      rewind(10)
      else if(data .eq. 3)then
      open(10,file = 'dta1',status='old')
      rewind(10)
      else if(data .eq. 4)then
      open(10,file = 'dta.5',status='old')
      rewind(10)
      else if(data .eq. 5)then
      open(10,file = 'dtv2.64',status='old')
      rewind(10)
      else if(data .eq. 6)then
      open(10,file = 'dtvfluxkero',status='old')
      rewind(10)
      else
      end if
      do 400 id=1,269
2      read(10,*)nr,ul,ug,hlexp,hgexp
c
c      Defining density of particle
c
      if(data .eq. 1)then
      dp=5.
      densp=2.48968
      dr=.2413
      else if(data .eq. 2)then
      dp=3.
      densp=2.49610
      dr=.2413
      else if(data .eq. 3)then
      dp=1.
      densp=2.96162
      dr=.2413
      else if(data .eq. 4)then
      dp=.5
      densp=2.48968
      dr=.2413
      else if(data .eq. 5)then
c      open(10,file='dtv2.64',status='old')
c      rewind(10)
      dp=2.64
      densp=1.63
      dr=.15
      else if(data .eq. 6)then
      dp=2.64
      densp=1.63
      dr=.15
      else
      end if
c      do 400 id=1,269
c     2     read(10,*)nr,ul,ug,hlexp,hgexp
      ulf=ul
      ugf=ug
      dpf=dp/304.8
c
      if(data .le. 4)then
c
c      Data for Armstrong experiment
c
      densl=1.
      st=72.7
      vis=1.31
c      stl=.160453
c      visl=.000879
c
```

```
      else if(data .eq. 5)then
c
c     Data for H-Coal water
c
      densl=1.
      st=72.7
      vis=1.
c      visl=.000670992
c      stl=.1665832
c
      else if(data .eq. 6)then
c
c     Data for Kerosene
c
      densl=.79
      st=28.6
      vis=1.39
c      stl=.063103
c      visl=.000939853
      else
      end if
      hl=.5
      hg=hgexp
      errg=.001
      ul=ul*.3048
      ulp=ul
      ug=ug*.3048
      ugp=ug
      vis=vis/1000.
      st=st/1000.
      densl=densl*1000.
      densp=densp*1000.
      denspp=densp
      dp=dp/1000.
      dpp=dp
      open(11,file='ubropt')
c
c
c             calculation of particle terminal velocity
c
5      r = ((0.61 + (0.037/(hg + 0.013)))*((hg + hl)**3))
      utpt = 1.
10    rept = (utpt*dp*densl)/vis
      cd = (24./rept)+(6./(1. + sqrt(rept))) + .3
      utp=(sqrt(((4./3.)*(9.81)*(dp)*(densp-densl))/(cd*densl)))
      if(abs(utpt-utp) .ge. .001)then
      i= i+1
      if(i .ge. 1200)then
      print*,'number of iteration i exeeded 1200'
      stop
      end if
      utpt = utp
      go to 10
      else
      end if
      if(dp .gt. .0025)then
      utp=.7*utp
      else
      end if
      ui = utp*(0.1**(dp/dr))
c
c
c             calculation of Richardson-Zaki exponent
c
15      rep = ((utp*dp*densl)/(vis))
```

```
      if(rep .lt. 0.2)then
      s = 4.65 + 20.*(dp/dr)
      else if (rep .ge. 0.2 .and. rep .lt. 1)then
      s = (4.4 + 18.*(dp/dr))/(rep**.03)
      else if (rep .ge. 1. .and. rep .lt. 200.)then
      s = (4.4 + 18.*(dp/dr))/(rep**.1)
      else if (rep .ge. 200. .and. rep .lt. 500)then
      s = (4.4/(rep**0.1))
      else
      s = 2.4
      end if
c
c
c             calculation of solid,liquid and gas holdups
c
11    a = (ui/((ug/hg) - (ul/hl)))
      if(abs(a) .lt. 1.14)then
      x = 1- 0.877*(ui/((ug/hg) - (ul/hl)))
      else
      x = 0
      end if
      hkt = r*hg
      hlft=((ul-((r*ug)*(1.-x)))/(ui*(1.-hg-hkt)))**(1./s)
      hlt=hkt*(1.-x) + hlft*(1.- hg-hkt +(x*hkt))
      hlt1=hlt
      hlt = (hlt + hl)/2.
      vgt=ug/hg
      hgavg=hge
      hst=1. - hlt - hgavg
      p1=hl - hlt
      p2=hg -hg
      if(abs(p1) .ge. errg .or. abs(p2) .ge. errg)then
      hl=hlt
      j=j + 1
      if(j .ge. 1400)then
      print*,'number of iteration j exceeded 1400'
      stop
      end if
      go to 5
      else
      hl=hlt1
      hg=hg
      hs=1. - hl - hg
      utb=(vgt*(hg+hl)-ul-ug)/(hlft*(1.-hg-hkt))
      utbmaster=utb
      end if
c      write(11,*)'nr=',nr,'  dpp=',dpp,'  ul=',ulp,'  ug=',ugp
c      write(11,*)'ulf=',ulf,'ugf=',ugf,'ulmf=',ulmf,'ugmf=',ugmf
c      write(11,*)'dpm=',dpm,'denspp=',denspp,'denspm=',denspm
c      write(11,*)'hl=',hlp,'  hle=',hlexp,'  hla=',hlast,'  hlk=',hlkim
c      write(11,*)'-----------------------------------------------'
      write(11,*)ulp,',',ugp,',',dpp,',',utbmaster
400   continue
      stop
      end
```

```
c             program flux.f
c             this program calculates holdups, drift flux
c             for studying effect of pressure on ubr
c
c             dp    - equivalent catalyst particle dia.     (M)
c             densp - catalyst density.                     (KG/M3)
c             densl - liquid density.                       (KG/M3)
c             st    - liquid surface tension.               (N/M)
c             vis   - liquid viscosity.                     (KG/M-S)
c             t     - system temperature.                   (K)
c             p     - pressure.                             (KG/M-S2)
c             g     - gravitational acceleration.           (M/S2)
c             dr    - reactor diameter.                     (M)
c             sv    - space velocity.                       (1/HR)
c             ul    - superficial liquid velocity.          (M/S)
c             ug    - superficial gas velocity.             (M/S)
c             hl    - liquid holdup.                        (-)
c             hg    - gas holdup.                           (-)
c             hs    - solid holdup.                         (-)
c             utp   - particle terminal velocity in liquid. (M/S)
c             ui    - Richardson-Zaki intercept.            (M/S)
c             errg  - allowable error on gas holdup         (-)
c             bh    - bed height.                           (M)
c             be    - bed expansion.                        (%)
c             utb   - bubble terminal vel. in liquid        (M/S)
c
c
c             intializatoin

c
c             read the  parameters
c
      open(12,file='drift')
      g=9.81
      rvol=83.14
      t=298.15
      ap=14.6961
c      ap=3000.
      apb=ap/14.5038
      print*,'INPUT SYSTEM NUMBER'
      print*,'INPUT system=1 IF SYSTEM IS GLASS BEADS - WATER - AIR
     +with dp=1 mm.'
      print*,'INPUT system=2 IF SYSTEM IS GLASS BEADS - WATER - AIR
     +with dp=5 mm.'
      print*,'INPUT system=3 IF SYSTEM IS CATALYST - KEROSENE - HELIUM
     +with dp=2.64 mm.'
      read*,system
      if(system .eq. 1)then
      open(10,file='dtaflux1',status='old')
      dp=.001
      dr=.2413
      densp=2961.62
      densl=1000.
      vis=.00131
      st=.0727
      amwair=28.964
      apcair=37.69291
      atcair=132.45
      call rks(amwair,apcair,atcair,rvol,t,apb,rhog)
      else if(system .eq. 2)then
      open(10,file='dtaflux5',status='old')
      dp=.005
      dr=.2413
      densp=2489.684
c      densp=2961.62
      densl=1000.
```

```
      vis=.00131
      st=.0727
      amwair=28.964
      apcair=37.69291
      atcair=132.45
      call rks(amwair,apcair,atcair,rvol,t,apb,rhog)
      else if(system .eq. 3)then
      open(10,file='dtvfluxkero',status='old')
      dp=.00264
      dr=.15
      densp=1630.
      densl=790.
      vis=.00139
      st=.0286
      amwhe=4.00
      apche=2.27
      atche=5.2
      call rks(amwhe,apche,atche,rvol,t,apb,rhog)
      else
      end if
c      g=9.81
c      rvol=83.14
c      t=298.15
c      ap=14.6961
c      ap=2000.0
      apb=ap/14.5038
c
c     Defining the value of density of liquid
      if(system .eq. 1)then
      rhol=1000.
      else if(system .eq. 2)then
      rhol=1000.
      else if(system .eq. 3)then
      rhol=790.
      else
      end if
      write(12,*)'t=',t,'ap=',ap,'rhol=',rhol,'rhog=',rhog
      rewind(10)
      do 400 id=1,138
      read(10,*)nr,ul,ug,hlexp,hgexp
      ulf=ul
      ugf=ug
      hl=.5
      hg=.05
      errg=.001
      ul=ul*.3048
      ulp=ul
      ug=ug*.3048
      ugp=ug
      if(system .eq. 1)then
      go to 210
      else if(system .eq. 2)then
      go to 220
      else if(system .eq. 3)then
      go to 230
      else
      end if
c
c     Calculating the bubble rise velocity ubr
c
210   if(ul.lt..095.and.ug.lt..09)then
      ubr=1.5937E-05*((((rhol-rhog)**.175)*(g**.175))/
     + (rhog**.35))*(dp**(-.7544))*(ul**(-.9584))*(ug**
     + (-.7860))*(vis**.025)*(st**.175)
      else if(ul.ge..095.or.ug.ge..09)then
      ubr=2.97555E-03*((((rhol-rhog)**.175)*(g**.175))/
```

```
     + (rhog**.35))*(dp**(-.7544))*(ul**(-.5558))*(ug**
     + (.7714))*(vis**.025)*(st**.175)
      else
      end if
      go to 600
220   if(ul .le. .0674) then
      ubr=3.69566E-03*((((rhol-rhog)**.179)*(9.81**.179))/
     + (rhog**.358))*(dp**-.7544)*(ul**-.4219)*(ug**.0569)
     + *(vis**.025)*(st**.179)
      else if(ul .gt. .0674)then
      ubr=2.46924E-02*((((rhol-rhog)**.179)*(9.81**.179))/
     + (rhog**.358))*(dp**-.4111)*(ul**-.8027)*(ug**.66211)*
     + (vis**.025)*(st**.179)
      else
      end if
      go to 600
230   if(ul.le.0.0572.and.ug.gt..015.and.ug.le..04572)then
      ubr=4.8881E-06*((((rhol-rhog)**.5)*(g**.5))/
     + (rhog))*(dp**(-.7544))*(ul**(-.4219))*(ug**.0569)*
     + (vis**0.025)*(st**.5)
      else if(ul.le.0.0572.and.ug.gt..04572.and.ug.le..0763)
     + then
      ubr=9.77621E-06*((((rhol-rhog)**.5)*(g**.5))/(rhog))
     + *(dp**(-.7544))*(ul**(-.4219))*(ug**.0569)
     + *(vis**.025)*(st**.5)
      else if(ul.gt..0572.and.ul.lt..0733.and.ug.gt..015.and.
     + ug.le..0763)then
      ubr=1.99806E-04*((((rhol-rhog)**.5)*(g**.5))/
     + (rhog))*(dp**(-.4111))*(ul**(-.8027))*(ug**.6621)*
     + (vis**.025)*(st**.5)
      else
      end if
      go to 600
600   ubrp=ubr
      utb=ubr
c
c
c             computations
c             calculation of minimum fluidization liquid
c             superficial velocity ulmf
      remfo = (sqrt(((33.7)**2.) + (0.0408)*(ar)) - 33.7)
      ulmfo = (remfo*vis)/(dp*densl)
      ulmf = (ulmfo*(1.-(376.*(ug**0.327)*(vis**0.227)
     +       *(dp**0.213)/((densp - densl)**(0.423)))))
c
c
c             calculation of particle terminal velocity
c
5     r = ((0.61 + (0.037/(hg + 0.013)))*((hg + hl)**3))
      utpt = 1.
10    rept = (utpt*dp*densl)/vis
      cd = (24./rept)+(6./(1. + sqrt(rept))) + .3
      utp=(sqrt(((4./3.)*(9.81)*(dp)*(densp-densl))/(cd*densl)))
      if(abs(utpt-utp) .ge. .001)then
      utpt = utp
      go to 10
      else
      end if
      if(dp .gt. .0025) then
      utp=.7*utp
      else
      end if
      utpp=utp
      ui = utp*(0.1**(dp/dr))
c
c             calculation of Richardson-Zaki exponent
```

```
c
15      rep = ((utp*dp*densl)/(vis))
      if(rep .lt. 0.2)then
      s = 4.65 + 20.*(dp/dr)
      else if (rep .ge. 0.2 .and. rep .lt. 1)then
      s = (4.4 + 18.*(dp/dr))/(rep**.03)
      else if (rep .ge. 1. .and. rep .lt. 200.)then
      s = (4.4 + 18.*(dp/dr))/(rep**.1)
      else if (rep .ge. 200. .and. rep .lt. 500)then
      s = (4.4/(rep**0.1))
      else
      s = 2.4
      end if
c
c
c             calculation of solid,liquid and gas holdups
c
11    a = (ui/((ug/hg) - (ul/hl)))
      if(abs(a) .lt. 1.14)then
      x = 1- 0.877*(ui/((ug/hg) - (ul/hl)))
      else
      x = 0
      end if
      vgl = utb
      hkt = r*hg
      hlft=((ul-((r*ug)*(1.-x)))/(utp*(1.-hg-hkt)))**(1./s)
      vgt=(ul+ug+(hlft*(1.-hg-hkt)*(vgl)))/(hg+hl)
      hlt=hkt*(1.-x) + hlft*(1.- hg-hkt +(x*hkt))
      hlt1=hlt
      hlt = (hlt + hl)/2.
      hgt=(ug/vgt)
      hgavg=hgt
      hst=1. - hlt - hgavg
      p1=hl - hlt
      p2=hg -hgavg
      if(abs(p1) .ge. errg .or. abs(p2) .ge. errg)then
      hl=hlt
      hg=hgavg
      go to 5
      else
      hl=hlt1
      hg=hgavg
      hs=1. - hl - hg
      end if
c
c     CALCULATING THE DRIFT FLUX
c
381   flux5=hg*(ubr+ul*((1.-hl)/hl)-ug)
c      write(12,*) nr,  hl, hlexp, hg,  hgexp
c      write(12,*) nr,ul,ug,ubr,ubr2,hl,hg,flux5
      write(12,*) nr,ul,hg,flux5,ubr
400     continue
500     stop
        end
      subroutine rks(amwgas,apcgas,atcgas,rvol,t,apb,rhog)
c
c     Calculating density of gas at high pressure using
c     Redwich-Kwong equation
      agas=(.42748*(rvol**2.)*(atcgas**2.5))/apcgas
      bgas=(0.08664*rvol*atcgas)/apcgas
      vlgas=(rvol*t)/apb
20    v2gas=((rvol*t)/apb)+bgas-(agas*(vlgas-bgas))/((t**.5)*apb*
     + vlgas*(vlgas+bgas))
      if(abs(v2gas-vlgas) .le. (v2gas/1000.))then
      go to 25
      else
```

```
      v1gas=v2gas
      go to 20
      end if
25    rhog=(1./v2gas)*amwgas*1000.
      return
      end
```

APPENDIX D

PREDICTIVE CORRELATIVE PROCEDURE TO DETERMINE PROPERTIES OF WHITEROCKS BITUMEN COMPUTER CODE

```
c       program thesis/progms/prog6/6.f calculates the properties
c       of Whiterocks bitumen and its fractions
c       such as density, viscosity, surface tension

      dimension xm(60),ym(60),xe(20),ye(20),xg(10),yg(10),
     + xstart(10),xfinish(10),apc(10),aPcf(10)
      dimension Tbpfr(10),sgf(10),Tcfr(10),wf(10),rhohpht(10),
     + amwf(10),xf(10),frno(10),tbpfr(10),wtfr(10),Tbpred(10)
      dimension amu2ratio(10),anucf(10),zc(10),aanu2ht(10),
     + amu2hpht(10),rhorref(10),rhoref(10),ak(10),anu2ht(10)
      dimension Tredr(10),beta(10),apsf(10),asp(10),bsp(10),csp(10),
     + dsp(10), rhocf(10),rhospht(10),Tcff(10)
      dimension aphiriedel(10),vcfriedel(10),amu2ht1(10),
     + Tcfr1(10),tcriedel(10,10),delcg(10),rhoredhtmod(10)
      dimension apbymf(10),apsurf(10)
      aphp=1500.00
c      aphp=14.6961
      htff=600.0
      htfr=htff+459.67
      open(8,file='sum')
c
c     Fitting the graphs
c
c     Calculating the parameter 'de' of the extrapolated curve
c
c     Defining the value of parameter 'dm' of the main curve
c     which is calculated by non-regression analysis
c
      dm=1764.016
c
c     Defining upper limit of 'y' for main curve
c
      yml=54.0
c
c     Calculating upper limit of 'x' for main curve
c
      xml=2.*abs((dm*yml)**0.5)+460.
c
c     Fixing the limits xl and yl of the extrapolated curve
c
      yl=yml
      xl=xml
c
```

```
c     Fixing the vortex vl of the extrapolated curve
c
      vl=1600.
c
c     Calculating 'de'
c
      de=-(((xl-vl)**2.)/(4.*(yl-100.)))
c
c     Generating the curves
c
c     Main curve
c
      open(7,file='curve.m')
      write(7,*) 460.,0.
      delcm=yml/60.
      do 30 im=1,60
      ym(im)=(im*delcm)
      xm(im)=2.*abs((dm*ym(im))**.5)+460.
      write(7,*) xm(im),ym(im)
30    continue
c
c     Extrapolated curve
c
      delce=(100.-yml)/20.
      do 40 ie=1,20
      ye(ie)=yml+(ie*delce)
      xe(ie)=vl-abs(((-4.*de*(ye(ie)-100.))**.5))
      write(7,*) xe(ie),ye(ie)
40    continue
c
c     Calculating true boiling point of fraction in Rankine (tbpfr)
c
      open(10,file='dtTbp')
c
c     Main curve
c
      open(6,file='delcgfile3')
      do 50 ig=1,10
      read(6,*) delcg(ig)
      wt=delcg(ig)/100.
      delcgsum=delcgsum+delcg(ig)
      yg(ig)=delcgsum
c
      if(yg(ig) .gt. yml)then
      go to 100
      else
      end if
      xstart(ig)=2.*abs(((dm*(yg(ig)-delcg(ig)))**0.5))+460.
      xfinish(ig)=2.*abs(((dm*yg(ig))**0.5))+460.
      go to 120
c
c     Extrapolated curve
100   xstart(ig)=vl-(abs((-4.*de*((yg(ig)-delcg(ig))-100.)))**.5)
      xfinish(ig)=vl-(abs((-4.*de*(yg(ig)-100.)))**.5)
120   xg(ig)=(xstart(ig)+xfinish(ig))/2.
      tbpfr(ig)=xg(ig)+459.67
      write(10,*) ig,tbpfr(ig),wt
50    continue
c
c     Calculating bulk temperature and overall Watson Charecterization
c     factor by eqn. 6.4 and 6.1
      tbpmf=(460+vl)/2.
      tbpmr=tbpmf+459.67
      sgm=0.985
      akwm=(tbpmr**0.333333)/sgm
      akwmactual=11.5
```

```
      tbpmrc=((akwmactual*sgm)**3.)
      rewind (10)
      do 10 i=1,10
      read (10,*) frno(i),tbpfr(i),wtfr(i)
      Tbpfr(i)=tbpfr(i)
      akwf=akwm
      sgf(i)=(Tbpfr(i)**0.333333)/akwf

c     Calculating Critical Temperature of fraction using eqn. 6.5
      Tcfr(i)=24.2787*((Tbpfr(i))**0.58848)*(sgf(i)**0.3596)

c     Calculating Critical Pressure of fraction using eqn. 6.6
      Tcff(i)=Tcfr(i)-459.67
      apc(i)=9.08740-2.15833*(log10(Tbpfr(i)))+3.35417*(log10(sgf(i)))+
     + 5.64019*((log10(sgf(i)))**2.)
      aPcf(i)=(10**apc(i))

c     Calculating Accentric Factor of fraction using eqn. 6.7
      Tbpred(i)=Tbpfr(i)/Tcfr(i)
      wf(i)=(-log(aPcf(i)/14.696)-5.671485+(5.809839/Tbpred(i))+
     + 0.867513*log(Tbpred(i))-0.1383536*(Tbpred(i)**6.))/
     + (12.439604-(12.755971/Tbpred(i))-9.654169*log(Tbpred(i))+
     + (0.316367*(Tbpred(i)**6.)))
c
c     Calculating Critical Compressibility zc using eqn. 6.41
      zc(i)=1./(3.41+1.28*wf(i))

c     Calculating Molecular Weight of fraction using eqn. 6.8
      amwf(i)=0.000045673*(Tbpfr(i)**2.1962)*(sgf(i)**(-1.0164))
c
      xmm=xmm+wtfr(i)/amwf(i)

c     DENSITY CALCULATIONS
c
c     Calculating Density of fraction at high temp.-high pr.
c
c     Using Riedeal Correlation + Chuch and Prausnitz Correlation
c
c     Calculating Critical Density using eqn. 7.2
c
      rhorref(i)=1.+0.85*(1.-((459.67+60.)/Tcfr(i)))+(1.6916+0.9846*
     + wf(i))*((1.-((459.67+60.)/Tcfr(i)))**0.333333)
      rhoref(i)=0.999024*sgf(i)
      rhocf(i)=(rhoref(i)/rhorref(i))
c
c     Calculating Density of fraction at saturation pr.- high temp.
c
c     Using eqn. 6.18
c
      Tredr(i)=htfr/Tcfr(i)
      rhospht(i)=rhocf(i)*(1.+0.85*(1.-Tredr(i))+(1.6916+0.9846*
     + wf(i))*((1.-Tredr(i))**0.333333))
      al4=al4+(wtfr(i)/(rhospht(i)))
c
c     Calculating Saturation Pressure at high pr. using eqn. 6.26
c
      asp(i)=5.671485+12.439604*wf(i)
      bsp(i)=5.809839+12.755971*wf(i)
      csp(i)=0.867513+9.654169*wf(i)
      dsp(i)=0.1383536+0.316367*wf(i)
      apsf(i)=(2.7182818**(asp(i)-(bsp(i)/Tredr(i))-csp(i)*log(Tredr
     + (i))+dsp(i)*(Tredr(i)**6.)))*aPcf(i)

c     Calculating Density of fraction at high pr.-high temp.
```

```
c     using eqn. 6.25 and 6.32

c     Using eqn 6.32
c
      beta(i)=(1./rhocf(i))*(1./(10.73*Tcfr(i)))*(1.-0.89*(wf(i)**
     + 0.5))*exp(6.9547-76.2853*Tredr(i)+191.306*(Tredr(i)**2.)-
     + 203.5472*(Tredr(i)**3.)+82.7631*(Tredr(i)**4.))
      write(9,*)'beta=',beta(i)
c
c     Using eqn. 6.25
c
      rhohpht(i)=rhospht(i)*((1.+9.*beta(i)*(aphp-apsf(i)))**(1./9.))
      a15=a15+(wtfr(i)/(rhohpht(i)))
c
c     VISCOSITY CALCULATIONS AT HIGH PRESSURE HIGH TEMPERATURE
c
c     Calculating ak(i) from eqn. 6.43
c
      ak(i)=5.808+4.93*wf(i)
c
c     Calculating modified reduced viscosity using eqn.6.48
c
      rhoredhtmod(i)=1.85-3.95*(htfr/Tcfr(i))+(.53+.2*ak(i))*((1.-(htfr
     + /Tcfr(i)))**0.333333)
        aanu2ht(i)=.507222*(rhoredhtmod(i)**2.756673)
c
c     Calculating Critical Viscosity of fraction using eqn. 6.40
c
      anucf(i)=0.0061154*((Tcfr(i)**(5./6.))/(amwf(i)**(0.5)))*
     +   (((669.97337*zc(i))/aPcf(i))**0.333333)
c
c     Calculating kinematic viscosity at high temperature using eqn. 6.49
c
      anu2ht(i)=(2.7182818**aanu2ht(i))*(anucf(i))
      amu2ht1(i)=rhospht(i)*anu2ht(i)
c
c     Incorporating high pressure effects using eqn. 6.57
c
      amu2ratio(i)=((aphp-14.696)/1000.)*(0.0239+0.01638*(amu2ht1(i)
     + **0.278))
      amu2hpht(i)=(10.**amu2ratio(i))*(amu2ht1(i))
c      write(8,*)'i/anu2ht/amu2ht1/amu2hpht/mean bpf=',i,anu2ht(i),
c     + amu2ht1(i),amu2hpht(i),xg(i)
c
10    continue
      rho1mht=(1./a14)
      rho1mhpht=(1./a15)
      write(8,*) 'rho1mht/rho1mhpht=',rho1mht,rho1mhpht
c
c     Calculating Mole Fraction of each fraction using eqn.6.9
      do 450 imw=1,10
      xf(imw)=(wtfr(imw)/amwf(imw))/xmm
      amwm=amwm+xf(imw)*amwf(imw)
450   continue
      write(8,*)'molecular wt. of mixture=',amwm
c
      write(8,*)'htff=',htff,'htfr=',htfr,'aphp=',aphp
c
      write(8,*)
      do 480 i=1,10
      write(8,*) 'i/xf/mbp/Tcfr/apcf=',i,xf(i),tbpfr(i),Tcfr(i),apcf(i)
480   continue
c     Calculating standard deviation using eqn 6.53
c
      n=10
```

```
      do 490 i=1,10
c      do 490 i=2,3
      rhoredhtmodavg=rhoredhtmodavg+rhoredhtmod(i)
      rhosphtavg=rhosphtavg+rhospht(i)
490   continue
      rhoredhtmodavg=rhoredhtmodavg/10.
c      rhosphtavg=rhosphtavg/2.
      do 491 i=1,10
c      do 491 i=2,3
      rhoredhtmodstd=rhoredhtmodstd+((rhoredhtmod(i)-
     +  rhoredhtmodavg)**2.)
      rhosphtstd=rhosphtstd+((rhospht(i)-rhosphtavg)**2.)
491   continue
      rhoredhtmodstd=((rhoredhtmodstd/(n-1))**0.5)
c      rhosphtstd=((rhosphtstd/(n-1))**0.5)
      write(8,*)
      write(8,*)'redhtmodavg/rhoredhtmodstd=',
     + rhoredhtmodavg,rhoredhtmodstd
      write(8,*)
      do 492 i=1,10
      write(8,*)'i/wtfr/rhoredhtmod/rhospht=',
     + i,wtfr(i),rhoredhtmod(i),rhospht(i)
492   continue
      do 493 i=1,10
c      do 493 i=2,3
c
c     Applying Arrhenius eqn. 6.52

      xsigmaln=xsigmaln+xf(i)*log(amu2ht1(i))
493   continue
c
c     Calculating the Coefficient using eqn. 6.55
c
      coeff=0.12455*(rhoredhtmodstd**(-9.339631))
c
c     Calculating dynamic viscosity using eqn. 6.56
c
      amu2ht1m=exp(xsigmaln*coeff)
c
c     Calculating experimentally extrapolated viscosity using eqn. 6.73
c
      extraamu2ht1m=exp(13.686193*((100./htff)**1.048743))
      error=((extraamu2ht1m-amu2ht1m)/extraamu2ht1m)*100.
c
c     Calculating Viscosity of Mixture at High Temperature
c     and High Pressure
c
c     Direct Method
c
      amu2ratiom=((aphp-14.6961)/1000.)*(0.0239+0.01638*
     + (amu2ht1m**0.278))
      amu2hpht1m=(10.**amu2ratiom)*(amu2ht1m)
      write(8,*)
      do 495 i=1,10
      write(8,*)'i/amu2ht1/amu2hpht=',i,amu2ht1(i),amu2hpht(i)
495   continue
      write(8,*)
      write(8,*)'amu2ht1m/extraamu2ht1m/error/coeff=',
     + amu2ht1m,extraamu2ht1m,error,coeff
      write(8,*)'amu2hpht1m=',amu2hpht1m
c
c     Calculating Accentric factor of mixture
      do 460 i=1,10
      wm=wm+xf(i)*wf(i)
460   continue
c
```

```
c     Calculating Critical Temperature and Critical Pressure
c     of mixture using mixing rule and Riedel Correlation
c     eqns. 6.12,6.13,6.14
c
      do 500 i=1,10
      vcfriedel(i)=(1./(rhocf(i)/amwf(i)))
      sigmaphiriedel=sigmaphiriedel+(xf(i)*vcfriedel(i))
500   continue
c
      do 510 j=1,10
      aphiriedel(j)=(xf(j)*vcfriedel(j))/(sigmaphiriedel)
510   continue
c
      do 520 i=1,10
      do 530 j=1,10
      tcriedel(i,j)=8.*(((((vcfriedel(i)**0.333333)*(vcfriedel
     + (j)**0.333333))**0.5)/((vcfriedel(i)**0.333333)+
     + (vcfriedel(j)**0.333333)))**3.)*((Tcfrl(i)*Tcfrl(j))**0.5)
530   continue
520   continue
c
      do 540 i=1,10
      do 550 j=1,10
      tcmriedel=tcmriedel+aphiriedel(i)*aphiriedel(j)*
     + tcriedel(i,j)
550   continue
540   continue
c
c     Critical Pressure calculation using eqn 7.15
c
      do 560 i=1,10
      aapcmriedel=aapcmriedel+xf(i)*(Tcfr(i)/aPcf(i))
560   continue
      apcmriedel=(1./((1./tcmriedel)*aapcmriedel))
c
c      CALCULATING SURFACE TENSION BETWEEN HYDROGEN AND BITUMEN
c      AND BITUMEN FRACTIONS
c
c      Calculating Surface Tension at High Temperature
c
c      Calculating P/M (parachor) ratio using eqn. 6.59
c
       do 138 i=1,10
       apbymf(i)=1.6652*((Tcfr(i)**0.05873))*(sgf(i)**(-0.64927))
       apsurf(i)=apbymf(i)*amwf(i)
138    continue
c
c      Calculating Density of Hydrogen at High Temperature and
c      then at High Pressure using Redlich-Kwong equation
c
c      Defining value for molecular wt. of hydrogen
c
       amwh2=2.0158
c
       rvol=83.14
       apch2=13.0
       Tch2k=33.2
       vch2=65.0
       awh2=-0.22
       aprh2=aphp/(apch2*14.5038)
c       aprh2=14.6961/(apch2*14.5038)
       Trh2=(htfr/1.8)/Tch2k
c
c      Calculating Density of Hydrogen by Redlich-Kwong equation
c      (eqns. 6.61,6.62,6.63)
```

```
c
149     aphpb=aphp/14.5038
c       149     aphpb=14.6961/14.5038
        avolh2=(0.42748*(rvol**2.)*(Tch2k**2.5))/apch2
        bvolh2=(0.08664*rvol*Tch2k)/apch2
        v2rkh2=(rvol*(htfr/1.8))/(aphpb/14.5038)
150     v3rkh2=((rvol*(htfr/1.8))/aphpb)+bvolh2-(avolh2*(v2rkh2-
     + bvolh2))/(((htfr/1.8)**0.5)*aphpb*v2rkh2*(v2rkh2+bvolh2))
        if(abs(v3rkh2-v2rkh2) .le. (v3rkh2/1000.))then
        go to 155
        else
        v2rkh2=v3rkh2
        go to 150
        end if
155     rhohphtrkh2=(1./v2rkh2)*amwh2
        write(8,*) 'rhohphtrkh2=',rhohphtrkh2
c
c       Calculating Surface Tension of Hydrogen and Mixture at high
c       temperature using eqn. 6.60
c
        do 501 i=1,10
        surfmht=surfmht+(apsurf(i)*(((rholmht*xf(i))/amwm)
     + -((rhohphtrkh2*0)/amwh2)))
501     continue
c
c       Incorporating Hydrogen as the 11th component with Parachor

c       factor=15. and yi=1 (Perry pg 3-288)
c
        surfmht=surfmht+15.*(0-(rhohphtrkh2/amwh2))
        surfmht=surfmht**4.
        write(8,*)'surfmht=',surfmht
c
c       Calculating Surface Tension of Hydrogen and Mixture at
c       High Temperature and High Pressure using eqn. 6.60
        do 505 i=1,10
        surfmhpht=surfmhpht+(apsurf(i)*(((rholmhpht*xf(i))/amwm)))
505     continue
        surfmhpht=surfmhpht+15.*(0-(rhohphtrkh2/amwh2))
        surfmhpht=surfmhpht**4.
        write(8,*)'surfmhpht=',surfmhpht
800    stop
       end
```

APPENDIX E

COMPUTER CODE FOR TPEB REACTOR SCALE-DOWN

```
c             program 7.f for designing laboratory reactor

c             This program estimates liquid velocity for proto reactor
c
c             postscript 'p' stands for large-scale
c             postscript 'm' stands for small-scale
c             dp    - equivalent catalyst particle dia.      (M)
c             densp - catalyst density.                      (KG/M3)
c             densl - liquid density.                        (KG/M3)
c             st    - liquid surface tension.                (N/M)
c             vis   - liquid viscosity.                      (KG/M-S)
c             t     - system temperature.                    (K)
c             aphp  - pressure.                              (PSI)
c             g     - gravitational acceleration.            (M/S2)
c             dr    - reactor diameter.                      (M)
c             sv    - space velocity.                        (1/HR)
c             ul    - superficial liquid velocity.           (M/S)
c             ug    - superficial gas velocity.              (M/S)
c             hl    - liquid holdup.                         (-)
c             hg    - gas holdup.                            (-)
c             hs    - solid holdup.                          (-)
c             utp   - particle terminal velocity in liquid.  (M/S)
c             ui    - Richardson-Zaki intercept.             (M/S)
c             errg  - allowable error on gas holdup          (-)
c             sbh   - bed height.                            (M)
c             ebh   - exapanded bed height.                  (M)
c             utb   - bubble terminal vel. in liquid         (M/S)
c
c
c             CALCULATIONS FOR LARGE-SCALE REACTOc
c             read the  parameters
c
      g=9.81
      t=699.81
      hlpreqd=0.380
      hgpreqd=0.30
      ulp=.02
      ugp= 0.0
      dpp= 0.005
      dbp=.003474710
      drp= 1.0
      denspp= 906.8403
c     Properties of bitumen and hydrogen at 800 F and 2000 psi
      denslp= 729.217
      stp= 0.01396285
      visp= 0.00079
      densgp=4.58652
      hlp=.4
      hgp=.3
```

```
      errg=.001
      aphp=2000
      open(11,file='dsinsumo')
c
c
c             computation of calculation of minimum fluidization
c             liquid superficial velocity ulmfp
5      i = 0
      j = 0
      j1 = 0
      l = 0
      call mflsv(dpp,denslp,denspp,visp,ugp,ulmf)
      ulmfp=ulmf
c
c             calculation of particle terminal velocity
c
      call ptv(dpp,denslp,visp,denspp,drp,utp,ui)
      utpp=utp
      uip=ui
c
c             calculation of Richardson-Zaki exponent
c
      call rze(utpp,dpp,denslp,visp,drp,s)
      sp=s
c
c
c             calculation of solid,liquid and gas holdups hlp and hgp
      rp = ((0.61+(0.037/(hgp+0.013)))*((hgp+hlp)**3.))
c
c     Calculating bubble rise velocity ubrp
c
      call brv(denslp,densgp,ulp,ugp,g,dpp,visp,stp,ubr)
      ubrp=ubr
11    ap = (uip/((ugp/hgp) - (ulp/hlp)))
      if(abs(ap) .lt. 1.14)then
      xp = 1- 0.877*(uip/((ugp/hgp) - (ulp/hlp)))
      else
      xp = 0
      end if
      vglp = ubrp
      hktp = rp*hgp
      hlftp=((ulp-((rp*ugp)*(1.-xp)))/(uip*(1.-hgp-hktp)))**(1./sp)
      vgtp=(ulp + ugp + (hlftp*(1. - hgp - hktp)*(vglp)))/(hgp+hlp)
      hltp=hktp*(1.-xp) + hlftp*(1.- hgp-hktp +(xp*hktp))
      hltp = (hltp + hlp)/2.
      hgtp=(ugp/vgtp)
      hgavgp=hgtp
      hstp=1. - hlt - hgavg
      plp=hlp - hltp
      p2p=hgp -hgavgp
      if(ugp .gt. 0.0)then
      if(abs(plp) .ge. errg .or. abs(p2p) .ge. errg)then
      go to 20
      else
      go to 21
      end if
      else
      end if
      if(ugp .eq. 0.0)then
      if(abs(plp) .ge. errg)then
      go to 20
      else
      go to 21
      end if
      else
      end if
```

```
20    hlp=hltp
      hgp=hgavgp
      go to 5
21    hlp=hltp
      hgp=hgavgp
      if(xx .eq. 1)then
      go to 26
      else
      end if
      if((hlp-hlpreqd).ge.0.001)then
      ulp=ulp-.00005
      go to 5
      else if((hlpreqd-hlp).ge.0.001)then
      ulp=ulp+.00005
      go to 5
      else
      end if









      ww=ww+1
      if(ww .eq. 1)then
      ugp=.00649995
      hgp=.3
      hgl=.4
      go to 5
      else
      end if
25    if((hgp-hgpreqd) .ge. 0.001)then
      ugp=ugp-.00005
      go to 5
      else if((hgpreqd-hgp) .ge. 0.001)then
      ugp=ugp+0.00005
      go to 5
      else
      xx=1
      go to 5
      end if
      go to 26
26    write(11,*)'hlp=',hlp,'    ','hgp=',hgp,'    ','ubrp=',ubrp
      write(11,*)'ulp=',ulp,'    ','ugp=',ugp,'    ','ulmfp=',ulmfp
      hsp=1. - hlp - hgp
      hsm=hsp
      hlm=hlp
      hgm=hgp
      hktm=hktp
      rm=rp
      hltm=hltp
      hgtm=hgtp
      hlhgp=hlp+hgp
      chn2p=((ulp-rp*ugp)/(uip*(1.-hgp-hktp)))**(1/sp)
c
c
c           calculation of entrainment height tdhp
c
      call eh(rp,hgp,xp,ulp,ugp,uip,sp,hlp,dbp,denslp,visp,densgp,m
     + ,str,tdh)
      mp=m
      strp=str
      tdhp=tdh
```

```
      write(11,*) 'mp=',mp,'   ','strp=',strp,'   ','tdhp=',tdhp
c
c               similarity calculations
      dpm= 0.0026
      dbm=.003231610
      drm= 0.15
      denspm= 906.8403
      denslm= 729.217
      stm= 0.01396285
      vism= 0.00079
      densgm=densgp
      rholm=denslm
      rhogm=densgm
      ulm=ulp
      ugm=ugp
      jm=0
c
c
      im = 0
      jlm = 0
      lm = 0
c      call mflsv(dpm,denslm,denspm,vism,ugm,ulmf)
c      ulmfm=ulmf
c
c               calculation of particle terminal velocity
c
      call ptv(dpm,denslm,vism,denspm,drm,utp,ui)
      utpm=utp
      uim=ui
c
c               calculation of Richardson-Zaki exponent
c
      call rze(utpm,dpm,denslm,vism,drm,s)
      sm=s
246   ugm11=ugm
      ulm11=ulm
111   am=(uim/((ugm/hgm)-(ulm/hlm)))
      if(abs(am) .lt. 1.14)then
      xm=1-0.877*(uim/((ugm/hgm)-(ulm/hlm)))
      else
      xm=0
      end if
      hlftm=(hltm-hktm*(1-xm))/(1-hgm-hktm+xm*hktm)
c
c     Calculating bubble rise velocity ubrm
c
      call brv(denslm,densgm,ulm,ugm,g,dpm,vism,stm,ubr)
      ubrm=ubr
      if(xl .eq. 1)then
      go to 310
      else
      end if
      vglm=ubrp
      ulm=uim*(1-hgm-hktm)*((hlftm)**sm)+rm*ugm*(1-xm)
      f=ulm+ugm+(hlftm*(1.-hgm-hktm)*vglm)
      ugm=(hgtm*f)/(hgm+hlm)
      plm=ulm-ulm11
      p2m=ugm-ugm11
```

```
      if(abs(p1m) .ge. .000001 .or. abs(p2m) .ge. .000001)then
      go to 246
      else
      end if
      xl=xl+1
      if(xl.eq.1.)then
      call brv(denslm,densgm,ulm,ugm,g,dpm,vism,stm,ubr)
      ubrm=ubr
      else
      end if
310   write(11,*)'ulm=',ulm,'    ','ugm=',ugm,'    ','ubrm=',ubrm
c      write(11,*)'ulmfm=',ulmfm
      hgm1=hgp
248   hktm = rm*hgm1
      call brv(denslm,densgm,ulm,ugm,g,dpm,vism,stm,ubr)
      ubrm=ubr
      vglm=ubrm
      hlftm=((ulm-((rm*ugm)*(1.-xm)))/(uim*(1.-hgm-hktm)))**(1./sm)
      vgtm=(ulm + ugm + (hlftm*(1. - hgm - hktm)*(vglm)))/(hgm+hlm)
      hltm=hktm*(1.-xm) + hlftm*(1.- hgm-hktm +(xm*hktm))
      hlm = hltm
      hgm=(ugm/vgtm)
      if(abs(hgm-hgm1) .gt. .001)then
      hgm1=hgm
      go to 248
      else
      end if
      hsm=1. - hlm - hgm
      hlhgm=hlm+hgm
c
c
c                  calculation of minimum fluidization liquid
c                  superficial velocity ulmfm
c

      call mflsv(dpm,denslm,denspm,vism,ugm,ulmf)
      ulmfm=ulmf
      write(11,*)'ulmfm=',ulmfm
c
c                   calculating the coefficient for practical
c                   scale down
c
c     hgm and hktm are replaced here by hgp and hktp because
c     hgm and hktm are not the applicable value at this stage
c
      chn2m=((ulm-rm*ugm)/(uim*(1.-hgp-hktp)))**(1/sm)
c
      if(dpm.gt..0025)then
      xo=(ubrp)/((g**.5)*(4.8881E-06*(dpm**(-.7544))*(ulm**
     + (-.4219))*(ugm**.0569)*(vism**.025)*(stm**.5)))
      else
      xo=(ubrp)/((g**.179)*(1.5569E-05*(dpm**(-.7544))*(ulm
     + **(-.9584))*(ugm**(-.7860))*(vism**.025)*(stm**.179)))
      end if
      write(11,*)'xo=',xo
      if(dpm.gt..0025)then
      rhogreqd=(-1.+sqrt(1+(4.*(xo**2.)*rholm)))/(2.*(xo**2.))
      else
      yo=(xo**(1./.179))
      write(11,*)'yo=',yo
      rhogreqd=(-1.+sqrt(1+(4.*yo*rholm)))/(2.*yo)
      end if
      write(11,*)'rhogreqd=',rhogreqd
      call brv(denslm,rhogreqd,ulm,ugm,g,dpm,vism,stm,ubr)
      ubrmman=ubr
      write(11,*)'ubrmman=',ubrmman
```

```
c
c     Calculating particle disengaging height
c
      call eh(rm,hgm,xm,ulm,ugm,uim,sm,hlm,dbm,denslm,vism,densgm,m
     + ,str,tdh)
      mm=m
      strm=str
      tdhm=tdh
      write(11,*) 'mm=',mm,'    ','strm=',strm,'    ','tdhm=',tdhm
c
c     Reactor design
c
c     sv = liquid hourly space velocity (vol/vol-hr)
c     rr = recycle ratio ( )
c     sbh = stagnant bed height (m)
c     ebh = expanded bed height (m)
c     bhtr = bare height of reactor (m)
c     thtr = total height of reactor (m)
c     ahtr = additional height of reactor (m)
c
c
c     Length of commercial reactor
c
      svp=1.
      rrp=.2
      sbhp=(3600*ulp*rrp)/svp
      ebhp=sbhp/hsp
      bhtrp=ebhp+tdhp
      thtrp=bhtrp*1.1
      ahtrp=thtrp-bhtrp
      thtrpf=thtrp*3.28
c
c
c     Length of laboratory reactor
c
      svm=1.
      rrm=.2
      sbhm=(3600*ulm*rrm)/svm
      ebhm=sbhm/hsm
      bhtrm=ebhm+tdhm
      thtrm=bhtrm*1.05
      ahtrm=thtrm-bhtrm
c
c     Increasing the space velocity in model
      svmodm=svp*(dpp/dpm)
      sbhmodm=(3600*ulm*rrm)/svmodm
      ebhmodm=sbhmodm/hsp
      bhtrmodm=ebhmodm+tdhm
      thtrmodm=bhtrmodm*1.05
      ahtrmodm=thtrmodm-bhtrmodm
      write(11,*)'sbhp=',sbhp,'    ','ebhp=',ebhp,'    ','tdhp=',tdhp
      write(11,*)'sbhmodm=',sbhmodm,'    ','ebhmodm=',ebhmodm,'    ',
     + 'tdhmodm=',tdhm
c
c
c     Calculating liquid axial despersion coefficient
c
      ezlp=(((drp)**1.5)*(ulp))/(26.0*(dpp**.5)*(hlp))
      ezlm=(((drm)**1.5)*(ulm))/(26.0*(dpm**.5)*(hlm))
      write(11,*)'ezlp=',ezlp,'    ','ezlm=',ezlm
c     Keeping track of ubrm with pressure
c
      aphpi=aphp-100
      open(12,file='pro.m')
      do 400 i=1,1000
      aphpi=aphpi+5
```

```
c       read(10,*) nr,aphp
c
c       Calculating Density of Hydrogen at High Temperature and
c       then at High Pressure using Redlich-Kwong equation
c
c       Defining value for molecular wt. of hydrogen
c
        amwh2=2.0158
c
        rvol=83.14
        apch2=13.0
        Tch2k=33.2
        awh2=-0.22
        aprh2=aphp/(apch2*14.5038)
        Trh2=(t)/Tch2k
c
c       Calculating Density of Hydrogen by Redlich-Kwong equation
c
149     aphpb=aphpi/14.5038
        avolh2=(0.42748*(rvol**2.)*(Tch2k**2.5))/apch2
        bvolh2=(0.08664*rvol*Tch2k)/apch2
        v2rkh2=(rvol*(t))/(aphpb/14.5038)
150     v3rkh2=((rvol*(t))/aphpb)+bvolh2-(avolh2*(v2rkh2-
     + bvolh2))/(((t)**0.5)*aphpb*v2rkh2*(v2rkh2+bvolh2))
        if(abs(v3rkh2-v2rkh2) .le. (v3rkh2/1000.))then
        go to 155
        else
        v2rkh2=v3rkh2
        go to 150
        end if
155     rhohphtrkh2=(1./v2rkh2)*amwh2
        rhogm1=1000*rhohphtrkh2
        densgm=rhogm1
        call brv(denslm,densgm,ulm,ugm,g,dpm,vism,stm,ubr)
        ubrmman1=ubr
        if(rhogm1 .ge. rhogreqd)then
        apreqd=aphpi
        write(11,*)'Adjusted density exceeded rhogreqd'
        write(11,*)'rhogreqd=',rhogreqd,'    ','rhogm1=',rhogm1,
     + '    ','apreqd=',apreqd,'     ','ubrmman1=',ubrmman1
        go to 420
        else
        end if
400     continue
420     write(11,*)
c
c
c       Calculating Density of Nitrogen at High Temperature and
c       then at High Pressure using Redlich-Kwong equation
c
c       Defining value for molecular wt. of nitrogen
c
        amwn2=28.0
        rvol=83.14
        apcn2=33.9
        Tcn2k=126.2
        vcn2=89.5E-06
        awn2=0.040
        aprn2=aphp/(apcn2*14.5038)
        Trn2=(t)/Tcn2k
c
c       Calculating Density of Ntrogen by Redlich-Kwong equation
c
        aphpb=aphp/14.5038
```

```
      avoln2=(0.42748*(rvol**2.)*(Tcn2k**2.5))/apcn2
      bvoln2=(0.08664*rvol*Tcn2k)/apcn2
      v2rkn2=(rvol*(t))/(aphpb/14.5038)
159   v3rkn2=((rvol*(t))/aphpb)+bvoln2-(avoln2*(v2rkn2-
     + bvoln2))/(((t)**0.5)*aphpb*v2rkn2*(v2rkn2+bvoln2))
      if(abs(v3rkn2-v2rkn2) .le. (v3rkn2/1000.))then
      go to 158
      else
      v2rkn2=v3rkn2
      go to 159
      end if
158   rhohphtrkn2=(1./v2rkn2)*amwn2
      rhogn2=1000*rhohphtrkn2
      volfracn2=(rhogreqd-rhogm)/(rhogn2-rhogm)
      volfrach2=(1.-volfracn2)
      write(11,*)'rhogm=',rhogm,'    ','rhogn2=',rhogn2
      write(11,*)'volfrach2=',volfrach2,'    ','volfracn2=',volfracn2
c
c     Calculating the flows
      qtp=.7854*(drp**2.)*(ulp)
      qfp=qtp*rrp
      qep=3600*24*qfp*denslp
      volcatp=(.7854*3600*(drp**2.)*ulp*rrp)/svp
c
      qtmodm=.7854*(drm**2.)*(ulm)
      qfmodm=qtmodm*rrm
      qemodm=24*3600*qfmodm*denslm
      volcatmodm=(.7854*3600*(drm**2.)*ulm*rrm)/svmodm
c
c     Calculating volumetric flow of gas qgm through each
c     orifice of the laboratory reactor
c     no=number of orifice in distributor plate
      no=16.
      qgm=(.7854*(drm**2.)*ugm)/no
      write(11,*)'qtp=',qtp,'    ','qfp=',qfp
      write(11,*)'qep=',qep,'    ','volcatp=',volcatp
      write(11,*)'qtmodm=',qtmodm,'    ','qfmodm=',qfmodm
      write(11,*)'qemodm=',qemodm
     + ,'    ','volcatmodm=',volcatmodm
      write(11,*)'volumetric flow thru orifice qgm=',qgm
      write(11,*)'db from bubpr1.f is',' ','dbp=',dbp,'     ','dbm=',dbm
      write(11,*)
      write(11,*)'     ','  sv','  rr','  sbh','  ebh','  thtr','  ahtr'
      write(11,*)
      write(11,*)'proto',svp,rrp,sbhp,ebhp,thtrp,ahtrp
      write(11,*)
      write(11,*)'model',svm,rrm,sbhm,ebhm,thtrm,ahtrm
      write(11,*)
      write(11,*)'modelmod',svmodm,rrm,sbhmodm,ebhmodm,thtrmodm,ahtrmodm
      write(11,*)
      write(11,*)
      write(11,*)'        ul  ug  hl  hg  hs  ubr  chn2'
      write(11,*)
      write(11,*) '  proto', ulp, ugp, hlp, hgp, hsp, ubrp, chn2p
      write(11,*) '  model', ulm, ugm, hlm, hgm, hsm, ubrm, chn2m
410   stop
      end
      subroutine mflsv(dp,densl,densp,vis,ug,ulmf)
      ar=((dp**3.)*(densl)*(densp-densl)*9.81)/(vis**2.)
      remfo = (sqrt(((33.7)**2.) + (0.0408)*(ar)) - 33.7)
      ulmfo = (remfo*vis)/(dp*densl)
      ulmf = (ulmfo*(1.-(376.*(ug**0.327)*(vis**0.227)
     +       *(dp**0.213)/((densp - densl)**(0.423)))))
      return
      end
```

```
      subroutine ptv(dp,densl,vis,densp,dr,utp,ui)
      utpt = 1.
10    rept = (utpt*dp*densl)/vis
      cd = (24./rept)+(6./(1. + sqrt(rept))) + .3
      utp=(sqrt(((4./3.)*(9.81)*(dp)*(densp-densl))/(cd*densl)))
      if(abs(utpt-utp) .ge. .001)then
      i= i+1
      if(i .ge. 1200)then
      write(9,*)'number of iteration i exceeded 1200'
      print*,'number of iteration i exeeded 1200'
      stop
      end if
      utpt = utp
      i=0
      go to 10
      else
      end if
      if(dp .gt. .0025)then
      utp=.7*utp
      else
      end if
      ui = utp*(0.1**(dp/dr))
      return
      end
      subroutine rze(utp,dp,densl,vis,dr,s)
      re = ((utp*dp*densl)/(vis))
      if(re .lt. 0.2)then
      s = 4.65 + 20.*(dp/dr)
      else if (re .ge. 0.2 .and. re .lt. 1)then
      s = (4.4 + 18.*(dp/dr))/(re**.03)
      else if (re .ge. 1. .and. re .lt. 200.)then
      s = (4.4 + 18.*(dp/dr))/(re**.1)
      else if (re .ge. 200. .and. re .lt. 500)then
      s = (4.4/(re**0.1))
      else
      s = 2.4
      end if
      return
       end
       subroutine brv(densl,densg,ul,ug,g,dp,vis,st,ubr)
       rhol=densl
       rhog=densg
       if(dp .gt. .0025)then
       if(ul.le.0.0572.and.ug.gt..0.and.ug.le..04572)then
       ubr=4.8881E-06*((((rhol-rhog)**.5)*(g**.5))/
      + (rhog))*(dp**(-.7544))*(ul**(-.4219))*(ug**.0569)*
      + (vis**0.025)*(st**.5)
       else if(ul.le.0.0572.and.ug.gt..04572.and.ug.le..0763)
      + then
       ubr=9.77621E-06*((((rhol-rhog)**.5)*(g**.5))/(rhog))
      + *(dp**(-.7544))*(ul**(-.4219))*(ug**.0569)
      + *(vis**.025)*(st**.5)
       else if(ul.gt..0572.and.ul.lt..0733.and.ug.gt..015.and.
      + ug.le..0763)then
       ubr=1.99806E-04*((((rhol-rhog)**.5)*(g**.5))/
      + (rhog))*(dp**(-.4111))*(ul**(-.8027))*(ug**.6621)*
      + (vis**.025)*(st**.5)
       else
       end if
       else
       if(ul.lt..095.and.ug.lt..09)then
       ubr=1.5937E-05*((((rhol-rhog)**.175)*(g**.175))/
      + (rhog**.35))*(dp**(-.7544))*(ul**(-.9584))*(ug**
      + (-.7860))*(vis**.025)*(st**.175)
       else if(ul.ge..095.or.ug.ge..09)then
       ubr=2.97555E-03*((((rhol-rhog)**.175)*(g**.175))/
```

```
     + (rhog**.35))*(dp**(-.7544))*(ul**(-.5558))*(ug**
     + (.7714))*(vis**.025)*(st**.175)
      else
      end if
      end if
      return
      end
      subroutine eh(r,hg,x,ul,ug,ui,s,hl,db,densl,vis,densg,m
     + ,str,tdh)
      d = 0
      m = 1
c
c     Assuming value of solid holdup in the first cell
c
      hsp1 = .0005
c
c     Calculating value of solid holdup in liquid-solid region
c     using eqn.(8)
c
28    hsfp1 = (hsp1)/((r*hg*x)+(1. - hg - r*hg))
c
c     Calculating value of solid holdup in the second cell using
c     eqn.(4)(
      vsfp1 = ((ul - (ug*r*(1. - x*hsfp1)))/((1. -
     +       hg - r*hg)*(1.- hsfp1))) - (ui*((1. -
     +       hsfp1)**(s - 1)))
      hsfp2 = ((ug*r*x*hsfp1) - ((1. - hg - r*hg)*
     +       (vsfp1*hsfp1))+((1. - hg - r*hg)*(d)))/
     +       (ug*r*x)
c
c     Calculating values of solid holdup in the second cell
c     using eqn.(4)
      hsp2 = (r*hg*x*hsfp2)+((1.-hg-r*hg)*hsfp2)
      if(hsp2  .lt. hs)then
      d = (vsfp1*hsfp1)
      hsp1 = hsp2
      m = m + 1
      if(m .ge. 50)then

      print*,'mp =',50
      stop
      end if
      go to 28
      else
      apl=(ug/hg-ul/hl)
c
c     Calculating terminal velocity of bubble
c
      utbt=1.
31    rebt=(utbt*db*densl)/vis
      cdb=(24./rebt)+(6./(1.+sqrt(rebt)))+.3
      utb=(sqrt(((4./3.)*(9.81)*(db)*(densl-densg))/(cdb*densl)))
      if(abs(utbt-utb) .ge. .001)then
      utbt=utb
      go to 31
      else
      end if
      reb=((db*utb*densl)/vis)
c     Calculate Strouhal no. str for alternate shedding (Fan pg.102)
      str=1/((2420*((reb)**(-1.02)))+0.776)
      tdh=m*((ug/hg)/apl)*(db/str)
      end if
      return
      end
```

APPENDIX F

DIMENSIONAL ANALYSIS FOR SIMILARITY CRITERIA

F.1 Analysis for Liquid Holdup ϵ_l

Writing the general functional dependence of liquid holdup ϵ_l, on various parameters.

$$\epsilon = f(u_l, u_g, (u_l - u_g), d_p, d_r, \rho_p, \rho_l, (\rho_p - \rho_l), \mu_l, \mu_g, \mu_{eff}, \sigma, g, \kappa, x, n, \nu) \tag{F.1}$$

Dimensions of various parameters are as follows.

$$\begin{aligned} u_l &= (\frac{L}{T}) \\ u_g &= (\frac{L}{T}) \\ (u_l - u_g) &= (\frac{L}{T}) \\ d_p &= (L) \\ d_r &= (L) \\ \rho_l &= (\frac{M}{L^3}) \\ \rho_p &= (\frac{M}{L^3}) \\ (\rho_p - \rho_l) &= (\frac{M}{L^3}) \end{aligned}$$

$$
\begin{aligned}
\mu_l &= (\frac{M}{LT}) \\
\mu_g &= (\frac{M}{LT}) \\
\mu_{eff} &= (\frac{M}{LT}) \\
\sigma &= (\frac{M}{T^2}) \\
g &= (\frac{L}{T^2}) \\
\kappa &= (-) \\
x &= (-) \\
\epsilon_l &= (-) \\
\epsilon_g &= (-) \\
\nu &= (\frac{1}{T})
\end{aligned}
\tag{F.2}
$$

Incorporating the dimensional form of the parameters in Equation (F.1), we have:

$$
\begin{aligned}
(-) = (L/T)^{\alpha_1}(L/T)^{\alpha_2}(L/T)^{\alpha_3}(L)^{\alpha_4}(L)^{\alpha_5}(M/L^3)^{\alpha_6}(M/L^3)^{alpha_7} \\
(M/L^3)^{\alpha_8}(M/LT)^{\alpha_9}(M/LT)^{\alpha_{10}}(M/LT)^{\alpha_{11}}(M/T^2)^{\alpha_{12}} \\
(L/T^2)^{\alpha_{13}}(1/T)^{\alpha_{14}}(-)^{\alpha_{15}}(-)^{\alpha_{16}}(-)^{\alpha_{17}}
\end{aligned}
\tag{F.3}
$$

Collecting the exponent of same units, we have:

For unit *Length* (L)

$$
\begin{aligned}
0 = \alpha_1 + \alpha_2 + \alpha_3 + \alpha_4 + \alpha_5 - 3\alpha_6 - 3\alpha_7 \\
-3\alpha_8 - \alpha_9 - \alpha_{10} - \alpha_{11} + \alpha_{13}
\end{aligned}
\tag{F.4}
$$

For unit *Mass* (M)

$$0 = \alpha_6 + \alpha_7 + \alpha_8 + \alpha_9 + \alpha_{10} + \alpha_{11} + \alpha_{12} \tag{F.5}$$

For unit *Time* (T)

$$\begin{aligned} 0 = &-\alpha_1 - \alpha_2 - \alpha_3 - \alpha_9 - \alpha_{10} - \alpha_{11} \\ &-2\alpha_{12} - 2\alpha_{13} - \alpha_{14} \end{aligned} \tag{F.6}$$

From Equation (F.5), we have:

$$\begin{aligned} \alpha_1 = &-\alpha_2 - \alpha_3 - \alpha_9 - \alpha_{10} - \alpha_{11} \\ &-2\alpha_{12} - 2\alpha_{13} - \alpha_{14} \end{aligned} \tag{F.7}$$

Substituting the values of α_1 in Equation (F.3), we have:

$$\begin{aligned} 0 = &-\alpha_2 - \alpha_3 - \alpha_9 - \alpha_{10} - \alpha_{11} - 2\alpha_{12} - 2\alpha_{13} \\ &-\alpha_{14} + \alpha_2 + \alpha_3 + \alpha_4 + \alpha_5 - 3\alpha_6 - 3\alpha_7 \\ &-3\alpha_8 - \alpha_9 - \alpha_{10} - \alpha_{11} + \alpha_{13} \end{aligned} \tag{F.8}$$

therefore

$$\begin{aligned} 0 = &\alpha_4 + \alpha_5 - 3\alpha_6 - 3\alpha_7 - 3\alpha_8 - 2\alpha_9 \\ &-2\alpha_{10} - 2\alpha_{11} - 2\alpha_{12} - \alpha_{13} - \alpha_{14} \end{aligned} \tag{F.9}$$

From Equation (F.3), we have:

$$\alpha_9 = \alpha_1 + \alpha_2 + \alpha_3 + \alpha_4 + \alpha_5 - 3\alpha_6$$
$$-3\alpha_7 - 3\alpha_8 - \alpha_{10} - \alpha_{11} + \alpha_{13} \tag{F.10}$$

But, from Equation (F.4), we have:

$$\alpha_{10} + \alpha_{11} = -\alpha_6 - \alpha_7 - \alpha_8 - \alpha_9 - \alpha_{12} \tag{F.11}$$

therefore

$$\alpha_9 = \alpha_1 + \alpha_2 + \alpha_3 + \alpha_4 + \alpha_5 - 3\alpha_6$$
$$+3\alpha_7 + 3\alpha_8 + \alpha_6 + \alpha_7 + \alpha_8$$
$$+\alpha_9 + \alpha_{12} + \alpha_{13} \tag{F.12}$$

and therefore

$$0 = \alpha_1 + \alpha_2 + \alpha_3 + \alpha_4 + \alpha_5 - 2\alpha_6$$
$$-2\alpha_7 - 2\alpha_8 + \alpha_{12} + \alpha_{13} \tag{F.13}$$

From Equation (F.4) we have:

$$\alpha_6 = -\alpha_7 - \alpha_8 - \alpha_9 - \alpha_{10} - \alpha_{11} - \alpha_{12} \tag{F.14}$$

and from Equation (F.3) we have:

$$\alpha_1 = -\alpha_2 - \alpha_3 - \alpha_4 - \alpha_5 + 3\alpha_6 + 3\alpha_7$$
$$+3\alpha_8 + \alpha_9 + \alpha_{10} + \alpha_{11} - \alpha_{13} \qquad \text{(F.15)}$$

and from Equation (F.5) we have:

$$\alpha_2 = -\alpha_1 - \alpha_3 - \alpha_9 - \alpha_{10} - \alpha_{11}$$
$$-2\alpha_{12} - 2\alpha_{13} - \alpha_{14} \qquad \text{(F.16)}$$

Substituting the value of α_1, from Equation (F.14), in Equation (F.15) we have:

$$\begin{aligned} \alpha_2 = \alpha_2 &+ \alpha_3 + \alpha_4 + \alpha_5 - 3\alpha_6 - 3\alpha_7 \\ &-3\alpha_8 - \alpha_9 - \alpha_{10} - \alpha_{11} + \alpha_{13} - \alpha_3 \\ &-\alpha_9 - \alpha_{10} - \alpha_{11} - 2\alpha_{12} - 2\alpha_{13} - \alpha_{14} \\ = \quad &\alpha_4 + \alpha_5 + \alpha_9 + \alpha_{10} + \alpha_{11} + \alpha_{12} - \alpha_{13} - \alpha_{14} \end{aligned} \qquad \text{(F.17)}$$

therefore

$$\alpha_4 = -\alpha_5 - \alpha_9 - \alpha_{10} - \alpha_{11} - \alpha_{12} + \alpha_{13} + \alpha_{14} \qquad \text{(F.18)}$$

Substituting the values of α_6 and α_4, from Equations (F.13) and (F.18), Equation (F.14), we have:

$$\begin{aligned}
\alpha_1 = & -\alpha_2 - \alpha_3 - \alpha_4 - \alpha_5 + 3\alpha_6 + 3\alpha_7 \\
& +3\alpha_8 + \alpha_9 + \alpha_{10} + \alpha_{11} - \alpha_{13} \\
= & -\alpha_2 - \alpha_3 - (-\alpha_5 - \alpha_9 - \alpha_{10} - \alpha_{11} - \alpha_{12} \\
& +\alpha_{13} + \alpha_{14}) - \alpha_5 + 3(-\alpha_7 - \alpha_8 - \alpha_9 - \alpha_{10} \\
& -\alpha_{11} - \alpha_{12}) + 3\alpha_7 + 3\alpha_8 + \alpha_9 + \alpha_{10} + \alpha_{11} - \alpha_{13} \\
= & -\alpha_2 - \alpha_3 + \alpha_5 + \alpha_9 + \alpha_{10} + \alpha_{11} + \alpha_{12} \\
& -\alpha_{13} - \alpha_{14} - \alpha_5 - 3\alpha_7 - 3\alpha_8 - 3\alpha_9 - 3\alpha_{10} \\
& -3\alpha_{11} - 3\alpha_{12} + 3\alpha_7 + 3\alpha_8 + \alpha_9 + \alpha_{10} + \alpha_{11} - \alpha_{13} \\
= & -\alpha_2 - \alpha_3 - \alpha_9 - \alpha_{10} - \alpha_{11} - 2\alpha_{12} - 2\alpha_{13} - \alpha_{14} \qquad \text{(F.19)}
\end{aligned}$$

therefore

$$\alpha_1 = -\alpha_2 - \alpha_3 - \alpha_9 - \alpha_{10} - \alpha_{11} - 2\alpha_{12} - 2\alpha_{13} - \alpha_{14} \qquad \text{(F.20)}$$

$$\alpha_4 = -\alpha_5 - \alpha_9 - \alpha_{10} - \alpha_{11} - \alpha_{12} + \alpha_{13} + \alpha_{14} \qquad \text{(F.21)}$$

$$\alpha_7 = -\alpha_6 - \alpha_8 - \alpha_9 - \alpha_{10} - \alpha_{11} - \alpha_{12} \qquad \text{(F.22)}$$

Therefore

$$\begin{aligned}
\epsilon_l = & C_1(u_l)^{\alpha_1}(u_g)^{\alpha_2}(u_l - u_g)^{\alpha_3}(d_p)^{\alpha_4}(d_r)^{\alpha_5}(\rho_p)^{\alpha_6}(\rho_l)^{\alpha_7}(\rho_p - \rho_l)^{\alpha_8} \\
& (\mu_l)^{\alpha_9}(\mu_g)^{\alpha_{10}}(\mu_{sl})^{\alpha_{11}}(\sigma)^{\alpha_{12}}(g)^{\alpha_{13}}(\nu)^{\alpha_{14}}(\kappa)^0(x)^0(n)^0 \qquad \text{(F.23)}
\end{aligned}$$

Substituting the values of α_1, α_4 and α_6 from Equation (F.20),(F.21) and (F.22), in Equation (F.23), we can write

$$\begin{aligned}\epsilon_l = C_1(u_l)^{-\alpha_2-\alpha_3-\alpha_9-\alpha_{10}-\alpha_{11}-2\alpha_{12}-2\alpha_{13}-\alpha_{14}} \\ \times(u_g)^{\alpha_2}(u_l-u_g)^{\alpha_3} \\ \times(d_p)^{-\alpha_5-\alpha_9-\alpha_{10}-\alpha_{11}-\alpha_{12}+\alpha_{13}+\alpha_{14}} \\ \times(d_r)^{\alpha_5} \\ \times(\rho_p)^{-\alpha_6-\alpha_8-\alpha_9-\alpha_{10}-\alpha_{11}-\alpha_{12}} \\ \times(\rho_l)^{\alpha_6}(\rho_p-\rho_l)^{\alpha_8} \\ \times(\mu_l)^{\alpha_9}(\mu_g)^{\alpha_{10}}(\mu_{eff})^{\alpha_{11}}(\sigma)^{\alpha_{12}}(g)^{\alpha_{13}}(\nu)^{\alpha_{14}}\end{aligned} \tag{F.24}$$

Therefore

$$\begin{aligned}\epsilon_l = C_1\left(\frac{u_g}{u_l}\right)^{\alpha_2}\left(\frac{u_l-u_g}{u_l}\right)^{\alpha_3}\left(\frac{\mu_l}{\mu_l d_p\rho_p}\right)^{\alpha_9}\left(\frac{\mu_g}{u_l d_p\rho_l}\right)^{\alpha_{10}}\left(\frac{\mu_{eff}}{\mu_l d_p\rho_l}\right)^{\alpha_{11}} \\ \left(\frac{\sigma}{u_l{}^2 d_p\rho_p}\right)^{\alpha_{12}}\left(\frac{gd_p}{u_l{}^2}\right)^{\alpha_{13}}\left(\frac{d_p\nu}{u_l}\right)^{\alpha_{14}}\left(\frac{d_r}{d_p}\right)^{\alpha_5}\left(\frac{\rho_p}{\rho_l}\right)^{\alpha_7}\left(\frac{\rho_p-\rho_l}{\rho_l}\right)^{\alpha_8}\end{aligned} \tag{F.25}$$

Since ν does not have a strong effect on the average liquid holdup in the three-phase region, we can neglect it.

Further

$$\mu_{eff} = f(\mu_l, d_p, \epsilon_l, \epsilon_g) \tag{F.26}$$

Then Equation (F.25) becomes

$$\begin{aligned}\epsilon_l = f(\frac{u_g}{u_l}, \left(\frac{u_l-u_g}{u_l}\right), \left(\frac{\mu_l}{\mu_l d_p\rho_l}\right), \left(\frac{\sigma}{u_l{}^2 d_p\rho_l}\right) \\ \left(\frac{gd_p}{u_l{}^2}\right), \left(\frac{d_r}{d_p}\right), \left(\frac{\rho_p}{\rho_l}\right), \left(\frac{\rho_p-\rho_l}{\rho_l}\right))\end{aligned} \tag{F.27}$$

Now

$$\begin{aligned} \frac{u_l - u_g}{u_l} &= 1 - \frac{u_g}{u_l} \\ &= f\left(\frac{u_g}{u_l}\right) \end{aligned} \tag{F.28}$$

and

$$\begin{aligned} \frac{\rho_p - \rho_l}{\rho_l} &= \frac{\rho_p}{\rho_l} - 1 \\ &= f\left(\frac{\rho_p}{\rho_l}\right) \end{aligned} \tag{F.29}$$

Therefore Equation (F.27) becomes

$$\epsilon_l = f\left[\left(\frac{u_g}{u_l}\right), \left(\frac{\mu_l}{u_l d_p \rho_l}\right), \left(\frac{\sigma}{{u_l}^2 d_p \rho_l}\right), \left(\frac{g d_p}{{u_l}^2}\right), \left(\frac{d_r}{d_p}\right), \left(\frac{\rho_l}{\rho_p}\right)\right] \tag{F.30}$$

Now

$$\begin{aligned} Re_p &= Particle\ Reynolds\ number \\ &= \left(\frac{u_l d_p \rho_l}{\mu_l}\right) \end{aligned} \tag{F.31}$$

$$\begin{aligned} We_p &= Particle\ Weber\ number \\ &= \left(\frac{{u_l}^2 d_p \rho_l}{\mu_l}\right) \end{aligned} \tag{F.32}$$

$$\begin{aligned} Fr_p &= Particle\ Froudes\ number \\ &= \left(\frac{{u_l}^2}{g d_p}\right) \end{aligned} \tag{F.33}$$

Therefore

$$\epsilon_l = f\left((\frac{u_l}{u_g}), (Re_p), (Fr_p), (We_p), (\frac{d_r}{d_p}), (\frac{\rho_l}{\rho_p})\right) \tag{F.34}$$

F.2 Analysis for Gas Holdup ϵ_g

The functional relationship for the gas holdup ϵ_g can be written as

$$\begin{aligned}\epsilon_g = f(&u_l, u_g, (u_l - u_g), d_p, d_r, \rho_p, \rho_l, (\rho_p - \rho_l),\\ &\mu_l, \mu_g, \sigma, g, \nu, \kappa, x, n, d_o, d_b)\end{aligned} \tag{F.35}$$

For a coalescing bubble regime d_b becomes practically independent of d_o and at low pressure ϵ_g has a weak dependence on ρ_g and μ_g.

Further

$$d_b = f(d_p, u_l, u_g, \mu_l, \rho_l, \sigma) \tag{F.36}$$

Therefore Equation (F.35) becomes

$$\begin{aligned}\epsilon_g = f(&u_l, u_g, (u_l - u_g), d_p, d_r, \rho_p, \rho_l,\\ &\mu_g, \mu_l, \sigma, g, \nu, \kappa, n)\end{aligned} \tag{F.37}$$

Carrying out the dimensional analysis, similar to section (.1), we have:

$$\epsilon_g = f\left((\frac{u_l}{u_g}), (Re_p), (Fr_p), (We_p), (\frac{d_r}{d_p}), (\frac{\rho_l}{\rho_p})\right) \tag{F.38}$$

APPENDIX G

FORMULATION OF BUBBLE MODEL AT HIGH PRESSURE

In their model, Ramakrishna et al. (2) have neglected the effect of ρ_g. Their approach needs to be refined when ρ_g becomes considerable at high pressures. The equations developed below include the effect of ρ_g and are used in the model, proposed in Chapter 4, to calculate the bubble diameter in a high pressure TPEB.

As indicated by Ramakrishna et al.(2), the various forces acting on the bubble are:

$$\text{Buoyant force, } F_B = v(\rho_l - \rho_g)g \tag{G.1}$$

$$\text{Viscous force, } F_V = 6\pi r_e \mu_l v_e \tag{G.2}$$

$$\text{Surface tension force, } F_{ST} = \pi d_o \sigma cos\alpha \tag{G.3}$$

$$\text{Inertial force, } F_I = \frac{d(Mv_e)}{dt} \tag{G.4}$$

$$= \frac{Q^2(\frac{11\rho_l}{16} + \rho_g}{12\pi(\frac{3}{4\pi})^{2/3}} \tag{G.5}$$

When the density of gas ρ_g cannot be neglected, the momentum of gas transfered to the bubble has to be included. Assuming that the gas comes to a rest immediately after entering the bubble, the expression for the force on the bubble due gas momentum F_M is derived below.

$$\text{Gas momentum force, } F_M = \frac{m(V_1 - V_2)}{t} \tag{G.6}$$

where

V_1 = velocity of gas at the orifice.

V_2 = velocity of gas in the bubble.

Assuming that the gas comes at rest, immediately after entering the bubble, we have:

$$V_2 = 0 \tag{G.7}$$

and

$$F_M = \frac{dm}{dt} V_1 \tag{G.8}$$

now

$$\begin{aligned} V_1 &= Q/((\pi {d_o}^2)/4) \\ &= 4Q/(\pi {d_o}^2) \end{aligned} \tag{G.9}$$

and

$$\frac{dm}{dt} = \rho_g Q \tag{G.10}$$

therefore

$$\begin{aligned} F_M &= (\rho_g Q)(\frac{4Q}{\pi {d_o}^2}) \\ &= \frac{4\rho_g Q^2}{\pi {d_o}^2} \end{aligned} \tag{G.11}$$

Carrying out the force balance *without* neglecting the gas density, we have:

$$F_B - F_V - F_{ST} - F_I + F_M = 0 \tag{G.12}$$

Substituting the values of F_B, F_V, F_{ST}, F_I and F_M from Equations (G.1), (G.2), (G.3), (G.4) and (G.11) respectively in Equation (G.12), we have:

$$\begin{aligned} & V_E(\rho_l - \rho_g)g - \tfrac{3}{2}\mu_l Q(\tfrac{4\pi}{3}){V_E}^{-1/3} \\ & -\pi d_o \sigma cos\alpha - \left((Q^2(\tfrac{11\rho_l}{16} + \rho_g){V_E}^{-2/3})/(12\pi(\tfrac{3}{4\pi})^{2/3})\right) \\ & + \left((4\rho_g Q^2)/(\pi {d_o}^2)\right) = 0 \end{aligned} \tag{G.13}$$

therefore

$$\begin{aligned} V_E(\rho_l - \rho_g)g = & \frac{3}{2}\mu_l Q(\frac{4\pi}{3}){V_E}^{-1/3} + \pi d_o \sigma cos\alpha \\ & + \frac{Q^2(\frac{11\rho_l}{16} + \rho_g){V_E}^{-2/3}}{12\pi(\frac{3}{4\pi})^{2/3}} - \frac{4\rho_g Q^2}{\pi {d_o}^2} \end{aligned} \tag{G.14}$$

and therefore

$$V_E = \frac{1}{(\rho_l - \rho_g)g}(2.418\mu_l Q V_E{}^{-1/3} + 3.1416 d_o \sigma cos\alpha$$
$$+Q^2(0.6875\rho_l + \rho_g)(0.0474)V_E{}^{-2/3} - \frac{1.273\rho_g Q^2}{d_o{}^2}) \qquad \text{(G.15)}$$

The bubble movement, in the second stage, was expressed in their model by Ramakrishna et al. by Equation (16)

$$\frac{d(Mv')}{dt} = V\rho_l g - 6\pi r\mu_l v' - \pi d_o \sigma cos\alpha \qquad \text{(G.16)}$$

where V = instantaneous volume of the bubble and is given by

$$V = V_E + Qt \qquad \text{(G.17)}$$

In Equation (G.16), the terms containing ρ_g are neglected.

If ρ_g is included in the formulation, Equation (16) becomes

$$\frac{d(Mv')}{dt} = V(\rho_l - \rho_g)g - 6\pi r\mu_l v' - \pi d_o \sigma cos\alpha + \frac{4\rho_g Q^2}{\pi d_o{}^2} \qquad \text{(G.18)}$$

where, the last term in Equation (G.18) denotes the contribution due to gas momentum.

Now the velocity v' pertains to the centre of the bubble and is made up of the velocity of the centre due to expansion, dr/dt and the velocity, v with which the bubble base moves.

Therefore

$$v' = v + \frac{dr}{dt} \qquad \text{(G.19)}$$

where r is the instanteneous radius of the bubble. Thus, the L.H.S. of Equation (G.16) becomes

$$\frac{d(Mv')}{dt} = \frac{d}{dt}\left(M(v+\frac{dv}{dt})\right) \tag{G.20}$$

$$= \frac{d}{dt}\left(Mv + M\frac{dr}{dt}\right) \tag{G.21}$$

$$= \frac{d}{dt}(Mv) + \frac{d}{dt}(M\frac{dr}{dt}) \tag{G.22}$$

$$= M\frac{dv}{dt} + v(\frac{dM}{dt}) + \frac{d}{dt}(M\frac{dr}{dt}) \tag{G.23}$$

But, as pointed out by Ramakrisna et al.

$$\begin{aligned}\frac{d}{dt}(M\frac{dr}{dt}) &= \frac{d}{dt}(Mv) \\ &= \frac{Q^2(\frac{11\rho_l}{16})V^{-2/3}}{12\pi(\frac{3}{4\pi})^{2/3}}\end{aligned} \tag{G.24}$$

where

v is the velocity of the centre of the bubble due to bubble expansion.

In Equation (G.24), ρ_g has been neglected.

If we include ρ_g, Equation (G.24) becomes

$$\frac{d}{dt}(M\frac{dr}{dt}) = \frac{Q^2(\frac{11\rho_l}{16}+\rho_g)V^{-2/3}}{12\pi(\frac{3}{4\pi})^{2/3}} \tag{G.25}$$

Substituting the value of V in Equation (G.25), we have:

$$\frac{d}{dt}(M\frac{dr}{dt}) = \frac{Q^2(\frac{11\rho_l}{16}+\rho_g)(V_E+Qt)^{-2/3}}{12\pi(\frac{3}{4\pi})^{2/3}} \tag{G.26}$$

Now

$$\begin{aligned} M &= V(\frac{11\rho_l}{16} + \rho_g) \\ &= (V_E + Qt)(\frac{11\rho_l}{16} + \rho_g) \end{aligned} \tag{G.27}$$

and

$$\frac{dM}{dt} = (\frac{11\rho_l}{16} + \rho_g)Q \tag{G.28}$$

Substituting Equations (G.17), (G.23), (G.24), (G.27) and (G.28) in Equation (G.18), we have:

$$\begin{aligned} &(V_E + Qt)(\tfrac{11\rho_l}{16} + \rho_g)\tfrac{dv}{dt} + v(\tfrac{11\rho_l}{16} + \rho_g)Q \\ &+6\pi(\tfrac{3}{4\pi})^{1/3}(V_E + Qt)^{1/3}\mu_l v = \\ &(V_E + Qt)(\rho_l - \rho_g)g - (\tfrac{3\mu_l Q}{2(\frac{3}{4\pi})^{1/3}})(V_E + Qt)^{-1/3} \\ &-(Q^2(\tfrac{11\rho_l}{16} + \rho_g)(V_E + Qt)^{-2/3})/(12\pi(\tfrac{3}{4\pi})^{2/3}) \\ &-\pi d_o \sigma cos\alpha + (4\rho_g Q^2)/(\pi {d_o}^2) \end{aligned} \tag{G.29}$$

Dividing Equation (G.29) by

$$(\frac{11\rho_l}{16} + \rho_g)(V_E + Qt) \tag{G.30}$$

Equation (G.29) becomes

$$\frac{dv}{dT} + A(\frac{v}{T}) = B - GT^{-4/3} - ET^{-5/3} - CT^{-1} + HT^{-1} \tag{G.31}$$

where

$$A = 1 + \frac{6\pi(\frac{3}{4\pi})^{1/3}(V_E + Qt)^{1/3}\mu_l}{Q(\frac{11\rho_l}{16} + \rho_g)} \quad (G.32)$$

$$= 1 + \frac{11.693(mV_E)^{1/3}\mu_l}{Q(\frac{11\rho_l}{16} + \rho_g)} \quad (G.33)$$

where, in Equation (G.33), following approximation is applied.

$$(V_E + Qt)^{1/3} = (mV_E)^{1/3} \quad (G.34)$$

where

$$m = \frac{2V_E + Qt}{2V_E} \quad (G.35)$$

and

$$B = \frac{(\rho_l - \rho_g)g}{Q(\frac{11\rho_l}{16} + \rho_g)}$$

$$= \frac{(\rho_l - \rho_g)g}{Q(0.6875\rho_l + \rho_g)} \quad (G.36)$$

$$C = \frac{d_o\sigma cos\alpha}{(\frac{11\rho_l}{16} + \rho_g)Q}$$

$$= \frac{3.1416d_o\sigma cos\alpha}{Q(0.6875\rho_l + \rho_g)} \quad (G.37)$$

$$\begin{aligned} E &= \frac{Q}{12\pi(\frac{3}{4\pi})^{2/3}} \\ &= 0.0689Q \end{aligned} \tag{G.38}$$

$$\begin{aligned} G &= \frac{3\mu_l}{2(\frac{3}{4\pi})^{1/3}(\frac{11\rho_l}{16} - \rho_g)} \\ &= \frac{2.418}{(0.6875\rho_l + \rho_g)} \end{aligned} \tag{G.39}$$

$$\begin{aligned} H &= \frac{(4\rho_g Q^2)}{\pi {d_o}^2 Q(\frac{11\rho_l}{16} + \rho_g)} \\ &= \frac{1.273\rho_g Q}{{d_o}^2(\frac{11\rho_l}{16} + \rho_g)} \end{aligned} \tag{G.40}$$

$$T = V_E + Qt \tag{G.41}$$

Using the boundary conditions

at $t = 0$

$v = 0$

$T = V_E$

and integrating Equation (G.31) with respect to t, we have:

$$V = \frac{1}{T^A}\left(\frac{B}{A+1}(T^{A+1} - {V_E}^{A+1}) - \left(\frac{C-H}{A}\right)(T^A - {V_E}^A)\right.$$
$$-\frac{G}{A-1/3}(T^{A-1/3} - {V_E}^{A-1/3})$$
$$\left.-\frac{E}{A-2/3}(T^{A-2/3} - {V_E}^{A-2/3})\right) \qquad \text{(G.42)}$$

Integrating Equation (G.42) with respect to 't', we have:

$$x = \frac{B}{2Q(A+1)}(V^2 - V_E^2) - \left(\frac{C-H}{AQ}\right)(V - V_E)$$
$$-\frac{3G}{2Q(A-1/3)}(V^{2/3} - V_E^{2/3}) - \frac{3E}{Q(A-2/3)}(V^{1/3} - V_E^{1/3})$$
$$-\frac{1}{Q(-A+1)}(V^{-A+1} - V_E^{-A+1})$$
$$\times\left(\frac{B}{A+1}V_E^{A+1} - \left(\frac{C}{A}\right)V_E^A - \frac{G}{A-1/3}V_E^{A-1/3}\right.$$
$$\left.-\frac{E}{A-2/3}V_E^{A-2/3}\right) \qquad \text{(G.43)}$$

APPENDIX H

SAMPLE CALCULATIONS FOR REACTOR DESIGN

H.1 Sample Calculations for Scale-down Procedure

H.1.1 Large Scale Reactor

1. Processing capacity $(Q_T)_p = 90$ tons/day of bitumen.

2. Operating conditions:

   (a) Solid phase: Ni-Alumina catalyst.

   (b) Liquid phase: Bitumen.

   (c) Gas phase: Hydrogen.

   (d) Temperature: 700 K.

   (e) Pressure: 13.78 MPa.

   (f) LHSV: 1.0 vol. of fresh feed/vol. of catalyst-hr.

3. $(d_r)_p = 1.0$ m.

4. Hydrodynamic properties:

   (a) Solid phase:

   - $(d_p)_p = 0.005$ m. (spherical shape).

- $(\rho_p)_p = 906.8$ kg/m^3.

  for

  Apparent density of catalyst = 700.0 kg/m^3.

  Pore volume = 0.00044 m^3/g.

(b) Liquid phase:

$(\rho_l)_p = 729.217$ kg/m^3.

$(\mu_l)_p = 0.00079$ (N.s)/m^2.

$(\sigma)_p = 0.01396$ N/m.

(c) Gas phase:

$(\rho_g)_p = 4.587$ kg/m^3.

5. $(\epsilon_l)_p = 0.3$

   $(\epsilon_g)_p = 0.35$

6. By using algorithm in section 7.9.

   $(u_l)_p = 0.01$ m/sec.

   $(u_g)_p = 0.01245$ m/sec.

7. $(R_r)_p = 5.0$

8.

$$(Q_T)_p = \frac{\pi(1.0)^2(0.01)}{4} = 0.007854 \text{ m}^3/\text{sec}.$$

9.

$$(Q_f)_p = \frac{0.007854}{5} = 0.00157 \text{ m}^3/\text{sec}.$$

10.

$$\begin{aligned}(Q_e)_p = (Q_f)_p &= 0.00157 \text{ m}^3/\text{sec.} \\ &= 135.65 \text{ m}^3/\text{day.} \\ &= 98.92 \text{ Tons/day.}\end{aligned}$$

11.

$$\begin{aligned}(Vol_{cat})_p &= \frac{3600\text{x}\pi 1.0^2\text{x}.01}{4\text{x}5\text{x}1} \\ &= 5.655 \text{ m}^3\end{aligned}$$

12.

$$\begin{aligned}(H_s)_p &= \frac{3600\text{x}.01}{5\text{x}1} \\ &= 7.2 \text{ m.}\end{aligned}$$

13.

$$(H_e)_p = \frac{7.2}{0.35} = 20.57 \text{ m.}$$

14.

$$(d_b)_p = 0.0034 \text{ m.}$$

for

$$(d_o)_p = 0.0016129 \text{ m.}$$

15.

$$(tdh)_p = 0.1798 \text{ m.}$$

16.

$$(ah)_p = 0.1(20.57 + 0.1798) = 2.076 \text{ m.}$$

17.

$$(H_t)_p = (20.57 + 0.1798 + 2.076) = 22.84 \text{ m.}$$

H.1.2 Laboratory Reactor

1. (a) $(\epsilon_l)_m = 0.3$.

   (b) $(\epsilon_g)_m = 0.35$.

   (c) $(R_r)_m = 5.0$.

   (d) $(\rho_p)_m = 906.8$ kg/m^3.

   (e) $(\rho_l)_m = 729.217$ kg/m^3.

   (f) $(\sigma)_m = 0.01396$ N/m.

   (g) $(\rho_g) = 4.587$ kg/m^3.

2. $(d_p)_m = 0.0026$ m.

3. $(u_l)_m = 0.004175$ m/sec.

   $(u_g)_m = 0.005608$ m/sec.

4. The plot of drift flux vs. gas holdup in Figure 5.6 in Chapter 5 indicates that the flow is in the dispersed bubble regime.

5.

$$\begin{aligned} E_{zlp} &= \frac{(1.0)^{3/2}(0.01)}{26(0.005)^{1/2}(0.3)} \\ &= 0.0182 \text{ m}^2/\text{s}. \end{aligned}$$

$$\begin{aligned} E_{zlm} &= \frac{(0.15)^{3/2}(0.004175)}{26(0.0026)^{1/2}(0.3)} \\ &= .0006 \text{ m}^2/\text{s}. \end{aligned}$$

6.

$$\frac{(S_v)_m}{(S_v)_p} = \frac{0.0182}{0.0006} = 30.28.$$

7.

$$(S_v)_m = (1.0)\frac{0.005}{0.0026} = 1.92.$$

8. We select $(S_v)_m = 1.92$ vol. of fresh feed/vol. of cat.-hr.

9.

$$\begin{aligned}(Q_T)_m &= \frac{\pi(0.15)^2(0.004175)}{4} \\ &= 0.000738\text{m}^3/s. \\ &= 1.173 \text{ gpm.}\end{aligned}$$

$$\begin{aligned}(Q_f)_m &= \frac{0.000738}{5} \\ &= 0.0001476 \text{ m}^3/s. \\ &= 0.2346 \text{ gpm.}\end{aligned}$$

10.

$$\begin{aligned}(Vol_{cat})_m &= \frac{3600\pi(0.15)^2(0.004175)}{(4)(5)(1.92)} \\ &= 0.0277 \text{ m}^3\end{aligned}$$

$$(H_s)_m = \frac{3600(0.004175)}{(5.0)(1.92)} = 1.56 \text{ m.}$$

$$(H_e)_m = \frac{1.56}{0.35} = 4.47 \text{ m.}$$

$(d_b)_m = 0.0029$ m.

$(tdh)_m = 0.043$ m.

$(H_t)_m = 4.74$ m.

11. $(\rho_g)_{reqd} = 10.34$ kg/m^3.

12. $(Vol)_{N_2} = 0.0974$ %.

$P_{reqd} = 32.796$ MPa. (4760 psi.).

H.2 Calculation for $(N_o)_p$ and L_c

From above calculations we have

(a) $(u_g)_p = 0.01245$ m/s.

(b) $(u_g)_m = 0.0056$ m/s.

(c) $(d_r)_p = 1.0$ m.

(d) $(d_r)_m = 0.15$ m.

(e) $(N_o)_m = 16.0$

(f) $d_o = 0.0016$ m. $= 0.0635$ in.

$$(N_o)_p = \frac{(d_r)_p{}^2 (u_g)_p (N_o)_m}{(d_r)_m{}^2 (u_g)_m}$$

$$= \frac{(1.0)^2 (0.01245)(4)}{(0.15)^2 (0.0056)}$$

$$= 1580.96$$

Assuming square layout for the orifice, L_c, the center to center distance between two orifices is given by

$$L_c = 0.886\,(A_p/A_{th})\,d_o$$

where

A_p = crossection area of the plate $(\text{ft})^2$.

$= \frac{\pi(d_r)_p^{\,2}}{4}$

$= \frac{\pi 1.0^2 3.28^2}{4.}$

$= 8.45(\text{ft})^2$

A_{th} = total orifice area $(ft)^2$.

$= \frac{\pi(D_p)^2 N_p}{4}$

$= \frac{\pi(0.0635)^2(1581)}{576}$

$= 0.0348(\text{ft})^2$

Therefore

$L_c = 0.886\left(\frac{8.45}{0.0348}\right)^{1/2}(0.0635)$

$= 0.878$ in.

$= 0.0223$ m.

APPENDIX I

LIST OF SYMBOLS

a	exponent, in [5.11]
a_{kf}	factor defined by [6.46]
a_r	parameter in generalized wake model
ah	additional height above the expanded bed in the reactor, m^2
A	coefficient, in [4.4]
A_1	coefficient, in [5.22]
A_2	coefficient, in [5.24]
A_3	coefficient, in [6.31]
A_4	coefficient, in [6.37]
A_p	cross-sectional area of distributor plate, m^2
A_s	surface area of catalyst particle, m^2
A_r	cross-sectional area of reactor, m^2
A_{th}	total area of orifices on distributor plate, m^2
A_v	ares of plates in a viscometer, m^2
b	exponent, in [5.11]
B	coefficient, in [4.5]
B_1	coefficient, in [6.32]
B_2	coefficient, in [6.38]
Bo	Bond number
c	exponent, in [5.11]
$c1$	concentration of component in reactor, $mol\ m^{-3}$

c_1	concentration of component at entrance of reactor, $mol\ m^{-3}$
C	coefficient, in [4.6]
C_2	coefficient, in [6.39]
C_3	coefficient, in [6.39]
C_4	coefficient, in [6.40]
C_5	coefficient, in [6.41]
C_6	coefficient, in [6.42]
C_7	coefficient, in [6.33]
C_{Db}	coefficient of viscous drag for bubble
C_{Dp}	coefficient of viscous drag for solid particle
C_e	concentration of a component in effluent stream, $mol\ m^{-3}$
C_f	concentration of a component in feed, $mol\ m^{-3}$
C_m	coefficient, in [6.58]
$Coeff$	coefficient, in [7.]
d	exponent, in [5.11]
d_b	diameter of bubble, m
d_e	factor, in [6.69]
d_o	diameter of orifice, m
d_v	distance between plates in a viscometer, m
d_N	parameter in stagewise partition model
d_p	effective diameter of particle, m
d_r	diameter of reactor, m
D	coefficient, in [6.34]
e	exponent, in [5.11]
E	coefficient, in [4.7]
E_{zl}	liquid axial dispersion coefficient, $m^2\ s^{-2}$
F_B	bouyant force on single bubble, N

F_I	inertial force on single bubble, N
F_M	gas momentum force on single bubble, N
F_r	particle Froude number
F_{ST}	surface tension force on single bubble, N
F_V	viscous force on single bubble, N
F_{vp}	viscous force on plate in a viscometer, N
g	acceleration due to gravity, $m\ s^{-2}$
G	coefficient, in [4.8]
G_1	coefficient, in [6.67]
h	height of secondary bubble from face of orifice, m
H	coefficient in Appendix G, in [G.40]
H_e	expanded bed height, m
H_s	stagnant bed height, m
H_t	total height of reactor, m
HWU	height of wake shedding unit in stagewise partition model
IBP	initial boiling point of bitumen, $°F$
K	coefficient, in [5.11]
K_1	coefficient, in [5.26]
K_w	Watson characterization factor, $°R^{1/3}$
K_{wf}	Watson characterization factor of fraction, $°R^{1/3}$
K_{wm}	Watson characterization factor of mixture, $°R^{1/3}$
L	charecteristic length of the reactor, m
L_c	center to center distance between two orifices, m
m	mass of gas in bubble model, kg
M	mass of single bubble, kg
mf_f	mole percent of fraction
Mo	Morton number

MW_f	molecular weight of fraction
MW_l	molecular weight of liquid phase
MW_m	molecular weight of mixture
MW_v	molecular weight of vapor phase
M_1	factor, in [6.58]
n	Richardson-Zaki exponent in generalized wake model
n_1	number of fractions in a mixture
N	stage number in stagewise partition model
N_o	number of orifices on the gas distributor
N_w	gas flow rate number
P	pressure, *psia*
P^*	parachor factor
P_{cf}	critical pressure of fraction, *psi*
P_{sf}	saturation pressure of fraction, *psia*
P_{rsf}	reduced saturation pressure of fraction, *psia*
P_{cm}	critical pressure of mixture, *psi*
P_e	Peclet number
P_i^*	parachor factor of i^{th} component
P_{reqd}	adjusted pressure in reactor, MPa
q_{df}	drift flux of the gas phase in three phase system, $m\ s^{-1}$
q_{df}''	drift flux of the gas phase in two phase system, $m\ s^{-1}$
Q	volumetric flow through single orifice, $m^3\ s^{-1}$
Q_D	processing capacity of the reactor, $kg\ s^{-1}$
Q_e	effective flow rate of effluent out of reactor, $mol\ m^{-3}$
Q_f	fresh feed rate through the reactor, $m^3\ s^{-1}$
Q_g''	volumetric flow rate of the gas phase through the reactor, in a two phase system, $m^3\ s^{-1}$

Q_l''	volumetric flow rate of the liquid phase through the reactor, in two phase system, $m^3\ s^{-1}$
Q_T	total feed rate through reactor, $m^3\ s^{-1}$
r	instantaneous radius of secondary bubble, m
r_E	radius of bubble at end expansion stage, m
r_o	radius of orifice, m
rr	rate of reaction, $mol\ s^{-1}$
R	gas constant, $ft^3\ psia\ lbmol^{-1}\ R^{-1}$
R_r	recycle ratio for reactor
R_v	radius of the cone in a viscometer, m
Re_b	bubble Reynold number
Re_p	particle Reynold number
R_1	reaction rate constant
s_{gf}	specific gravity of fraction at 60° F
s_{gm}	specific gravity of mixture at 60° F
$(s_{gm})_{cal}$	calculated specific gravity of mixture at 60° F
$(s_{gm})_{exp}$	experimental specific gravity of mixture at 60° F
S_r	Strouhal number
S_v	liquid hourly space velocity, h^{-1}
t	time variable, s
t_b	temperature of fraction, $°F$
t_{be}	boiling point of bitumen in extrapolated region on the SIMDIS curve, $°F$
t_c	time for closure of primary bubble, s
t_{eb}	end boiling point, $°F$
t_{ib}	intial boiling point, $°F$
t_{mb}	mean boiling point, $°F$

t_i	time for interference between primary and secondary bubbles, s
tdh	total particle disengaging height, m
T	coefficient in Appendix G, in [G.41]
T_b	normal boiling point, $°R$
T_{bf}	mean boiling point of fraction, $°R$
T_{cf}	critical temperature of fraction, $°R$
T_{cm}	critical temperature of mixture, $°R$
T_f	temperature of fraction $°R$
T_{cm}	critical temperature of mixture, $°R$
T_{rf}	reduced temperature of fraction,
$TPEB$	Three Phase Ebullieted Bed
u_{br}	effective bubble rise velocity w.r.t. liquid-solid region in three phase ebullieted bed, $m\ s^{-1}$
u_g	gas superficial velocity, $m\ s^{-1}$
u_i	Richardson-Zaki intercept in the generalised wake model
u_l	liquid superficial velocity, $m\ s^{-1}$
u_b	mean bubble rise velocity relative to column, $m\ s^{-1}$
$u_{br\,mod}$	adjusted effective bubble rise velocity w.r.t. liquid-solid region in three phase ebullieted bed, $m\ s^{-1}$
u_{lmf}	minimum fluidization liquid velocity in three phase system, $m\ s^{-1}$
u_{tb}	terminal velocity of single bubble rising through a liquid column, $m\ s^{-1}$
u_{tp}	terminal velocity of single solid particle in a liquid column, $m\ s^{-1}$
u_{tr}	liquid velocity for transition from coelesced to dispersed regime, $m\ s^{-1}$
v	instantaneous velocity of tip of bubble, $m\ s^{-1}$

v' velocity of single bubble during detachment stage, $m\ s^{-1}$

v_{cf} critical volume of fraction, $ft^3\ lbm^{-1}$

v_{ci} critical volume of i^{th} component, $ft^3\ lbm^{-1}$

v_g gas linear velocity in three phase system, $m\ s^{-1}$

v_g'' gas linear velocity in two phase system, $m\ s^{-1}$

v_l liquid linear velocity in three phase system, $m\ s^{-1}$

v_{lf}'' solid linear velocity in solid-liquid region, $m\ s^{-1}$

v_{sf}'' solid linear velocity in solid-liquid region, $m\ s^{-1}$

V instantaneous volume of rising bubble, m^3

V_A additional volume of gas entering bubble during its closure, m^3

V_E volume of bubble at end of expansion stage, m^3

Vol_{cat} volume of catalyst in reactor, m^3

$(Vol)_{C_4H_{10}}$ volume of butane to be mixed with hydrogen fed to reactor, m^3

$(Vol)_{N_2}$ volume of nitrogen to be mixed with hydrogen fed to reactor, m^3

V_R volume of reactor, m^3

V_T total volume of bubble, m^3

V_s instantaneous volume of growing secondary bubble, m^3

V_v relative velocity of plates in a viscometer, m/s

V_1 velocity of gas at single orifice, $m\ s^{-1}$

V_2 velocity of gas inside bubble, $m\ s^{-1}$

V_3 value of vortex of parabola in the extrapolated region of SIMDIS curve, $°F$

w_b total weight % of bitumen distilled at temperature t_b

w_{be} weight percent of bitumen distilled in extrapolated region of SIMDIS curve

w_{ff} weight fraction of fraction

W_A work of adhension per unit interficial area, $kg\ s^{-2}$

We_p	Weber number
x	ratio of solid holdup in the liquid-solid region in the generalised wake model
x_1	temperature at which the inverted parabola starts in the extrapolated region of SIMDIS curve, $°F$
x_i	mole fraction of i^{th} component in liquid phase
x_{vf}	volume fraction of fraction
y	distance travelled by bubble from the orifice, m
y_1	value of weight percent of bitumen distilled at the ordinate at which the inverted parabola starts in the extrapolated SIMDIS curve
y_i	mole fraction of i^{th} component in vapor phase
Z_{cf}	critical compressibility factor

Greek letters

α	liquid contact angle, rad
α_v	angle of the cone in a viscometer, m
β	coefficient, in [6.35]
β_T	pressure coefficient for viscosity, MPa^{-1}
β_{Tp}	predicted pressure coefficient for viscosity, MPa^{-1}
$\Delta(s)_{gm}$	difference between $(S_{gm})_{cal}$ and $(S_{gm})_{cal}$
ϵ_g	gas holdup in three phase ebullieted bed
ϵ_g''	gas holdup in two phase system
ϵ_{gc}	calculated gas holdup
ϵ_{ge}	experimental gas holdup

ϵ_κ	$\kappa\epsilon_g$
ϵ_l	liquid holdup in three phase ebullieted bed
ϵ_{lc}	calculated liquid holdup
ϵ_{le}	experimental gas holdup
ϵ_{lf}''	liquid holdup in liquid-solid region of a three phase ebullieted bed
ϵ_s	solid holdup in three phase ebullieted bed
ϵ_{sf}	solid holdup in solid liquid region
λ_r	rotational speed in a viscometer, rad/s
λ_v	shearing strain in a viscometer
κ	ratio of the wake volume to the bubble volume in the generalised wake model
μ_{app}	apparent dynamic viscosity of three phase ebullieted bed, $kg\ m^{-1}\ s^{-1}$
$\mu_{ext,m}$	extrapolated experimental value of dynamic viscosity, $kg\ m^{-1}\ s^{-1}$
μ_f	dynamic viscosity of fraction, $kg\ m^{-1}\ s^{-1}$
μ_{hp}	dynamic viscosity at high pressure, $kg\ m^{-1}\ s^{-1}$
$\mu_{hp,f}$	dynamic viscosity of fraction at high pressure, $kg\ m^{-1}\ s^{-1}$
$\mu_{ht,f}$	dynamic viscosity of fraction at high temperature, $kg\ m^{-1}\ s^{-1}$
μ_m	dynamic viscosity of mixture, $kg\ m^{-1}\ s^{-1}$
μ_o	dynamic viscosity at atmospheric pressure, $kg\ m^{-1}\ s^{-1}$
μ_l	liquid viscosity, $kg\ m^{-1}\ s^{-1}$
ν	shedding frequency for two succcesive vortices in the bubble wake, s^{-1}
ν_c	critical kinematic viscosity of fraction, $m^2\ s^{-1}$
ν_f	kinematic viscosity of fraction, $m^2\ s^{-1}$
ν_{rf}	reduced kinematic viscosity of fraction
$\nu_{ht,f}$	kinematic viscosity of fraction at high temperature, $m^2\ s^{-1}$
ω_f	acentric factor of fraction

ω_m acentric factor of mixture

ϕ critical volume fraction of fraction

ρ_c critical density of fraction, $g\ cm^{-3}$

ρ_g gas density, $kg\ m^{-3}$

$\rho_{ht,f}$ density of fraction at high temperature, $g\ cm^{-3}$

$\rho_{ht,rf}$ reduced density of fraction at high temperature

$\rho_{hthp,f}$ density of fraction at high temperature and high pressure, $g\ cm^{-3}$

ρ_l density of liquid phase, $g\ cm^{-3}$

ρ_{rf} reduced density of fraction

$\rho_{rf,mod}$ modified reduced density

$(\rho_{rf,mod})_{avg}$ average of modified reduced density of fractions, $g\ cm^{-3}$

$(\rho_{rf,mod})_{std}$ standard deviation of modified reduced density of fractions, $g\ cm^{-3}$

$\rho_{r,ref}$ reduced density of fraction at 60° F, $g\ cm^{-3}$

$\rho_{ref,f}$ density of fraction at 60° F, $g\ cm^{-3}$

ρ_v density of vapor phase, $g\ cm^{-3}$

$\rho_{60,f}$ density of fraction at $60°F$, $g\ cm^{-3}$

ρ_p particle (solid) density, $kg\ m^{-3}$

ρ_{N_2} density of nitrogen, $kg\ m^{-3}$

$\rho_{C_4H_{10}}$ density of butane, $kg\ m^{-3}$

σ surface tension, $N\ m^{-1}$

σ_m surface tension of mixture, $N\ m^{-1}$

θ angle between the center of bubble and bubble open edge, rad

θ_c liquid contact angle, rad

θ_r deflection of spring in a viscometer, rad

θ_E angle at end of expansion stage, rad

θ_i instantaneous θ during bubble closure, rad

τ shearing stress in a viscometer, N/m^2

τ_r rotational torque in a viscometer, $N - m$

Subscripts

a = property at atmospheric pressure

c = calculated value

e = experimental value

p = parameter for commercial (proto) system

m = parameter for scaled down (model) system

BIBILOGRAPHY

1. Beattie, C. I., Boberg, T. C. and McNab, G. S., "Reservoir Simulation of Cyclic Steam Stimulation in the Cold Lake Oil Sands", SPE Regional Meeting, Bakerfield, California, April 5-7, 1989.

2. Johnson, L. A. Jr., Fahy L. J., Romanowski, L. J., Jr, Thomas, K. P. and Hutchinson, H. L., "An Evaluation of a Steam Flood Experiment in a Utah Tar Sand Deposit", J. Pet. Tech., May 1982, 1119.

3. Johnson, L. A., Jr., Fahy, L. J., Jr., Barbour, R. V. and Thomas, K. P., "Echoing In-Situ Combustion Oil Recovery Project in a Utah Tar Sands", J. Pet. Tech., Feb. 1980, 295.

4. Miller, J. D. and Misra, M., "Hot Water Process Development for Utah Tar Sand", Fuel Proc., Tech., 1982, 6, 27.

5. Rendall, J. S., "Solvent Extraction Process", U. S. Patent No. 4, 160,718, 1979.

6. Miller, J. D. and Misra, M., "Concentration of Utah Tar Sands by a Ambient Floatation Process", Int. J. Miner. Proc., 1982, 9, 269.

7. Hanson, F. V. and Oblad, A. G., "The Fluidized-Bed Pyrolysis of Bitumen-Impregnated Sandstone from the Tat Sand Deposits of Utah", Proc. The Fourth UNITAR/UNDP International Conference on Heavy Crude and Tar Sands, 5, Extraction Upgrading and Transportation, 1989, 421.

8. Dorius, J. C., "The Pyrolysis of Bitumen-Impregnated Sandstone from the PR Spring (Utah) Deposits in a Fluidized Bed", Ph.D. Dissertation, University of Utah, Salt Lake City, Utah, 1985.

9. Oblad, A. G., Bunger, J. W., Hanson, F. V., Miller, J.D., Ritzma H. R. and Seader J. D.,"Tar Sand Research And Development at the University of Utah", Ann. Rev. Energy, (1987), 283.

10. Tsai, C. H., Deo M. D., Hanson F. V. and Oblad A. G.,"Characterization and Potential Utilization of Whiterocks (Utah) Tar Sands Bitumen".

11. Hupka, J., Miller, J. D., Prepr, SME-AIME Ann. Meet., 82-85, Callas, Feb. 14-18, 1984, 10.

12. Venkatesan, V. N., "Fluid Bed Thermal Recovery of Synthetic Crude from Bituminous Sands of Utah", Ph.D. Dissertation, University of Utah, Salt Lake City, Utah, 1979.

13. Wang, J., "The Production of Hydrocarbon Liquids From a Bitumen-Impregnated Sandstone from the Circle Cliffs (Utah) Deposits, Ph.D. Dissertation, University of Utah, Salt Lake City, Utah, 1987.

14. Shun, D. W., "The Fluidized Bed Pyrolysis of Bitumen-Impregnated Sandstone from the Circle Cliff (Utah) Deposits", Ph.D. Dissertation, University of Utah, Salt Lake City, Utah, 1987.

15. Brechtel, C., "Hydrocracking Utah Tar Sands Products", M.S. Thesis, University of Utah, Salt Lake City, Utah, 1987.

16. Longstaff, D., Ph.D. Dissertation, University of Utah, Salt Lake City, Utah, 1992.

17. Fan, L. S., Gas-Liquid-Solid Fluidization Engineering, Butterworth Series in Chemical Engineering, Edinburgh, 1989.

18. Tarmy, B. L., M. Chang, C. A. Coulaloglou and P. R. Ponzi, "The Three-Phase Hydrodynamic Characteristics of the EDS Coal Liquefaction Reactors; Their Development and Use in Reactor Scaleup", International Symposium on Chemical Reaction Engineering, Sept. 10-13, 1984.

19. Vasalos I. A., Bild E. M., Rundell D. N. and J. W. Gurman, "Study of Ebullieted Bed Fluid Dynamics for H-Coal", Quarterly Report No. 6 to U. S. Department of Energy, Contract No. EF-77-C-01-2588, June, 1979.

20. Virant, M. L., "The Kinetics of the Hydrodesulfurization Process", Appl. Catal., (1983), 6(2), 137.

21. Schuman, S. C. and Shalit H., "Hydrodesulfurization", Catal. Rev., (1970), 4(2), 245.

22. Schuit, G. C. A. and Gates B. C., "Chemistry and Engineering of Catalytic Hydrodesulfurization", AIChE J., (1973), 19(3), 417.

23. Beaton, W. I., Chemical Reaction as a Means of Separation-Sulfur Removal, ed. Crynes G. A., Marcel Dekker, New York, 1977, 1.

24. Gates, B. C., Katzer J. R. and Schuit G. C. A., Chemistry of Catalytic Processes, McGraw-Hill, 1979.

25. Grange, P., "Catalytic Hydrodesulfurization", Catal. Rev.-Sci. Eng., (1980), 21(1), 135.

26. Speight, J. G., The Desulfurization of Heavy Oils and Residual, Marcel Dekker, New York, 1981.

27. Virant, M. L. and Mourgues L. de, J. Chem. Phys., 1982, 79, 45.

28. Topsoe, H., Clausen, B. S., Topsoe N. and Pederesen E., "Basic Research in Hydrodesulfurization Catalysts", I&EC FUNDAM., 1986, 25, 25.

29. Drushel, H. V., ACS Div. of Petrol. Chem., Preprints, (1972), 17(4), F92.

30. Laine, R. M., "Comments on the Mechanism of Hetrogeneous Catalyst of the Hydrodenitrogenation Reaction", Catal. Rev. Sci.-Eng., 25(3), 459.

31. Karos, R. M., Bank S., Hofmann J. E. and M. I. Kay, "Hydrodenitrogenation of Shale Oil", ACS Div. Petrol. Chem., Preprints, 1967, 12(4), B-165.

32. Rollmann, L. D., "Catalytic Hydrogenation of Model Nitrogen, Sulfur and Oxygen Compounds", J. Catal., 1977, 46, 243.

33. Badilla-Ohlbaum, R., Pratt, C. K. and Trimm D. L., "A Study of Nickel-Molybdate Coal-Hydrodeoxygenation Catalyst Using Model Feedstock", Fuel, 1979, 58(4), 309.

34. Furimsky, E., "Chemistry of Catalytic Hydrodeoxygenation", Catal. Rev. Sci.-Eng., 1983, 25(3), 421.

35. Dautzenberg, F. M., and Deken J. C. de, "Modes of Operation in Hydrodemetallization", Symposium on Development in Hydrodemetallization Catalysts, ACS Div. of Petrol. Chem., Preprint, 1985, 8.

36. Ware, R. A. and Wei, J., "Hydrodemetallation Reaction Selectivity on Modified Co-Mo Catalysts", Symposium on Development in Hydrodemetalization Catalysts, ACS Div. of Petrol. Chem., Preprint, 1985, 62.

37. Ware, R. A. and J. Wei, "Catalytic Hydrodemetallation of Nickel Porphyrins", J. Catal., 1985, 93, 100.

38. Takeuchi, C. S., Asaoka, S., Nakata, S. and Shiroto, Y., "Characteristics of Residue Hydrodemetallation Catalysts", Symposium on Development of Hydrodemetallization Catalyst, ACS Div. of Petrol. Chem., Preprints, 1985, 96.

39. Galiasso, R., Gracia, J., Caprioli, L., Pazos, J. M. and Soto, A., "Reaction of Porphyrinic and Nonporphynic Molecules During Hydrodemetallization of Heavy Oils", Symposium on Development in Hydrodemetallization Catalysts, ACS Div. of Petrol. Chem., Preprints, 1985, 50.

40. Chianelli, R. R., "Fundamental Studies of Transition Metal Sulfide Hydrodesulfurization Catalysts", Catal. Rev.-Sci. Eng., 1984, 26(3,4). 361.

41. Topsoe, H. and Clausen, "Importance of Co-Mo-S Type Structures in Hydrodesulfurization", Catl. Rev.-Sci. Eng., 1984, 26, 395.

42. Beuther, H. and Schmid, B. K., Proceedings of the 6th World Petroleum Congress, 1963, 3, 297.

43. Ohtsuka, T., "Catalyst for Hydrodesulfurization of Petroleum Residua", Catal. Rev.-Sci. Eng., 1977, 16(2), 291.

44. Kato, J., Shimada, K., Suzuki, M., Ose, H. and Ohshima S., Kogyo Kagakushi, Japan, 1971, 74(6), 1156.

45. Thakur, D. S. and Thomas M. G., "Catalyst Deactivation in Heavy Petroleum and Synthetic Crude Processing: A Review", Appl. Catal., 1985, 15(2), 197.

46. Mosby, J. F., Buttke, R. D., Cox, J. A. and Nikolaides, C., "Process Characterization of Expanded-Bed Reactors in Series", Chem. Eng. Sci., 1986, 41, 989.

47. Dautzenberg, F. M., George, S. E., Ouwerkere, C. and Sie, S. T., Advances in Catalytic Chemistry Symposium, Salt Lake City, Utah, May, 1982.

48. Dautzenberg, F. M. and Deken J. C. de, "Reactor Development in Hydrotreating and Conversion of Residues", Catal. Rev.-Sci. Eng., 1984, 26, 421.

49. Toulhoat, H., Plumail, J. C., Martino, G. and Jacquin, Y., "New HDM Catalysts Design and Performance for Demetallization and Conversion", Symposium on Development in Hydrodemetallization Catalysts, ACS Div. of Petrol. Chem., Preprints, 1985, 85.

50. Voorhie A. Jr. and Smith W. M., "Advances in Hydrocracking", Advances in Petroleum Chemistry and Refining, ed. McKetta, J. J. Jr., Interscience Publishers, John Wiley & Sons, New York, VII, 1964, 168.

51. Rapp, L. M. and Van Driesen, R. P., "H-Oil Process Gives Product Flexibility", Hydrocracking Handbook, Gulf Publishing Company, 1972.

52. Department Report to DOE, March 1990.

53. Robbers, J. A., Paterson N. J. and Lane W. T., Hydrocarbon Process. Petrol. Refiner, 1961, 40(6), 147.

54. Adams, N. R., Watkins C. H. and Stine, L. O., "Flexibility of the Lomax Process", Chem. Eng. Progs., 1961, 57(12), 55.

55. Sterba, M. J. and Watkins, C. H., "Production of Gasoline from Distillation", 48th Annual Meeting of the Western Petroleum Refiners Association, San Antonio, Texas, March 28-30, 1960. Adapted in Oil Gas J., 1960, 58(21), 102.

56. Billon, A., Derrien, M., Lavergne, J. C., Nonnenmarcher, H., Oettinger and Reitz, O., "What BASF-IFP Hydrocracking Will Do", Hydrocarbon Processing, 1966, 45(3), March, 129.

57. Johnson, A. R., Alpert, S. B. and Lehman L. M., "Refining Applications of the H-Oil Process", 33rd Midyear Meeting of the American Petroleum Institute's Division of Refining, Philadelphia, Penn., May, 16, 1968.

58. Duir, J. H., "Hydrocrack Now in Single Stage", Hydrocarbon Processing, 1967, 46(9), Sept., 121.

59. "Isomax", Hydrocarbon Process. Petrol. Refiner, 1962, 41(9), 153.

60. Beuther H., McKinley, J. B. and Flinn, R. A., "Catalytic Hydrocracking", Symposium on A Decade of Progress in Petroleum Technology, Division of Petroleum Chemistry American Chemical Society, Chicago meeting, September 3-8, 1961, 6(3).

61. Sullivan, R. F., "Catalytic Effect on Yield and Product Properties in Hydrocracking", Desulfurization of Petroleum, by Maurice William Ranney, Noyer Data Corporation.

62. Chen, H. H., Montgomery, D. S. and Strausz, O. P., "Hydrocracking of Athabasca Bitumen Using Oil-Soluble Organometallic Catalyst. Part I: Influence of Temperature and Catalyst Activity", AOSTRA J. of Research, 1988, 4(1), 45.

63. Chen, H. H., Montgomery, H. S. and Strausz, O. P., "Hydrocracking of Athabasca Bitumen Using Oil-Soluble Organometallic Catalyst. Part II: Comparision of Metal Naphthenates and Metal Acetylacetonates with Nickel Carboxylate as Oil-Soluble Liquid Phase Hydrocracking Catalysts", AOSTRA J. of Research, 1988, 4(2), 143.

64. Chen, H. H., Montgomery, H. S. and Strausz, O. P., "Hydrocracking of Athabasca Bitumen Soluble Organometallic Catalyst. Part III. Optimization of Liquid-Phase Hydrocracking Conditions for Mixtures of Nickel and Molybdenum Naphthenates and Coking Studies on the Hydrocracked Product", AOSTRA J. of Research, 1989, 5(1), 33.

65. Archibald, R. C., Greensfelder B. S., Holzmann, G. and Rowe, D. H., "Catalytic Hydrocracking of Aliphatic Hydrocarbons", Ind, Eng. Chem., 1960, 52, 745.

66. Coonradt, H. L. and Garwood W. E., "Modification of the Relative Rates of Competitive Hydrocracking Reaction", Preprints, Div. Petrol. Chem. Am. Chem. Soc., 1967, 12(4), B-47.

67. Flinn, R. A., Larson, O. A. and Beuther, H., "The Mechanism of Catalytic Hydrocracking", Ind. Eng. Chem., 1960, 52, 153.

68. Haensd, V., Pollitze, E. L. and Watkins, C. H., Preprints, World Petrol. Congr., 1963, 6th, sec. III, paper 17.

69. Langlois, G. E., Sullivan, R. F. and Egan, C. J., "The Effect of Sulfiding a Nickel on Silica-Alumina Catalyst", J. Phys. Chem., 1966, 70, 3666.

70. Pier, M. Z., Elektrochem, 1949, 53, 291.

71. Scott, J. W., Manson, H. F. and Kozlonski, Petrol. Refiner., 1960, 39(4).

72. Speight, J. G., The Chemistry and Technology of Petroleum, Marcel Dekker, 1980.

73. Coonradt, H. L., "The Mechanism of Hydrocracking Reactions of Paraffins and Olefins", 140th Meeting of the American Chemical Society, Chicago, Illinois, September 3-8, 1961.

74. Frye, C. G., "Hydroisomerization of Olefins", preprint, Div. Petrol. Chem. Am. Chem. Soc., 1961, 7, No. 4, A-21.

75. Sullivan, R. F., J. Am. Chem. Soc., 1961, 83, 1156.

76. Langlois, G. E., "Chemistry of Hydrocracking and Hydrotreating", ACS Symposium Series 20, ed. Ward, J. W. and Qader, S. A.

77. Speight, J. G., The Desulfurization of Heavy Oils and Residual, Marcel Dekker, 1981.

78. Galiasso, R., Gracia, J., Caprioli, L., Pazos, J. M. and Soto, A., "Reaction of Porphyrinic and Non Porphynic Molecules During Hydrodemetallization of Heavy Oils", Symposium on Development in Hydrodemetallization Catalysts, ACS Div. of Petrol. Chem., Preprints, 1985, 50.

79. Asoaka, S., Nakata, S., Shirito, Y. and Takeuchi, C., "Asphaltene Cracking in Catalytic Hydrotreating of Heavy Oils. Studies of Changes in Asphaltene Structure During Catalytic Hydroprocessing", I&EC Process Des. & Dev., 1983, 22, 242.

80. ASTM D524-81, Method to Determine Ramsbottom Carbon.

81. Johanson, E. S., US Patent 2,987,465, 1961.

82. Brownell, L. E., Encyclopedia of Chemical Technology, ed. Kirk, R. E. and Othmer, D. F., Interscience Encyclopedia, New York, 1951,6, 516.

83. Thompson, A. R., Encyclopedia of Chemical Technology, ed. Kirk, R.E. and Othmer, D. F., Interscience Encyclopedia, New York, 1955, 4, 619.

84. Johnson, T. E., Murphy, J. R. and Tasker, K. G., "Combined Cracking Process Boost Fuel Yield", Technology (Oil and Gas J.), July 1, 1985, 50.

85. Beaton, W. I., McDaniel, N. K., McWhirter, W. E., Petersen, R. D. and Driesen Van R. P., "Resid Hydrocracking Expands Crude Processing Flexibility", Technology (Oil and Gas J.), July 7, 1986, 47.

86. Li, A. and Lin, D., "Scaleup Performance and Thermal Stability Analysis of H-Oil and H-Coal Ebullated Bed Reactor", Proceeding of the 2nd World Congress of Chemical Engineering, 1981, IV, 170.

87. Ashland Synthetic Fuels Inc., Final Report to U. S. Department of Energy, Contract No. DE-AC05-76ET10143, April, 1984.

88. Oloman, C. and Watkinson A. P., "The Electroreduction of Oxygen to Hydrogen Peroxide on Fluidized Cathodes", Can. J. Chem. Eng. 1975, 53, 268.

89. Kusakabe, K. S., Morooka and Kato, Y., "Charge Transfer Rate in Liquid-Solid and Gas-Liquid-Solid Bed Electrodes", J. Chem. Eng., Japan, 1981, 14(3), 208.

90. Blum, D. B. and Toman, J. J., "Three-Phase Fluidization in a Liquid Phase Methanator", AIChE Symposium Series, 1977, 73(161), 115.

91. Sastry, N. V. S., N. Epstein, A. Hirata, I. Koshijima and M. Izumi, "Zinc Hydrosulphite by Three-Phase Fluidization Experimental and Modelling", Can. J. Chem. Eng., (1983), 61, 635.

92. Ermakova, A., Ziganshin, G. K., Stefoglo, E. F. and Slin'ko M. G., Theor. Osnovy Khim. Tekhnol. 1973, 7(1), 35.

93. Gartsman, A. N., Ermakova, A., Bakhbalova, V. P. and Rassadmkova N. I., "Mass Transfer with Chemical Reaction in Three-Phase System Gas-Liquid-Solid Catalyst", Int. Chem. Eng., 1977, 17, 697.

94. Volpicell, G. and Massimilla, L., Pulp Paper Mag., Canada, 1965, 66(10), T512, October.

95. Sherwin, M. B. and Frank, M. E., "Make Methanol by Three Phase Reactor", Hydrocarbon Processing, 1976, 55(11), 122.

96. Scott, C. D. and Hancher, C. W., "Use of a Tapered Fluidized Bed as a Continuous Bioreactor", Biotech. Bioeng., 1976, 18, 1393.

97. Holladay, D. W., Hancher, C. W. Scott, C. D. and Chilcote, D. D., J. Water Pollution Control Fed., 1978, 50, 2573.

98. Lee, D. D., Scott, C. D. and Hancher, C. W., J. Water Pollution Control Fed. 1979, 51, 974.

99. Shen, Y. M. and Wang, B. L., Research Report, No.2, Chen-du Institute of Municipal Engineering, China, 1980.

100. Hirata, A., Hosaka, Y., Mukai, H. and Kaiho, M., Water Purification and Liquid Waste Treatment, 1982, 23, 15.

101. Hosaka, Y., Kaihon, M. and Hirata, A., "Biological Treatment of Phenolic Wastewater in a Three Phase Fluidized Bed", Water Sci. and Technol., 1985, 17(8), 1437.

102. Donaldson, T. L., Strandberg, G. W., Hewitt, J. D. and Shields, G. S., "Biooxidation of Coal Gasification Wastewater", Environ. Prog., 1984, 3, 248.

103. Forster, C. F., Boyes, A. P., Hay, B. A. and Butt J. A., "An Aerobic Fluidized Bed Reactor for Wastewater Treatment", Chem. Eng. Res. Des., 1986, 64(6), 425.

104. Ostergaard, K., Studies of Gas-Liquidization, Danish Technical Press, Copenhagen, 1969.

105. Epstein, N., "Criterion for Initial Contraction or Expansion of Three-Phase Fluidized Beds", Can. J. Chem. Eng., 1976, 59, 259.

106. Ermakova, A., Ziganshin, G. K. and Slinko, M. G., "Hydrodynamics of a Gas-Liquid Reactor with a Fluidized Bed of Solid Matter", Theor. Found. Chem. Eng., 1970, 4, 84.

107. Dhanuka, V. R., Ph. D. Thesis, University of Salford, England, 1978.

108. Jean, R. H., Ph. D. Dissertation, The Ohio State University, 1988.

109. Fan, L. S., Satija, S. and Wisecarver, K., "Pressure Fluctuation Measurements and Flow Regime Transition in Gas-Liquid-Solid Fluidized Bed", AIChE J., 1986, 32(2), 338.

110. Song. G. H., Bavarian, F., Fan, L. S., Buttke, R. D. and Peck L. B., AIChE Annual Meeting, New York, Nov. 15-20, 1987.

111. Wen, C. Y. and Yu, Y. H., Chem. Eng. Prog. Symposium Series, 1986, 62(62), 100.

112. Fan, L. S., Matsuura, A. and Chern S. H., "Hydrodynamic Characterization of a Gas-Liquid-Solid Fluidized Bed Containing a Binary Mixture of Particles", AIChE J., 1985, 31(11), 1801.

113. Muroyama, K. and Fan L. S., "Fundamentals of Gas-Liquid-Solid Fluidization", AIChE J., 1985, 31, 1.

114. El-Temtamy, S. A. and Epstein, N., "Contraction or Expansion of Three-Phase Fluidized Beds Containing Fine/Light Solids", Can. J. Chem. Eng., 1980, 57, 520.

115. Idogawa, K., Ikeda, K., Fukuda, T. and Morooka, S., "Behavior of Bubbles of the Air Water System in a Column Under High Pressure", Int. Chem. Eng., 1986, 26(3), 468.

116. Michelsen, M. L. and Ostergaard, K., "Hold-Up and Fluid Mixing in Gas-Liquid Fluidised Beds", Chem. Eng. J., 1970, 1, 37.

117. Kim, S. D., Baker, C. G. J. and Bergougnou, M. A., "Phase Holdup Characteristics of Three Phase Fluidized Beds", Can. J. Chem. Eng., 1975, 53(2), 134.

118. Catros, A., Bernard, J. R., Briens, C. and Bergougnou, M. A., "Gas Holdup Above the Bed Surface and Grid Gas Jet Hydrodynamics for Three-Phase Fluidized Beds", Can. J. Chem. Eng., 1985, 63(5), 754.

119. Bhatia, V. K. and Epstein, N., "Three-Phase Fluidization: A Generalized Wake Model, Fluidization and Its Applications, ed. Angelino, H., Couderc, J. P., Gilbert, H. and Laguerie, C., Cepadues-Editions, Toulouse, 1974, 380.

120. Armstrong, E. R., "Heat Transfer and Hydrodynamic Studies in Three-Phase Fluidized Beds", M. E. Sc. Thesis, The University of Western Ontario, London, Canada, 1975.

121. Dakshinamurthy, P., Subramanyam, V. and Rao, J. N., "Bed Porosities in Gas-Liquid Fluidization", I&EC Process Des. & Dev., 1971, 10(3), 322.

122. Saberian-Broudjenni, Wild, M. G., Charpentier, J. C., Fortin, Y., Euzen, J. P. and Patoux, R., Entropie, 1984, 120, 30.

123. Song, G. H. and Fan, L. S., Proceedings of the 3rd World Congress of Chemical Engineering, III, Tokyo, Sep., 1986, 504.

124. Bhaga, D. and Weber, M. E., "Bubble in Viscous Liquids: Shape, Wakes and Velocities", J. Fluid Mech., 1981, 105, 61.

125. Darton, R. C. and Harrision, D., "TITTLE", Inst. Chem. Engrs. Symposium Series, 38, Multi-Phase Flow Systems, I, Inst. Chem. Engr., London, 1974.

126. Ostergaard, K., Fluidization, Soc. Chem. Ind., London, 1964, 58.

127. Peterson, D. A., Tankin, R. S. and Bankoff, "Bubble Behavior in a Three-Phase Fluidized Bed", Int. J. Multiphase Flow, 1987, 13(4), 477.

128. Page, R. E. and Harrison, Fluidization and Its Applications, ed. Angelino, H., Couderc, J. P., Gibert, H. and Laguerie, C., Cepadues-Edition, Toulouse, 1974, 393.

129. Rigby, G. R. and Capes, C. E., "Bed Exapansion and Bubble Wakes in Three-Phase Fluidization", Can. J. Chem. Eng., 1970, 48(4), 343.

130. Fan, L. S., Tsuchiya, K. and Miyahara, T., Fluidization '88 Science and Technology-Conference Paper 3rd China-Japan Symposium, ed Kwauk, M. and Kunii, D., Science Press (Beijing, China), 1988, 204.

131. Lee, J. C., Proceeding of the 3rd European Symposium on Chemical Reaction Engineering, Pergamon Press, Oxford, 1965, 211.

132. Boys, C. V., Society for Promoting Christan Knowledge, London, 1890.

133. Chang, H. S. and Kim, S. D., Hwahak Konghak (J. Korean Inst. Chem. Engrs.), 1979, 17, 407.

134. Davies, R. M. and Taylor, G. I., "The Mechanicss of Large Bubble Rising Through Extended Liquids and Through Liquids in Tubes", Proc. Roy. Soc., 1950, A200, 375.

135. Matsuura, A. and Fan, L. S., "Distribution of Bubble Properties in a Gas-Liquid-Solid Fluidized Bed", AIChE J., 1984, 30(6), 894.

136. Coppus, J. H. C., Rietema, K. and Ottengraf, S. P. P., "Wake Phenomena Behind Spherical Bubbles and Solid Spherical-Cap Bodies", Trans. Int. Chem. Engrs., 1977, 55(1), 122.

137. Tsuchiya, K. and Fan, L. S., AIChE Annual Meeting Maimi Beach, Nov. 2-7; Chem. Eng. Sci., 1988, 43(5), 1167.

138. Darton, R. C. and Harrison, D., Fluidization Technology, ed. Kearirns, D. L., I, Hemisphere, 1976, 399.

139. El-Temtamy and Epstein, N., Proceedings of the 2nd Pacific Area Chemical Engineering Congress (PACHEC), Denver. 1977, 1397; "Bubble Wake Solids Content in Three-Phase Fluidized Beds", Int. J. Multiphase Flow, 1978, 4, 19.

140. Richardson, J. F. and Zaki, W. N., "Sedimentation and Fluidization: Part I", Trans. Inst. Chem. Engrs., 1954, 32, 35.

141. Darton, R. C. and Harrision D., "Gas and Liquid Hold-Up in Three-Phase Fluidization", Chem. Eng. Sci., 1975, 30, 581.

142. Epstien, N., "Criterion for Initial Contraction or Expansion Of Three-Phase Fluidized Beds", Can. J. Chem. Eng., 1976, 54, 259.

143. Jean, R. H. and Fan, L. S., "Letter to the Editor", Can. J. Chem. Eng., 1987, 65, 351.

144. El-Temtamy, S. A. and Epstein N., "Simultaneous Solid Entrainmrnt and Deentrainment Above a Three-Phase Fluidized Bed", Fluidization, ed. Grace, J. R. and Matsen, J. M., Plenum Press, 1980, 519.

145. Morooka, S., Uchida, K. and Kato, Y., "Recirculating Turbulent Flow of Liquid in Gas-Liquid-Solid Fluidized Bed", J. Chem. Eng. Japan, 1982, 15(1), 29.

146. Bhaga, D. and Weber, M. E., "Holdup in Vertical Two And Three Phase Flow Part I: Theoretical Analysis", Can. J. Chem. Eng., 1972, 50(3), 323.

147. Bhaga, D. and Weber, M. E., "Holdup in Vertical Two and Three Phase Flow Part II: Experimental Investigation", Can. J. Chem. Eng., 1972, 50(3), 329.

148. Tadaki, T. and S. Maeda, "Shape and Velocity of Single Air Bubble Rising in Various Liquids", Kogaku Kogaku, (1961), 25, 254.

149. Sastry, N. V. S., N. Epstein, A. Hirata, I. Koshijima and M. Izumi, "Zinc Hydrosulphite by Three-Phase Fluidization Experimental and Modelling", Can. J. Chem. Eng., (1983), 61, 635.

150. Perry, R. H., Green, D. W. and Malonney, J. O., 1988, Chemical Engineers' Handbook, Sixth Edition, McGraw Hill Book Company, New York, 1988, p 18-58.

151. Page, R. E. and Harrison D., Fluidization and its Application, ed. Angelino H., Coudere J. P., Gilbert H. and Laguerie C., Cepadues-Edition, Toulouse, 1974.

152. Lapidus, L. and J. C. Elgin, "Mechanics of Vorticle-Moving Fluidized Systems", AIChE J., 1957, 3, 63.

153. Tsuchiya, K. and Fan L. S., AIChE Annual Meeting, Miami Beach, Nov., 2-7, 1986; "Near-Wake Structure of a Single Gas Bubble in a Two-Dimensional Liquid-Solid Fluidized Bed: Vortex Shedding and Wake Size Variation", Chem. Eng. Sci., (1988), 43, 1167.

154. Idogawa, K., Ikeda, K., Fukuda, T. and Morooka, S., "Behavior of Bubbles of the Air-Water System in a Column Under High Pressure". Int. Chem. Engng., 1986, 26, 468.

155. Ramakrishna, S., Kumar, R. and Kuloor, N. R., "Studies in Bubble Formation - I Bubble Formation Under Constant Flow Conditions". Chem. Engng. Sci., 1968, 24, 731.

156. Azabel, D., Two Phase Flows in Chemical Engineering, Cambridge University Press, Cambridge, 1981.

157. Tsuge, H. and Hibino, S., "Bubble Formation from a Submerged Single Orifice Accompanied by Pressure Fluctuations in Gas Chamber", J. Chem. Eng. Japan, 1978, 11, 173.

158. Rothbart, H. A., Mechanical Design and Systems Handbook, Harold A. Rothbart, Editor in Chief, McGraw Hill Book Co., New York, 1964.

159. Datta, R. L., Napier, D. H. and Newitt, D. M., "The Properties and Behaviour of Gas Bubbles Formed at a Circular Orifice". Conference on Formation and

Properties of Gas Bubbles, Institution of Chemical Engineers, Burlington House, London, 1950.

160. Davidson, J. F., Schüler, B. O. G., 1960, "Bubble Formation at an Orifice in an Inviscid Liquid". Tran. Instn. Chem Engrs., 1960, 38, 335.

161. Tsuge, H., 1986, "Hydrodynamics of Bubble Formation From Submerged Orifices". Chapter 9, Encyclopedia of Fluid Mechanics, 3, Cheremisinoff N. ed., Gulf Publishing Corp., 1985, 191-232.

162. Towell, G. D., Strand, C. P.and Ackerman, G. H., "Mixing Theory Related to Practice", AIChE- I. Chem. E. Symp. Ser., 1965, 10, 97.

163. Bhatia, V. K., "Gas Holdup of a Bubble Swarm in Two Phase Vertical Flow", AIChE. J., 1969, 15, 466.

164. Nicklin, D. J., "Two-Phase Bubble Flow", 1962, Chem. Eng. Sci., 17, 693.

165. Tadaki, T. and Maeda, S., "Shape and Velocity of Single Air Bubble Rising in Various Liquids", 1961, Kogaku Kogaku, 25, 254.

166. Marquardt, D. W., "An Algorithm For Least - Square Estimation Of Nonlinear Parameters", J. Soc. Ind. App. Math., 1963, 11, 431.

167. Baker C. G. J., Personal Communication, July 26, 1991.

168. Viswanathan S., Kakar, A. S. and Murti, P. S., "Effect of Dispersing Bubbles into Liquid Fluidized Beds on Heat Transfer and Holdup at Constant Bed Expansion", Chem. Eng. Sci., 1964, 20, 903.

169. Lee J. C., Proceedings of the 3rd European Symposium On Chemical Reaction Engineering, Pergamon Press, Oxford, 1965, 211.

170. Ostergaard, K., "On the Growth of Air Bubbles Formed at a Single Orifice in a Water Fluidized Bed", Chem. Eng. Sci., 1966, 21, 470.

171. Rigby G. R., Blockland, Van G. P., Park, W. H. and Caper, C. E., "Properties of Bubbles in Three-Phase Fluidized Beds as measured by an Electroresistivity Probe", Chem. Eng. Sci., 1970, 25, 1729.

172. Song, G. H. and Fan, L. S., Proceedings of the 3rd World Congress of Chemical Engineering, 1986, III, Tokyo, September, 504.

173. Adamson, A., W., Physical Chemistry of Surfaces, 4th ed., John Wiley, 1982.

174. Wallis, G. B., One-Dimensional Two-Phase Flow, McGraw-Hill Book Company, New York, 1980.

175. Zuber, N. and Findlay, J. A., "Average Volumetric Concentration in Two-Phase Flow Systems", 1965, J. of Heat Transfer, Nov.

176. Redlich, O. and J. N. S. Kwong, "On The Thermodynamics Of Solution. V. An Equation Of State: Fugacities Of Gaseous Solution", Chem. Rev., 1949, 44, 233.

177. Mehrotra, A. K. and Svrcek, W. Y., "Measurement And Correlation Of Viscosity, Density And Gas Solubility For Marguerite Lake Bitumen Saturated With Carbon Dioxide", AOSTRA J. Res., 1984, **1**, 51.

178. Mehrotra, A. K. and Svrcek, W. Y., "Viscosity, Density And Gas Solubility Data For Oil Sand Bitumens. Part I: Athabasca Bitumen Saturated With CO And C_2H_6", AOSTRA J. Res., 1985, **1**, 263.

179. Mehrotra, A. K. and Svrcek, W. Y., "Viscosity, Density And Gas Solubility Data For Oil Sand Bitumens. Part II: Peace River Bitumen Saturated With N_2, CO, CH_4, CO_2 and C_2H_6", AOSTRA J. Res., 1985, **1**, 269.

180. Mehrotra, A. K. and Svrcek, W. Y., "Viscosity, Density And Gas Solubility Data For Oil Sand Bitumens. Part III: Wabasca Bitumen Saturated With N_2, CO, CH_4, CO_2 and C_2H_6", AOSTRA J. Res., 1985, **2**, 83.

181. Mehrotra, A. K., Sarkar, M. and Svrcek, W. Y., " Bitumen Density And Gas-Solubility Predictions Using The Peng-Robinson Equation of State", AOSTRA J. Res., 1985, **1**, 215.

182. Mehrotra, A. K., and Svrcek, W. Y., "Properties Of Cold Lake Bitumen Saturated With Pure Gases And Gas Mixtures", Can. J. Chem. Eng., 1988, **66**, 656.

183. Jacob, F. A., "Viscosity Of Gas-Saturated Bitumen", J. Can. Pet. Tech., 1980, October-December, 46.

184. JEFFRI Mannual, courtesy of D. B. Robinson and Associates and S. K. Sim and C. J. Chen, "Behavior Of Bitumen Mixtures During In Situ Recovery", AOSTRA agreement 184, Final Report, July, 1983.

185. AOSTRA/ARC, Viscosity Assessment Report No. 8586-30, October, 1985.

186. Helper, L. G. and Hsi, C. ed., AOSTRA Technical Handbook On Oil Sands,

187. Whorlow, R. W., Rheological Techniques, John Wiley and Sons, Rexdale, Ontario, 1980.

188. Middleman, S., The Flow of High Polymers, Interscience, New York, 1968.

189. Schramm, L. L., Smith, R. G. and Stone, J. A., "A Surface Tension Method for the Determination of Aniomic Surfactants in Hot Water Processing of Aniomic Oil Sands", Colloids and Surfaces, 1984, 11, 107.

190. Potoczny, A. M., Vargha-Butler, E. I., Zubovits and Neumann, A. W., "Surface Tension of Bitumen II.: Solvent andFractionation Effects", AOSTRA J. Res., 1984, 1, 118.

191. American Petroleum Institute, Technical Data Book-Petroleum Refining, 4th Ed., API, Washington, DC, 1983.

192. Watson, K. M., "Thermodynamics Of The Liquid State", Ind. Eng. Chem., 1943, 35, 398.

193. Riedel, L., "A New Universal Vapor Pressure Formula", Chem. Ing.-Tech., 1954, 26, 83.

194. Riazi, M. R., and Daubert, T. W., "Simplify Property Prediction", Hydrocarbon Process., 1980, 59(3), 115.

195. Chuch, P., L., and J. M. Prausnitz, "Vapor-Liquid Equiblibrium At High Pressure: Calculation Of Critical Temperature, Volume, and Pressure Of Nonpolar MixtureS", AIChE J., 1967, 13, 1107.

196. Hankinson, R., W., and G. H. Thomson, "Calculate Liquid Densities Accurately", Hydrocarbon Processing, 1979, 58 (9), 277.

197. Maxwell, J. B., Data Book On Hydrocarbons-Application For Process Engineering, D. Van Nostrand Co. Inc., New York, 1950.

198. Hwang, S., C. Tsonopoulos, J. R. Cunningham and G. M. Wilson, "Density, Viscosity, And Surface Tension Of Coal Liquids At High Temperature And Pressure", Ind. Engr. Chem. Process Des. Dev., 1982, 21, 127.

199. Abbott, M. M, and T. G. Kaufmann, "Correlation of Orthobaric Kinematic Viscoscity Of Liquid n-Alkanes", 1970, Can. J. Chem. Eng., 48, 90.

200. Uyehara, O. A. and K. M. Watson, "A Universal Viscosity Correlation", Nat. Petrol. News, 1944, 36, R-714.

201. Lydersen, A. L., Greenkorn, R. A. and Hougen, O. A., "Generalized Thermodynamic Properties of Pure Fluids", Univ. Wiscounsin Eng. Exp. Sta. Report, 4, Madison, October 1955.

202. Kendell, J. and Manroe, K. P., "The Viscosity of Liquid II. The Viscosity-Composition Curve for Ideal Liquid-Mixture", J. Am. Chem. Soc., 1917, 39, 1787.

203. Arrhenius, S., Zeil. Physik. Chem., 1, 285, 1887.

204. Hatschek, E., The Viscosity Of Liquids, D. Van Nostrand Company, New York, 1928.

205. Kouzel, B., "How Pressure Affects Liquid Viscosity of Liquids", Hydrocarbon Process., 1965, 44(3), 277.

206. Quayle, O. R., "The Parachors Of Organic Compounds An Interpretation And Ctalogue", Chem. Rev., 1953, 53, 439.

207. Nokay, R., "Estimate Petrochemical Properties", Chem. Eng., 1959, 66(4), 147.

208. Weinaug, C. F. and Katz, D. L., "Surface Tension of Methane-Propane Mixture", Ind. Eng. Chem., 1943, 35, 329.

209. Abbott, M. M., T. G. Kaufmann and L. Domash, "A Correlation For Predicting Liquid Viscosity Of Petroleum Fractions", Can. J. Chem. Eng., 1971, 49, 379.

210. Oblad, A. G., J. W. Bunger, F. V. Hanson, J. D. Miller, H. R. Ritzma and J. D. Seader, "Tar Sand Reaserch And Development At The University Of Utah", Ann. Rev. Energy, 1987, 12, 283.

211. Smith, J. M., Chemical Engineering Kinetics, McGraw-Hill Book Company, New York, 1981.

212. Muroyama, K., Hashimoto, K., Kawabata, T. and Shioto, M., Kagaku Kogaku Ronbunshu, 1978, 4, 622.

213. Kato, J., Shimida, K., Suzuki, M., Osc, H. and Ohshima, S., Kogyo, Kagakushi, Japan, 1971, 74(6), 1156.

214. American Society of Mechanical Engineers Section VIII, Div. 1, "Rules for Construction of Pressure Vessels", 1991.

215. Richardson, D. R., "How to Design Fluid-Flow Distributor", Chemical Engineering, 1961, May, 1.

216. Litz, W. J., "Design of Gas Distributor", Chemical Engineering, 1972, November, 13.

217. American Society of Mechanical Engineers Section II-A SA-240-89, "Specification for Heat Resisting Chromium and Chromium Nickel Stainless Steel Plate, Sheet and Strip for Pressure Vessels", 1989.

218. American Society of Mechanical Engineers Section II-A SA-182/SA-182M-89, "Specification for Forged or Rolled Alloy Steel Pipe Flanges, Forged or Rolled Alloy Steel Pipe Flanges, Forged Fittings and Valves and Parts for High Temperature", 1989.

219. American Society of Mechanical Engineers Section II-A SA-193/SA-193 M-89, "Specification for Alloy Steel and Stainless Steel Bolting Material for High-Temperature Service", 1989.

220. American Society of Mechanical Engineers Section II-A SA-194/SA-194M-89, "Specification for Carbon and Alloy Steel Nuts for Bolts for High Pressure and High Temperature Services", 1989.

221. American Society of Mechanical Engineers Section II-A SA-312/SA-312M-89, 'Seamless and Welded Austenitic Stainless Steel Pipes", 1989.